# Transport and control of exciton complexes in 2D hybrid materials


DISSERTATION ZUR ERLANGUNG DES DOKTORGRADES
DER NATURWISSENSCHAFTEN (DR. RER. NAT.)
DER FAKULTÄT FÜR PHYSIK
DER UNIVERSITÄT REGENSBURG

vorgelegt von

Jonas David Ziegler
aus Viechtach

im Jahr 2022

Promotionsgesuch eingereicht am: 03.11.2022
Die Arbeit wurde angeleitet von: Prof. Dr. Alexey Chernikov
Prüfungsausschuss:
Prof. Dr. Vladimir Braun
Prof. Dr. Alexey Chernikov
Prof. Dr. David A. Egger
Prof. Dr. Dominique Bougeard

Datum Promotionskolloquium: 30.01.2023

# Contents

# Chapter 1
# Excitons as a tool for future technology and research

Around 2.5 million years ago, the first use of tools by archaic humans is documented and marks one of the most important steps in human evolution [1, 2]. Over many thousands of years, the use of sticks and stones transitioned to the bronze and iron ages by the discovery of smelting, e.g. extracting metals from mineral ore [3, 4]. The industrial revolution based on the development of the steam engine, drastically changing the society [5, 6], was followed by the digital revolution enabled by the sophisticated control of electron movement on the micrometer- and later even nanometer-scale, determining modern life [7, 8].

While this advancement of technology and science is often pinpointed to certain, distinct breakthroughs, the solid foundation of all modern progress is the necessary fundamental theoretical and experimental research accumulated over decades or even centuries by many people of the scientific community. One of these transformative, world-changing inventions surely was the transistor by J. Bardeen, W. Shockley and W. Brattain in 1948 [9–13]. At that time however, working computers already existed for years based on vacuum tubes and immense theoretical programming work [14–16].

Ultimately, the transistor completely replaced vacuum tubes by the miniaturization, improved fabrication techniques and the use of silicon in the following decades, shaping the modern world as we know it today [17]. Since then, silicon-based devices completely dominate the market from computer chips to solar cells, with few exceptions such as light emitting diodes and more specialized sensors. The ever-growing demand of faster computation or highly-efficient solar cells is currently barely satisfied by even smaller and highly-sophisticated fabrication techniques. New materials and concepts are needed for the necessary step towards a new generation of devices, just like the silicon transistor paved the way for the life we know today [18, 19].

Future progress is based on todays fundamental research, forming our perception of the world, in contrast to magic or divine powers explaining the world and

mechanisms in that distant past. Thorough understanding through fundamental research of electron motion and the role of defects in silicon and III-V semiconductors for example allowed the development of state-of-the-art computer chips, detectors, lasers and LEDs [20–25]. Recently emerging nano-materials might be the basis of future devices and understanding of the underlying processes of these systems is therefore essential.

In the field of light-harvesting for electricity generation, a crucial strategy to reduce the use of fossil fuels and minimize the impact of climate change [26], silicone-based solar cells currently dominate the market [27]. New materials and concepts include organic blends or quantum dots and hold the potential to transform the field of photovoltaics, with hybrid organic-inorganic perovskites being one of the most promising candidates. Hybrid perovskites were explored from 1978 on [28], with an increase of attention beginning in the late eighties by the discovery of layered hybrid perovskites. They resemble natural quantum wells, as a semiconducting inorganic layer is sandwiched by organic barriers. Here, groups from Japan [29–46] and Greece [47–55] investigated the structural, electronic and optical behavior of a large group of different three- and two-dimensional compounds, while a group from the US already worked on technologies such as a transistor devices [56–70]. However, the crucial step was the integration into solar cells by A. Kojima and coworkers in 2009, promoting hybrid perovskites from interesting fundamental research objects to one of the most promising materials for light harvesting [71]. From then on, both the research interest and the solar cell efficiency skyrocketed, reaching values above 25% [72–75] profiting from all the knowledge and fabrication recipes persistently acquired for the last 40 years. Still, many open questions remain regarding the excitonic binding energy [35, 44, 76–81], the interaction with phonons [82–89] and the role of the relatively high defect density [90–92]. Eventually, the fundamental research boosted and still drives the evolution of efficient solar cells

Despite this radical improvement and the prospects for industry due to the low-cost solution-based fabrication, major drawbacks include the use of poisonous lead and the low environmental stability under illumination and hydration [93–97]. The search for a more stable compound also brought layered perovskites back into the spotlight due to the encapsulating properties of the organic barrier layers.

However, the two-dimensional nature of layered perovskites leads to the formation of stable excitons, electron-hole pairs bound by Coulomb forces, in contrast to free carriers in silicone, with drastic implications for solar cells: the neutral excitons need to diffuse to one of the contacts to recombine instead of being directly

guided by an electric field. The diffusion coefficient describes the speed of the random-walk-like transport and is governed by scattering events with phonons, defects and other excitons [98–100]. Thorough understanding of the underlying mechanism determining the diffusion is therefore undeniably important for efficient devices[101–104]. Yet, at the start of this project, diffusion of excitons in 2D perovskites was neither experimentally nor theoretically investigated. Additionally, the tightly bound excitons in combination with the mechanically soft perovskite lattice and subsequently strong exciton-phonon interaction represent a major challenge for existing transport models [88]. The organic structures with a high number of atoms per unit cell further complicate theoretical computation [105–108]. Understanding the underlying vibronic-, electronic- and excitonic interactions [37, 109–117], let alone demonstrating mobile excitons, is therefore key for layered perovskites to hold their promise for future opto-electronic applications [118–120].

Excitons could also play a role in the future of computing, where currently several different approaches and ideas are investigated. Here, the research diversity guarantees to find the next generation of technology, since most other designs will probably never progress beyond fundamental research projects. Beside the highly promising field of quantum computing [121–123], concepts include the additional use of the spin of a carrier [124–126] or optical computers [127–130], where photons are the carrier of information and employed for computing. Here, the triumph of optical fibers in replacing electric wires for information transport across large distances is a promising example [131, 132]. However, instead of electrons, excitons could transport information, benefiting from the strong light-matter interaction, providing an excellent interface between electronics and optics [133, 134]. Here, the crucial parameters facilitating the applicability are the exciton binding energy, e.g. the stability, and the mobility. While inorganic materials such as GaAs possess efficient transport, the exciton binding energy is only a few meV and excludes the use at room temperature. Organic crystals on the other side contain strongly bound but localized excitons. Material systems combining sufficient mobility and tightly bound excitons are two-dimensional semiconductors such as transition metal dichalcogenides (TMDCs).

The successful demonstration of stable monolayer graphene directly put the class of layered van der Waals materials in the spotlight of solid state physics and started this vibrant research field of atomically thin layers [135–137]. Until today, different layered materials with properties ranging from semiconducting to magnetic are discovered, while the van der Waals nature enables the combination

independently of lattice constants allowing sheer endless combinations [138–140]. Here, the ease of fabrication enabled the participation of groups all around the world, as inexpensive bulk crystal are commercially available and the exfoliation can be done using regular sticky tape [141–144].

The layered nature allows us to stack independently of the alignment angle due to van der Waals interactions between the layers. This opened the field of moiré physics, where two twisted layers exhibit excotic new properties depending on the alignment angle [145–151]. Here, the rapid development of complex and clean heterostructures in combination with extensive knowlegde of the material system led to the discovery of fascinating effects such as Wigner-Seitz crystals [152–155]. However, while van der Waals heterostructures even serve as an alternative tool to ultra cold atoms to study correlated many body physics[156–167], the development of advanced excitonic devices still poses a major challenge. The difficulty in spatially controlling excitons stems from their electrically neutral nature, making them insensitive to electric fields. However, the atomically thin nature of TMDCs enables other tuning mechanisms, such as strain engineering, e.g. local stretching or compressing of the layer, or by changing the dielectric environment. Due to the size of the electron-hole-pair, the exciton is significantly sensitive to its surrounding dielectric environment, which then can be used to change fundamental properties [168–174] . This sensitivity is strong enough to use excitons as a new investigation tool. Employed as dielectric sensor for correlated states in nearby materials, excitons in TMDCs for example allow optical readout of the quantum hall effect in bilayer graphene [175] or study Hubbard-model physics in a moiré lattice [158, 176]. Other current approaches to gain control of excitons take advantage of the dipole moment of interlayer excitons, electron-hole pairs separated to different layers of a heterostructure. The direct and extrinsic control of exciton movement allows not only the development of future devices such as excitonic transistors [177–180], but also the investigation of more exotic exciton physics such as the excitonic valley-hall effect [181–186].

In this thesis, we investigate the spatial propagation of excitonic quasi-particles in monolayer $WSe_2$ and layered perovskites and explore ways of controlling excitons. In the first part, we utilize gallium-arsenide nanowires to locally strain a single layer $WSe_2$ encapsulated in insulating hexagonal boron nitride (hBN). As stretching the lattice leads to a decrease of the band gap, this geometry allows to create one dimensional potential channels in the two dimensional layer. The impact of strain on the energetic landscape is directly determined by photoluminescence measurements, where also underlying changes of the finestructure can

be resolved, due the encapsulation in the atomically flat hBN ensuring narrow spectral linewidths. Then, we employ time-and spatially resolved PL to directly monitor the effect of strain on the exciton diffusion and successfully demonstrate the guiding along a 1D-channel both at cryogenic temperatures and ambient conditions.

Exciton propagation will also be the main theme of the second part, focusing on layered organic-inorganic perovskites. Here, we investigate the nature of exciton diffusion of such a hybrid material, as organic and inorganic systems are often characterized by contrasting, underlying transport mechanisms. On the one side, the so-called hopping transport model is used to describe the slow movement between localized states in most organic crystals, while band-like transport is observed for many inorganic crystals. Here, we adopt the encapsulation in hBN for thin sheets of the layered perovskite $PEA_2PbI_4$ in order to drastically increase the environmental stability. The temperature dependence of the diffusion coefficient is one of the key parameters to distinguish different transport mechanism and is directly determined by spatially- and temporally-resolved microscopy in the temperature range of 5 K to 300 K. Additionally, for a second perovskite system with a slightly different organic spacer molecule, namely $BA_2PbI_4$, the phase transition with a predicted change of the effective mass allows to assess current exciton models.

Finally, we achieve electrical control of the optical response of layered perovskites by fabricating gate-tunable field effect devices. The observation of highly stable trions, excitons with an additional Coulomb-bound charge carrier, serves as future approach to control the spatial propagation. The electrical control of the charge carrier density also allows to extend the investigation of correlated many-body physics to layered perovskites, while the adjustable optical response might lead to future nanoscale opto-electronic devices.

Before discussing these experimental results in chapter 4 and 5, we give a brief overview of the two material systems and important concepts of excitons and their transport properties in chapter 2. Subsequently, chapter 3 describes in detail the sample fabrication based on two different techniques and should also serve as guideline to easily reproduce the employed methods and samples. Additionally, the experimental techniques used to investigate key exciton properties, such as reflectance contrast spectroscopy and two-photon excitation photoluminescence are presented in chapter 3, including the corresponding analysis of the data. Lastly, the results are summarized in chapter 6 with a final remarks on future research directions and applications.

# Chapter 2
# 2D van der Waals semiconductors

The discovery of stable, atomically thin layers opens the way for intriguing mechanical and opto-electronic properties as well as displays an ideal playground for exploring excitonic properties. Here, the weak van der Waals interaction between strongly in-plane bound layers allows this exfoliation down to the single layer and also gives those materials the name van der Waals crystals. This second chapter serves as introduction into the field of two-dimensional semiconductors and lays the basic foundation of the investigated 2D materials. First, the crystal structure and resulting electronic properties of the two investigated material systems, namely transition metal dichalcogenides (TMDCs) and layered hybrid perovskites, are described. Both, the demonstrated differences but also similarities of these seemingly contrasting materials will follow us throughout this thesis. The next two chapters deal with their most important parallel: Excitons, strongly bound electron-hole pairs which dominate the optical properties. After focusing on their basic properties and discussing the restrictions introduced by the two-dimensional electronic structure, the real space movement of these quasi-particles through the crystal is outlined on the basis of different transport models.

## 2.1 Transition metal dichalcogenides

### Crystal structure

Transition metal dichalcogenides are a subclass of the general material class of the chalcogenides and consist of one transition metal atom M and two chalcogen atoms X [187, 188]. This results in the stochiometric formula $MX_2$, where the focus of this thesis will be on the semiconducting compound $WSe_2$, which is very closely related to other prominent TMDCs consisting of either tungsten or molybdenum as metal and sulfur or selenium as chalcogenide. Probably the most famous one is $MoS_2$ or "moly", which was described as early as 1923 [189] and has found its way into everyday life as engine oil. TMDCs are so-called van der Waals crystals, which are strongly bound layers stacked together by van der Waals forces. These

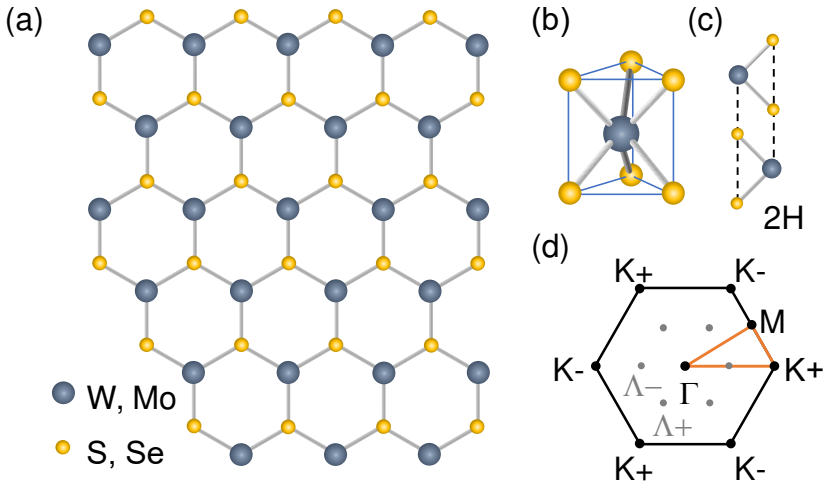


**Figure 2.1:** **(a)** Crystal structure of a single layer transition metal dichalcogenides in the top view with chalcogenides in yellow and the transition metal atoms in blue. **(b)** Trigonal prismatic unit cell, highlighting the two chalcogen atoms on top of each other. **(c)** Naturally ocurring 2H phase, where alternating layers are rotated by 180°. **(d)** First Brillouin zone of the hexagonal lattice of a TMDC monolayer including the symmetry points K, Λ , Γ and M. Adapted from with permission from [190].

layers can easily slide in respect to each other, creating the low-friction used in lubricants and, for the case of graphite, in pencils [135, 136].

The top view in Fig. 2.1(a) shows the hexagonal lattice of a single layer with a two-atomic base, resulting in the reduced $D_{6h}$ point group with an in-plane lattice constant of 3.3 Å for $WSe_2$ [188]. A single monolayer consists of three layers of atoms, where the transition metal atoms are sandwiched between two layers of chalcogen atoms, as further illustrated by 2.1(b), creating a trigonal prismatic unit cell. Multiple layers can form in different phases and stacking orders, with the most common and naturally occuring 2H phase shown in 2.1(c) [190, 191]. Here, neighboring layers are rotated by 180° and stacked in ABAB order, where the metal atoms are on top of the chalcogen atoms of an adjacent layer and vice versa. Other phases are the also semiconducting 3R and the metallic 1T phase. The strong in-plane covalent bonds and only weak out-of-plane van der Waals interaction allows the separation of layers by mechanical exfoliation down to a single layer [135, 136]. In contrast to the bulk material and even-numbered layers, thin uneven-numbered layers lack an inversion center, most prominently in the monolayer limit [192, 193]. In addition to quantum confinement effects, this strongly affects the opto-electronic properties such as second harmonic generation further and is detailed later on. From the hexagonal lattice in real space directly

follows a hexagonal lattice in k-space, with the first Brillouin zone presented in 2.1(d). The center is the high symmetry point Γ surrounded by the other high symmetry points K and M, whereas the low symmetry point Λ is located at 0.55 between Γ and K [194–196]. For the monolayer or thin, uneven numbered layers, opposing K- and Λ-points are not equal. This is a direct consequence of time-reversal symmetry requiring opposing spins at opposing positions in k-space. The inequality of opposing K-valleys due to the broken inversion symmetry is resembled by introducing the valley index $\tau = \pm 1$. This is generally directly associated with the symmetry points K+ and K- (or Λ+ and Λ-). The impact on optical properties will be discussed after briefly introducing the general electronic structure.

## Electronic structure

Initially, TMDCs were only known in their bulk form and therefore categorized as indirect band gap semiconductors [188, 194, 195, 197, 198]. The discovery of a sudden transition into a direct band gap semiconductor in the monolayer limit alongside the fascinating spin-valley dynamics lead to an increasing interest in atomically thin materials, tremendously facilitated by the low-cost and straightforward fabrication [199–201]. The evolution towards the direct gap is prototypically shown for $MoS_2$ in Fig. 2.2(a), which is qualitatively similar for other TMDCs. For layers down to the bilayer, the valence band maximum is located at the Γ-point while the conduction band minimum is at the Λ-point, making the transition momentum indirect. In order to understand the change to a direct gap in the monolayer limit, the atomic orbitals contributing to the relevant points in k-space need to be considered [199, 200].

At the extrema of high symmetry points the contributions from different orbitals are well defined, the valence band edge at the Γ-point is formed by a combination of molybdenum $d_z$ and sulfur $p_z$ orbitals [202, 203]. Both the interlayer orientation and the location at the sulfur atoms, e.g. on the exterior of the layer, leads to a high sensitivity on the surrounding and interlayer coupling. Similarly, the conduction band minimum at the Λ-point is mainly made up by $p_x$ and $p_y$ orbitals of the corresponding chalcogen. Contrarily, mainly the molybdenum $d$ orbitals, firmly localized in the middle of a single layer, form both the conduction and valence band edges at the $K$ point. Hence, when decreasing the layer number the wave function overlap at the Λ- and Γ-point also decreases and leads to an energy shift, while the K-point remains nearly unchanged [204, 205]. In total, this leads to the scenario depicted in Fig. 2.2(a), where the indirect transition from

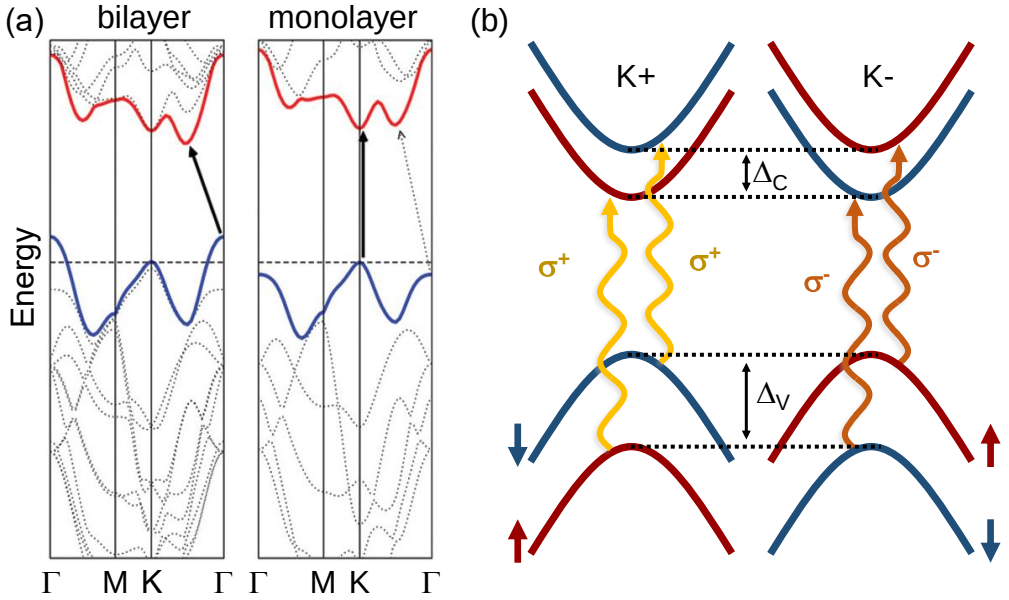


**Figure 2.2:** **(a)** DFT-calculation of the $MoS_2$ band structure for a bilayer and monolayer, transitioning from an indirect to a direct band gap. Adapted with permission from [200]. **(b)** Schematic electronic band structure for $WSe_2$ including spin orbit coupling. $\Delta_{V/C}$ denotes the spin orbit splitting in the respective bands and different spin orientations of the bands are indicated by blue and red colours. Only a $\sigma^+$ transition is allowed at the K+ point, while at the K- point only a $\sigma^-$ transition is possible.

Γ to Λ increases substantially in the monolayer limit, making the unaffected K-K transition the direct transition.

In addition to the peculiar evolution of the band gap, the orbitals of the heavy metal atoms also lead to strong spin-orbit interactions [204–207]. This leads to a significant splitting of both the valence and conduction bands at the K-points. For $WSe_2$ the calculated values are on the order of $\Delta_V = 470$ meV and $\Delta_C$ =-40 meV, whereas the values for Mo-based TMDCs are generally lower due to the lighter metal atoms [205]. In combination with the previously discussed inversion symmetry breaking, this leads to the opposite signs of the splitting in oppsite valleys, as shown in 2.2(b) [208–210]. This spin-valley locking allows to selectively address either the K+ or K- valley by $\sigma^+$ or $\sigma^-$ polarized light, respectively [192, 206, 211, 212]. Combining these selection rules with spin conservation and the negative spin-orbit splitting in the conduction band, this makes the lowest lying transition a forbidden one, as depicted in 2.2(b) [208, 209]. Before considering the implications on the electro-optical properties, the discussion of the crystal and electronic structure is extended to a second class of low-dimensional materials, the layered hybrid perovskites.

## 2.2 Layered organic-inorganic hybrid perovskites

Historically, calcium titanate with the chemical formula $CaTiO_3$ was found by the german geologist Gustav Rose in the Ural mountains and named *perovskite* after the russian Lev Perovski [213]. Later, the name was extended to all structures with the chemical formula of $ABX_3$, which is one of the most abundant crystal classes today and contains many different materials with highly diverse properties[213, 214].

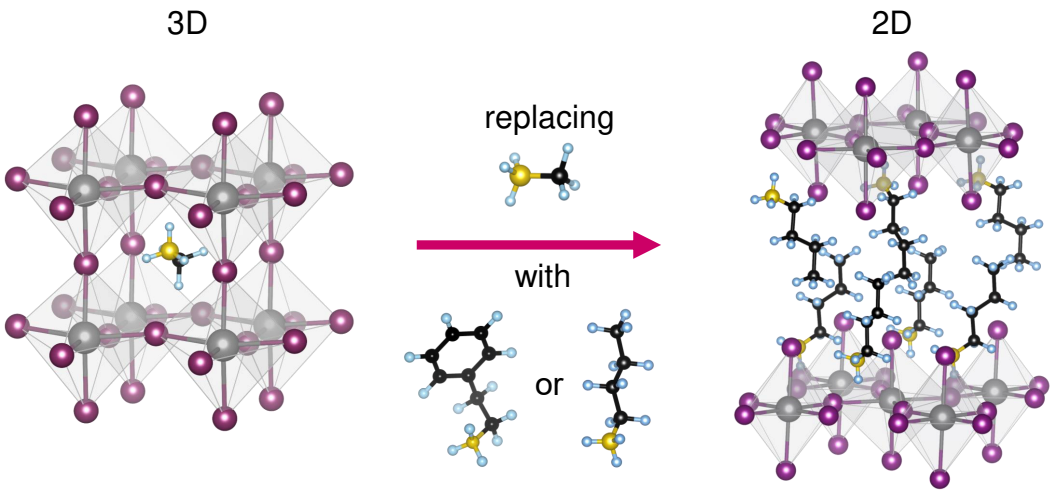


**Figure 2.3:** Cubic structure of the prototypical 3D organic-inorganic hybrid perovskite methylammonium lead iodide. The layered 2D Ruddlesden-Popper phase perovskites are created by increasing the size of the organic spacers, isolating single layers. Two widely used spacers, namely phenylethylammonium (PEA) and butylammonium (BA) are shown in the middle. Crystallographic data obtained from [215] and [216].

Today, the term perovskite often means hybrid organic-inorganic metal halide perovskites, which gained immense attraction for their rapid increase of photovoltaic efficiency up to more than 25% for an all-perovskite solar cell over the course of a few years [71, 74, 217]. Figure 2.3(a) shows the prototypical cubic methylammonium lead iodide $CH_3NH_3PbI_3$, where the cation A is the organic methylammonium (MA) together with the inorganic B cation being lead Pb and the anion X being a halogen atom, such as iodine $I$, bromide $Br$ or chlorine $Cl$ [28, 215]. In contrast to the sophisticated fabrication of silicon at high temperatures, hybrid metal halide perovskite are manufactured by low-cost wet chemistry [60, 83, 218]. Crystals can be grown from solution or thin-films directly deposited by spin coating. Current challenges include the low environmental stability under

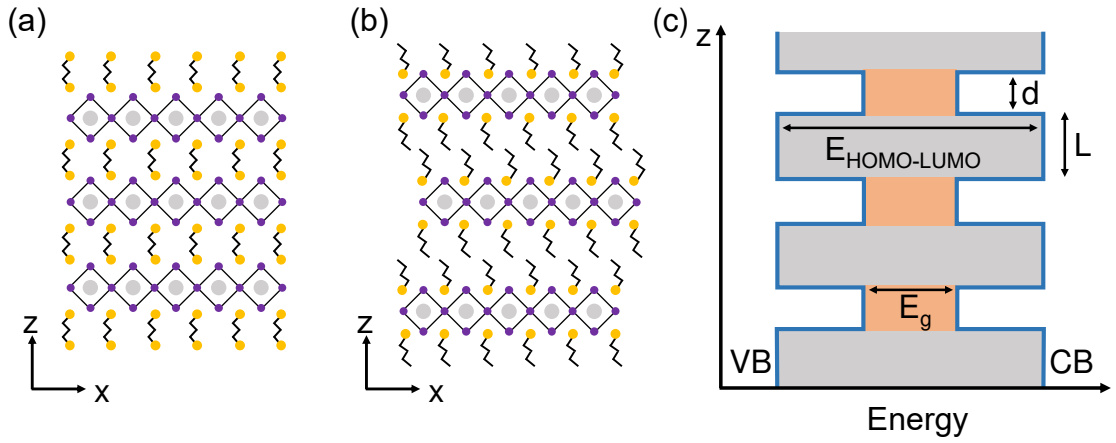


**Figure 2.4:** **(a)** Dion-Jacobson phase of 2D layered perovskites, where neighbouring layers share a diammonium spacer. **(b)** In the Ruddlesden-Popper phase each layer consists of an inorganic layer, sandwiched between two organic spacers. The layers are then weakly bound by van der Waals interactions.**(c)** Energy diagram of the layered perovskite structure with type-I band aligment, where the bandgap of the inorganic layer lies inbetween the HOMO-LUMO gap of the organic spacer. The quantum well structure can be chemically tuned by both the length L of the organic spacer molecule and the quantum well thickness d.

illumination and moisture as well as substituting the long-term poisonous lead [219, 220].

The rush for more efficient and stable perovskite structures also brought renewed interest to layered hybrid organic-inorganic structures, after being first synthesized and investigated more than twenty years ago [29, 31, 42, 49, 56]. As depicted in 2.3, layered perovskites form by increasing the size of the organic spacers, which need to be small enough to for the 3D perovskite lattice to crystallize. The limiting factor for the size is often estimated by the Goldschmidt's Tolerance Factor, which treats the ions as hard spheres and allows mainly two organic ions for 3D hybrid perovskites: methylammonium $CH_3NH_3$ and formamidinium $CH_5N_2$ [221, 222].

In contrast to that, the layered perovskites can crystallize with many many different organic spacers, as the space between layers can be is separate from the layer itself. Layered perovskites can adopt diverse structures, where the most popular one can be grouped into two different phases: Dion-Jacobsen and Ruddlesden-Popper (RP)[223]. While the inorganic layers share the organic barrier molecule in the Dion-Jacobsen phase as depicted in Fig. 2.4(a) resulting in the general formula of $ABX_4$, each inorganic layer has two organic spacers on each side in the RP phase [29, 48, 224, 225]. In the latter, the layers are then weakly bound by

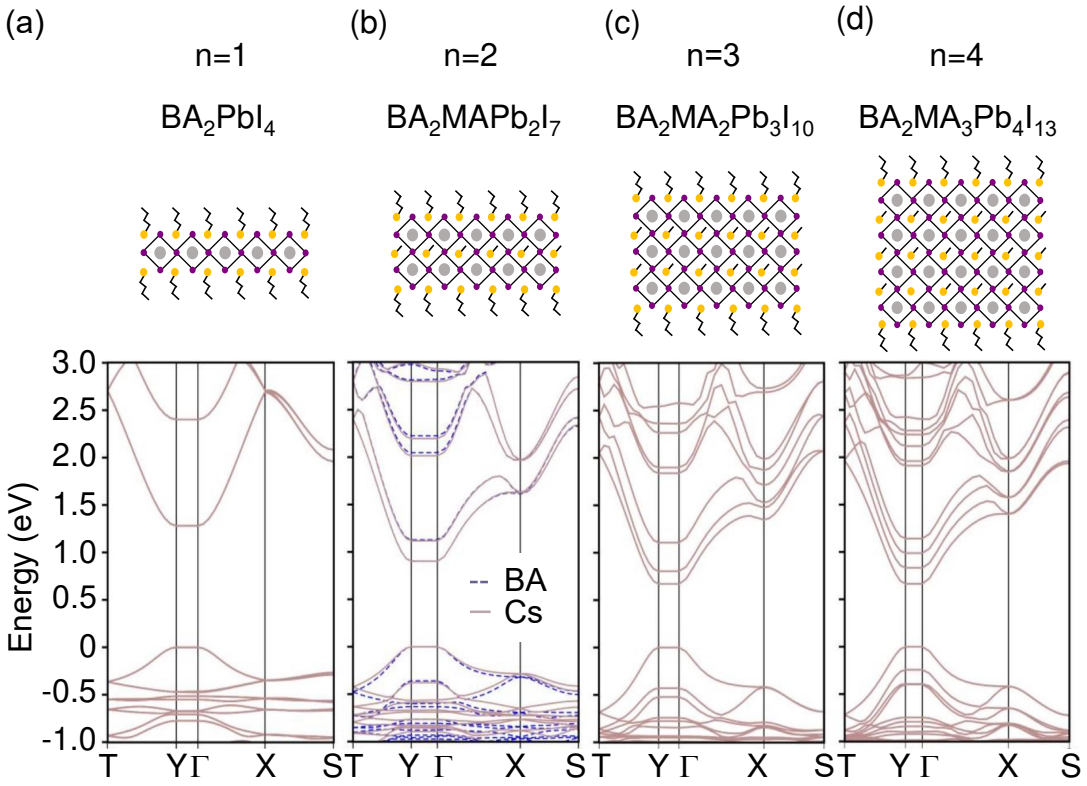


**Figure 2.5:** Bandstructure of Ruddlesden-Popper phase layered perovskites obtained from DFT-calculations by replacing the organic by a Cs-atom. With increasing number of inorganic layers per spacers the bandgap decreases from one layer (a) to four layers (d) per sheet. The calculated bandstructure in (b) shows a comparison between the approximation by replacing the organic with a single Cs-atom and the calculation with the organic structure. Adapted with permission from [226]

van der Waals interactions, similar to TMDCs. This leads to the chemical formula of $A_2BX_4$ and is shown in Fig. 2.4(b).

The main focus of this thesis is on two prototypical members of the RP phase, namely phenylethylammonium lead iodide ($C_6H_5CH_2CH_2NH_3\,PbI_4$, from now on PEA) and butylammonium lead iodide ($C_4H_9NH_3\,PbI_4$, now called BA), where the two spacer molecules are shown in detail in Fig. 2.4. For BA, shown in Fig. 2.4(b), the resulting crystal structure at room temperature has an orthorhombic space group with the parameters $a = 8.428\,\text{Å}$, $b = 8.986\,\text{Å}$ and $c = 26.233\,\text{Å}$[227]. In contrast to PEA, the closely related BA undergoes a phase transition around 270 K, where the lattice constants and angles change [114, 227]. While the general crystal symmetry not necessarily changes across this phase transition, important parameters such as lattice constant and tilt angle change and directly impact the electronic properties discussed later.

The layered structure creates ideally ordered natural quantum wells, as the stoichiometrically fixed crystalline structure strongly reduces interfacial disorder and roughness [110]. As depicted in Fig. 2.4, most layered hybrid perovskites show type-I band aligment with the inorganic bandgap lying between the HOMO-LUMO gap of the organic spacer [66, 228, 229]. The chemical flexibility allows to tune the quantum well parameters, the spacer thickness L can be varied by using longer or shorter spacer molecules, for example different alkylammonium chains $C_nH_{2n+1}NH_3$ from n=4-18 [30, 155, 227, 230]. Additionally, the lateral size of the spacer impacts the crystal structure by steric effects and can for example be precisely modified by functionalization, e.g. replacing a single hydrogen atom by another larger atoms such as fluoride [70, 231].

The chemical flexibility and progress in synthesis also allows tuning of the quantum well thickness d by increasing the thickness of the inorganic layer [57, 232–234]. As shown in the top row of Fig. 2.5, the quantum well thickness increases by incorporating additional inorganic layers per spacer. As the number of inorganic layers increases, quantum confinement and dielectric effects decrease and the crystal approaches the properties of the 3D crystal [226, 235].

Similar to the case of TMDCs, detailed knowledge of the electronic structure is crucial for understanding the complex properties. Enormous theoretical efforts have made substantial advances regarding understanding the electronic structure, despite the complex nature of complex hybrid organic-inorganic systems. One reason is the complex hybridization of both valence and conduction band between the metal s- and p-orbitals and the halide p-orbitals [228, 236]. Another complication lies in the large unit cells with a high number of atoms due to the organic parts. An effective approximation is replacing the organic part by a single cesium atom, which yields results surprisingly similar to the full structure [108]. The calculated band structure for the different thicknesses shown in the bottom panel of Fig. 2.5 was calculated using Cs instead of the full organic spacer, the comparison is shown for n=2. Fig 2.5(b) also demonstrates the systematic decrease of the band gap with increasing number of inorganic layers for a single sheet due to the changing quantum confinement, along with the formation of additional subbands [226].

Besides the expected changes of the band gap by tuning the quantum well parameters, the electronic properties severly depend on the exact lattice parameters. Hybrid perovskites are often characterized with a *soft* lattice, which means the crystal has low bulk moduli and can be easily mechanically compressed [237–240]. This is ascribed to the relatively weak interaction inside the lattice caused by the

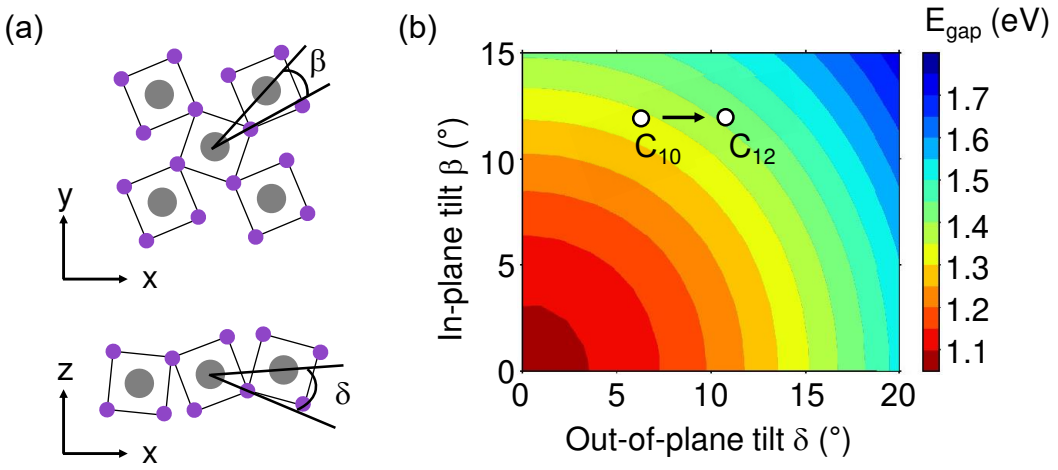


**Figure 2.6:** **(a)** Top view of the lattice where $\beta$ resembles the in-plane tilt angle. Bottom panel shows the side view with the out-of-plane $\delta$ tilt angles of neighboring inorganic octahedra. **(b)** Impact of the tilt angles on the calculated band gap of $Cs_2PbI_4$, tilt angles of the two different alkylammonium spacers, where $C_n$ refers to the number of carbon atoms in the alkyl-chain. Adapted with permission from [229].

low total charge forming the ionic lattice. Importantly, this leads to low energy phonons and large, anharmonic lattice distortions [87, 88, 241, 242]. This softness also causes a small change of the organic spacer molecule to severly impact the band gap by small changes of the octahedral tilt [114, 229]. The latter describes the distortion of the inorganic octahedras, defined as the in-plane tilt angle $\beta$ (Fig. 2.6(a) top) and out-of-plane tilt $\delta$ (Fig. 2.6(a) bottom). The impact of the tilting is illustrated in Fig. 2.6(b), calculated for the exemplary structure of $Cs_2PbI_4$. A drastic change of about 200 meV occurs by increasing the length of the alkylammonium chain from 10 to 12 Carbon or C atoms ( from decyl- to dodecylammonium)[229]. Similar changes occur at the phase transition, where a small change of the tilt angle already drastically changes important parameters such as the band gap and effective mass of the charge carriers [114, 227]. The changes at the phase transition are also particularly relevant in the context of the excitonic properties studied in this thesis.

## 2.3 Exciton complexes in two dimensions

The previous sections outline the crystal structure and the resulting electronic properties, where we briefly discuss photo-excited electrons of the single-particle band structure. However, one of the fundamental interactions in solid state physics, the Coulomb interaction, holding crystals or molecules together, also exists between charges inside the crystal. This leads to the formation of strongly bound electron-hole pairs from excited charge carries, known as excitons.

### 2.3.1 Coulomb-bound electron hole pairs

The concept of excitons as Coulomb-bound electron-hole pairs is the solid-state analogy to the hydrogen atom [243–245]. The Coulomb-interaction not only enables bound states, but also impacts the band structure via the electron-electron interaction [171–173, 246, 247]. This leads to a renormalization of the band gap $E_{gap}$ to higher energies compared to the single particle band gap, which is especially important when comparing experimentally determined values with theoretical calculations of a single particle structure.

Excitons are traditionally separated into Frenkel- and Wannier-Mott excitons, where the latter description is closely related to the hydrogen model and successfully applied for TMDCs and perovskites [245, 248]. In general, Frenkel-type excitons are characterized by a high binding energy in the eV-range and localized to a single atomic site, while Wannier-Mott excitons exhibit smaller binding energies and a wave function spreading over many lattice sites. The exciton binding energy is obtained from the 2D hydrogen model where the effective masses $m_e$ and $m_h$ of electron and hole, respectively, take the place of electron and proton masses. Here, the effective masses approximate the movement of the carriers in the periodic potential of the crystal. Additionally, the dielectric surrounding of the crystal needs to be taken into account, while the reduced dimensionality directly enhances the interaction of the confined carriers, resulting in following solution of the 2D hydrogen model [244, 245]:

$$E_X = E_{gap} - \frac{1}{2}\frac{\mu e^4}{(4\pi\epsilon_0\epsilon_{ext})^2\hbar^2}\frac{1}{(n-\frac{1}{2})^2} + \frac{\hbar^2 K^2}{2M}, \text{ with } \mu = \frac{m_e \cdot m_h}{m_e + m_h} \tag{2.1}$$

with $\mu$ being the reduced mass and $M = m_e + m_h$ the total or translational mass and $K = k_e + k_h$ the combined electron and hole momentum or total exciton momentum. In analogy to the hydrogen model, $n = 1, 2, 3, ...$ denotes the prin-

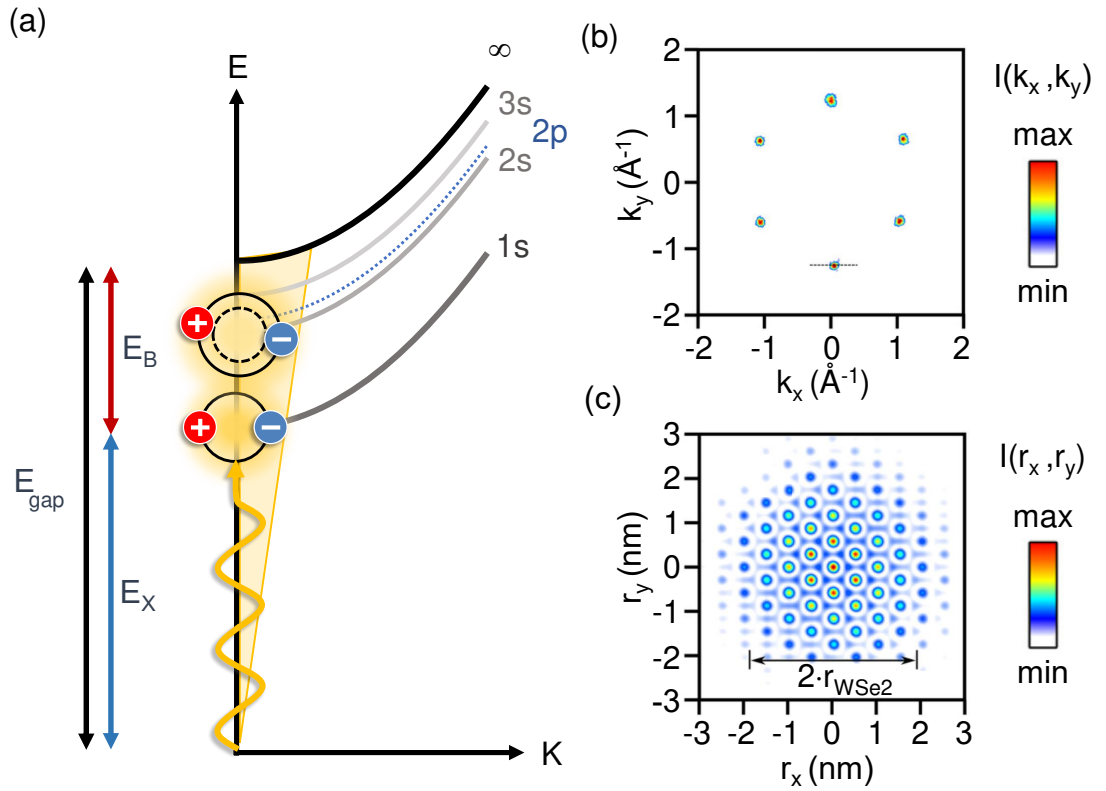


**Figure 2.7:** **(a)** Exciton band structure with the band gap $E_{gap}$, the exciton binding energy $E_B$ and the resulting energy needed to excite an exciton $E_X$. Similar to the hydrogen atom, higher excited states are labeled by 2s and 2p until the continuum $\infty$ is reached above the binding energy. The momentum conservation restricts transitions to $\Delta K \cdot c \leq E_{photon}$, where K denotes the combined exciton momentum, and is indicated by the yellow light cone. **(b)** Momentum distribution of excitons in the six K-valleys in $WSe_2$ obtained from the excitonic contribution to the conduction band. **(c)** Real-space representation of excitons represented by the electron density distribution of the exciton wave function obtained by Fourier transforming the momentum resolved data. Here, the underlying hexagonal lattice is directly visible. Adapted with permission from [249]

cipal quantum number. While the binding energy of the excited states decreases quadratically with n, the Bohr radius increases linearly with n [244, 245].

The resulting exciton dispersion is schematically shown in Fig. 2.7(a). The recombination of the ground state n=1 exciton then occurs at the energy $E_X$ and is also called optical band gap, as it is the lowest dipole-allowed optical transition [250]. Upon recombination, the momentum needs to be conserved, creating the so-called light cone for excitons, where the exciton momentum $K$ can be matched by the light dispersion, i.e. equal to the in-plane momentum of the photon, $q_{photon}$ [250]. The energy of the emitted photon is the electronic band gap $E_{gap}$ reduced by the exciton binding energy $E_B$, the second term in equation 2.1. The excitonic

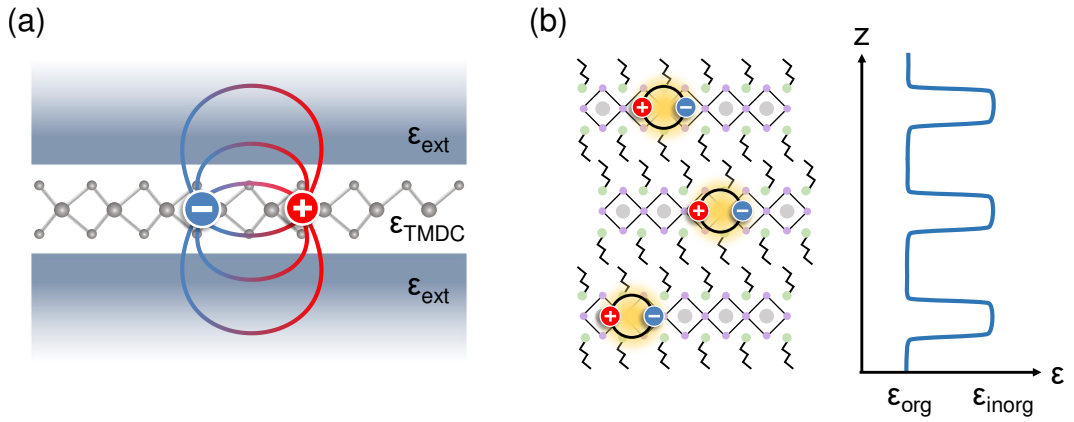


**Figure 2.8:** **(a)** Illustration of the dielectric screening of excitons restricted to the two-dimensional layer but a three-dimensional Coulomb interaction. Electric field lines extend outside the two-layer and cause substantial sensitivity on the environment. Adapted with permission from [254]. **(b)** Screening of excitons in layered perovskites, where the dielectric constant periodically changes between the organic $\epsilon_{org}$ and inorganic $\epsilon_{in}$ dielectric.

dispersion for TMDCs is shown in Fig. 2.7(b), where the six different K-valleys are directly measured by time-resolved angular-resolved photo emission spectroscopy from Ref. [249]. Additionally, the real-space distribution can be obtained by Fourier transformation of the momentum-resolved data, where the extension of the exciton across multiple lattice constants can be seen in Fig. 2.7(c) [249, 251]. The size of the exciton can then be described by the Bohr radius, which can be estimated to be around 1.7 nm for $WSe_2$ [249, 252, 253].

An important consideration for monolayer TMDCs and layered perovskites in this context is non-uniform screening of the layers and their surrounding [246][226]. The electric field lines between electron and hole lie not only inside the layer, but also extend outside the material, where the dielectric constant can differ strongly from the high dielectric constant of TMDCs, as depicted in Fig. 2.8(a). A more realistic scenario is the asymmetric example where the vacuum dielectric constant, or a thin layer of adsorbed water, exists on top of the layer and the dielectric constant of the substrate from below. For layered perovskites, the dielectric constant periodically changes between the organic and the higher dielectric constant of the inorganic layer. For both materials, this not only changes the excitonic binding energy as can be seen from the dependence on the dielectric constant in equation 2.1, but also renormalizes the fundamental band gap due to the repulsive electron-electron interaction. In terms of theoretical modeling, this is often accounted by replacing the Coulombic $\frac{1}{r}$ - dependence, where $r = r_e - r_h$, by a modified effective

potential:

$$V(r) = -\frac{\pi e^2}{(1+\epsilon_{ext})}\left[H_0\left(\frac{r}{r_0}\right) - Y_0\left(\frac{r}{r_0}\right)\right] \tag{2.2}$$

with the Struve and Neumann functions $H_0$ and $Y_0$ depending on the effective screening length $r_0$. This potential scales for short ranges as $log(r)$ for $r << r_0$ and results for large distances $r >> r_0$ in the regular $\frac{1}{r}$ dependence. This leads to a deviation from the standard hydrogen model, in agreement with experimental observations [246, 253, 255], while more accurate models based on the GW approximation, Bethe-Salpeter equation and including the finite thickness of the monolayer exist [256, 257]. The general scaling of Coulomb interactions and therefore binding energy then strongly depends on the dielectric constant of both the material itself and the surrounding, as well as the thickness of the material [170–173, 258].

Also, the strong dependence on the dielectric environment allows deterministic tuning of the binding energy via the surrounding. In layered perovskites, changing the organic spacers to strongly-screening, polar spacers allows to modify the exciton binding energy by more than one order of magnitude [259, 260]. In TMDCs on the other side, using proximate graphene or periodically-structured substrates with different dielectric constants allows to tune key excitonic properties [171, 172, 174]. Recently, using the even more pronounced dependence of excited states on the dielectric environment, $WSe_2$ monolayers are employed as sensors for strongly-correlated phases in twisted heterostructures and graphene[158, 175].

In the same way, the environmental sensitivity can also be a source of disorder. Although the excitonic transitions are defined at certain, discrete energy levels, the resonance is not a delta-function like peak, but is broadened. In addition to strain fluctuations, dielectric disorder, where a fluctuating dielectric constant of the environment directly impacts the exciton energy, is one source of disorder, depicted in Fig. 2.9(a) [173]. As the exact energy of the transition strongly depends on the randomly changing potential, the broadening is of inhomogeneous nature and commonly described by a gaussian function, as illustrated in Fig.2.9(b). For TMDCs, this can be greatly reduced by introducing a constant dielectric surrounding by fully encapsulating the monolayer between two ultra-flat sheets of hBN [173, 261–263].

Looking back at the solution of the 2D hydrogen model in Eq. 2.1 and the exciton band structure presented in Fig. 2.7, the resulting emission or absorption spectrum is presented in Fig. 2.9(c). Here, the ground state appears as sharp

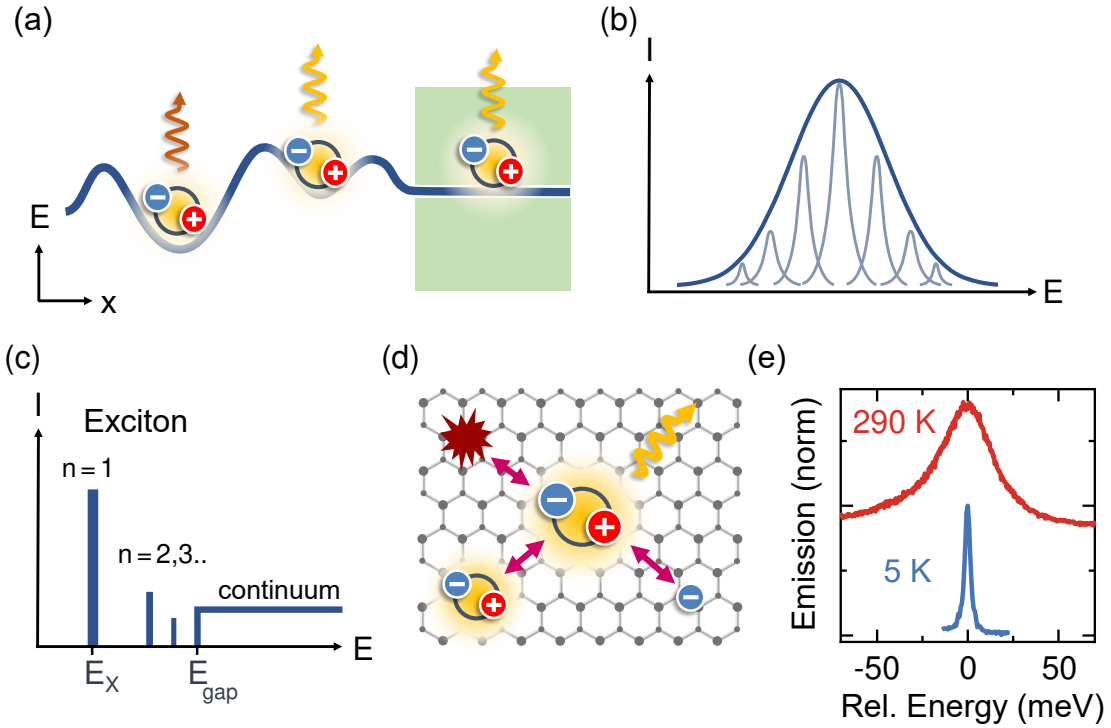


**Figure 2.9:** **(a)** Disorder in the potential landscape of the exciton leading to inhomogeneous broadening, where a constant dielectric environment suppresses dielectric disorder. **(b)** Resulting inhomogeneous broadening as result of an ensemble of peaks. **(c)** Symbolic exciton spectrum with ground (n=1), excited states (n=2,3) and the continuum above the band gap. **(d)** Illustration of different interactions an exciton is subject to leading to homogeneous broadening. **(e)** Exemplary broadening of the emission spectra of the ground state exciton resonance in $WSe_2$ at cryogenic and room temperature.

line with the excited states at higher energy approaching the band gap with the continuum. These states are also subject to fundamental broadening mechanism depicted in Fig. 2.9(d),which can not be avoided such as the radiative broadening [244][264]. Here, the uncertainty principle already gives a broadening depending on the radiative lifetime $\tau_{rad}$ of the exciton according to $\Delta E_{rad} = \hbar/\tau_{rad}$. The high oscillator strength of TMDCs leads to a short radiative lifetime and consequently high radiative broadening. This is especially important when other forms of broadening, such as scattering with phonons, charge carriers or other excitons, are negligible, e.g. at low temperatures and low excitation densities. For both, encapsulated TMDCs and layered perovskites, the linewidth broadening is increasingly dominated by scattering with phonons [110, 264]. This strongly depends on the phonon population and therefore the temperature, but also on the available final state for the scattered exciton. Figure 2.9(e) directly visualizes the broadened emission of the ground state exciton in $WSe_2$, where the radia-

tive recombination governs the spectrum at low temperatures, while at elevated temperatures additional broadening from phonon-scattering dominates. Here, the quasi-elastic scattering with low energy phonons of the accoustic phonon branch leads to a linear increase of the broadening with temperature due to the linearly increasing number of available phonons [265, 266]. At higher temperatures, more and higher energy acoustic and also optical phonon modes become available and lead to a super-linear increase of the linewidth. In general, phonons not only scatter with excitons, but also with other excitonic quasi-particles introduced in the next section.

These scattering events of the exciton take place during the lifetime $\tau$, e.g. the average time between excitation and recombination, of an exciton, which consists radiative- and non-radiative contributions $\tau_{non-rad}$, . Therefore, an overall lifetime is given by a combination of all these effects via the following equation:

$$\frac{1}{\tau} = \frac{1}{\tau_{eff-rad}} + \frac{1}{\tau_{non-rad}} \tag{2.3}$$

Here, the radiative part is given as effective lifetime, as also the relaxation of excitons inside the light cone needs to be taken into account, in contrast to the purely radiative lifetime $\tau_{rad}$ [250, 267]. For bright excitons the lifetime is dominated by the short effective radiative lifetime, especially at low temperatures. The non-radiative contributions, for example given by defect recombination, plays a crucial role for dark states discussed in the next section.

### 2.3.2 Dark, charged and other exciton complexes

In the previous sections we already mentioned that some optical transitions are dipole forbidden due to spin selection rules or missing momentum conservation. However, excitons formed by electron and holes from these states normally do not emit light or can be directly optically excited and are therefore called *dark* excitons [268–272]. It is instructive to return to the single-particle band structure, as the different valleys of electron and hole can be better visualized in this manner.. As for monolayer $WSe_2$ the lowest lying transition is forbidden, different dark exciton states emerge as depicted in Fig. 2.10. These include the spin-forbidden K-K transition and the two momentum-forbidden excitons forming with the conduction band electron sitting in the $\Lambda$ and $K-$ valley, respectively.

Yet, dark excitons can still emit light and conserve spin or momentum. The strong spin-orbit interaction induces an additional spin-mixing of the topmost

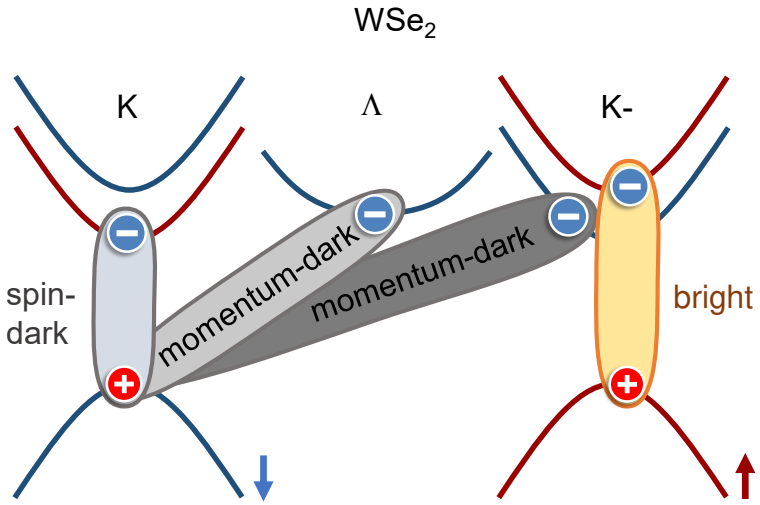


**Figure 2.10:** Dark excitons in $WSe_2$. Momentum-indirect excitons formed from a hole in one K-valley and the electron either in the other K-valley or the Λ-valley are generally allowed by the selection rules, but forbidden by momentum conservation. Spin-dark excitons are the lowest lying exciton in tungsten-based TMDCs, but forbidden by spin conservation in the in-plane polarization. The lowest bright excitons are formed by electron and hole from the same K-valley and the same spin-orientation of the band. Additionally, both spin- and momentum forbidden excitons with the hole residing in one K-valley and the electron in the upper conduction band of the other valley exist (not shown).

valence band, which results in two excitonic states. While the transition of one is completely forbidden, the other one is allowed in z-polarization, e.g. emitting in the in-plane direction. This allows to directly access the spin-dark state $D_0$ using in-plane detection or using a high NA objective, which partially collects the in-plane light [273–275].

Additional processes can contribute to the radiative recombination of dark excitons, similar to the absorption of light in indirect semiconductors. Momentum-dark states, forming between holes in the K valley and electrons in the K- valley or Λ valley, can emit light through phonon scattering processes. Here, an additional phonon ensures momentum-conservation, leading to a transition energy shifted by the phonon energy. This energy shift is discrete, as only phonons with the right momentum and therefore distinct energy scatter the exciton into the light cone, creating the phonon-sidebands observed below the purely-excitonic transition [276–278]. The binding energy energy of the momentum-indirect state between K and K-, in literature often labeled as $I_0$, is slightly lower compared to the $D_0$, due to the repulsive short-range exchange interaction of the electron- and hole spin [277, 279].

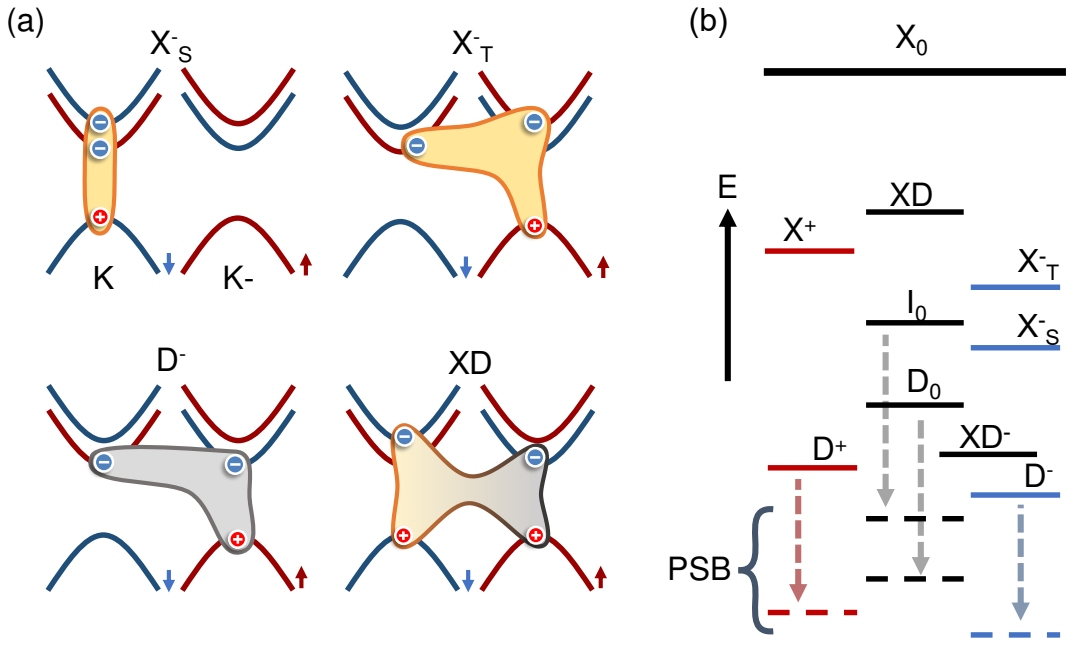


**Figure 2.11:** **(a)** Schematic representation of different composite excitonic particles. Bright negatively charged trions ($X_S^-$ and $X_T^-$), the dark trion ($D^-$) and one configuration of the neutral biexciton ($XD$) are shown from top to bottom and left to right. **(b)** Schematic energy diagram of different bright and dark excitonic states in $WSe_2$, including positively- (red) and negatively (blue) charged excitons as well as the recombination assisted by an additional phonon (PSB)

However, as equation 2.1 shows, the excitonic transition energy is determined by the binding energy and therefore crucially depends on the effective mass of the respective valley. This increases the binding energy of the $K - \Lambda$ exciton enough to lower the transition energy below the bright exciton state [271, 280]. The direct transition is dark due to momentum conservation, but there are observation of a transient phonon sideband before scattering further down to the dark K-K state [281]. The energy difference between the dark and bright exciton is therefore determined by both the conduction band splitting $\Delta_c$ and the difference in binding energy of the two states. The

Considering coexisting dark and bright states brings us back to the topic of the hydrogen, which forms the diatomic molecule $H_2$ under normal conditions. Similarly, two excitons can form a biexciton [282–285]. One possible biexciton $XD$, formed by the spin-dark and bright state, is shown in 2.11(a). Also, if we consider additional free charges, excitons can form trions by binding an electron or hole, in analogy to hydrogen ions. In TMDCs, the two K valleys lead to two different bright negative states, the singlet $X_S^-$ and the triplet $X_T^-$, as depicted in 2.11(a) [282, 286–289]. The two states are split by the exchange interaction, as

both spin and valley impact the short-range Coulomb interaction [290]. On the other hand, there is only one positive trion. The additional hole sits in the other K valley due to Pauli blocking. The same argument holds for the dark trions, where the additional electron or hole sits in the opposite valley [279, 291, 292]. The different states and schematic energy diagram for $WSe_2$ are presented in Fig. 2.11, where also the charged biexciton $XD^-$, a five-body state consisting of 2 holes and 3 electrons, is shown [279, 293]. Recently, even so-called hexcitons and oxcitons have been proposed at very high electron densities, consisting of one hole and 5 or 7 electrons, respectively [294].

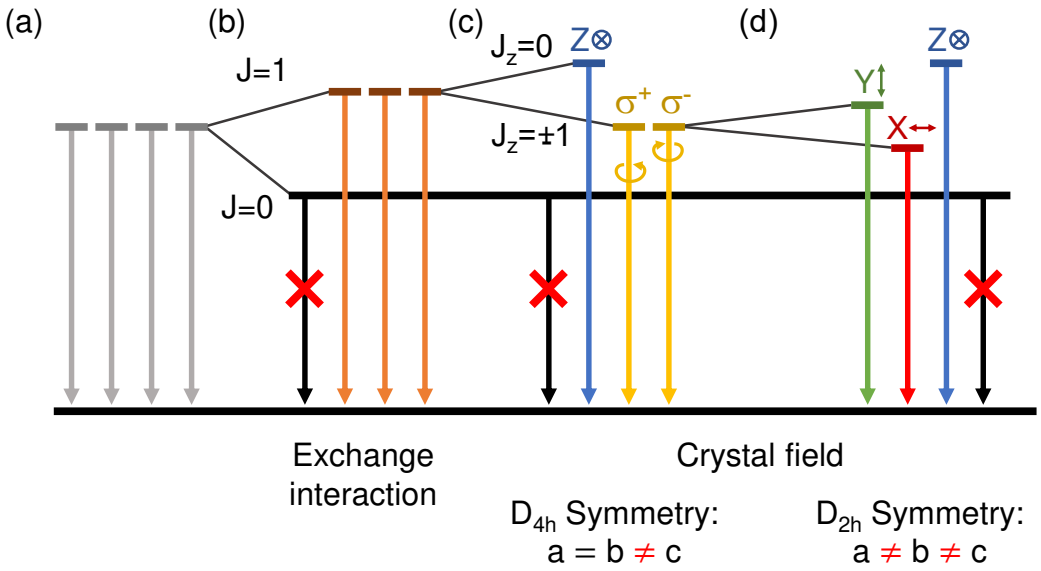


**Figure 2.12: Exciton finestructure in 2D perovskites** **(a)** Schematic energy diagram of 2D perovskites without interaction and symmetry considerations consisting of 4 degenerate transitions. **(b)** Dark singlet and bright triplets are split due to exchange interaction. **(c)** Taking the 2-dimensional symmetry into account, the exchange interaction and the crystal field further split the bright triplets into two states with in-plane and one with out-of-plane dipole moment. **(d)** Reducing the symmetry further additionally lifts the degeneracy of the in-plane polarized states along the x-and y-direction.

Turning to layered perovskites, different excitonic states are less explored. The emission is dominated by strongly bound excitons with binding energies between 0.2 and 0.5 eV, depending on the material and quantum well size [29, 43, 45, 226]. However, the origin and ordering of different states is still under debate [37, 295–299]. In principle, the exchange interaction splits states with different spin configuration, as shown in Fig. 2.12 [297, 300, 301]. This splits the degenerate states into the dark singlet and three degenerate triplet states with total angular momentum $J = 0$ and $J = 1$, respectively. The additional two-dimensional nature

further lifts the degeneracy of the bright triplet into 2 states with in-plane dipole moment $J_z = \pm 1$ and one state with out-of-plane dipole moment $J_z = 0$. Figure 2.12 also summarizes the resulting selection rules, where the out-of-plane state can only be optically active with the electric light field in the z-direction, while the two degenerate states are circularly polarized. Reducing the symmetry further also separates those two states into linearly polarized states. Here, layered perovskites are often described by a tetragonal symmetry [46], e.g. $a = b \neq c$, while recent results show a small splitting of the in-plane polarized states of up to 2 meV [302–304]. The lifted degeneracy and linear polarization indicates lower symmetry without in-plane symmetry. More recently, dark excitons have been directly observed for different 2D hybrid perovskites by mixing bright and dark states using an in-plane field [299, 303]. The dark state is found to be the lowest-lying exciton state in all investigated materials with dark-bright splitting of 18-27 meV.

Additionally, biexcitons have been observed with high binding energies of around 40 meV, nearly twice the binding energy of biexcitons in TMDCs [41, 305]. Contrarily, trions have not yet been shown in layered perovskite, but have been observed in perovskite quantum dots [306–310] and transiently in 3D perovskites [311] at higher excitation densities. The doping of layered perovskites with free charge carriers has proven to be a major challenge, which is mainly faced by chemically introducing dopants to the spacer molecules [312].

Currently, there is also a debate about attributing different transitions to states coupled to one distinct phonon mode, e.g. phonon sidebands [37, 110, 114, 115, 117], or the occurence of polaronic states [109, 111–113, 116]. Both of these scenarios are based on the strong exciton-phonon interaction and the observation of multiple peaks in emission and absorption around the main exciton transition. The interaction with phonons will be especially important for the exciton diffusion, discussed in the next section.

## 2.4 Exciton diffusion

Excitons as composite particles inherit some aspects from their composing particles such as mass or momentum. Unlike electrons however, excitons are charge neutral and therefore not subject to electric fields. Still, after the excitation excitons are not stationary, but move by diffusion freely through the crystal. Here, a vivid example helps our physical intuition: If we place a drop of ink in a glass of water, it is quite intuitive that the ink disperses more and more, until the whole liquid is dyed, even without stirring. Another example is when small particles dispersed in air slowly spread inside a closed room, such as the fragrance of a perfume or small, infectious virus particles. These particles move with their thermal velocity and randomly change direction due to collision events with other particles or the medium itself. The dispersion of ink in water then follows from concentration differences: in the beginning, the ink is concentrated in the droplet in the middle. Subsequently, more ink particles will move from the droplet into the surrounding water until the concentration is homogeneously spread. From an energetic point of view, this can be described by minimizing the free energy in the system by increasing the entropy by more available states of the dispersed system [100].

The particle flux $J$ of this collective motion is determined by the diffusion coefficient $D$, which is related to the local density $n(x)$ of particles via Fick's first law [98]:

$$J = -D\,\nabla n \tag{2.4}$$

Additionally, for describing the pure movement, the number of particles needs to be conserved, e.g. after dropping the ink or creating a certain density of excitons, and by using Fick's first law we arrive at the diffusion equation, Fick's second law:

$$\frac{\partial n}{\partial t} = -\nabla\, J = \nabla\,(D\,\nabla n) = D_{const}\,\Delta n \tag{2.5}$$

where the last equation is only valid for constant diffusion coefficients. The pace of the collective dispersion is therefore directly given by the diffusion coefficient. Additionally, the finite lifetime $\tau$ of excitons and non-linear effects such as exciton-exciton annihilation need to be taken into account [313–316]. The latter is a bi-molecular, non-radiative recombination process of one exciton and the simultaneous higher excitation of another exciton [317]. This process is governed by the Auger rate $R_A$ and additionally contributes to the recombination. Further, higher order processes can exist but do not play any role for the studied systems. Overall,

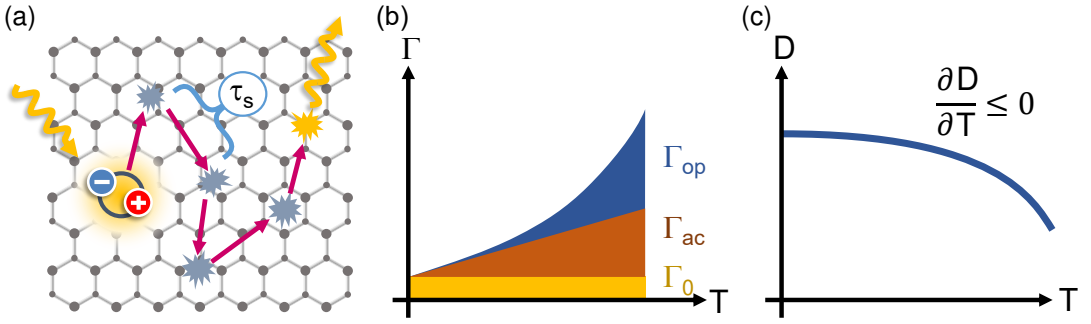


**Figure 2.13: Band-like semi-classical transport characteristics.** **(a)** Exciton freely propagating through the crystal until scattering events randomly change momentum and direction, after the characteristic scattering time $\tau_s$. **(b)** Scattering rate $\Gamma$ as function of temperature for the different scattering mechanisms with acoustic $\Gamma_{ac}$ and optical $\Gamma_{op}$ phonons as well as temperature independent scattering $\Gamma_0$. **(c)** Characteristic temperature dependence of the diffusion coefficient in the semi-classical free propagation model. For low temperatures the linearly increasing scattering is compensated by a similar gain in kinetic energy, whereas at higher temperatures the non-linear increase of the scattering leads to a decreased diffusion.

this leads to the extended diffusion equation by including the recombination term $R(n)$:

$$\frac{\partial n}{\partial t} = D_{const}\,\Delta n - R(n) \quad \text{with} \quad R(n) = \frac{n}{\tau} - R_A n^2 \tag{2.6}$$

The average distance an exciton then travels is also dependent on the lifetime $\tau$ and given by the diffusion length $L_D$ [99, 318]

$$L_D = \sqrt{2\,D\,\tau} \tag{2.7}$$

When excitons travel freely through the crystal, they frequently scatter with phonons, other excitons or defects, as depicted in Fig. 2.13(a) leading to random changes of their momentum. In the semi-classical model, the resulting diffusion coefficient can then be estimated by the frequency of scattering events from the Einstein-Smoluchowski relation [99, 319]:

$$D = \frac{k_B\,T\,\tau_s}{M} \tag{2.8}$$

where $k_B$ is the Boltzmann constant and $M$ the total mass of the particle, for excitons $M = m_e + m_h$ and assuming that the kinetic energy of a particle is given by the thermal energy at temperature $T$. The diffusion coefficient is therefore governed by the time between two scattering events, the scattering time $\tau_s$ [320].

Here, a crucial assumption of the diffusion model for excitons is that in between those scattering events, excitons travel ballistically. For electron transport in semiconductors, this is labeled as semi-classical or band-like transport [320]. Therefore, the diffusion model is technically limited to the regime before the scattering time reaches the lifetime of excitons, as the transport is then no longer mediated by scattering.

Characteristic for band-like transport is the temperature dependence of the diffusion coefficient [321, 322]. In systems with dominant linear acoustic phonon scattering, such as TMDCs and layered perovskites, the scattering at low temperatures increases linearly due to the increasing population of this phonon branch. This cancels with the general linear temperature dependence from equation 2.8, assuming constant exciton mass. The characteristic temperature dependence of band-like diffusion with $\frac{\partial D}{\partial T} \leq 0$ is schematically depicted in Fig. 2.13(b). The decrease of the diffusion constant at elevated temperatures is due to additional optical and high energy linear acoustic phonon modes activated at higher temperatures.

Contrary to freely propagating excitons, in strongly disordered systems, excitons can not move freely through the crystal and are localized at certain points of the lattice. This is often the case for Frenkel excitons in organic crystals, which are localized to a single atomic site, but also applies for systems with strong exciton-phonon coupling [86, 318, 323–325]. Here, the exciton interacts strongly with the crystal lattice and forms a polaron, which can be self-localized depending on the discrete interactions and parameter [86, 326, 327]. Independent of the localization mechanism, the excitons are then located at potential minima illustrated in Fig. 2.14(a) and diffuse via hopping processes between these localization sites [328]. At low temperatures, this only possible via tunneling processes, which require some wave-function overlap such as Dexter energy transfer, or through the Förster resonance energy transfer (FRET) based on dipole-dipole interaction [318, 329, 330]. These processes crucially depend on the distance between sites and FRET additionally is highly sensitive on the overlap between emission and absorption resonances.

Excitons gain additional kinetic energy at elevated temperatures, while the localization energy $E_{loc}$ is mostly independent of temperature for static origins. This thermally activated transport is therefore characterized by a rising diffusion coefficient with increasing temperature, as shown in Fig. 2.14(b). Depending on the exact mechanism of both the localization itself and the hopping process, the

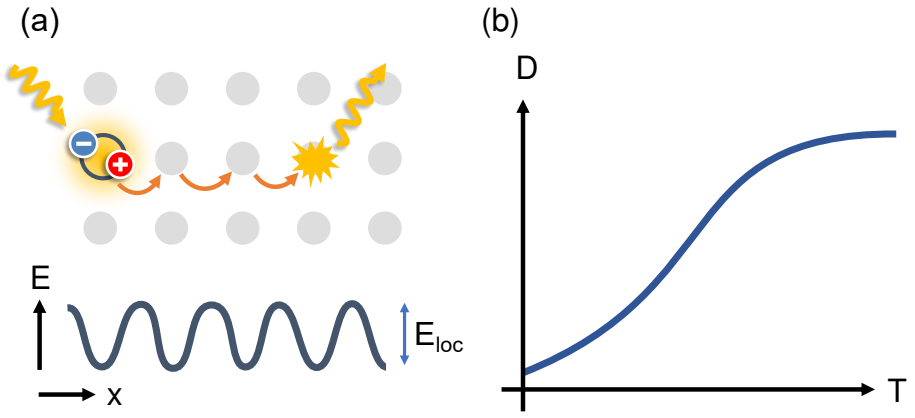


**Figure 2.14: Localization and hopping transport.** **(a)** Excitons stay localized at a site with the average localization energy $E_{loc}$ and hop from site to site by tunneling or FRET. **(b)** Characteristic temperature-dependence of the hopping transport by thermally-activated transport. At elevated temperatures where the kinetic energy is much larger than the localization energy the scattering with phonons starts to dominate again.

temperature dependence can be described by different models. A simple model to phenomenologically characterize the thermally-activated hopping transport is given by an Arrhenius-like exponential increase [328]:

$$D = D_0 \, e^{-\frac{1}{2}\frac{E_{loc}}{k_B T}} \tag{2.9}$$

The resulting temperature-dependence of the diffusion coefficient is schematically shown in 2.14(b). At elevated temperatures when the thermal energy is much higher than the localization energy, again the scattering starts to dominate and semi-classical transport can be observed. Especially in the case of layered perovskites, understanding the underlying exciton transport mechanism will be crucial for the discussion of the experimental results. Before, we will briefly introduce the sample fabrication in the next chapter and outline the experimental methods to measure exciton diffusion.

# Chapter 3
# Sample fabrication and spectroscopy techniques

## 3.1 Exfoliation of layered materials and van der Waals heterostructure fabrication

This chapter describes the delicate fabrication of van der Waals heterostructures and serve as hands-on guideline to create complex two-dimensional samples. Therefore, the step-by-step guide contains extensive pictures to facilitate reproducing the employed samples.As a substantial part of the work was the fabrication of heterostructures for different projects and the advancement of the fabrication method itself, the following instruction also includes tips and tricks encountered while fabricating different structures.

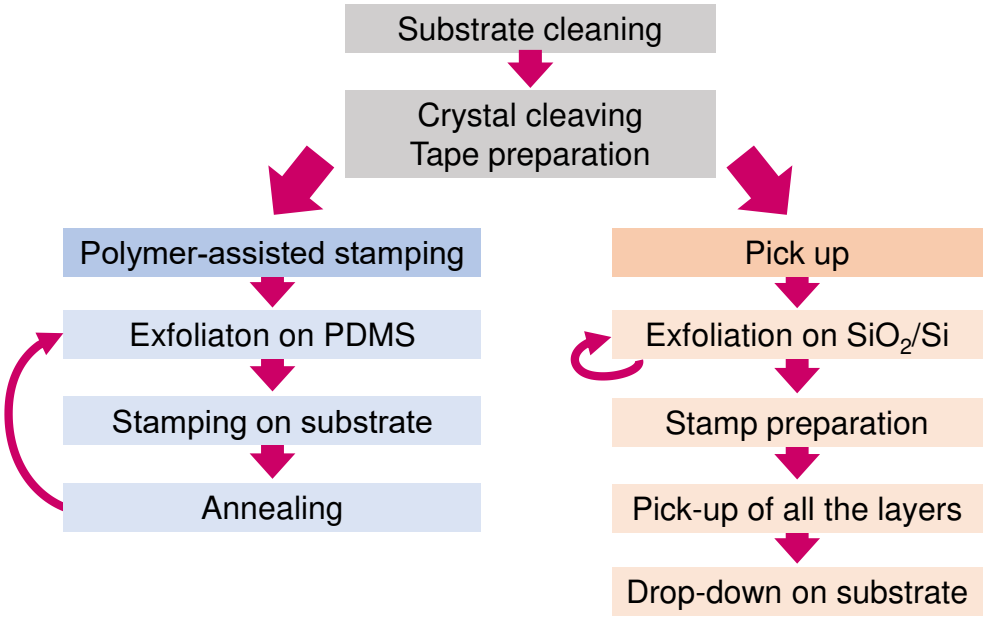


**Figure 3.1: Guide to the different types of exfoliation and stacking.** After similar cleaning and pre-processing, the two techniques are characterized by different exfoliation and the method of creating the final structure.

The chapter is organized along Fig. 3.1 and first necessary preparations such as thorough substrate cleaning and the cleaving of the bulk crystals are discussed. The exfoliation guide is then structured into two different methods, first the generally more straightforward polymer-assisted exfoliation and stamping and subsequently, the sophisticated pick-up method of directly exfoliated flakes.

## Substrate cleaning and bulk crystal cleaving

Before starting with the exfoliation, the substrates need to be as clean as possible. A 2 inch silicon wafer with 285nm $SiO_2$ is coated with a protective layer of PMMA and either commercially cut to small quadratic pieces with a size 4.9 mm or cleaved using a scriber with diamond tip and cleaving pliers. The substrates then undergo extensive cleaning depicted in Fig. 3.2. First, they are washed step-by-step in three different beakers with acetone, where the last one is sonicated for 60 s in an ultrasonication bath. The same is repeated with three beakers of isopropyl alcohol, again using 60 s of ultrasonication for the last beaker. The substrates are then transferred to another three beakers with de-ionized water and a last time undergo ultrasonication for 60s. Several beakers are used at each step as the residues are washed off by the solvent, but remain in the beaker. Transferring the substrates to a new beaker before ultrasonication drastically reduces the amount of debris left on the substrates. After the last bath, the substrates are finally blown dry by nitrogen and cleaned in an $O_2$ plasma oven for 5 min at 200 W in order to get rid of any remaining organic residues.

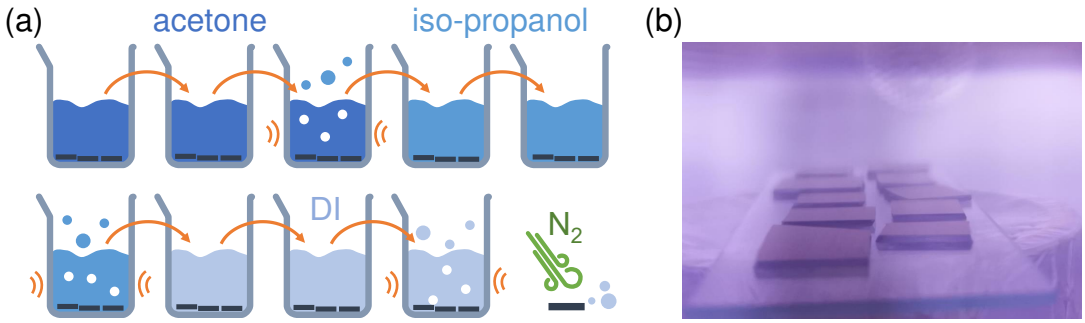


**Figure 3.2:** **(a)** Cleaning cascade in several baths of acetone, iso-propanol and deionized water (DI) with ultrasonic bath for the last beaker of each solvent. **(b)** Oxygen plasma cleaning of cleaved $SiO_2$/Si at high power.

The exfoliation process always starts with cleaving of the high quality bulk crystals and the quality of the cleaved crystals on the tape determines both the size and overall yield of exfoliated flakes. Some TMDCs such as as $MoS_2$ exist

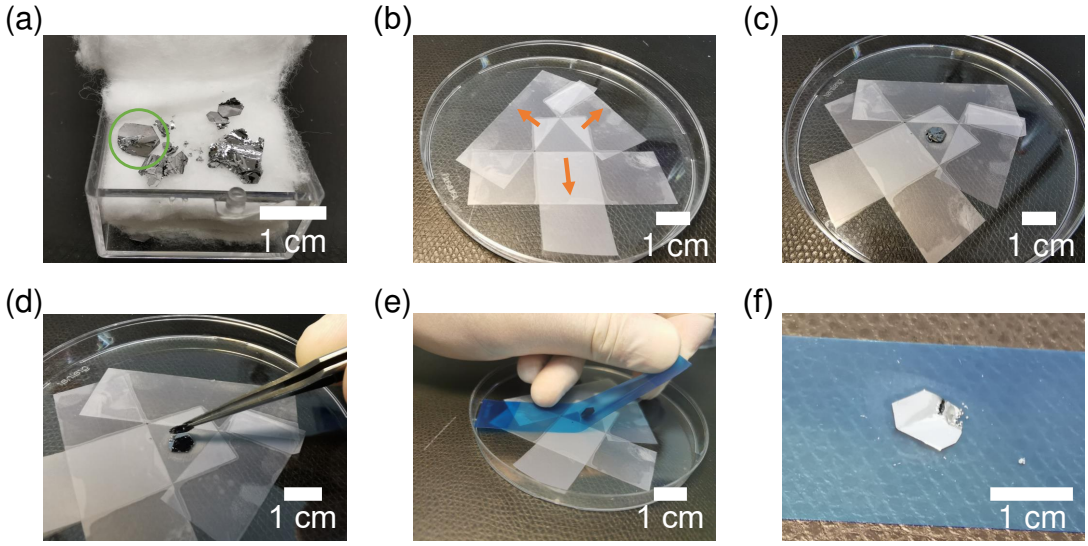


**Figure 3.3:** **(a)** $WSe_2$ bulk crystals from hq-graphene. **(b)** Scotch tape glued inside a petri dish for cleaving. **(c)** Bulk crystal on scotch tape, the flake is indicated in green in (a). **(d)** Cleaving of bulk crystal using tweezers. **(e)** Second cleaving for exfoliation using blue tape. **(f)** Blue tape with homogeneously cleaved bulk crystals used for further exfoliation.

as natural crystals, but nearly all produced samples are made from artificial bulk crystals fabricated by chemical vapor transport. Here, both commercially available bulk crystals (HQ-graphene and 2D semiconductors) and, more recently, bulk crystals with very low defect-densitites [331] from the group of James Hone from the Columbia university are used.

The process is depicted in Fig. 3.3. For TMDCs, inverted Scotch-tape (Scotch Magic$^{TM}$ tape) is tightly glued by additional tapes, where each stripe pulls on the inverted tape away from the others in order to be as firm as possible. Then, a piece of bulk crystal is directly placed on the tape and firmly pressed down. Using tweezers, the bulk crystal is carefully removed, chipping the bulk at an interface between layers and leaving a fresh and completely flat surface of the crystal on the tape. Here, it is crucial for the bulk crystal to be placed and removed completely parallel with the layered structure of the crystal. In a next step, a piece of blue tape (polyvinyl chloride backgrinding tape 224PR from Nitto) is lightly pressed on the newly cleaved bulk crystal on the tape and carefully removed. A nearly parallel tape lift-off helps to get a smoother surface. The blue tape is then ready for the next steps of exfoliation. Bulk graphite is exfoliated very similarly, except for the use of another scotch tape instead of blue tape to cleave the crystal for viscoelastic stamping.

The high-quality hexagonal boron nitride (hBN) crystals from Takashi Taniguchi from the National Institute for Material Science (Tsukuba, Japan) are cleaved using a slightly different method, outlined in Fig. 3.4. A small, single crystal hBN is selected by a shiny and smooth surface, which guarantees the right alignment of the stacking direction and cleaving axis parallel to the tape. The crystal is carefully picked up by tweezers without any pressure and placed on a scotch tape stripe. Then, a second scotch tape is added on top of the crystal and removed again, cleaving the whole crystal and creating a second, mirrored bulk crystal on the other tape. The tapes are repeatedly pressed together, where each time the two tapes are slightly misplaced so the crystals are packed as close as possible but without overlapping. When a sufficiently large area is covered with cleaved hBN crystals, the tape is ready to be used for further exfoliation. Small, single crystal perovskites are exfoliated in the same way.

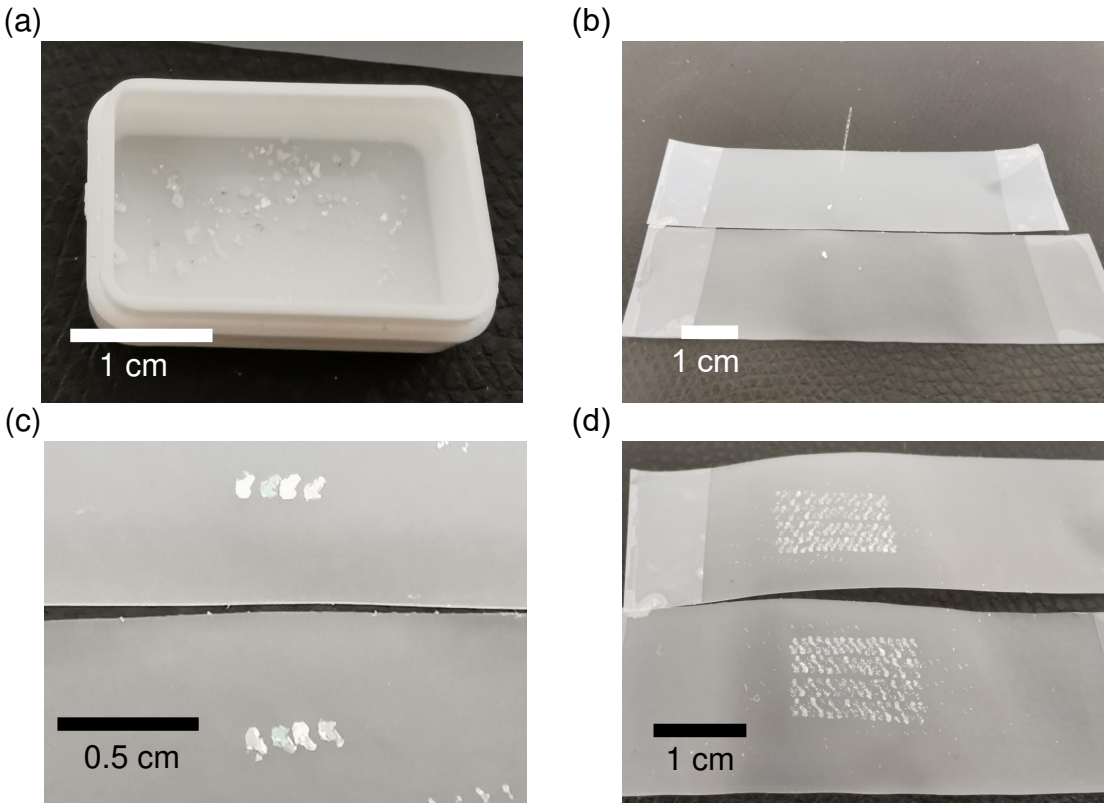


**Figure 3.4:** **(a)** Bulk single crystals of high quality hBN from NIMS in Japan. **(b)** Single crystal once cleaved using two sheets of scotch tape **(c)** Same crystal after three cleaving steps. **(d)** Scotch tapes with thinned-down hBN ready to use for exfoliation.

## Polymer-assisted exfoliation

This section presents the "all-dry viscoelastic stamping" established for single monolayer TMDC by Andres Castellanos-Gomez [332]. Viscoelasticity is a stress-dependent combination of viscous liquid-like and elastic properties, here exploited in Polydimethylsiloxane (PDMS), a widely used organic polymer. The viscoelasticity of PDMS allows the polymer to behave like a liquid without stress and over long times, whereas at short times or high stress it behaves more like a solid. Commercially available PDMS sheets (PDMS; WF-20-X4, Gel-Pak) are cut to roughly the size of the cleaved crystal on the tape as shown in Figs. 3.3(f) and 3.4(d). The PDMS is bonded to a polyester substrate by the manufacturer and covered with a thin transparent film.

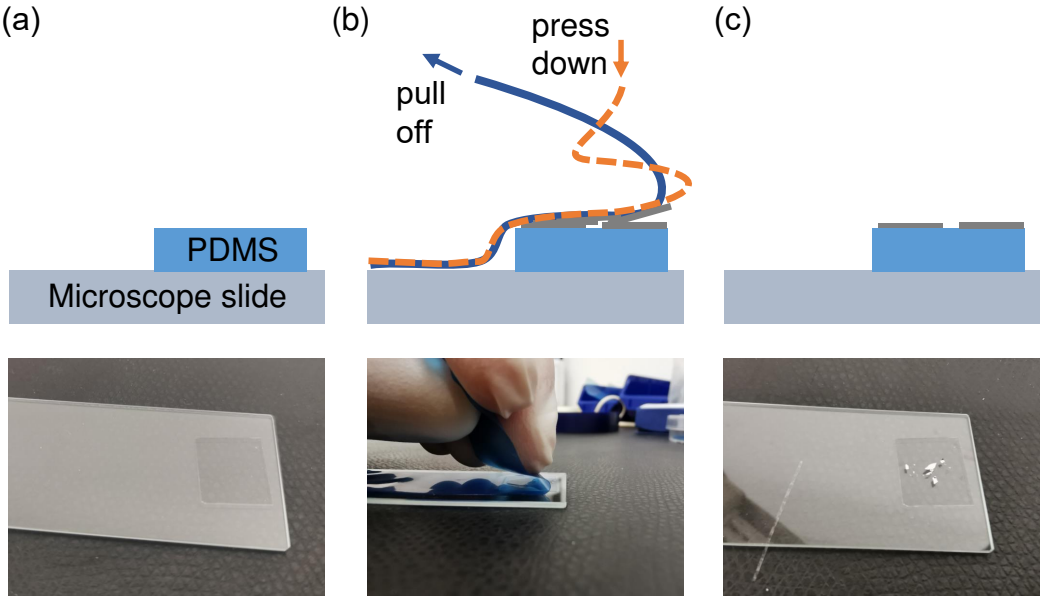


**Figure 3.5:** **(a)** Exemplary piece of PDMS on a microscope slide. **(b)** Schematic of the crucial exfoliation step and photograph of the indirect pressing using the stiffness of the tape. **(c)** Exfoliated $WSe_2$ flakes on PDMS with thicker pieces directly visible.

First, the protective thin film is removed and then the PDMS is slowly removed from its substrate layer using metallic tweezers. As shown in Fig. 3.5(a), the PDMS is then carefully placed on a microscope slide with the stickier substrate-side down, preventing the PDMS from being pulled off the glass by the tape in the following steps. Here, it is important to not touch or press on the PDMS, as any contamination will be in contact with the exfoliated layers. Next, the crystal-loaded tape is brought into contact with the PDMS layer by carefully pressing only on the far side of the tape, as shown in Fig. 3.5 (b). After the cleaved crystal is in

complete contact with PDMS, the tape is slowly removed by pulling back. Here, the removing speed is the crucial parameter, as the adhesion of the viscoelastic PDMS is higher when the tape is quickly removed. Therefore, one needs to find the right speed of around 0.5 - 1 cm/s between removing the tape too slow where no flakes are exfoliated and on the other side too fast resulting in broken and ripped flakes due to strain. This also depends on the cleaved crystal and should be adjusted for each newly cleaved crystal on blue tape, which is used for 10 - 20 exfoliation processes. During the exfoliation process, the speed is generally increased, as the weaker bound layers are already exfoliated.

The PDMS is then searched for monolayer TMDCs or suitable hBN, graphene and perovskite flakes using a microscope and a 10x objective. With a trained eye one quickly distinguishes between the contrast of different thicknesses and with the right technique large monolayers can be exfoliated, as shown in Fig. 3.6(a). If the hBN is only used to provide a homogeneous dielectric environment and protection from the environment, a thickness of 10-40 nm is desired. The flakes in this range are colored from light blue (10nm) to a purer white (30-40nm) on PDMS and should exhibit large enough, completely flat and clean areas. Thicker and colorful hBN layers suppress the transmission and view of the sample. Few-layer graphite (FLG) used as gate and contact for charge-tunable devices should be between 5-20 layers or 1-5 nm, in order to be rigid enough to not break during transfer but also thin enough to not create a large height change in the device. In general,graphene is barely visible on $Si0_2$;Si due to the low contrast and the desired thickness corresponds to very light grey to grey color.

Suitable flakes are marked on the microscope slide and the PDMS is cut to a size of a few mm. The glass slide is inverted and fixed by a custom build holder mounted on a x-y-z stage, which can be additionally tilted by adding screws from the bottom of the platform. The substrate is placed on a heatable sample holder, which uses low pressure to hold the substrate. For stamping hBN, the substrate is heated to 100°C, whereas for TMDCs a temperature of 70°C is used, as the high thermal expansion of PDMS can tear monolayers apart at elevated temperatures.

The inverted stamp is then placed on top of the final substrate, for example $SiO_2$/Si. By adjusting the focus plane of the 10x objective both, the substrate surface and the flake on the inverted stamp, can be seen. The flake is then roughly aligned to the desired position on the substrate and with the flake in focus the substrate is slowly lifted to approach the stamp. Here, the high stability

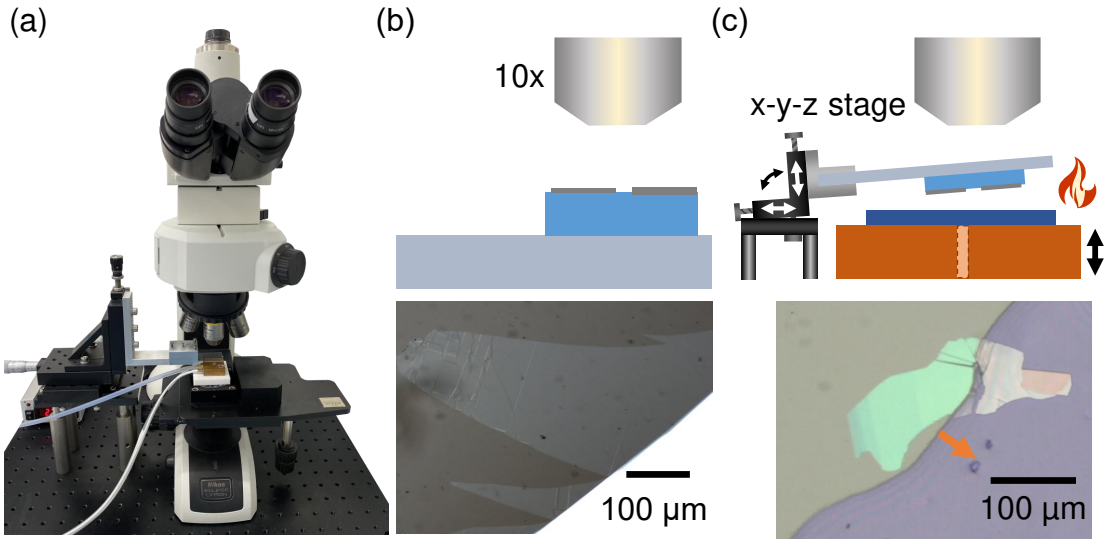


**Figure 3.6:** **(a)** Microscope setup used for searching flakes and all transfer processes. **(b)** The PDMS with exfoliated flakes is searched using a 10x objective, where an exemplary monolayer $WSe_2$ monolayer is shown in the bottom micrograph, where the bottom right shows bulk area with high, metallic refelction. **(c)** Stamping process using a slightly tilted x-y-z translational stage setup, where the substrate is heated to 70-100°C. Bottom micrograph shows the flake while slowly bringing the stamp and substrate into contact, where the color of the hBN changes from white to greenish due to interference effects with the $Si/SiO_2$ substrate.

of the microscope and its translational stage is used to lift the substrate slowly and controlled towards the flake. A small tilt along one horizontal axis the between the stamp and substrates determines the direction of contact and helps to control the contact line by slowing it down. Here, one should aim for a small, but observable tilt, as a high tilt leads to more strain on the stamp and can destroy the flake. The contact line is visible by a change of contrast, the same way the flakes change color when in contact with the substrate, as exemplary shown in Fig. 3.6. After the whole flake is in contact, the substrate is very slowly decreased, especially at the first crossing of contact line and flake. Through the viscoelasticity of PDMS, the speed of the retraction allows to control the adhesion of the flake and therefore the stamping process needs to be slow and controlled, with contact line speeds below 1 µm per second. After the contact line completely passed the flake, the stamp can be retracted faster, while one needs to be careful that the PDMS stamp still stays attached to the glass slide.

Then, the desired heterostructure is built by adding layer by layer using the same procedure. During the alignment of the next flake special care should be on areas with less adhesion, such as wrinkles or steps from pre-patterned contacts. Here, the direction of the contact line should be perpendicular to such a structure,

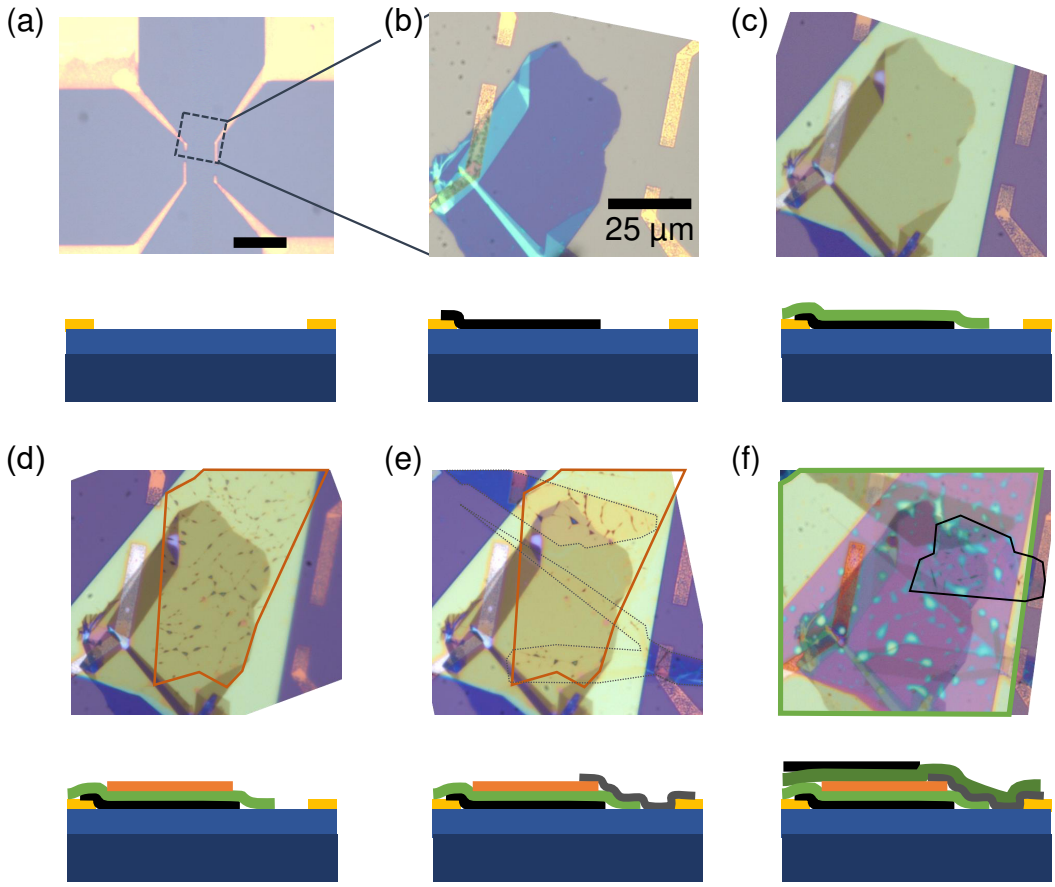


**Figure 3.7: Step-by-step fabrication of a $WSe_2$ device by PDMS exfoliation and stamping.** **(a)** Prepatterned gold contacts and bonding pads on a $Si/SiO_2$ substrate. **(b)** Transferred bottom gate, contacted by the gold and sufficiently overlapping with the substrate on the other side of the gold-contact. **(c)** Bottom hBN covering the bottom gate without containing the other contacts. **(d)** Monolayer $WSe_2$ flake (orange line) stamped on top, where residues form bubbles between the layers. **(e)** The $WSe_2$ contacted by FLG flakes indicated by dotted gray lines. The bubbles between the hBN and the $WSe_2$ have accumulated into bigger bubbles by annealing in between, leaving larger clean areas compared to (d). **(f)** Complete device with a top hBN covering the contacts and a small FLG top gate (black line).

when the alignment of the next flakes allows. Figure 3.7 shows step-by-step the fabrication of a gate-tunable device consisting of 7 layers in total, starting with the bottom FLG gate. Between each transfer step, it is crucial to anneal the sample in high-vacuum at 150°C for at least 2 h. This strongly increases the contact between layers, as interfacial contaminants become mobile and accumulate in bigger pockets. This can be directly seen between Fig. 3.7(c) and (d), where lots of small bubbles between the hBN and the $WSe_2$ aggregate into bigger ones leaving behind a clean interface [333–336]. This leads to a significant amount of such bubbles for samples with many different layers, such as devices, while

the most important interfaces for the quality of the sample are between the hBN and the TMDC or perovskite, leading to an increased dielectric disorder[173]. Nevertheless, bubbles between the bottom hBN and the substrate can introduce strain on the sample due to the height difference and between the hBN and a FLG flake can contribute to an inhomogeneous doping density.

Lastly, a few general notes on the PDMS exfoliation and stamping. First, when the yield of monolayer on PDMS is low, the first thing to do is a new bulk crystal on scotch tape, as a well-cleaved bulk crystal forms the basis for further exfoliation. Second, one should aim to keep the time between exfoliation and stamping of a certain flake as short as possible, best below 24 h. Third, hBN flakes stick very well to the substrate and most layered materials stick very well to hBN. Therefore, one should aim for a large bottom hBN which then fully supports all the other layers, simplifying the stamping process.

The pre-patterned gold contacts are a substantial step in the height profile, which can complicate the stamping due to reduced adhesion. Here, the FLG contact should extend in both directions across the gold contact to provide enough adhesion to the $SiO_2$, as for example the two contacts in Fig. 3.7(d) show.

## Direct exfoliation and polymer-free heterostructure fabrication

The growing complexity due to increasing number of layers and the observation of delicate features demands even higher quality of the structures and interfaces. Motivated by that, Wang *et al.* [141] introduced the first pick-up method for graphene, where only the topmost layer is in contact with the polymer and is used to subsequently pick-up the other layers. In combination with direct exfoliation, where an exfoliated layer has only been in contact with the material itself and the clean $SiO_2$ surface, this allows to build considerably cleaner heterostructures [143].

The direct exfoliation has been the primary method to obtain monolayer TMDCs or graphene until polymer-assisted methods using PDMS or PMMA (poly methyl methacrylate) gained popularity due to deterministic stamping and reliable yield of monolayers with comparatively large areas. Here, the most important aspect is the van der Waals force between the substrate surface and the layer. Therefore, both the substrate surface and the thinned-down bulk crystal should be as clean as possible. For direct exfoliation, bulk crystals are thinned down using scotch

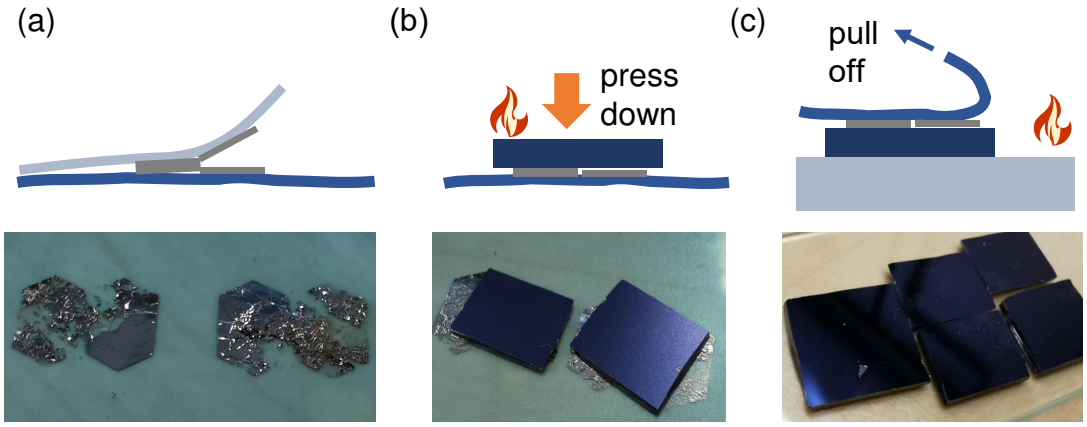


**Figure 3.8:** **(a)** Blue tape for direct exfoliation with two cleaved crystals directly next to each other to match the substrate size. **(b)** Hot $Si/SiO_2$ substrates placed upside down on the tape directly after plasma cleaning. **(c)** The chips with the tape are placed on a hot plate at $100°C$ for 60 s and the tape is immediately removed afterwards. The bottom picture shows exemplary substrates with exfoliated layers.

tape as shown in Fig. 3.3. An additional Scotch tape is used to transfer flakes on blue tape, where the flake is placed two or more times directly next to each other, in order to fit the size of the cleaved wafer. This is repeated several times on one blue tape, as depicted in Fig. 3.8(a).

The cleaned $Si/SiO_2$ are first either heated on a hot plate to 100°C or, even better, used directly from the hot plasma oven and directly placed on the blue tape. The substrates are pressed down with some force, where one should be careful to only press from the top and avoid lateral sliding. The substrates are then immediately inverted, placed on a microscope slide and again heated on a hot plate for about 60 s. Then, the tape is removed by pulling the tape away and holding the chips using tweezers. Here, the removing speed is not relevant, but one should be very cautious to not have any lateral sliding movements and to lift the tape straight away. Every blue tape is only used once, as the surface of the cleaved crystal should be as clean and flat as possible. The same method is used for all materials, except for layered perovskites where the temperature is reduced to 50°C due to their environmental sensitivity.

The substrates are then searched for suitable layers using a microscope. The contrast of the flakes strongly depends on the thickness of the $SiO_2$. For most of the projects we used a nominal oxide thickness of 285 nm, while 90 nm is also used in the community, providing good contrast for many different materials [337]. Here, one should aim to get used to a certain contrast to approximately determine the layer thickness by the bare eye through the oculars. In general, a camera could

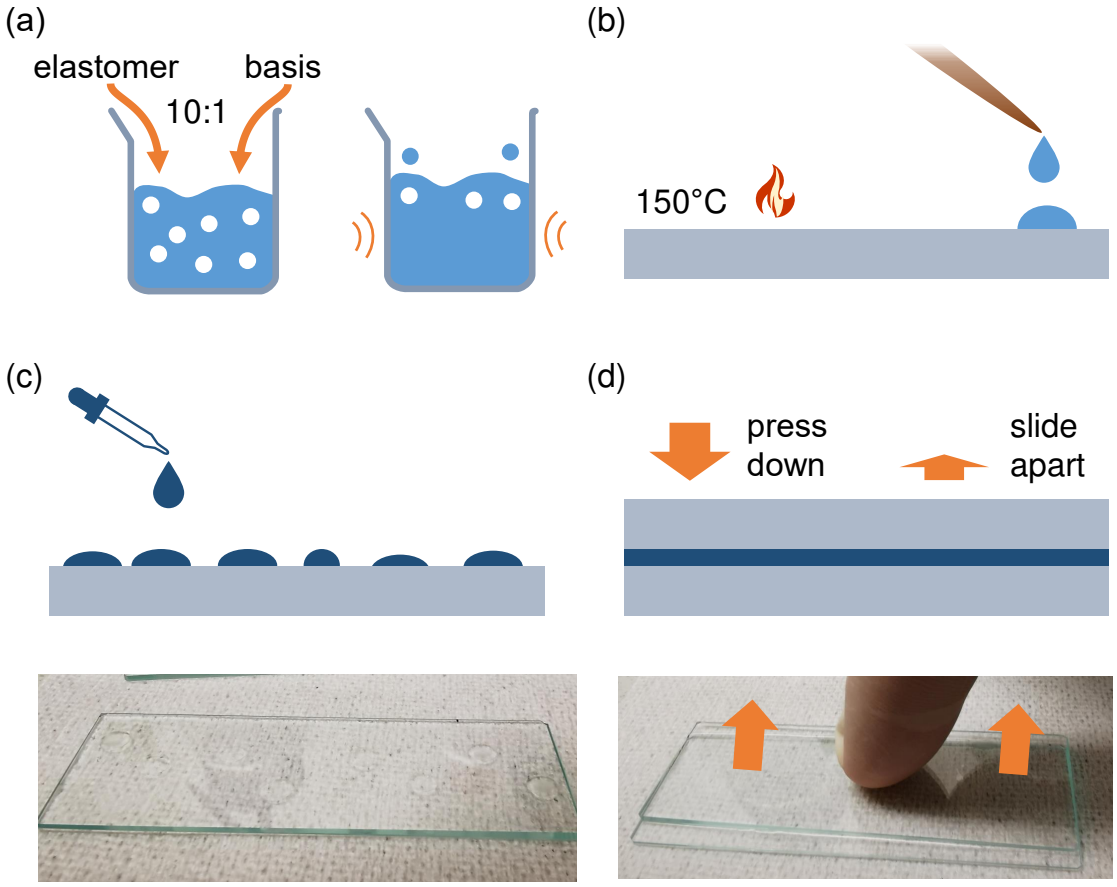


**Figure 3.9:** **(a)** The base and curing agent are mixed and incorporated air is eliminated by an ultrasonic bath. **(b)** One small drop of the PDMS mixture is dropped on a heated glass slide using a tooth pick. **(c)** A few drops of polycarbonate (PC) solution are dropped directly on top a standard microscope slide. **(d)** A second slide is pressed on top and evenly slid apart, creating a thin film.

be used to enhance the contrast by adjustments to the color coding, but is then very sensitive on the illumination. When all the needed flakes and some backup flakes for a device are exfoliated, the next step is preparing the stamp for pick-up. Here, we use modified approach to create the stamp.

First, a PDMS droplet is produced using the method illustrated in Fig.3.9(a) and (b) by mixing the elastomer and the curing agent (Dowsil 184) with a 10:1 ratio, for example 2 g of the elastomer and 0.2 g of the curing agent. The mixture incorporates a lot of air, which is removed by an ultrasonic bath for at least 10 min. Similarly, the air can be removed by placing the PDMS in a vacuum desiccator. Then, a clean microscope slide is heated on a hot plate to 150°C and a small drop of the mixture is dropped down using a tooth pick, as a pipette would lead to further air bubbles inside the drop. The droplet holds the shape through the high

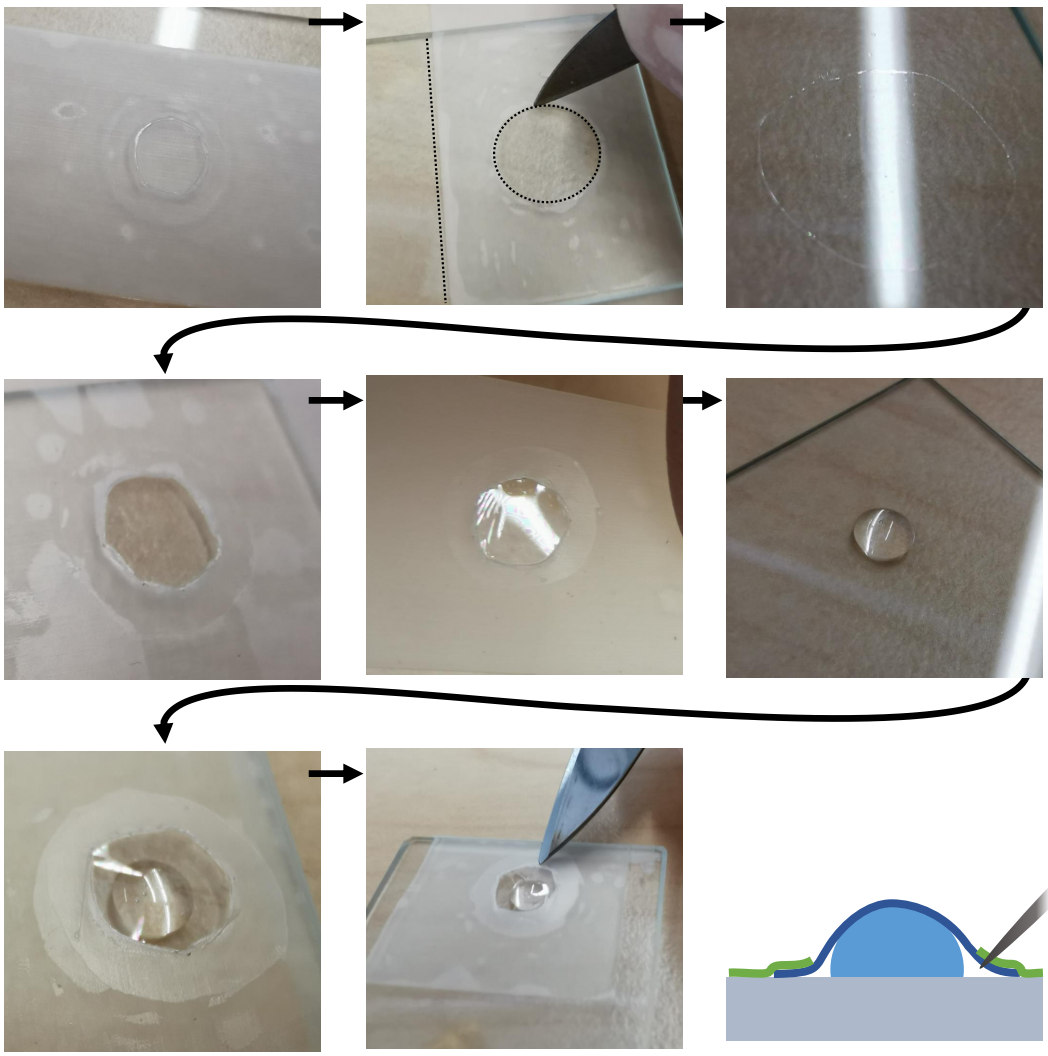

**Figure 3.10: Thin film transfer on PDMS stamp.** Two circular windows are cut into scotch tape, where the larger one is used to cut out a small, circular PC film. The circular PC is then transferred using the scotch tape with the smaller window and uniformly placed on top of the PDMS bubble. Before the film is melted on top, a small hole is created by a scalpel to let air escape, as depicted in the schematic illustration in the bottom right frame.

temperature and is left to cure for at least 1 h. One should aim for a round shape and a size of about 4-5 mm.

The next step is preparing a thin polycarbonate (PC) film, which ultimately allows to pick-up flakes. Therefore, PC granulate (Sigma aldrich) is dissolved in chloroform with a 6% weight ratio. A few drops (10-15) are placed on a clean microscope slide, as shown in Fig. 3.10(a). Then, a second glass slide is pressed on top and the two are slid apart. The evaporation of chloroform from the solution results in a homogeneous and thin polymer film, which is subsequently transferred

on top of the PDMS bubble, which is illustrated in Fig. 3.10. To do that, two stripes of scotch tape are placed on opposite sides of a clean microscope slide. A circle is cut into each of the tape stripes using a scalpel. One circle is 5 mm and the other a few mm larger. The tape with the larger circle is removed and placed directly on the PC-film and the film is cut using a scalpel along the circle. The tape then removes all the excess film, except for the round window. Then, the tape is placed with the hole centered on the thin PC film, which can be picked up by sticking to the outer edge of film. The tape with the suspended PC film in the circle is then carefully transferred onto the PDMS droplet. Here, it is important that the first contact of the film occurs in the center of the PDMS droplet and then stretched across. Here, the tape without any PC should be large enough to stick to the glass slide an provide enough support. Using a sharp scalpel, a small hole is poked into the overlapping area of the tape and PC to let air escape. Lastly, the stamp is heated to 125°C for about 2 min to facilitate a more homogeneous PC-film.

Having all the flakes and the stamp ready, it is important to make a detailed plan about where everything needs to be stacked, for example using PowerPoint. As one starts with the topmost layer and releases the complete stack in the end on the pre-patterned gold, every layer needs to be at the right position and orientation. The top hBN should cover all upcoming layers, in order to protect them from strain, as a few 10's of nm thick hBN is more rigid than all the other layer, only a small part of the top gate should stand out to contact the gold. Additionally, as the stack is viewed from the top through the microscope, the contrast is drastically reduced with each additional layer. Here, some markers outside the stack such as other flakes or even dirt on the substrate can help to orientate and should be indicated in the plan.

For the pick-up the same setup as for the polymer-assisted stamping is used and the stamp is inverted and placed above the sample holder. A few important steps are illustrated in Fig. 3.11, where the start is a FLG flake as top gate. The substrate with the flake is placed on the holder and heated to 125°C. The pick-up process itself starts by slowly making contact with the stamp by elevating the substrate. In general, the center of the droplet touches first and should be between 20-50 µm away from the stack. Then, the contact line is moved across the flake and only a few µm over the flake. In contrast to PDMS, PC is not viscoelastic and therefore the speed is not crucial, more important is that while going into contact no lateral shifts occur which could strain or even tear the flakes apart.

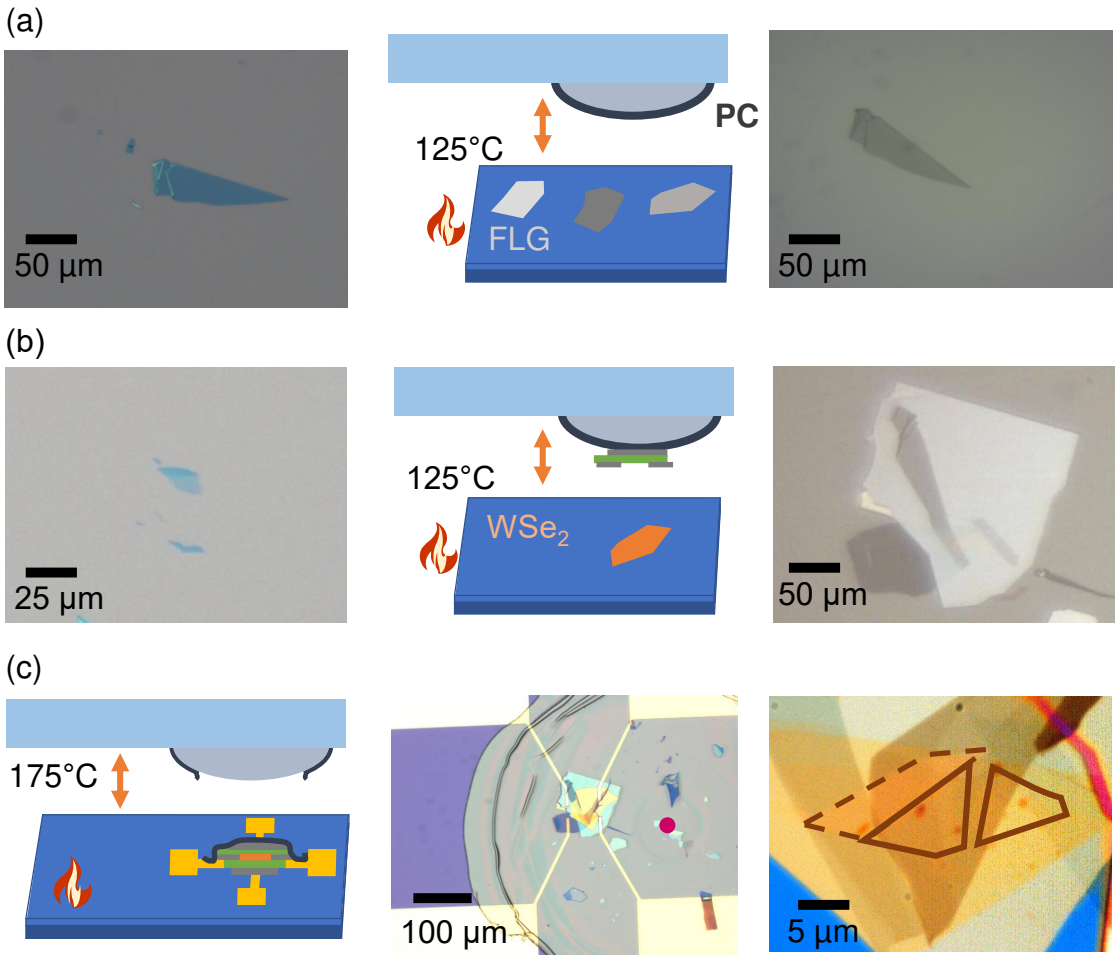


**Figure 3.11: Important steps for the pick-up process.** **(a)** From left to right: FLG top gate on $Si/SiO_2$ substrate. Schematic of the pick-up with the substrate heated to 125°C. Successfully picked up flake on the PC stamp. **(b)** Pick up of the $WSe_2$ flake with mono- and bilayer area. The low contrast in the picked up flake requires a well prepared stacking plan. **(c)** Drop-down of the flake by melting the PC at a temperature of about 150°C. The dot in the middle picture indicates the center of the stamp. The PC is then washed by chloroform and a high-resolution micrograph shows a slightly broken flake but drastically reduced bubbles between the layers. Solid lines represent the monolayer and dashed lines show bilayer areas.

Then, step-by-step the substrates with the next flakes are mounted and picked-up in the same way. In order to minimize the strain due to thermal expansion, one should try to keep the stamp always on $125°C$, which is either done by adding hot iron plates on top of the stamp or placing the stamp directly above the heated substrate when not in use. After the pick-up of the $WSe_2$, right picture in the middle row of 3.11, one nicely sees the top gate extending outside the top hBN, while all the other layer are below the hBN.

When the stack is finished, it is released onto the target substrate with pre-patterned gold contacts. Before going into contact, the temperature of the substrate is increased to 160°C, then the complete stack is brought into contact and the contact line is moved an additional 50-100µm over the flake. Then, the temperature is increased to 175°C, where special attention should be payed to counteract any lateral drift due to thermal stress of the setup by adjusting the translational stage. When the temperature reaches 175°C and the PC starts to melt, the substrate is slowly retracted and the contact line should not move, whereas a second contact line, between PDMS and PC, starts to form. The PC then easily detaches from the PDMS stamp and stays with the successfully transferred stack on the substrate. Lastly, the PC is washed away by subsequent rinsing in chloroform, acetone and isopropyl alcohol. The last picture is a high-resolution micrograph of the gate-and electric field-tunable area of both bi- and monolayer $WSe_2$, where only a few bubbles between the interfaces are visible, in contrast to the device from Fig. 3.7.

In order to build devices out of layered perovskites, the pick-up procedure is modified, as the hybrid material rapidly degrades above 100°C. Therefore, the viscoelastic polymer polypropylene carbonate (PPC) is used instead of PC. The PPC is dissolved in anisole (15% weight solution) and similarly prepared as thin film and then covering the PDMS stamp. In order to also reduce the light exposure of the perovskite while picking up, the device basis, consisting of a FLG bottom gate, insulating hBN and two FLG contacts, is stamped using PDMS. Then, the PPC is used to pick up first the hBN and then the perovskite at 40°C, where only the areas in contact with hBN are transferred. The stack is then immediately released onto the device structure by increasing the temperature to 50°C, where the PPC slightly melts and allows to release the stack without dispatching the polymer layer. An additional top gate can be added by PDMS stamping.

Finally, a few important things to keep in mind for a successful pick-up procedure and some suggestions for further improvements: All the exfoliated layers considered for pick-up should not contain any thick bulk pieces close by or even within the same flake, as the step in height profile decreases the adhesion between the flakes. The top hBN, one of the first flakes that are picked up, should cover all the following flakes to provide rigid support while stamping and protection after drop-down. The FLG top gate also should be not below roughly 5 layers, as thinner layers tend to rip during pick-up without the support from hBN. When the contact line moves while melting the PC, one should slightly increase the temperature to further soften the polymer. Here, one should not heat above 190°$C$,

as then the whole structure is melted into the PC until it ultimately sticks to the PDMS and can not be transferred anymore.

As all the layers are picked up and in the end released onto the gold contacts, one should allow for some error margin in stamping to still place all the gates and contacts on the desired gold contact. The error margin should also be applied for the distance between contacts and to the gates, as the direct touch of two FLG flakes results in a shortage. The margin also helps against the spontaneous floating of flakes, where flakes slightly move their position or angle on the stack directly after being picked up. This might be related to a large scale atomic reconstruction, when slightly mis-angled layers minimize their energy by forming domains with zero-angle and natural H-stacking. As the increased temperature increases the mobility of thin layers [143], one should decrease the temperature to create Moiré-structures, whereas for samples without a Moiré-structure an increased temperature might help to foster reconstruction [338].

However, there are important drawbacks of the pick-up technique in contrast to polymer-assisted stamping: First, the direct exfoliation process takes much more time and yields significantly smaller flakes. The direct exfoliation of one or two suitable TMDC monolayers can easily take a week, whereas the simultaneous exfoliation and stamping of 4 devices including the one shown in Fig.3.7 took roughly 5 days. Second, the process involves more and sensitive steps where a high accuracy despite low contrast is needed, making the process more likely to fail. The pick-up process definitely yields cleaner structures, which is especially important to achieve precise doping or homogeneous electric fields. However, there are also similar clean, small areas in between bubbles for the PDMS stamping approach. In conclusion, when a certain area needs be as clean as possible, the time is well invested into the pick-up processt, for example for gate-tunable devices or heterostructures consisting of two or more monolayer TMDC. For structures without any gate or contact, where a random, clean area is sufficient, the polymer-assisted stamping should suffice.

## 3.2 Optical spectroscopy of 2D materials

In this section we now turn to the optical investigation of van der Waals heterostructures, fabricated along the guide presented in the previous chapter. The general spectroscopic setup used to acquire all the data of this thesis is depicted in Fig.3.12. It offers a high flexibility of the excitation source and allows to measure with high spectral, temporal and spatial resolution.

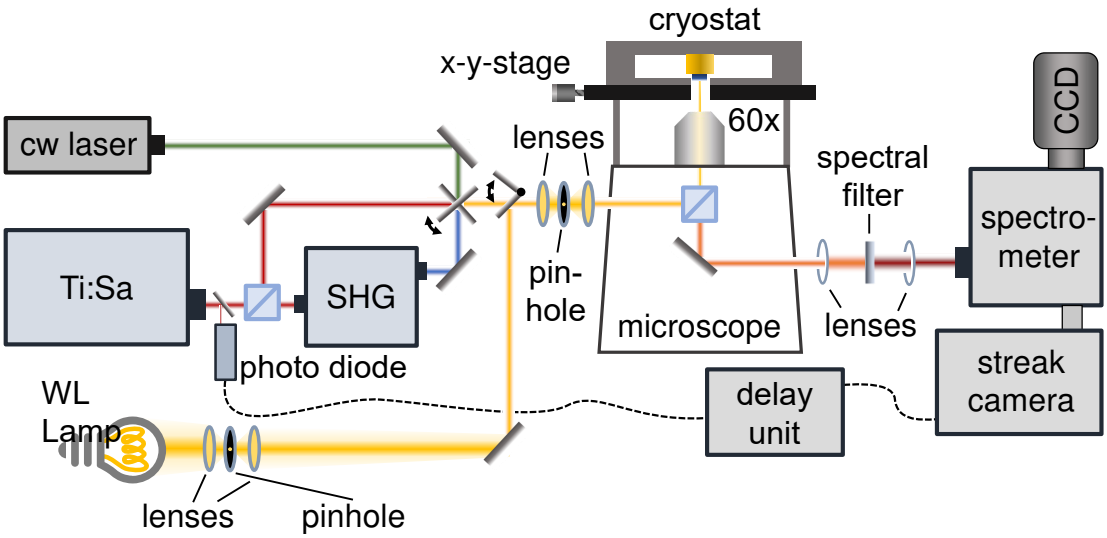


**Figure 3.12:** Schematic illustration of the spectroscopic setup.

Excitation lasers range from three continuous-wave (cw) solid state lasers (Laserglow) that emit spectrally narrow light at the central wavelengths of 405 nm, 473 nm or 532 nm to a wavelength-tunable titanium-sapphire laser (Chameleon Ultra II, Coherent) emitting 140 fs pulses with 80 MHz repetition rate. The Ti:Sa wavelength range of 680-1080 nm can be extended by the optional second harmonics generation device(HarmoniXX, APE), giving access to shorter wavelengths between 390-540 nm. Additionally, a spectrally broadband tungsten halogen lamp (250W, Newport) is used for reflectance contrast measurements. Here, the light is focused by a condenser lens on a small pinhole with 50 µm, serving as point-like source for the light, while a second condenser lense collimates the light after the pinhole. All the different excitation sources are combined into the same excitation path by flip-mirrors and the beam is spatially filtered by a pair of two lenses and a small pinhole with a diameter of 10-50 µm, depending on the power and spatial quality of the excitation source. For example, as only a small fraction of the light from the tungsten halogen lamp reaches the sample, most of the power should be transmitted through the pinhole, which is then chosen to be 50 µm. Contrarily, the

high power of the pulsed laser in the wavelength range of 750-900 µm allows to use a smaller pinhole of around 10 µm. Here, the higher spatial filtering is additionally more important for spatially resolved measurements. The light is then guided into the inverted microscope (Eclipse TI-U, Nikon), where a 60x objective (CFI S Plan Fluor ELWD 60XC, numerical aperture = 0.7, Nikon) focuses the excitation beam onto the sample, mounted in a Helium flow cryostat (KONTI Cryostat Type Microscope, CryoVac). The achievable spot size and therefore resolution is around 0.8 µm full width at half maximum (FWHM).

Inside the microscope, either a 10:90 (Reflection:Transmission) beamsplitter for PL or a 50:50 beamsplitter for the reflectance contrast measurement is used to direct the light on the sample and to the exit of the microscope. Using the 10:90 beamsplitter allows to collect 90% of the emitted light, while for the reflectance contrast measurements the changes to the reflected light are measured, where the 50:50 beamsplitter transmits in theory 25% of the initial power compared to 9% of the 10:90 beamsplitter. The excitation laser can then be spectrally cut by tunable filters with a cut-on slope below 3% (VersaChrome Edge, Semrock) or spatially filtered by an additional pinhole in the image plane and is subsequently guided through the entrance slit of the spectrometer (Acton SpectraPro SP-2300, Princeton Instruments). By adjusting the position of two lenses, the light is either focused onto a grating to achieve high spectral resolution or directly imaged onto a mirror, where the magnification is adjusted with the position of the lenses. For detection, two options are available: a charge coupled device (CCD) is used for steady state PL measurements and reflectance measurements, whereas a streak camera detector (C10910, Hamamatsu) allows time-resolved measurements with ps-resolution. A photo diode in combination with a delay stage provides synchronization with the Ti:Sa laser. The streak camera is operated in single photon counting mode, where light is only registered as one count when the intensity crosses a certain threshold value on a 2x2-binned pixel.

## Probing exciton complexes

Photoluminescence spectroscopy is a useful tool to study excitons and generally describes the detection of luminescence after photo-excitation. Here, the excitation laser creates eithe excitons, which relax to lower lying excitonic states such as trions and dark states, whereas some already recombine during that process. The light emitted from this excitonic distribution is then spectrally dispersed by the grating of the spectrometer and detected using a peltier-cooled CCD. Fig.3.13 shows an exemplary raw PL spectrum of an encapsulated $WSe_2$ monolayer ac-

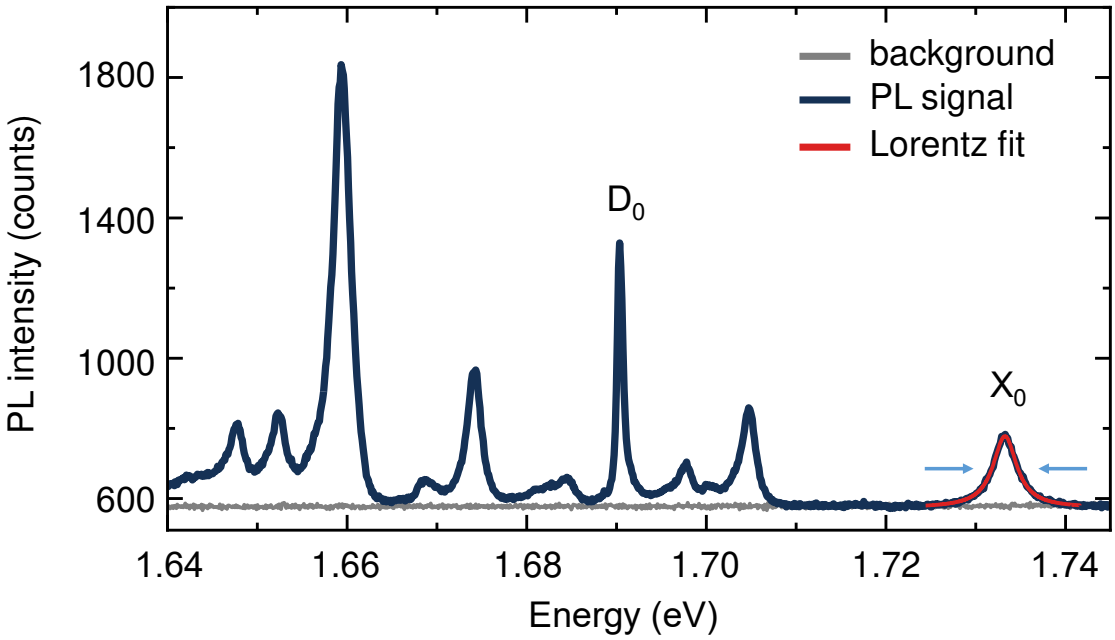


**Figure 3.13:** PL spectrum of an encapsulated $WSe_2$ monolayer at 5 K. The background, acquired data while the excitation is blocked, is shown in gray as comparison. The bright neutral exciton is exemplarily fitted with a Lorentz peak function.

quired at 5 K, where different excitonic states can be directly distinguished by their characteristic emission energy, such as the bright $X_0$ and dark $D_0$ states. Further details such as linewidth and a more accurately determined emission energy are extracted from fitting certain peak functions, such as a Lorentz function, to the data.

The reflectance contrast measurements are acquired in a similar way, whereas the data analysis requires a more sophisticated approach. The reflectance contrast $R_C$ requires a spectrum acquired at the sample position $R$, one as reference $R_{ref}$ on the $Si/SiO_2$ substrate and one background spectrum $R_{BG}$ and is then defined according to:

$$R_C = \frac{R - R_{ref}}{R_{ref} - R_{BG}} \tag{3.1}$$

Each spectrum is acquired with the same exposure time, which is adjusted to reach about 90% of the maximum signal of the CCD, most often in the range of a few hundred milliseconds. In order to achieve a reasonable signal-to-noise ratio, at least 100 frames are averaged to create each spectrum.

The exact shape of the spectra from a single monolayer on SiO2/Si is already governed by multi-layer interferences and therefore the thickness and dielectric

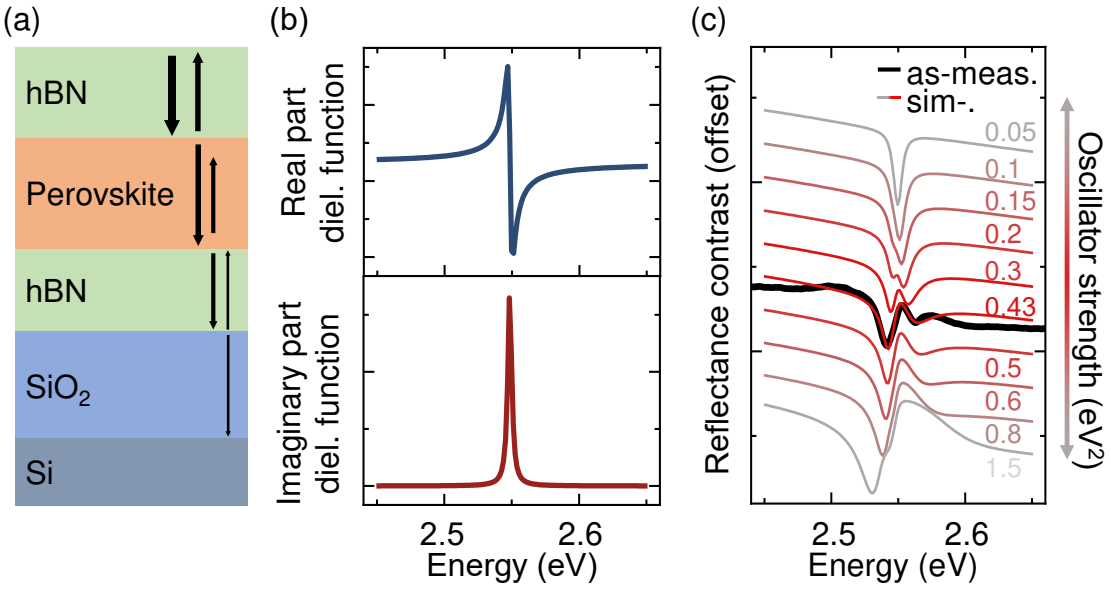


**Figure 3.14: Analysis of the reflectance contrast spectra (a)** Illustration of the multi-layer stack and light reflection and transmission at the interfaces. **(b)** Real and imaginary part of the model dielectric function consisting of a single lorentzian peak. **(c)** Reflectance contrast spectrum (black) and corresponding simulated reflectance contrast as function of the oscillator strength of a single excitonic transition.

function of each layer, which becomes increasingly complex with the number of different layers of the device [244]. This is taken into account by a transfer matrix method, where all the reflections of the light traveling through the crystal, as illustrated in Fig.3.14(a), are included [339, 340]. For the analysis, the dielectric function of graphite, hBN, $SiO_2$ and silicon are taken from literature. The dielectric function of the TMDC or perovskite layer is created by having Lorentzian oscillators for each relevant excitonic resonance $n$ and adjusting the resonance energy $E_n$, linewidth $\Gamma_n$ and oscillator strength $f_n$:

$$\varepsilon_{simulation}(E) = \varepsilon_{BG} + \sum_n \frac{f_n}{E_n^2 - E^2 - iE\Gamma_n} \tag{3.2}$$

where $\varepsilon_{BG}$ is an additional background dielectric constant. Using the different dielectric functions of the various materials of the heterostructure, the transfer matrix method models the reflectance contrast. Adjusting the thicknesses of each layer from both optical contrast and the resulting spectrum and modifying the parameterized dielectric function allows to obtain the dielectric function from the best fit to the data. This is especially challenging for perovskites, where also the exact thickness of the perovskite plays a crucial role. The exemplary dielectric function of a thin layer of PEA is depicted in Fig.3.14(b). This single resonance

evolves into a double-peak shape and fits well to the measured data shown in Fig.3.14(c) for the right parameters. For complex TMDC devices and perovskites in general the transfer matrix method with the parameterized dielectric function is crucial to accurately determine resonance energies and oscillator strengths.

In general, the reflectance contrast spectroscopy allows to determine the absorption of the investigated sample. However, for spectrally broad resonances with small oscillator strength, which are hard to resolve from the reflectance contrast, 2-photon excitation photoluminescence spectroscopy (TPLE) provides an alternative, for example to detect excited exciton states at high temperatures. Figure 3.15(a) illustrates the main advantage compared to linear spectroscopy, as two-photon excitation is only allowed for p-type states, suppressing direct optical transition and yielding a high signal-to-noise ratio. After excitation, excitons relax efficiently to the ground state via non-radiative processes and recombine radiatively. Consequently, the absorption of two photons excites one exciton, resulting in a characteristic quadratic dependence of the TPLE intensity on the excitation power, as displayed in Fig. 3.15(b) This allows to simultaneously obtain the ground state emission energy and the excited state absorption resonance, as illustrated by a typical spectrum as function of the two-photon excitation energy and the emission energy presented in Fig. 3.15(c).

### Exciton propagation from time- and spatially resolved photoluminescence

The previous section is focused on gaining spectral information from the emitted or reflected light. In order to learn about the spatial dynamics of excitons, the emitted light from recombining excitons can also be directly imaged by replacing the grating with a mirror. With the additional time-resolution of the streak camera, the underlying principle of exciton diffusion measurements is the following: We excite a certain exciton distribution, resembling the size and shape of the laser spot. Excitons traveling through the crystal and recombining after some distance lead to an increased width of the emission spot. Tracking these changes as function of time then allows to resolve the spatial dynamics of excitons. In practical terms, a small cross-section of the PL spot is directly imaged by the streak camera, as shown in Fig.3.16.

Here, the crucial point is the accurate calibration of the spatial scales on the streak camera sensor. A certified length reference is illuminated and the reflected

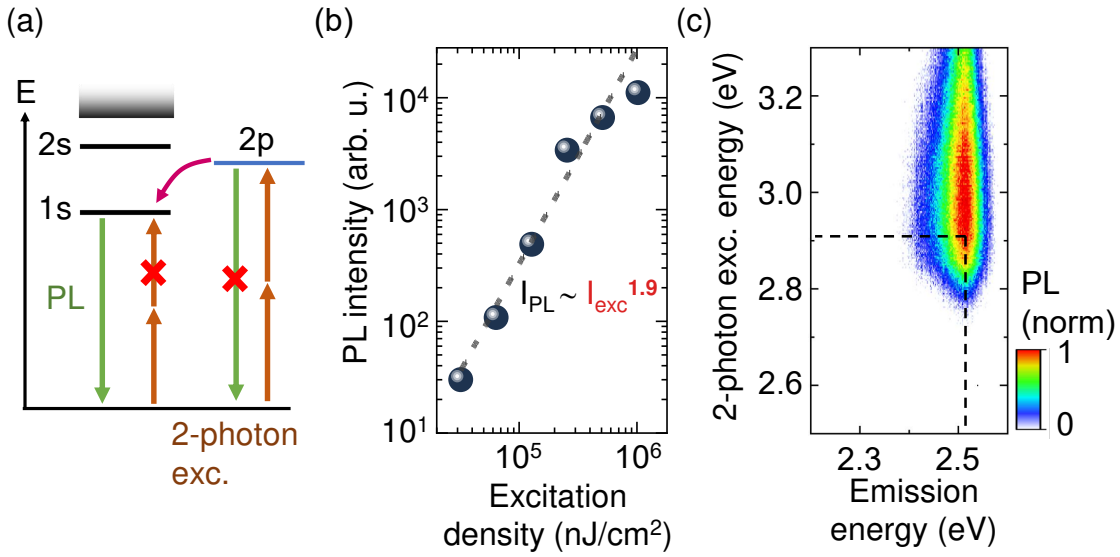


**Figure 3.15: Two-photon photoluminescence excitation spectroscopy** **(a)** Schematic of the two-photon excitation, which results in PL from the ground state. Forbidden transitions are indicated by a red cross. **(b)** Example normalized TPLE spectrum as a function of PL emission energy and two-photon excitation energy. **(c)** Excitation power dependence of the TPLE intensity illustrating the characteristic quadratic dependence of a two photon process.

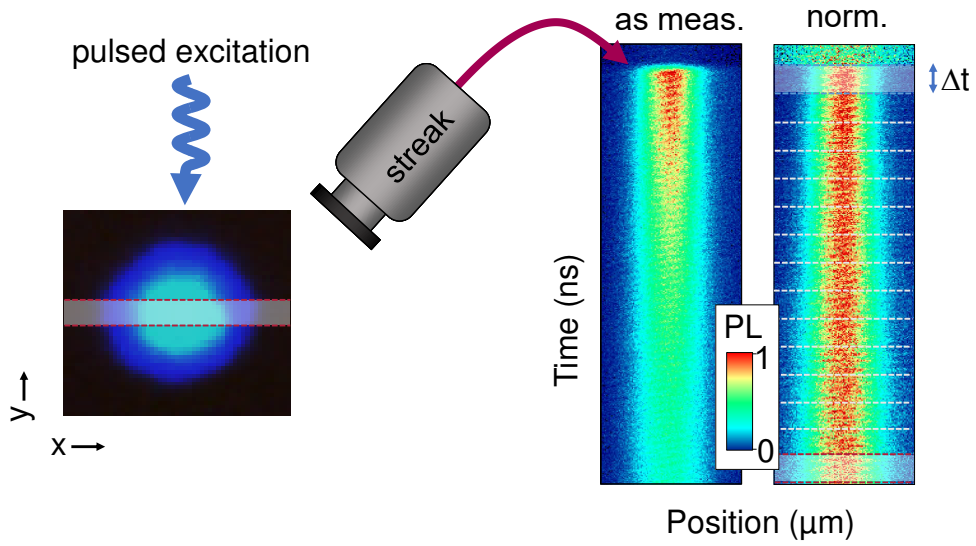


**Figure 3.16:** After the excitation with a short laser pulse, the streak camera images a small cross-section of the PL spot. The spatially- and time resolved image is normalized at each time and directly shows the broadening of the exciton distribution.

light allows to gauge the streak camera image to the right spatial sizes. Additionally, the broadband light illuminating the reference is filtered to a range of 50 nm around the desired center wavelength of the measurement to avoid uncertainties

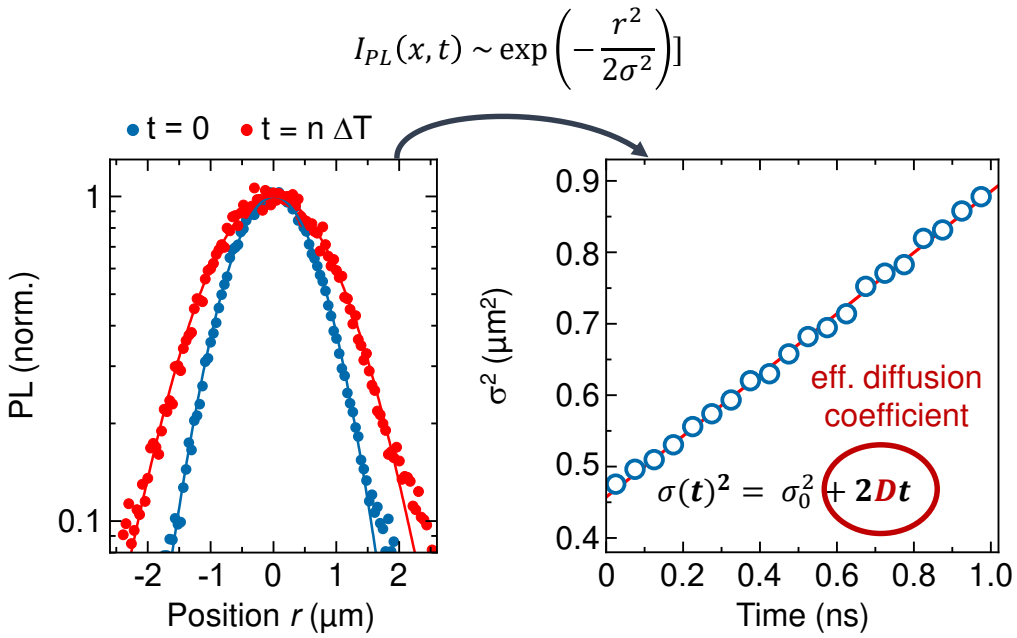


**Figure 3.17:** Determination of the diffusion coefficient from the linear increase of the squared width, extracted from fitting a Gaussian distribution to each temporal section.

from the dispersion and chromatic aberration of optical elements. The resulting spatially- and time resolved streak image directly shows the decaying PL intensity due to the finite lifetime of excitons. Normalizing the image at each time step then allows to directly illustrate the broadening of the PL spot and therefore exciton distribution.

For a quantitative analysis the streak image is divided into temporal sections integrating over a certain time $\Delta t$. The width of the spatially resolved PL profile at every temporal section is then determined by fitting a Gaussian peak function:

$$I_{PL}(t) \propto exp\left(-\frac{r^2}{2\sigma^2(t)}\right) \tag{3.3}$$

Then, the diffusion coefficient can be determined from the slope of the increasing squared width. Here, mean squared displacement (MSD) is often used for the central term $\sigma(t)^2 - \sigma_0^2$, representing the relative increase in spatial size over time. A linear increase $MSD \propto t^1$ is typically a clear hallmark of normal diffusion, whereas the subdiffusive regime is characterized by $MSD \propto t^{0<x<1}$ and ballistic transport by $MSD \propto t^2$ [318].

# Chapter 4

# Control of exciton propagation via strain engineering in 1D-2D hybrid structures

This chapter focuses on the results on manipulating the spatial dynamics of excitons, motivated by the challenges in building excitonic devices similar to electron transistors. The control of excitons, however, is much more complicated, as they are neutral quasi-particles. Figure 4.8(a) illustrates the general problem that neither an electric nor a magnetic field can constrain the movement of excitons along a certain directions. Therefore, we employ a different approach of creating low-energy channels confining excitons along a certain direction, as shown in Fig. 4.8(b).

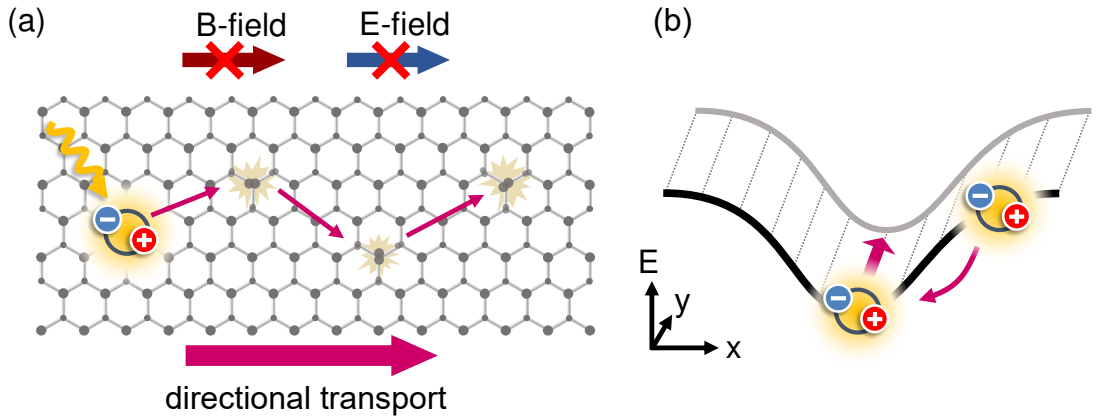


**Figure 4.1:** **(a)** Directional transport of excitons. **(b)** Controlling exciton movement by spatially tuning the energetic landscape.

This additional confinement is created by strain-tuning, where the crystal lattice of $WSe_2$ is stretched, changing the underlying band structure and creating quasi-1D channels. The high-quality hBN-encapsulated samples allow to observe subtle changes of the excitonic finestructure, in agreement with recent first-principle calculations. Using time- and spatially resolved photoluminescence spectroscopy, the resulting impact on the exciton diffusion is directly monitored. We create

quasi-one-dimensional channels with nearly 100% anisotropy of the exciton flow at cryogenic temperatures. Additionally, the strain-engineered confinement in combination with simultaneously suppressed exciton-phonon scattering allows similar observations at room temperature.The main results and some figures presented in this chapter are reported in the publication [341].

## 4.1 Strain engineering in monolayer TMDCs

The isolation of single, atomically thin sheets allows effective strain-tuning as the isolated layers are independent of any substrate. While the isolated layers can withstand strong deformations of up to several %, this stretching of the lattice leads to drastic changes of the bandstructure, as shown in Fig. 4.2 [342–346]. In $WSe_2$, a transition from the direct bandgap at the K point to an indirect bandgap between the conduction band $\Lambda$ point and the valence band K point is predicted for negative strain values, as shown in Fig. 4.2(c) [346]. Positive strain values, e.g. stretching the layer, further reduce the band gap at the K points. Local strain then can be used to create nanoscale potentials confining excitons [347, 348]. The concept of the sample is schematically illustrated in Fig. 4.3(a), where an encapsulated $WSe_2$ layer is placed on top of $GaAs/Al_{0.36}Ga_{0.64}As$ core/shell nanowires, providing a clean substrate to locally strain the monolayer.

The structure is fabricated by polymer-assisted exfoliation and stamping in order to efficiently transfer the strain from the nanowires, which are mechanically "scratched" on clean $Si/SiO_2$ substrates. The alternative method of dispersing the nanowires from an iso-propanol-based solution yielded a more homogeneous distribution of the nanowires on the sample, but resulted in a poor optical quality of the encapsulated layers. Figure 4.3(b) shows the hybrid 1D-2D structure, where the encapsulated $WSe_2$ monolayer covers multiple nanowires. The bottom panel provides a zoom-in of a particularly homogeneous nanowire employed for most of the experiments. The atomic force microscopy image presented in Fig. 4.3(c) shows the smooth deformation of the hBN-$WSe_2$-hBN to a height of around 90 nm over a width of over one µm.

In order to gain information on the energy landscape of the 1D-2D sample, the PL spot is scanned across the deformation along the y-direction. The PL data, presented in Figs. 4.3(d) and (e), shows a clear shift of the bright exciton resonance to lower energies in the vicinity of the nanowire. In order to accurately determine the spatial size of the deformation, the PL-scan is deconvoluted with the optical

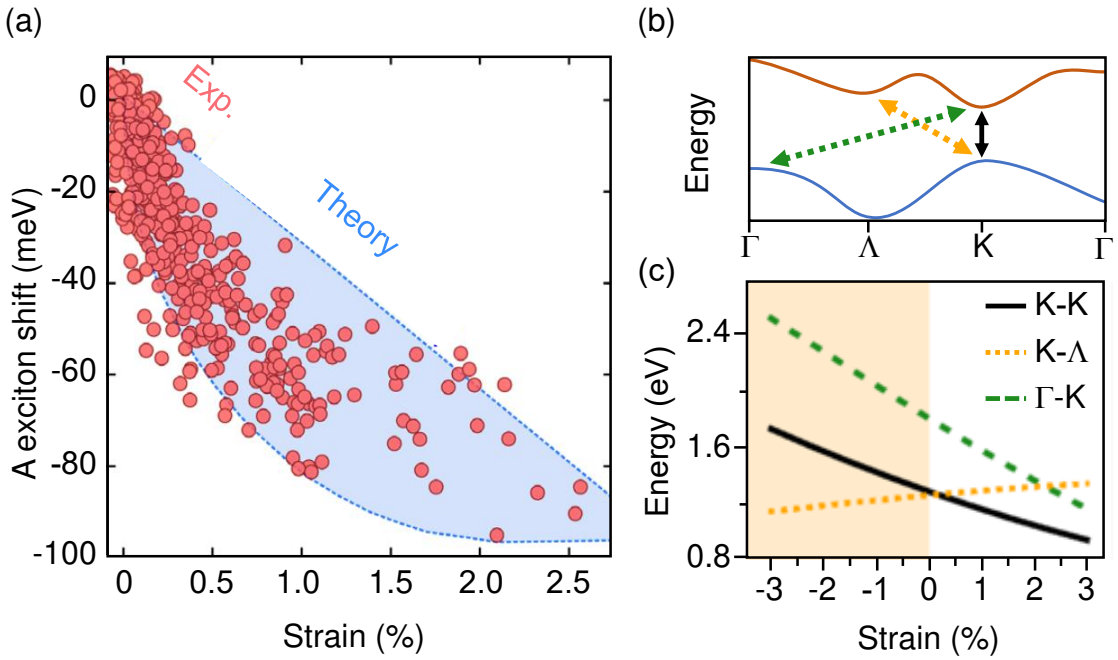


**Figure 4.2:** **(a)** Impact of strain on the main excitonic transition in $MoS_2$. Adapted with permission from [343]. **(b)** Direct $K - K$ and the two indirect $K - \Lambda$ and $\Gamma - K$ transitions in $WSe_2$. **(c)** Changes of the underlying band structure of $WSe_2$ under strain. At around zero strain the energetically lowest transition changes from indirect to direct. Adapted with permission from [346]

resolution, yielding a nearly constant potential and therefore strain in the middle of the deformation, shown in the right side of Fig. 4.3(d). It is important to note that the strain profile is not directly connected to the height deformation, as the lattice can relax over several hundreds of nm, similar to atomic reconstruction shown in heterostructures [349, 350]. Therefore, we consider a super-Gaussian strain profile, accurately describing the experimentally obtained exciton energy shift.

Here, the strain magnitude is estimated from first-principle DFT-LDA calculations yielding a relative energy shift as function of strain, e.g. a gauge factor of 63.2 meV/% for the bright exciton, in agreement with values reported in literature [351–353]. This results in a strain value of about 0.15% for the obtained potential depth of 10 meV. Exemplary PL spectra plotted in Fig. 4.3 demonstrate the energy shift with strain across the deformation.

However, multiple other sources can contribute to energy shifts of the excitonic resonance. For example, a change of the free carrier density in the vicinity of the nanowire also modifies the transition energy of the neutral exciton. A clear hallmark of additional free carrier is the emergence of the trion-states. With

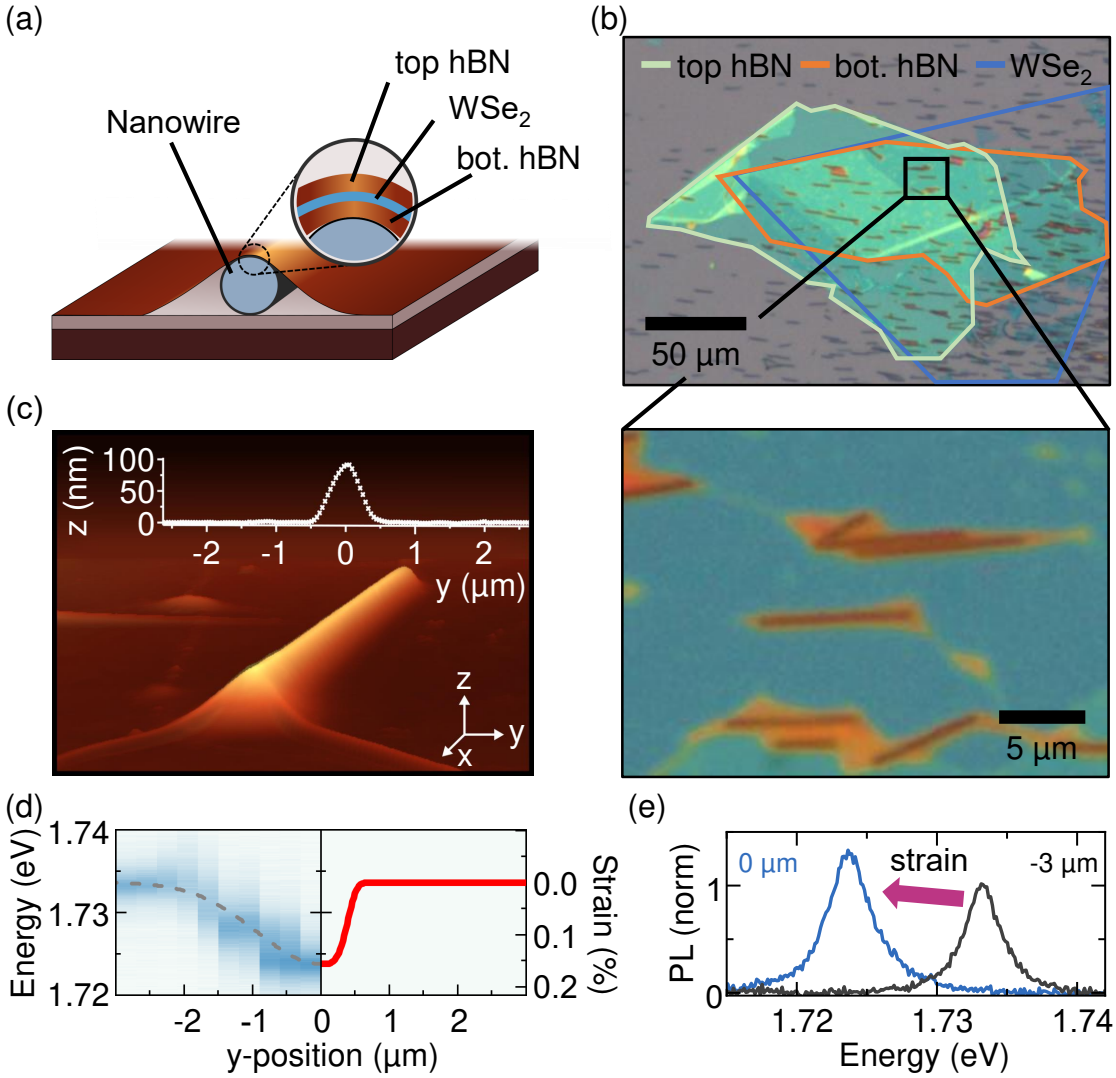


**Figure 4.3: Strain engineering in a hybrid 1D-2D $WSe_2$-device.** **(a)** Schematic of the hybrid device structure. **(b)** Optical micrograph of one investigated samples with an encapsulated $WSe_2$ monolayer on top of tens of nanowires. Zoom-in on a clean hybrid 1D-2D structure in the bottom panel. Orange colors represent bubbles and contaminants between the nanowires on the $Si/SiO_2$ substrate and the encapsulated monolayer. **(c)** Atomic force microscopy image showing the topography of the nanowire shown in (b). The lateral height profile through the center of the nanowire is shown in the inset. **(d)** Measured exciton energy as function of the spatial position at a temperature of 5 K. In addition to the as-measured $X_0$ energy (left) the right side shows the spatial strain profile extracted from de-convoluting the measured data with the optical detection spot and using the theoretically determined gauge-factor of $-63.2$ meV per % strain. **(e)** Exemplary PL spectra directly in the potential well on top of the nanowire and from the unstrained region in close proximity to the nanowire.

increasing doping density, the trion feature gain intensity due to the oscillator strength transfer from the neutral exciton. Simultaneously, the energy difference

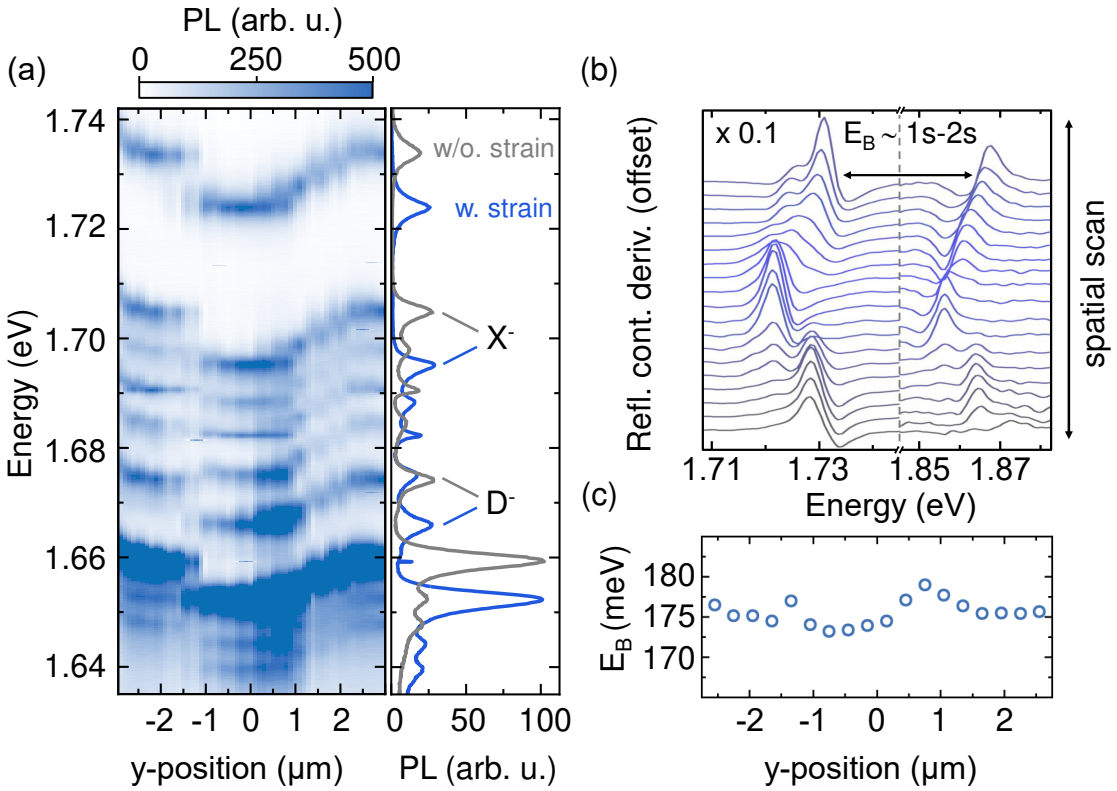


**Figure 4.4:** Impact of local strain on the emission and absorption spectrum of $WSe_2$ at 5 K **(a)** All the different excitonic states shift due to strain simultaneously as function of the spatial position. **(b)** Line scan of the reflectance contrast derivative, where the left side is multiplied by 0.1 for better visibility. **(c)** Constant exciton binding energy extracted from the energy separation between ground and excited state in (b) demonstrating a constant dielectric environment in the strained vicinity.

between the charged and neutral state increases arising from the elevated Fermi-energy and momentum-conservation. Figure 4.4(a) shows that both the intensity and relative energy separation of the trions $X^-$ stay constant across the deformation, indicating a constant doping density. This is also supported from similar observations for the dark trion $D^-$.

Additionally, the reflective contrast derivative, shown in Fig. 4.4(b), confirms a homogeneous dielectric screening across the potential. Therefore, we estimate the exciton binding energy from the separation between ground- and excited state by $E_B = 1.3\,(E_{1s} - E_{2s})$, where the factor of 1.3 is taken from literature [253]. As Fig. 4.4(c) shows, this results in a constant binding energy of around 175 meV with small variations on the order of 5 meV arising at the edge of the deformation due to broadened linewidth of the resonances. However, as variations of the binding energy are mostly counteracted by a similar shift of the band gap, the optical

transition energy of the exciton changes much less than the binding energy [171–173]. Therefore, as doping and dielectric fluctuations can be excluded, we attribute the shift of the resonance energy purely to strain.

## 4.2 Exciton finestructure splitting under strain

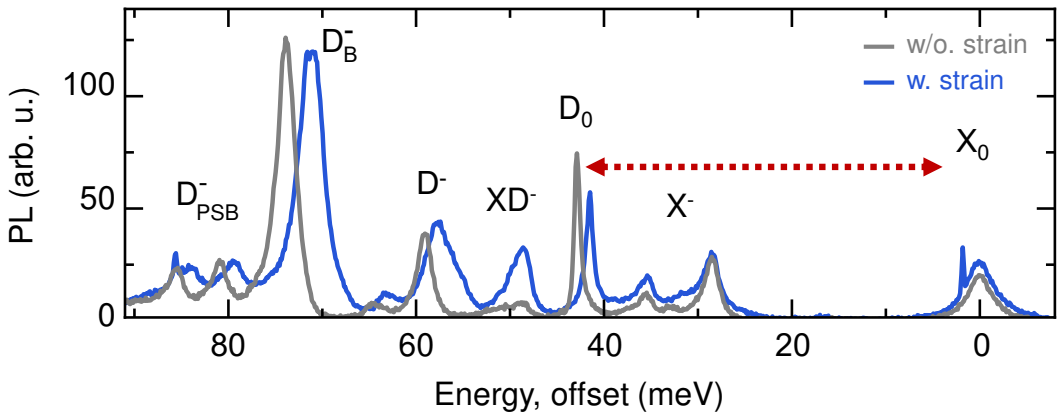


**Figure 4.5: Exciton finestructure under strain** Extended PL spectra of unstrained and strained area spectrally offset to relative energy with respect to the X0 resonance.

The high quality of the encapsulated layer and the geometry of the sample allowing measurements at liquid helium temperatures additionally provides access to an additional clear, but subtle hallmark of strain. The previous sections have shown the impact of strain as constant energy shift of all excitonic resonances to lower energies. A closer look, however, reveals a slight change of the energy separation between bright and dark states, as shown in Fig. 4.5. Here, the strained and unstrained PL spectra are spectrally offset to the relative position of the neutral, bright exciton. While the relative spectral position of the bright trion states is independent of the applied strain, all dark states are slightly shifted to a lower energy difference, e.g. a decrease of the dark-bright splitting.

The spectral separation between dark and bright exciton state has two contributions: the spin-splitting of the conduction band $\Delta_C$ and a difference in binding energy, due to slightly different effective masses and varying electron-hole exchange interaction due to different spins. However, the binding energy of both bright and dark exciton should in principle not change drastically with strain, as also experimentally observed in Fig. 4.4(c).

Therefore, this observation is attributed to a change of the energy separation between the spin-split bands in in the conduction band as illustrated in Fig. 4.6(a),

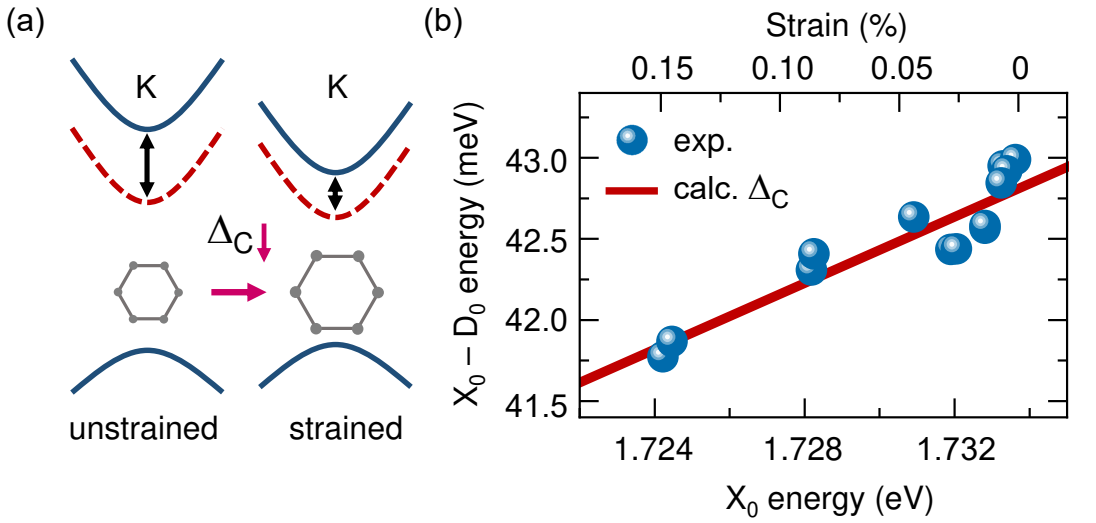


**Figure 4.6: Impact of strain on the excitonic dark-bright splitting (a)** Positive strain (extending the lattice) results in an overall redshift and an additional decrease of the conduction band splitting $\Delta_C$. **(b)** Measured energy splitting between the bright ($X_0$) and dark state ($D_0$), indicated in (a) as function of the bright state energy in comparison with the calculated energy separation (red line).

in agreement recent DFT-calculations, [346, 354]. Quantitatively, the observed continuous reduction of the dark-bright splitting agrees well with a theoretically calculated gauge factor of -6.4 meV per % strain, shown in Fig. 4.6(b). This introduces the combination of the absolute spectral shift of $X_0$ with the $X_0 - D_0$ separation thus as useful, characteristic signature of strain and its magnitude. Additionally, strain allows to the distinction of dark states formed by electrons from the lower conduction band. The observed shift is due to anisotropic strain, e.g. stretching the lattice in one direction, where one would expect roughly double the shift for isotropic strain.

Focusing on the charged excitons, Figure 4.7(a) and (b) depicts the relative energy shift with strain of the bright $X^-$(a) and dark trion $D^-$ with its two phonon sidebands $D^-_{PSB}$(b). In contrast to the constant energy of the bright state, the dark trion states shift as function of strain, identically to the neutral dark exciton. Here, both the dark trion $D^-$ and the two phonon sidebands $D^-_{PSB}$ shift equally, as the impact of strain on the distinct phonon modes is on the order of 1-3 $cm^{-1}$ per % strain and therefore below 0.01 meV at the present strain values [343, 355] Interestingly, the $D^-_B$ state shifts twice as far with strain compared to the other dark states, as shown in Fig. 4.7. Only recently, this state has been adressed as the brightened emission of the dark trion state $D^-_B$, formerly often labeled as $T_1$

in literature [278, 279, 292, 356]. Here, the spin- and momentum conservation is ensured by the remaining electron, conceptually like an electronic sideband.

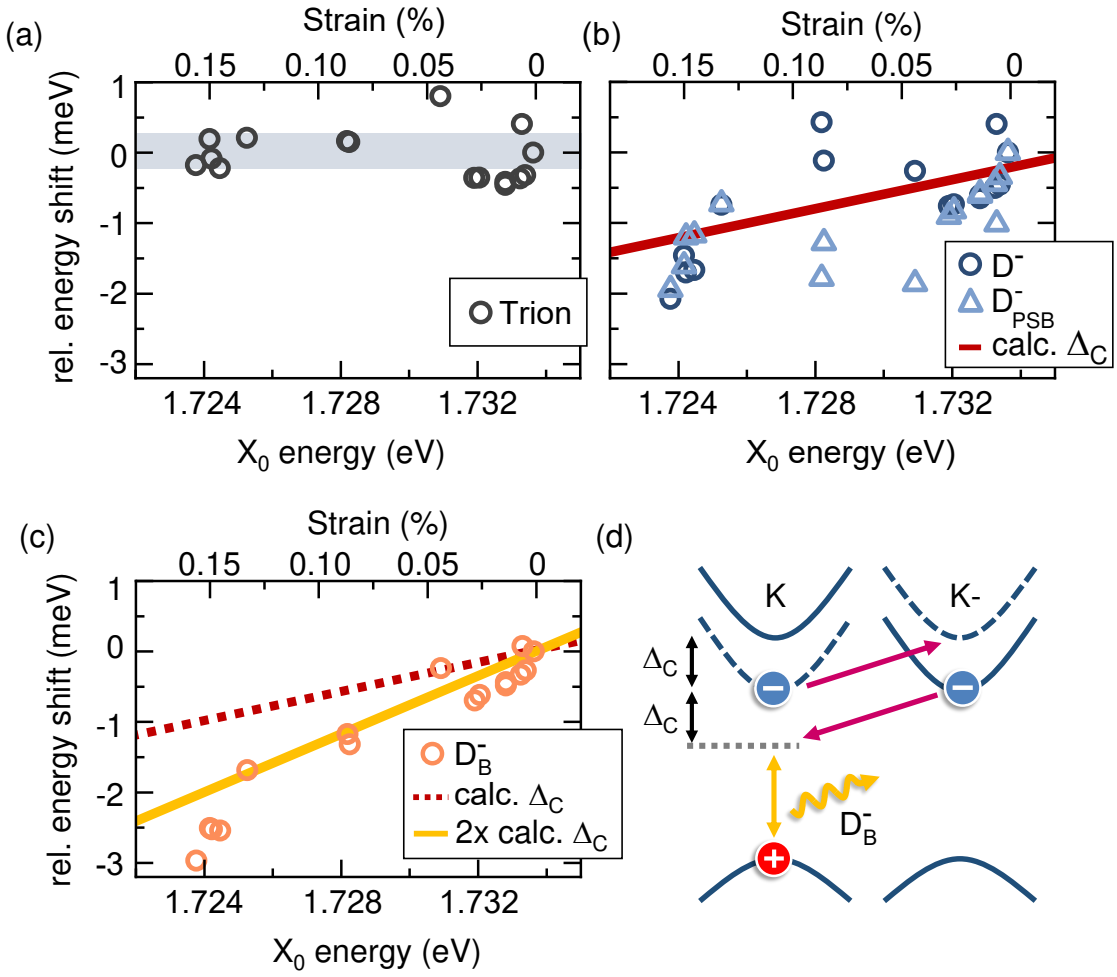


**Figure 4.7: Exciton finestructure splitting for different excitonic states** **(a)** Change of the trion binding energy as function of the bright state exciton. The expected dark-bright splitting is plotted as comparison. **(b)** Relative energy splitting of the dark trion $D^-$ and its sideband $D^-_{PSB}$ closely following the theoretical and experimental expectation of the dark-bright splitting. **(c)** Relative energy shift of the bright emission of the dark trion $D^-_B$ in comparison with the doubled dark-bright splitting. All graphs are equally scaled for comparison of the relative shifts. **(d)** Recombination pathway of the brightened dark trion.

Here, we experimentally observe evidence for the attributed bright recombination mechanism illustrated in Fig. 4.7(d) caused by the spin-valley mixing of the electrons in the two different valleys. The dark trion consists of two electrons in the lower conduction valley of K and K-valley and the hole in one of those valleys. The momentum-indirect electron then recombines directly with the hole by scattering to the same valley as the hole. In order to conserve the momentum, the

other electron is excited to the opposite valley. The emission energy is therefore reduced by $\Delta_C$ compared to the dark trion $D^-$. Applying strain will shift the dark trion similar to the $D_0$ state by the shift of the lower conduction band $\Delta_C$. The additional brightening mechanism of the $D_B^-$ state relative to the $D^-$ also depends on $\Delta_C$, introducing an additional scaling with strain. The relative energy ultimately should scale with twice the dark-bright gauge factor as function of strain. Indeed, as Fig. 4.7(c) shows, the relative energy shift of the $D_B^-$ scales twice as strong as the regular dark states, further supporting the brightening mechanism.

## 4.3 Exciton diffusion along strain-induced quasi-1D channels

The strain-engineered potential not only impacts the discussed spectral properties and implications on the fine structure, but also drastically impacts the spatial properties of excitons. First, we focus on the confinement at cryogenic temperatures supported by simulations based on the drift-diffusion model. Finally, we turn to room-temperature results with direct implications from strain-induced changes of the underlying band structure.

### 4.3.1 Anisotropic exciton propagation

We directly monitor the impact of strain on the exciton propagation using the transient microscopy setup. Therefore, we excite the sample directly in the vicinity of the nanowire-induced deformation and monitor a cross-section of the emitted PL in space and time using the streak camera. The excitation energy is tuned to around 1.77 eV, between the gound and first excited state, where no resonance is in close spectral proximity to exclude any strain-dependent changes of the absorption. Aligning the nanowire either parallel or perpendicular to the streak camera slit allows to determine the diffusion along different directions. Fig. 4.8(a) presents representative emission profiles directly after excitation and after 0.7 ns. Along the deformation (top panel) the PL emission broadens over time. In the perpendicular direction however, the spatial emission profile stays nearly constant. We quantitatively analyze the diffusion by fitting a Gaussian-distribution to the emission profile at different time intervals. Figure 4.8(b) shows the resulting time-dependence of the squared width $\Delta\sigma^2(t)$, or mean-squared displacement (MSD), along and perpendicular to the deformation. Additionally, the two directions are measured on an unstrained sample area close by as comparison. The

diffusion coefficient is then extracted from the slope via MSD $= 2Dt$, resulting in a value of $1.4\,\mathrm{cm}^2/\mathrm{s}$, similar to the diffusion of the unstrained area with around $1\,\mathrm{cm}^2/\mathrm{s}$. This value is also in agreement with recent literature values of hBN-encapsulated $WSe_2$, where the slightly lower values obtained here might be due to different doping densities [357].

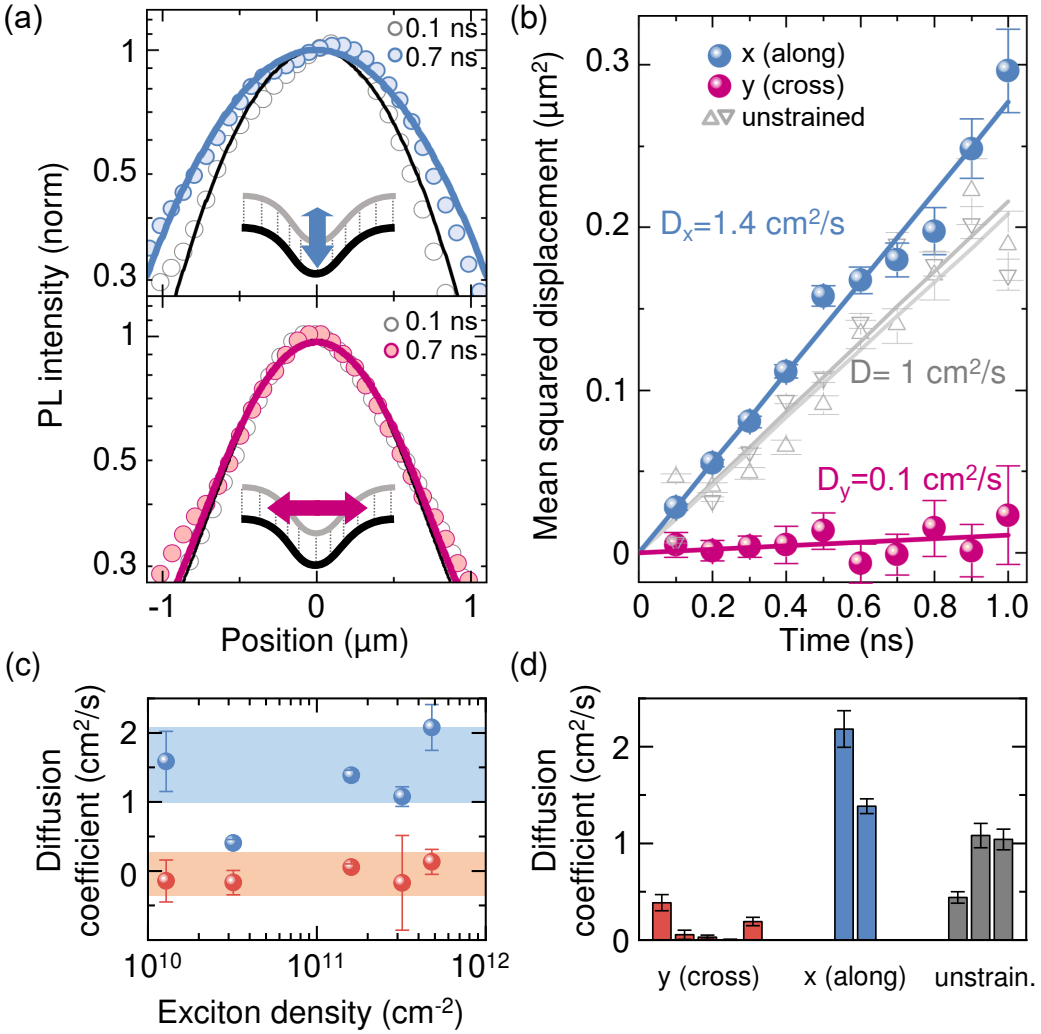


**Figure 4.8: Anisotropic exciton diffusion at cryogenic temperatures. (a)** Spatially-resolved PL emission profiles obtained closely after excitation and at a later time of 0.7 ns. Solid lines represent Gaussian fits to the data. Top panel depicts the spatial exciton distribution along the wire in the x-direction, while the bottom shows the corresponding emission profiles across the channel (y-direction). **(b)** Mean-squared displacement of the exciton distribution along and across the potential channel as well as from an unstrained area. Error bars display the standard error of the Gaussian fit. The displayed diffusion coefficient are extracted using $MSD = 2\,Dt$. **(c)** Diffusion coefficient as function of the excitation density for the x- and y-direction. **(d)** Summary of diffusion coefficients from different samples, all measured at cryogenic temperatures of 5 K.

In stark contrast, the propagation perpendicular to the nanowire is almost completely suppressed with a diffusion coefficient of 0.1 $cm^2/s$. We define the degree of anisotropy according to $\frac{D_x - D_y}{D_x + D_y}$, obtaining a value of 86 %. This signifies the strong suppression of the diffusion in one direction and free propagation into the other direction. The strongly anisotropic diffusion is independent of the excitation density, as illustrated in Fig. 4.8(c). Here, the resulting exciton density is varied over more than an order of magnitude, while an efficient propagation parallel and nearly complete vanishing diffusion perpendicular to the wire is observed for all densities. Similarly, the observation is also robust across different samples with similar strain-engineered potentials, as presented in Fig. 4.8(d).

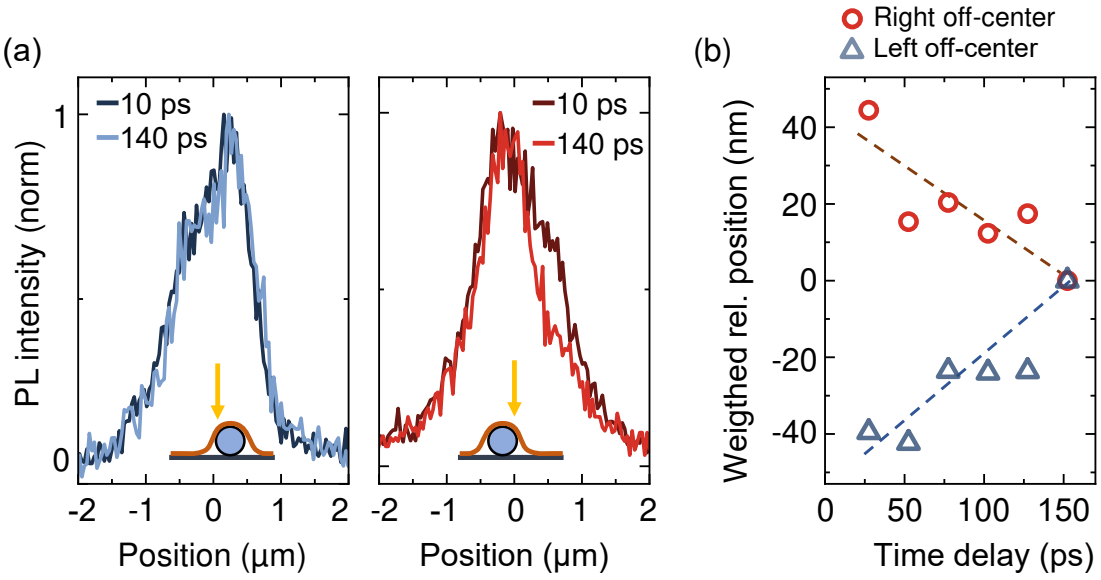


**Figure 4.9: Indication for funneling by off-center excitation.** **(a)** Normalized PL-profiles for excitation after excitation on the left (left) and right (right) sides of the 1D-channel. The dark and light spectra display the spatial distribution directly after excitation (10 ps) and after 140 ps, respectively. **(b)** Weighted relative position of the spatially-resolved PL-profiles between -2 µm and 2 µm, shifting to the middle for the two different excitation spots. Dashed lines are guides-to-the-eye.

In general, the demonstrated suppression of exciton propagation perpendicular to the deformation is expected from the corresponding change of the exciton energy, creating the potential channel shown in Fig. 4.3(d). Additionally, excitons located directly on a potential gradient should be efficiently guided along the gradient to the bottom of the potential, a process termed as funneling [347, 358–360]. In the investigated structure however, the spatial scale of the potential gradient on the edge of the deformation is below the diffraction limit of the setup. Still, there are some indications for funneling due to strain in the sample. First, the

PL intensity of the charged biexciton $XD^-$ is enhanced in the strained region, as directly observed in the spectra in Fig. 4.6 and also visible in the spatially resolved PL in Fig. 4.4(a) at an energy of 1.675 meV in the strained region. As composite species consisting of two or more excitonic particles, the density dependence of biexcitonic species generally follows a quadratic dependence. The biexciton therefore serves as clear indication for a higher density of excitons in the potential channel, despite the spatial size being below the resolution limit.

Secondly, there is also a direct spatial evidence attributed to funneling: The PL intensity shifts to the center of the strain-created potential minimum, when excitons are excited slightly off-center. Figure 4.9(a) depicts the normalized emission profiles at different times and for excitation on the left and right side of the potential channel, respectively. The shift is opposite for The weighted relative position, e.g. the spatial center of mass of the PL, clearly shifts opposite for excitation on the left and right flank of the potential well, as shown in Fig. 4.9(b). Despite the relatively small effect on the order of 50 nm, the according change of the shift when changing the excitation position supports the interpretation as funneling towards the middle of the potential channel.

### 4.3.2 Analysis with drift-diffusion model

The presented manipulation of the exciton motion crucially depends on the relation between the confinement energy and the kinetic energy of the particle. Here, the determined energy potential of the 1D-channel of around 10 meV is more than an order of magnitude higher than the thermal energy at cryogenic temperatures of around 0.5 meV and therefore should in principle fully constrain excitons. In order to get a quantitative understanding of the impact of such a strain potential on the exciton diffusion, we model the exciton dynamics affected by an underlying potential.

Therefore, the diffusion equation is modified by extending Fick's first law with an additional drift term, depending on the exact shape of the potential $u = u(\mathbf{r})$:

$$J = -D\,\nabla n - \frac{D}{k_B T}\, n\,\nabla u \tag{4.1}$$

Then, the continuity equation needs to be satisfied leading to

$$\frac{\partial n}{\partial t} = -\nabla\, J = \nabla\left(D\,\nabla n + \frac{D}{k_B T}\, n\,\nabla u\right) = D_{const}\,\Delta n + \frac{D_{const}}{k_B T}\,(\nabla n \cdot \nabla u + n\,\Delta u) \tag{4.2}$$

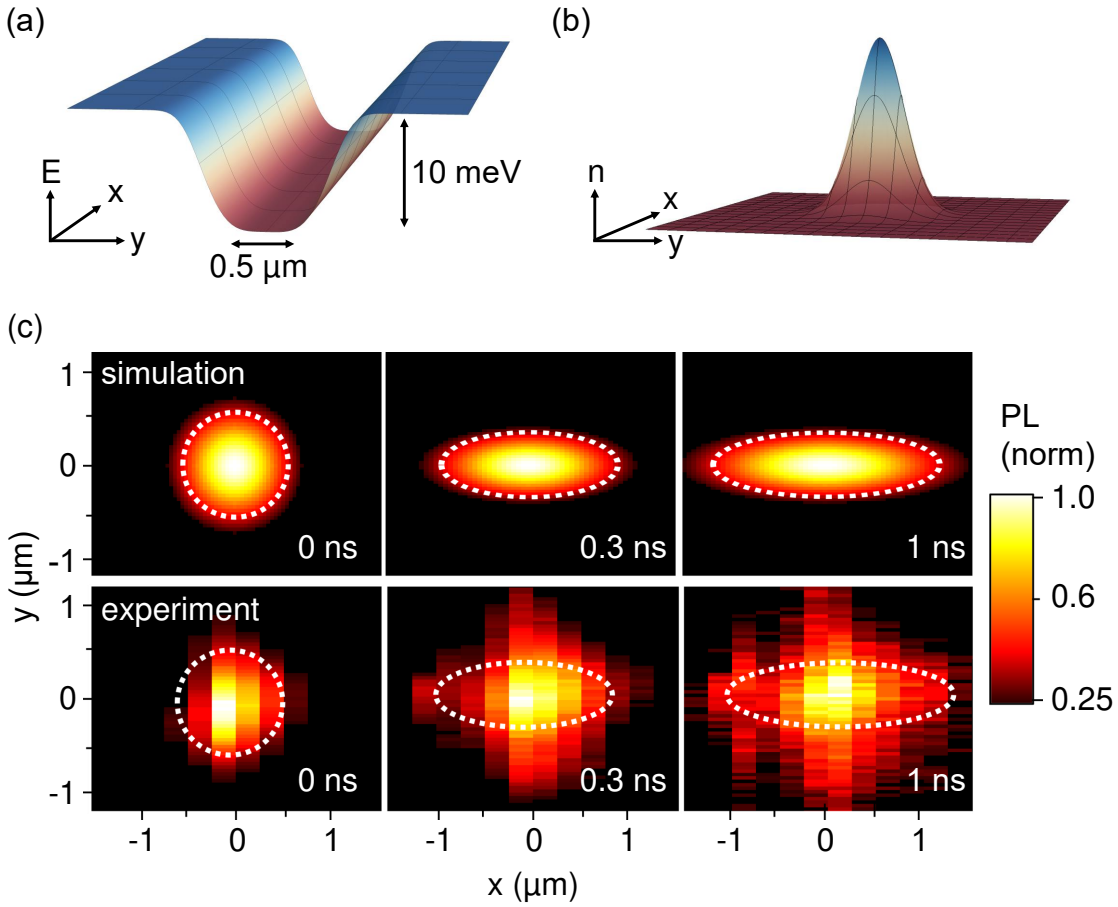


**Figure 4.10: Simulation of exciton diffusion in the presence of a 1D-channel.** **(a)** Exciton distribution at t=0 defined by a Gaussian distribution. **(b)** Schematic illustration of the 1D-channel in the underlying potential landscape. **(c)** Comparison of the simulated and measured 2D exciton density at different times in the top and bottom row, respectively. Dashed lines are guides-to-the-eye.

Again, assuming a spatially constant diffusion coefficient and taking the finite lifetime $\tau$ into account results in the modified diffusion equation:

$$\frac{\partial n}{\partial t} = D_{const}\,\Delta n + \frac{D_{const}}{k_B T}\left(\nabla n \cdot \nabla u + n\,\Delta u\right) - \frac{n}{\tau} \tag{4.3}$$

where we exclude non-linear terms such as the Auger-process for simplicity, in accordance with the absence of density-dependent effects in the experiment.

The attractive potential **u** is then constructed as super-gaussian function along the y-axis to closely resemble the experimentally obtained strain-created 1D-channel:

$$u = -\Delta E \cdot exp\left(-0.5^2\left(\frac{y}{\sigma_{channel}}\right)^4\right) \tag{4.4}$$

with the parameters $\Delta E = 9\,\text{meV}$ and $\sigma_{channel} = 0.5\,\mu\text{m}$, resulting in a FWHM of 0.6 µm, as illustrated in Fig. 4.10. Lastly, Fig. 4.10 shows the initial Gaussian-shaped exciton density $n = n_0\, exp\left(-\frac{x^2+y^2}{2\sigma_0}\right)$ with $\sigma_0 = 0.3\,\mu\text{m}$. Then, the time evolution of this initial exciton density is simulate by numerically solving the modified diffusion equation 4.3. A spatial grid with 200x200 points with a step size of 0.04 µm and temporal steps below 1 ps provides the necessary resolution, while the experimentally obtained diffusion coefficient D=1.4 $\text{cm}^2/\text{s}$ is chosen according to the experiment.

The simulated exciton density at different time steps is presented in the top row of Fig. 4.10(c), where the exciton density is normalized at each time. Here, the round and isotropic initial density becomes increasingly elongated and anisotropic over time. The distribution broadens regularly along the channel, while being completely localized perpendicular to the potential, further supporting the experimentally observed highly anisotropic transport. The bottom row shows time-resolved 2D photoluminescence images as comparison. Here, the detection cross-section of the streak camera is adjusted parallel to the y-direction and manually scanned along the x-direction in steps of 0.25 µm, while measuring the time- and spatially resolved PL at each point. The measured emission transiently develops an anisotropic, elongated shape along the channel after being initially symmetric. While there is some noise in the measured data, probably stemming from variations in the excitation spot due to the long overall measurement time and the difference in resolution along the x- and y-axis, the experiment agrees well with the model. In summary, excitons are efficiently confined along strain-created potential channels, where the low kinetic energy of the exciton at cryogenic temperatures facilitates the high anisotropy. The impact of a higher thermal energy will be discussed in the next section.

### 4.3.3 Strain-induced channels with reduced scattering

The high degree of anisotropy observed at liquid helium temperatures is generally expected to be lower at elevated temperatures, due to the higher kinetic energy of excitons, allowing to escape the potential. Figure 4.11 shows the time-dependent variance or MSD for the two directions measured at 290 K. Again, we see efficient diffusion along the nanowire with a diffusion constant of up to 13 $cm^2/s$, which is in the typical range of diffusion values for TMDCs in the linear regime at room temperature [361]. However, perpendicular to the 1D channel the propagation is strongly suppressed with a diffusion coefficient -0.8 $cm^2/s$, resulting in an anisotropy of 100%, analogous to the data acquired at 5 K. While other diffusion measurements at room temperature yield similar values around 0 $cm^2/s$, we attribute the observed negative diffusion, e.g. shrinking of the exciton distribution, to funneling effects.

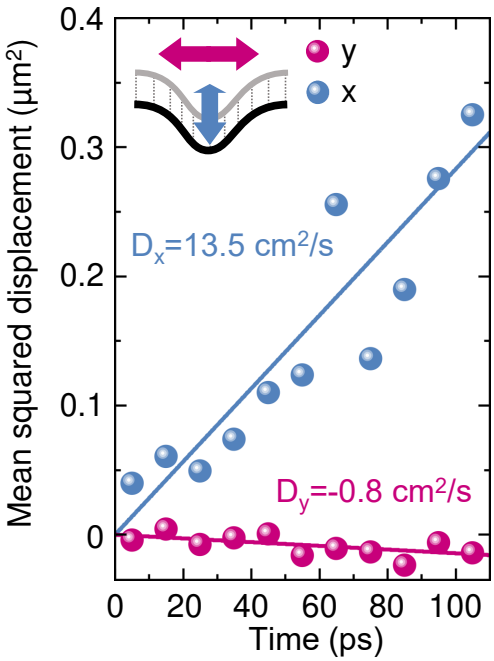


**Figure 4.11: Anisotropic exciton transport at room temperature** Mean squared displacement of the exciton distribution at different time intervals measured along (x-direction) and across (y-direction) the channel.

However, following the previous discussion, the confinement potential of around 10 meV should not be able to confine excitons with a thermal energy of 25 meV. Excitons with a kinetic energy higher than the depth of the 1D channel should be able to escape the potential and therefore exhibit a less pronounced anisotropy. Also, a similar potential depth is observed at room temperature, as shown in Fig.

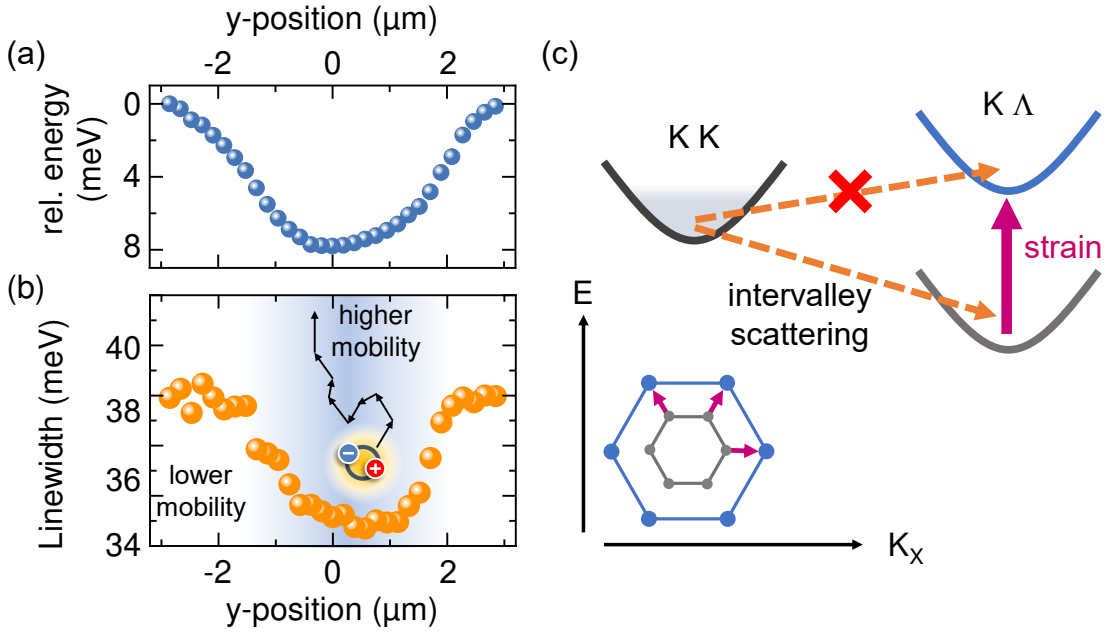


**Figure 4.12: Impact of strain on the scattering rate and multi-valley bandstructure at room temperature.** **(a)** Spatial scan of the exciton emission scan yields a similar potential at 290 K compared to 5 K. **(b)** Obtained excitonic linewidth as function of the y-coordinate showing a pronounced decrease with increasing strain. **(c)** Impact of en expanded lattice on the underlying multi-valley excitonic band structure, reducing the exciton scattering.

4.12(a) excluding additional effects, such as higher strain at room temperature due to different thermal expansion coefficients of $WSe_2$, hBN and the $SiO_2$. However, an additional feature of strain in $WSe_2$ is observed in the employed hybrid structures, the additional change of the exciton-phonon coupling. Figure 4.12(b) depicts the linewidth of the PL emission as function of the spatial coordinate across the deformation. The linewidth and therefore scattering decreases with increasing strain, reducing the momentum scattering in the confinement region.

This is in agreement with recent reports from literature showing a reduction of the exciton emission linewidth under strain due to changes of the fundamental multi-valley bandstructure [351, 352, 359, 362]. Figure 4.12 illustrates the impact of strain on the relative position of the $K\,K$ and the $K\,\Lambda$ states. In the unstrained lattice, excitons are efficiently scattered from the bright $K\,K$ state to the lower lying $K\,\Lambda$ state. Positive strain, e.g. stretching the lattice, shifts the indirect $K\,\Lambda$ exciton states to higher energies relative to the $K\,K$ state. This then results in a reduced scattering from the $K\,K$ into the $K\,\Lambda$ states due to strain-induced changes of the band structure. The reduction of the exciton-phonon scattering

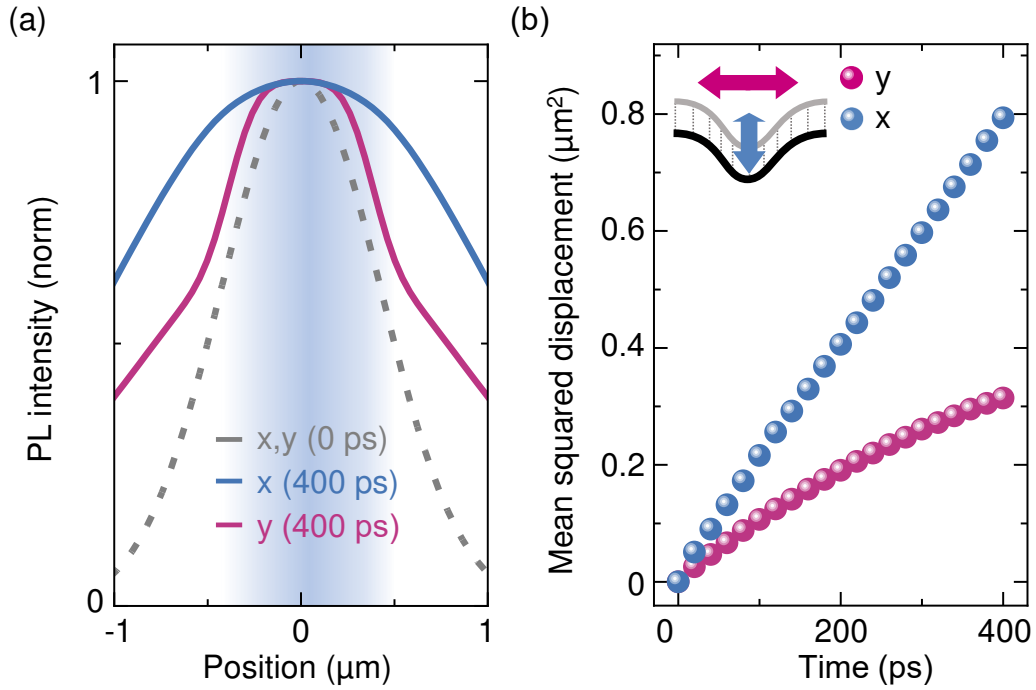


**Figure 4.13: Impact of position-dependent scattering on exciton diffusion.** **(a)** Modeled exciton distribution after 400 ps along (x) and across (y) the channel in comparison with the initial Gaussian distribution (dashed line). The strained channel is indicated by the shaded area. **(b)** Time-dependent mean squared displacement for the x- and y- direction showing linear diffusion along the channel and a non-linear localization behavior in the perpendicular direction.

leads therefore to a decrease of the linewidth, and ,more importantly, also impacts the exciton diffusion.

The strain-engineered quasi-1D channel design of our sample then leads to the unique scenario of both a confinement potential and a channel with suppressed scattering and therefore increased mobility. This is equivalent to a spatially-dependent exciton diffusion of the bright excitons along one direction, further contributing to the anisotropy. However, the experiment yields a composite diffusion including spin- and momentum dark excitons. This already demonstrates the difficulty of modeling exciton diffusion of a multi-valley band structure without sophisticated calculations taking the different states into account.

In order to demonstrate the general effect of strain-dependent exciton-phonon scattering we model the exciton diffusion by including a position-dependent diffusion coefficient $D(y)$, following the changes of the linewidth and emission energy. The non-constant diffusion coefficient leads to additional terms in equation 4.3

resulting in the modified diffusion equation:

$$\frac{\partial n}{\partial t} = D\Delta n + \nabla D \cdot \nabla n + \frac{D}{k_b T}\nabla n \cdot \nabla u + n\nabla u \cdot \nabla \frac{D}{k_b T} + \frac{D}{k_b T} n\Delta u - \frac{n}{\tau} \qquad (4.5)$$

The increase of the diffusion coefficient is estimated from calculations on non-encapsulated $WSe_2$ presented in Ref. [281], where the diffusion increases for biaxial strain of 0.3 % by more than a factor of 2. For the uni-axial relative strain of 0.15 % in our sample we therefore consider a moderate increase from 9 $cm^2/s$ to 12 $cm^2/s$ towards the center of the deformation. The resulting profiles after 400ps are depicted in Fig. 4.13(a), where the combined effect of the potential channel and the position-dependent diffusion still leads to high anisotropy of the exciton diffusion even at room temperature. The time-dependent mean squared displacement, depicted in Fig. 4.13(b) including both the confinement potential $u(y)$ and the position-dependent diffusion $D(y)$, highlights the suppression across the channel with a weakening increase of the width over time, while showing linear diffusion along the channel. Characterizing the localization to the 1D-channel, we find a degree of anisotropy of around 40%, highlighting the directional transport. However, taking only the potential landscape into account without the additional effect of position-dependent momentum scattering, the simulation yields a degree of anisotropy of around 20%. This highlights the importance of the strain-dependent diffusion and facilitates the anisotropy at room-temperature.

In summary, we achieved spatial control of excitons by effciently guiding them along strain-engineered potential channels both at cryogenic and room temperature. The sample design using clean GaAs/$Al_{0.36}Ga_{0.64}$As core/shell nanowires to strain encapsulated $WSe_2$ monolayers allows to resolve a characteristic change of the excitonic finestructure. The change of the spin-splitting energy by strain allows to directly distinguish spin-dark states and provides first experimental evidence for a unique brightened emission mechanism of the dark trion state. The demonstrated anisotropy of nearly 100% for exciton diffusion at cryogenic temperatures is fully consistent with a basic model obtained from the modified diffusion equation. Furthermore, considering the additional confinement, the limit of a true 1D regime is in reach at channel widths of around 60 nm at cryogenic temperatures, making the introduced plattform promising to study exciton transport in a truly 1D quantum confinement regime. Additionally, the observed strain-dependent exciton-phonon scattering results in efficient anisotropy even at room temperature.

# Chapter 5
# Exciton properties and transport in layered hybrid perovskites

In this chapter we will move the focus to excitons in two-dimensional perovskites. Hybrid erovskites emerged as highly promising candidates in optoelectronic devices, especially due to the rapid improvement of solar cells. The subgroup of 2D perovskites, where single layer are separated by organic spacers, have been studied already more than 40 years ago and gained renewed attention due to their two-dimensional character and enhanced stability. In contrast to their 3D counterpart, 2D perovskites host stable excitons even at room temperature.

However, the general efficiency of light harvesting- and emitting devices crucially depends on the elemental exciton structure and their interaction with phonons, as well as the underlying energy landscape. In a solar cell for example, excitons need to diffuse to one of the contacts to be separated and efficiently extracted, as neutral excitons are insensitive to electric fields. For the inverse design for light emission, the excitons should stay in the active area without long range transport to prevent quenching at defect sites.

Solar cells made from phase pure 2D perovskites reached efficiencies of up to 18%, while the exciton propagation was completely unexplored [363, 364]. In general, excitons are not necessarily mobile and especially in organic- or hybrid organic-inorganic systems, as investigated in the following, excitons can be localized at a single lattice site or defect. The defect density of the solution-grown crystals is notably higher than in monolayer TMDCs or quantum wells fabricated using highly controllable methods such as molecular beam epitaxy or chemical vapor deposition. Understanding underlying transport mechanisms could help to further improve device efficiency, but also contributes to learn more about fundamental interactions in the systems. Here, studying the Coulomb interaction in such a layered, hybrid material poses a new, interesting challenge. The soft lattice in combination with tightly bound excitons offers new aspects on exciton-phonon and electron-phonon interaction. This could help to add further insight to the ongoing discussion on the formation of polarons, which can lead to a higher,

renormalized mass or self-localization, similar to an inhomogeneous energy landscape restricting the exciton motion.

In this chapter we first demonstrate highly mobile excitons at room temperature and investigate the nature of the excitonic transport. Here, two distinct regimes, localization at low temperatures and free band-like transport at elevated temperatures, are found. Subsequently, we explore the exciton diffusion and binding energy across the phase transition of BA, challenging the general description of exciton in the soft 2D perovskite lattice. Interestingly, the predicted change of the effective mass of electron and hole has no observable impact on excitons, except for a shift of the emission energy of more than 100 meV. Those studies are supported by theoretical calculations of the shown band structure and valuable discussion with David A. Egger and Xiangzhou Zhu from the TU Munich. The data and several figures are published in the two references [365] and [366].

Finally, we demonstrate the existence of trions in 2D perovskites using a field-effect device geometry. Both, the positively and negatively charged trions exhibit a high binding energy on the order of 46 meV, and, while being nearly completely localized at cryogenic temperatures, are mobile at elevated temperatures of 50 K. The results and figures have been submitted but are at the current stage unpublished.

## 5.1 Mobile excitons in 2D perovskites

Here, we study the exciton diffusion in monocrystalline flakes of phenylethylammonium-lead iodide $PEA_2\ PbI_4$ (labeled PEA in the following). The lack of a phase transition over a large temperature range provides a clean system to study temperature-dependent diffusion. Bulk single crystals grown by Matan Menahem and Omer Yaffe from the Weizmann Institute of Science, Israel are exfoliated down to thin sheets using PDMS and immediately encapsulated in hBN. The encapsulation protects from moisture and oxidation, which drastically reduces the light induced degradation and the environmental degeneration over time. Figure 5.1(a) shows one of the studied, encapsulated thin flakes of PEA. The PEA flake has a thickness of around 60 nm - 90 nm and exhibits several steps of a few nm height, as depicted in the AFM image and profile in Fig. 5.1(b). Those steps are a direct consequence of the layered structure of 2D Ruddlesden-Popper perovskites, favoring the cleaving parallel to the sheets, as illustrated in Fig. 5.1(c). The representative emission spectrum in Fig. 5.2(d) features a single exciton resonance at an energy of 2.36 eV and a linewidth of 56 meV, extracted as FWHM of a Voigt-profile fit.

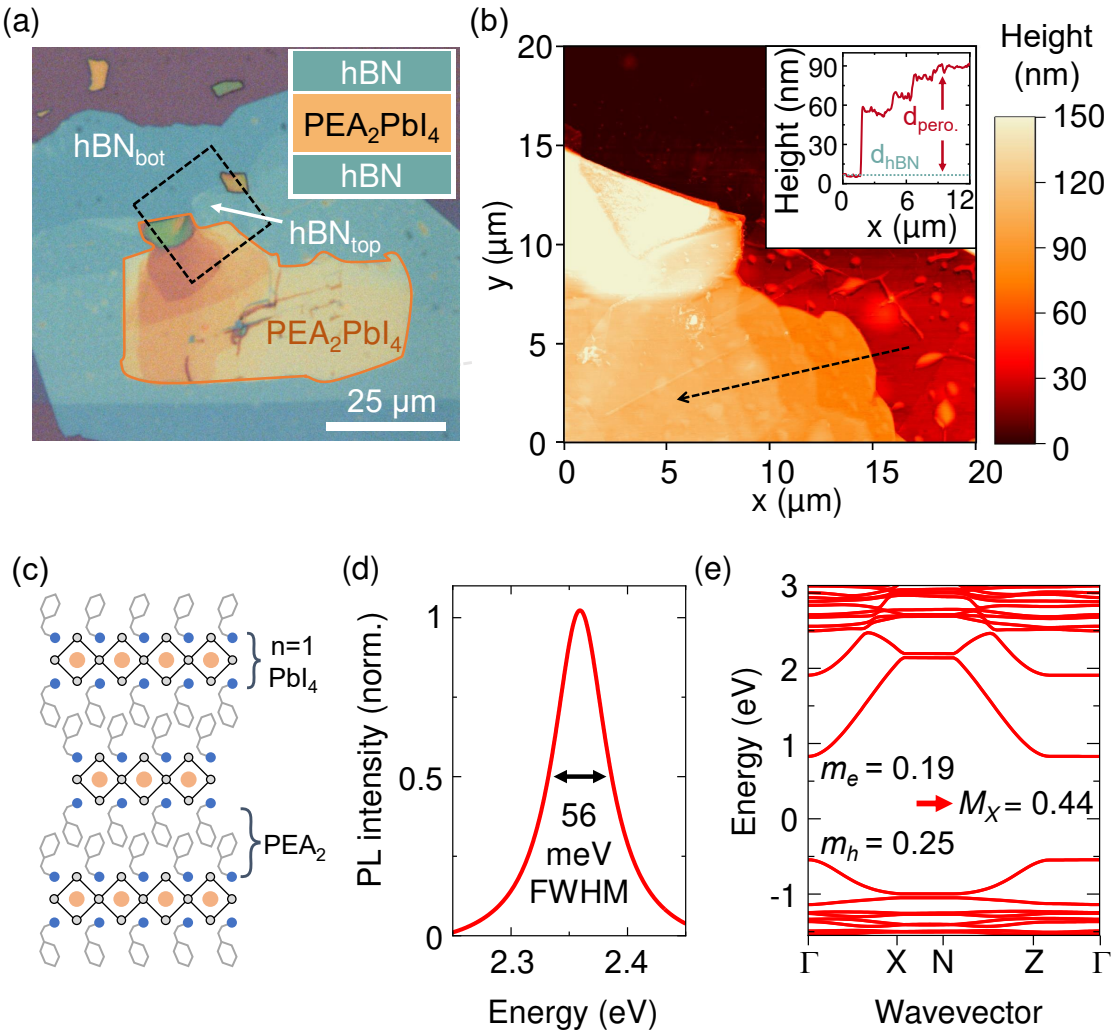


**Figure 5.1: Exfoliated 2D Ruddlesden-Popper perovskites encapsulated in hBN (a)** Optical micrograph of an exemplary encapsulated PEA flake. The inset shows the structure of the sample. **(b)** AFM image of the area indicated by the black square in (a) showing the terrace-like structure. Inset shows the height profile along the black arrow, resulting in a thickness between 60-90nm. **(c)** Illustration of the layered structure of PEA. **(d)** PL spectrum of PEA obtained at room temperature with a linewidth of 56 meV. **(e)** Calculated band structure of PEA, where the electron and hole masses of $0.19\,m_0$ and $0.25\,m_0$, respectively, result in a theoretical mass of $0.44\,m_0$ for the exciton. Calculation performed by Xiangzhou Zhu and David A. Egger, TU München.

In order to understand the underlying electronic band structure, Xiangzhou Zhu and David A. Egger derived the band structure depicted in Fig. 5.1(e,) using first-principles calculations including spin-orbit interaction. The fundamental gap is direct and located at the Γ-point, whereas the next direct transition is nearly at the doubled energy. The effective mass of electron and hole at the conduction band minimum and valence band maximum is $0.19\,m_0$ and $0.25\,m_0$, respectively.

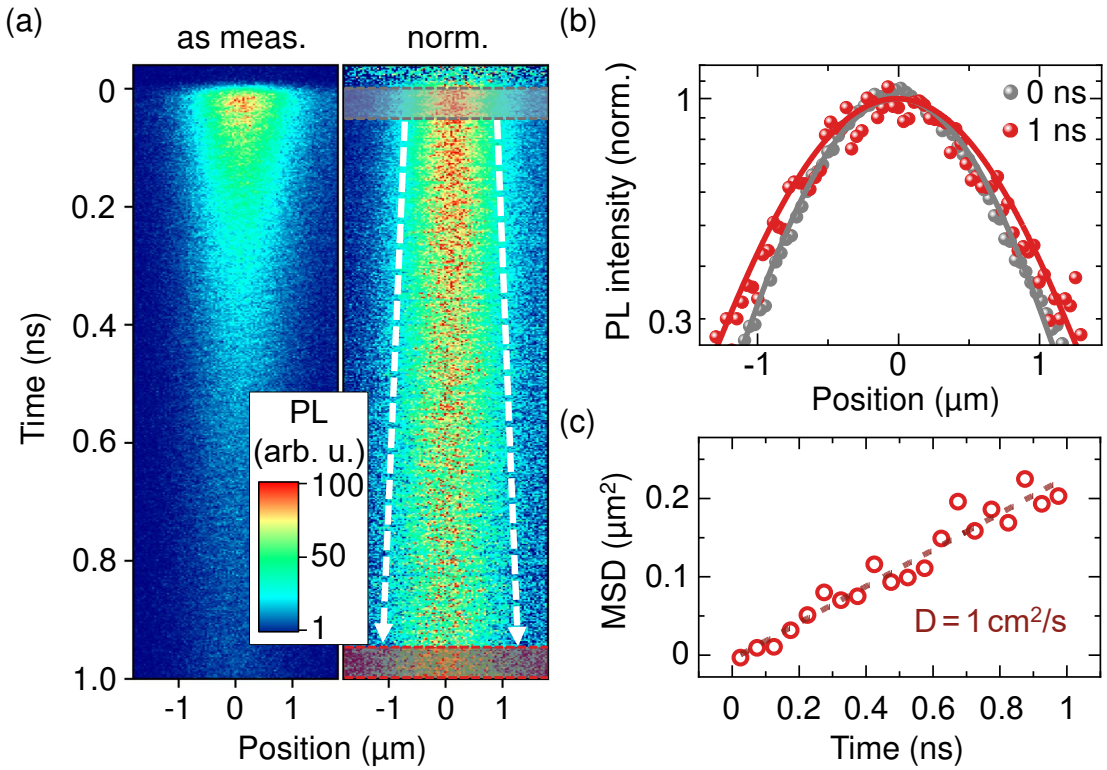


**Figure 5.2: Room-temperature exciton diffusion in 2D perovskites (a)** Streak-camera images measured on the sample shown in 5.1 shown as measured (left) and normalized at each time step using an excitation density of $6.5\,\mathrm{nJ/cm^2}$. **(b)** Representative spatial profiles extracted from (a) directly after excitation and at later time of 1 ns as indicated by the gray and red area. **(c)** Corresponding time-dependent mean-squared-displacement of the spatial profiles resulting in a diffusion coefficient of $1\,\mathrm{cm^2/s}$.

The resulting translational exciton mass $M_X$ is therefore $0.44\,m_0$, which is smaller than the effective mass of $0.69\,m_0$ for $WSe_2$, as comparison [205].

The exciton propagation is then directly monitored by time- and spatially resolved PL. Exemplary streak camera images after excitation with a density of $6.5\,\mathrm{nJ/cm^2}$ per pulse are shown in Fig. 5.2(a), both as measured and normalized at each time step, directly visualizing the broadening of the spatial profile. Then, the squared width of the spatial PL distribution is extracted from a Gaussian fit as depicted in 5.2(b), whereas the slope of the MSD (see 5.2(c)) yields the diffusion coefficient. For this measurement presented in 5.2, the diffusion coefficient is determined to be $1\,\mathrm{cm^2/s}$.

This value is not only reproducible across different sample positions and samples, but also remains unaffected when changing the excitation density, as illustrated by the two identical time-dependent MSD traces in 5.2(b), where the

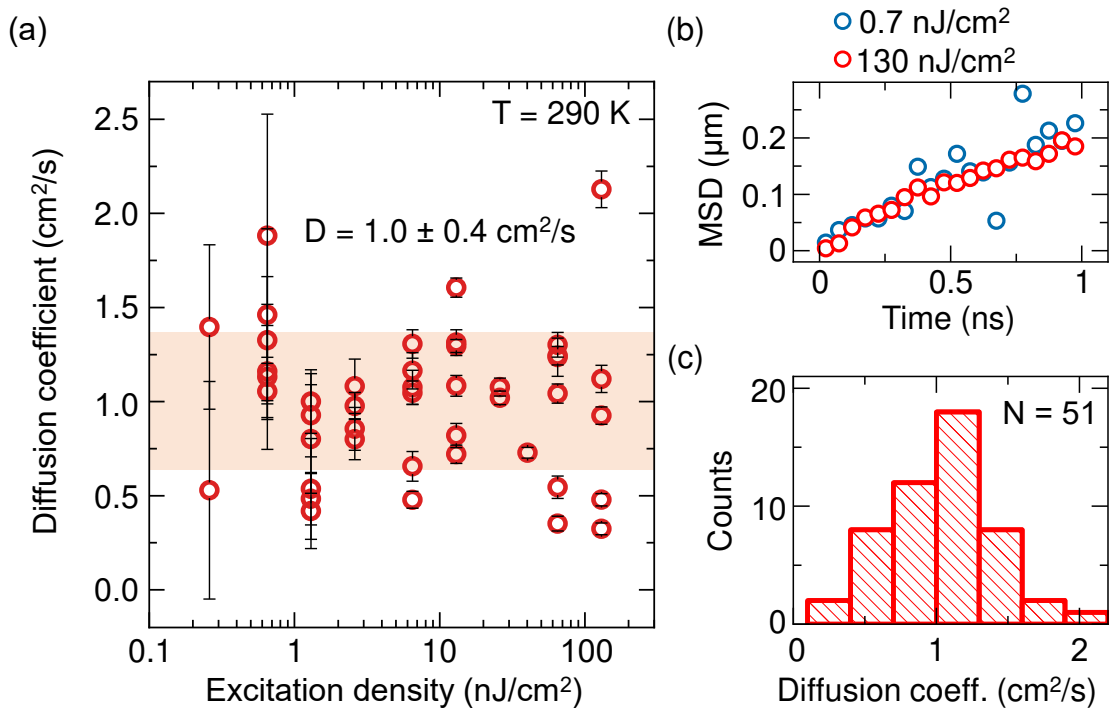


**Figure 5.3: Density-dependent exciton diffusion** **(a)** Summary of exciton diffusion measurements acquired for more than three orders of magnitude of excitation density and across different samples and positions. The red shaded area indicates the mean value including the standard deviation. **(b)** Mean-squared-displacement as function of time for two exemplary excitation densities. **(c)** Histogram of the 51 single measurements of exciton diffusion at room temperature.

excitation density per pulse is varied by more than 2 orders of magnitude. For comparison, an excitation density of 6.5 nJ/cm$^2$ per pulse corresponds to an exciton density of around $7 \cdot 10^8$cm$^{-2}$ and an average exciton distance of 0.8µm. The mean value across all of the 51 measurements is then extracted to be $1.0 \pm 0.4\,\mathrm{cm}^2/\mathrm{s}$ as summarized in Fig. 5.2(a) and shown as histogram in 5.2(c). This value is orders of magnitude higher than exciton diffusion in organic crystals [367, 368] and very similar to the results obtained on $WSe_2$and TMDCs in general [316, 361, 369]. Interestingly, it corresponds to an effective mobility of $40\,\mathrm{cm}^2/\mathrm{Vs}$ and is very close to the value obtained for electrons in 3D perovskites [88, 368].

In terms of direct comparison, the value of $1.0 \pm 0.4\,\mathrm{cm}^2/\mathrm{s}$ is higher than the earlier reported value of $0.2\,\mathrm{cm}^2/\mathrm{s}$ from Ref. [370], which might be related to the encapsulation in hBN and the different time scales investigated, where we focus on the early exciton diffusion in the first few 100 ps. Additionally, the measurement is reproduced in Ref. [231] yielding closer agreement with a value of $0.65\,\mathrm{cm}^2/\mathrm{s}$ for PEA.

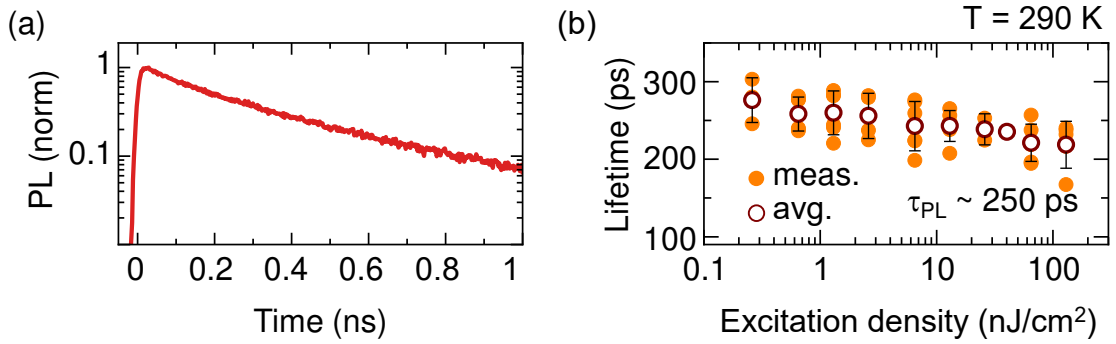


**Figure 5.4: PL lifetime in 2D perovskites (a)** Exemplary transient measured at an excitation density of 6.5 nJ/cm$^2$. **(b)** PL lifetimes as function of excitation density per pulse, showing all measurements and the average for each excitation density

Similarly, the exciton lifetimes are characterized by a single exponential decay with a lifetime of around 250 ps as illustrated in Fig. 5.4(a) and stays nearly constant across the change of excitation density. In general, exciton-exciton interaction can affect both exciton lifetime and diffusion [235, 316, 371]. However, given the general very low excitation conditions, the absence of a large density-induced change results in a low Auger-coefficient of around 0.06 cm$^2$/s, in agreement with the low reported Auger-coefficients for a similar 2D perovskite system [235].

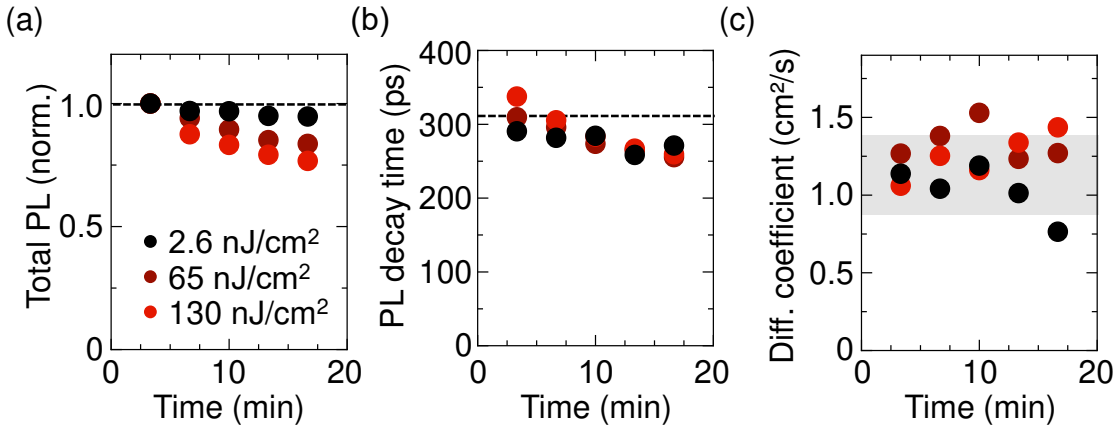


**Figure 5.5: Stability of 2D perovskites under illumination. (a)** Total PL as function of time under illumination for three different excitation densitites per pulse ranging from 2.6 nJ/cm$^2$ to 130 nJ/cm$^2$ under vacuum conditions. **(b)** Stability of the emission lifetime extracted from single exponential fits. **(c)** Corresponding diffusivity for each frame. Color code in (b) and (c) is shown in (a).

Additionally, for any density-dependent effect the influence of increasing degradation at higher excitation densities needs to be considered. Therefore, a short diffusion measurement with 3 min integration time is repeated several times under

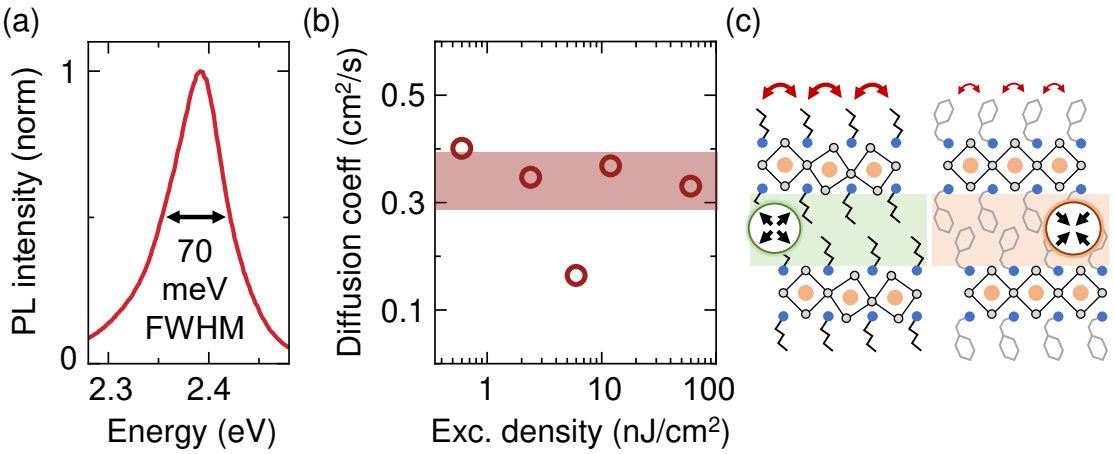


**Figure 5.6: Exciton diffusion in a second 2D perovskite system with different organic spacer (a)** Room temperature PL spectrum of BA-type 2D perovskite exhibiting a broader linewidth of 70 meV **(b)** Exciton diffusion coefficient as function of the excitation density per pulse for BA. **(c)** Schematic illustration of the difference in lattice stiffness due to more room in the interlayer space for a smaller organic.

continuous illumination and individually evaluated. Figure 5.5(a) shows the total PL for three different excitation densities, which slightly declines even for the highest excitation density to only around 75% of the initial value after more than 15 min under pulsed laser excitation. Typical for all subsequent measurements, the emission intensity is still at more than 90% of the starting value. The lifetime, depicted in Fig. 5.5(b), exhibits the same behavior, with a decreasing decay time for the highest excitation density and no effect for lower power.

Importantly, the diffusion coefficient, presented in Fig.5.5(c) shows no systematic change under illumination. Therefore the diffusion seems to remain stable against the degradation, while we attribute the small changes of PL yield and decay time to an increased non-radiative decay channel due to additional defects.

The reason for the spread of the diffusion and lifetime values is at the current stage unknown, but might be related to changes of the spatial energy landscape at different positions such as steps or fractures of single layers or large lattice defects. Both could also be related to the exfoliation process and subsequent encapsulation.

Interestingly, the results clearly change upon replacing the organic Phenylethylammonium spacer by an alkyl-chain like butyl-ammonium without changing the exciton-hosting inorganic $PbI_4$ layer. First, the PL emission shown in Fig. 5.6 is significantly broader with a FWHM of 70 meV. The diffusion coefficients are depicted as function of excitation density in Fig. 5.6(b) and similarly

remain constant across two orders of magnitude. However, the value of around $0.3\,\mathrm{cm}^2/\mathrm{s}$ is around three times smaller than for PEA, despite relatively similar exciton mass [366]. This is attributed to the steric effect of the smaller sized BA molecules compared to PEA, as illustrated in Fig. 5.6(c), reducing the stiffness of the lattice. Additionally, the aromatic rings of PEA form stronger pi-hydrogen bonds compared to the van der Waals interaction of BA [231, 370]. Together, this increases the exciton-phonon coupling and consequently reduces the diffusion coefficient for BA. The obtained value of $0.3\mathrm{cm}^2/\mathrm{s}$ is again slightly higher than observed in literature, while the change from PEA to BA is in good quantitative agreement[231, 235, 370]. Lastly, this steric effect is also used to engineer higher diffusion coefficients by increasing the size and interaction strength of the organic spacer [231, 370].

## 5.2 Temperature-dependent exciton propagation in 2D perovskites

An important observable to understand the nature of exciton diffusion is the corresponding temperature dependence, allowing to distinguish different diffusion regimes and mechanism. Therefore, we study exciton diffusion temperatures between 5 and 290 K using the cryostat. Figure 5.7(a) presents the time- and spatially resolved streak camera images obtained at 5 K and 100 K for both the as-measured and normalized data. First, focusing on the dynamics at 100 K, the exciton distribution is significantly longer-lived than at room-temperature (see Fig. 5.2(a)) and clearly shows a constant spatial broadening over time.

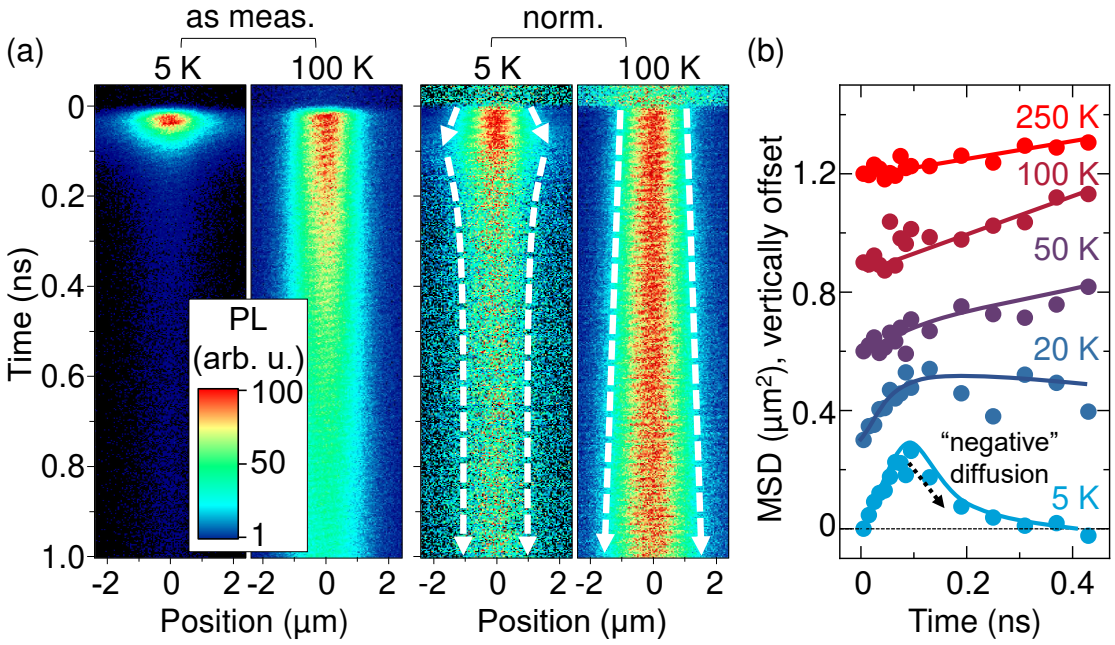


**Figure 5.7: Spatially-resolved exciton emission at different temperatures.** **(a)** Representativ streak camera images at cryogenic (5 K) and elevated (100 K) temperatures of the spatially and time resolved PL for an excitation density of 2.6 nJ/cm$^2$ per pulse. The left panel for each temperature is presented as-measured while the right one is normalized at each time step. **(b)** Temperature dependence of the time-resolved mean squared displacement. Dashed and solid lines are guides to the eye.

Secondly, the PL decay at 5 Kis dominated by a fast decay within the first 50 ps and an additional long-lived component. The normalized data illustrates the spatial broadening, also revealing two components governing the dynamics at low temperature. The corresponding time-dependent MSD traces for different

selected temperatures are shown in Fig. 5.7(b). Above 50 K, the spot area increases linearly, highlighting regular diffusion, whereas a highly unusual behavior is observed below 50 K. Here, after an initial fast expansion the distribution even shrinks, corresponding to negative effective diffusion.

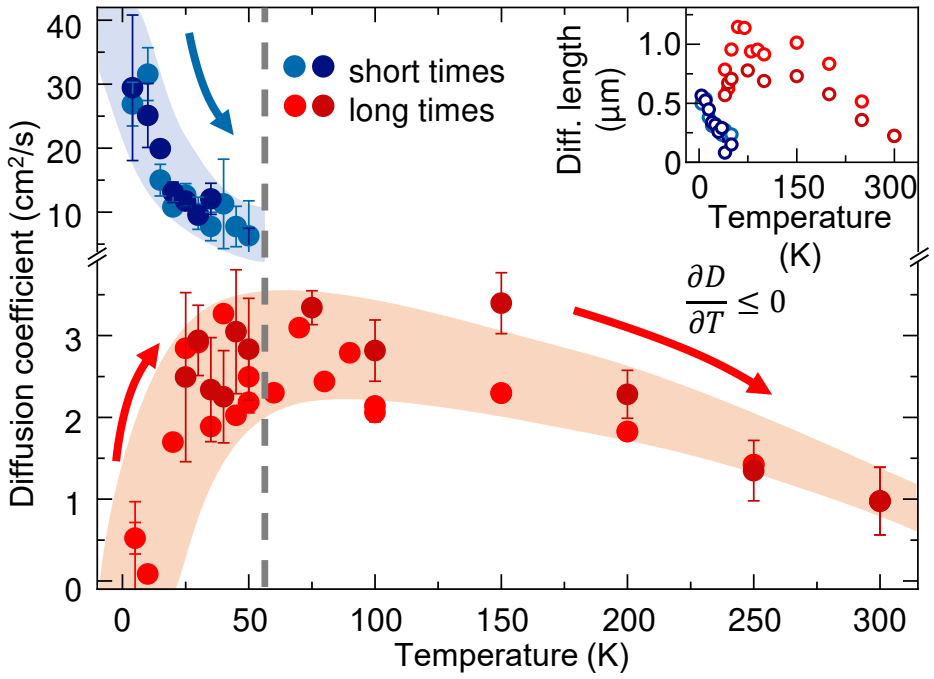


**Figure 5.8: Temperature dependent exciton diffusion.** Diffusion coefficients extracted at short (<50 ps, blue dots) and long times (>100 ps, red dots) after excitation. Two different samples are indicated by lighter and darker colors, respectively. The corresponding diffusion length $L_{diff} = \sqrt{2D\tau}$ is shown in the inset. Shaded areas are guides to the eye.

Figure 5.8 summarizes the corresponding diffusion values. Above 50 K, the diffusion coefficient either is constant or decreases with temperature, representing a clear hallmark for band-like transport. The diffusion coefficient then depends on the interplay between the random scattering events and exciton kinetic energy, which increases linearly with temperature. The scattering dynamics however, can show various behavior with temperature depending on the exact nature of the scattering. Defect scattering for example, is expected to be independent of temperature and therefore excluded to play a major role, as this would lead to an increasing diffusion with temperature. On the other side, the hybrid lattice hosts a broad range of low energy phonons, which can be increasingly populated at elevated temperatures and lead to the observed decrease of the diffusivity [110]. As shown in the inset of Fig. 5.8, the high diffusion of around 3 $cm^2/s$ and lifetimes

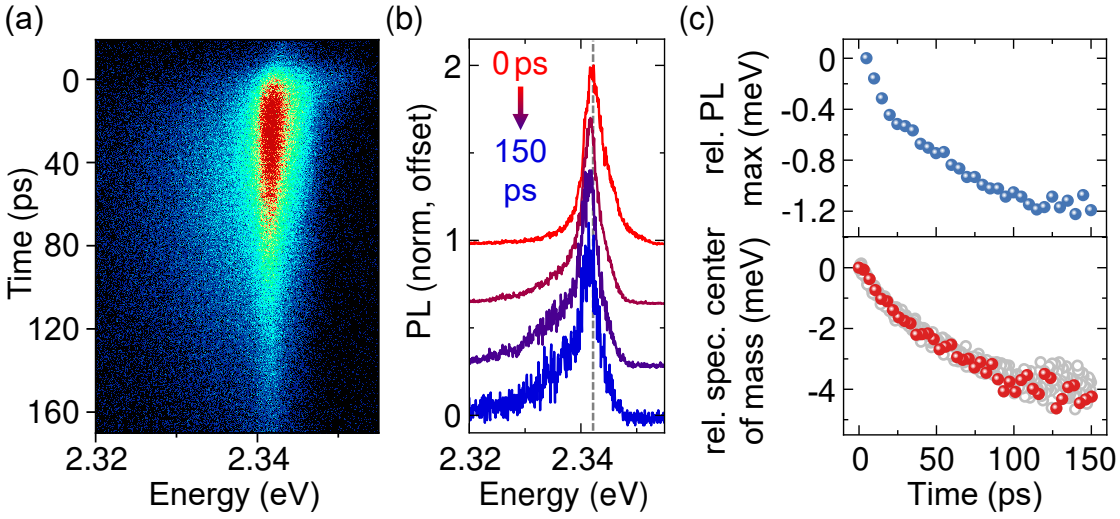


**Figure 5.9: Time- and spectrally resolved PL emission.** **(a)** Streak camera image as function of time and emission energy. **(b)** Selected PL spectra with a temporal delay of 50 ps for each spectrum. The symmetric peak red shifts and develops a low energy shoulder. **(c)** Extracted relative shift of the spectral position of the PL maximum (top panel) and relative shift of the spectral center of mass or weighted arithmetic mean. For the relative shift of the spectral center of mass every tenth value is highlighted in red.

above a nanosecond lead to diffusion lengths $L_{diff} = \sqrt{2D\tau}$ up to 1 µm at around 100 K.

This is strongly contrasted by the anomalous behavior at cryogenic temperatures below 50 K, even exhibiting effective negative diffusion at 5 K. Here, we separate different components dominating at different time delays after excitation: In the first few 10's of ps, the exciton distribution rapidly expands with diffusion coefficients as high as 30 $cm^2/s$, as shown by the blue dots in Fig. 5.8. However, this fast component decreases with temperature, suggesting freely moving excitons. The rapid diffusion corresponds to diffusion lengths of around 0.5 µm, despite the short lifetime of around 50 ps. After this initial fast, but short-lived diffusion and subsequent narrowing, the remaining exciton cloud exhibits a long lifetime with no apparent change of its spatial size and diffusion coefficients approaching zero. This corresponds to exciton localization and is supported by the thermal activation of the diffusion of this long-lived component, e.g. increasing diffusion coefficient with increasing temperature. Thus, long lived excitons are localized at temperatures below 50 K, yet become increasingly mobile at elevated temperatures.

In addition to the results from spatially-resolved PL, there are spectral fingerprints of localization. In a simplified picture, one would expect the localized state

to be lower in energy in order to efficiently capture excitons. Figure 5.9(a) shows a false-color plot of the spectrally-and time-resolved PL with representative spectra plotted in Fig. 5.9(b). Both show a slightly shift of the maximum and the overall PL intensity. For a quantitative analysis, Fig. 5.9 shows in the top panel the relative maximum of the PL and in the lower panel the relative spectral center of mass of the PL, corresponding to the photon energy at which most of the PL is emitted. The two curves show a shift or around 1 meV and 4 meV, respectively, over the first 100 ps and give an upper and lower estimate for the expected localization energy. This energy would already be enough to effectively suppress exciton motion with kinetic energies of around 0.5 meV at cryogenic temperatures.

More importantly, the spectrally-resolved PL also allows to estimate the scattering rate of excitons and ultimately the diffusion coefficient. Therefore, the linewidth, shown in Fig. 5.10(a), is extracted from the emission spectra using Lorentz peak fits and strongly broadens with increasing temperature. The linewidth broadening $\Gamma$ can be approximated by the phenomenological Debye-Einstein model to obtain a simplified expression for the scattering:

$$\Gamma(T) = \gamma_{acc} * T + \frac{\gamma_0}{e^{\frac{E_0}{k_B T}} - 1} \tag{5.1}$$

where $\gamma_{acc}$ describes the linear acoustic scattering coefficient and $\Gamma_0$ the relative phonon coupling with an effective phonon energy $E_0$. The parameters of the fit presented in Fig. 5.10(a) are $\gamma_{acc} = 50\,\mu eV/K$, $\gamma_0 = 165\,meV$ and $E_0 = 37\,meV$ and do not explicitly describe discrete phonon energies and are in agreement with similar reports [109, 115]. Then, the scattering time $\tau_s$ can be estimated from the linewidth according to: $\tau_s = \frac{\hbar}{\Gamma(T)}$, where using the linewidth approximation instead of raw data excludes the additional offset broadening $\Gamma_0$, attributed to radiative and potential inhomogeneous broadening.

Finally, we obtain the diffusion coefficient using a modified drift-diffusion model, extended by an additional localization term:

$$D = \frac{k_B\,T\,\tau_s}{M}\, e^{-\frac{1}{2}\frac{E_{loc}}{k_B T}} \tag{5.2}$$

The first term describes the semi-classical diffusion of carriers with mass $M$ mediated by the scattering time $\tau_s$. Here, we employ the calculated total exciton mass $M_X = 0.44\,m_0$ and the scattering time estimated from the PL linewidth broadening. The second term on the other side describes the thermal activation of localized excitons. Figure 5.10(b) shows the resulting diffusion coefficients for

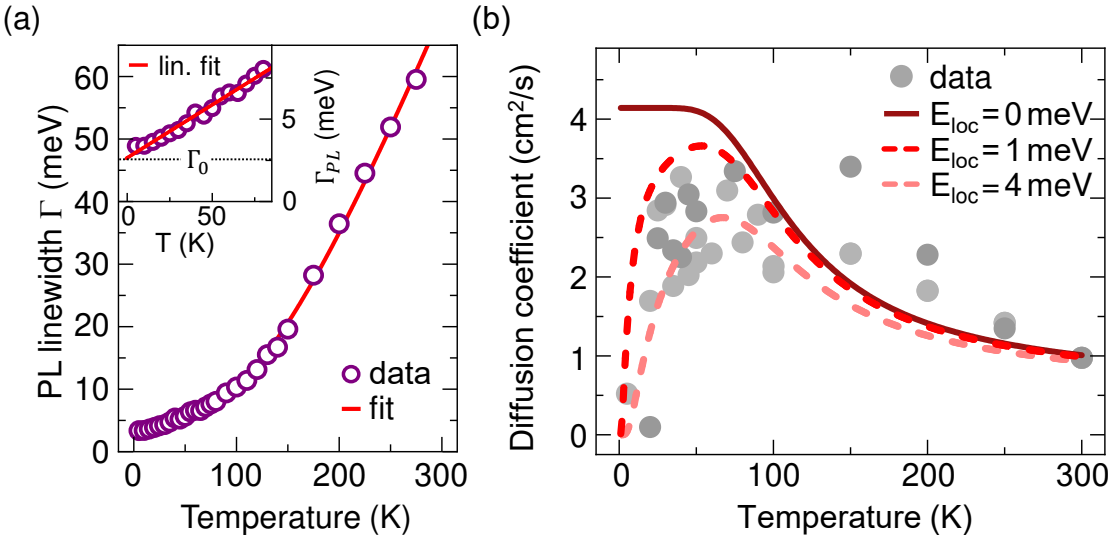


**Figure 5.10: Exciton-phonon interaction and modified drift-diffusion model.** **(a)** Temperature-dependent PL linewidth extracted from the FWHM of Lorentz fits including the fit using the phenomenological Debye-Einstein model. Inset shows the low-temperature data fitted with a linear function. **(b)** Measured diffusion values and estimate from the Drift-diffusion model including localization effects.

different localization energies together with the measured data. The dark red solid line represents the purely semi-classical model without localization effects. Interestingly, the basic model allows to accurately model both the absolute values and the temperature dependence at both cryogenic and elevated temperatures. This suggests that the diffusion at elevated temperatures is indeed dominated by the efficient exciton-phonon coupling. Especially the room-temperature values seem to be the intrinsic phonon-limit of diffusion.

However, there are important implications of the model to consider. First, the application of the semi-classical description is specified by the Mott-Yoffe-Regel criterion, which requires the mean free path $L_{free} = \sqrt{2D\tau_{scatt}}$ to be larger than the de-Broglie wavelength $\lambda_{dB} = \frac{\sqrt{2}\pi\hbar}{M_X k_B T}$ of the diffusing particle. Here, the mean free path describes the average distance an exciton travels between scattering events and the de-Broglie wavelength $\lambda_{dB}$ represents the size of the semi-classical wavepacket. For the presented case of PEA, $L_{free}$ is comparable or even smaller than $\lambda_{dB}$ at elevated temperatures, e.g. the exciton wavepacket scatters with phonons on spatial scales of the wavepacket itself. This can thus lead to additional quantum mechanical localization effects facilitated by interference effects between wavepackets moving in closed loops [266, 357]. However, this highly depends on the phase coherence inside the loop and therefore the elasticity if the scattering, which is strongly reduced for optical phonon scattering at elevated temperatures.

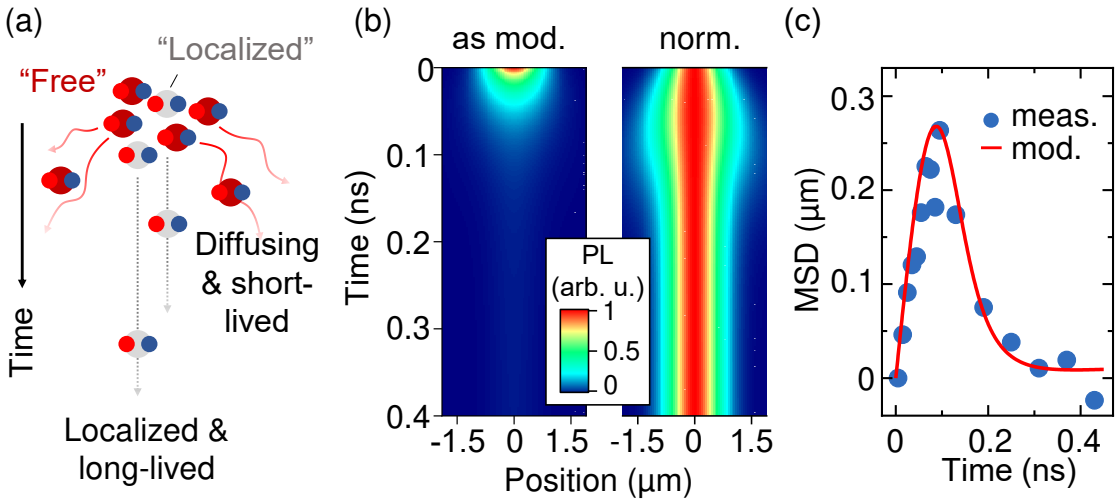


**Figure 5.11: Two-component diffusion model.** **(a)** Schematic illustration of the two-component diffusion, where a fraction of excitons diffusive freely and quickly recombine, while the others are localized and long-lived. **(b)** Simulated time- and spatially dependent PL of the two-component diffusion, left is as modeled and right is normalized at each timestep. **(c)** The evolution of the distribution area of the two-component modelin comparison to the measured data.

This can motivate additional quantum-mechanical treatment despite the accurate description of the observed diffusion by simplified semi-classical model.

Additionally, the anomalous regime observed at lowest temperatures requires further considerations. Here, the rapid diffusion only observed on short timescales suggests non-equilibrium dynamics. As we excite excitons non-resonantly, the relaxation and cooling might be slowed down at lowest temperatures, leading to hot excitons moving in a cold lattice. From equation 5.2 we can estimate an exciton temperature of 30-40 K required for a diffusion coefficient of 30 $cm^2/s$, while assuming the low scattering of a cold lattice. Here, the recent progress in determining the bright-dark splitting indicates a bottleneck effect for the scattering from the bright to the dark exciton state, as no optical phonon matches the energy difference [298, 299, 372, 373]. Therefore, one could attribute the initial lifetime below 100 ps to bright excitons relaxing to lower-lying dark states. In addition, overheating effects have been observed in perovskite nanocrystals [301]. Elevated temperatures then accelerate the cooling rate and decrease temperature difference, overall mitigating the effect of an overheated exciton population.

However, the observation of a subsequent negative effective diffusion can not be explained by only hot excitons but implies the interplay of additional excitonic components. Therefore, a simple two-component model of rapidly diffusing, but short-lived excitons and a long-lived localized distribution, illustrated

in Figure 5.11(a) is simulated by two Gaussian distributions. The spatial and temporal evolution shown in Fig. 5.11(b) shows the shrinking of the overall exciton cloud after the rapidly spreading excitons have recombined and only localized excitons remain. Using parameters closely related to the experiment of $D_{free} = 25\,\mathrm{cm}^2/\mathrm{s}$,$D_{loc} = 0.5\,\mathrm{cm}^2/\mathrm{s}$,$\tau_{free} = 0.05\,\mathrm{ns}$, $\tau_{loc} = 2\,\mathrm{ns}$ and a ratio of $\frac{n_loc}{n_free} = 0.03$, the model can accurately describe the observed mean squared displacement. It is important to note, that a detailed description highly depends on the non-equilibrium dynamics of excitons and the distinct localization mechanism and energy scale. However, this simple model correctly illustrates one of the scenarios that can lead to negative diffusion.

Finally, one of the main parameter of the semi-classical model is the exciton mass, derived from the sum of the conduction and valence band electron masses. Here, the strong exciton-phonon interaction can lead to the formation of polarons, strongly affecting the effective mass and even facilitating a temperature dependence of the mass [374]. This in turn could contribute to the observed decrease of the diffusion coefficient with increasing temperature by a increased polaron mass. Therefore further investigations and merging descriptions of the spectral signatures of polarons and the effect on the transport in 2D perovskites are needed [116, 375].

## 5.3 Excitons at the phase transition

The already discussed 2D perovskite BA exhibits a phase transition close to room temperature at 270 K, which was recently theoretically and experimentally reported to change the effective mass of electron and hole [114, 227, 376]. This provides the opportunity to investigate the influence of a changing mass of valence and conduction band carriers on exciton diffusion and binding energy.

Figure 5.12(a) depicts the underlying mechanism of the phase transition, which has been recently attributed to an order-disorder transition [377]. At elevated temperatures, the octahedra exhibit strong anharmonic fluctuations, while the octahedra get locked at a high tilt angle $\delta$ at the phase transition [227]. This phase transition directly impacts the optical response by shifting the excitonic resonance by more than 100 meV. The spectra in Fig. 5.12(b) demonstrate this shift of the PL of encapsulated BA layers when the temperature reaches around 270 K, corresponding to the reported transition temperature [114, 227, 377]. Additionally, while the linewidth continuously increases with temperature, there is no obvious change across the phase transition in contrast to the large energy shift.

Xiangzhou Zhu and David A. Egger from the TU München provide theoretical insight by calculating the band structure, including spin-orbit coupling, which is shown in Fig. 5.12(c) and demonstrates a similar shift of the band gap. The experimentally observed change in emission energy is therefore partially attributed to changes on the underlying single-particle level. Those arise from the change of the average distortion angle $\delta$ of the lead-iodide octahedra, as depicted in Fig. 5.12(a). A larger distortion angle reduces the wavefunction overlap and increases the band gap [229, 376]. Simultaneously, the bandwidth reduces, which in turn leads to higher masses. Theoretically, the total exciton mass $M = m_e + m_h$ increases by an factor of 1.5 going from the HT to the LT, as also experimentally observed in previous diamagnetic shift experiments in Ref. [114]. Together, the phase transition should not only change the optical response, but additionally manifest itself in a change of the exciton binding energy and, assuming band-like transport as shown in the previous section for the closely related PEA, also impact exciton diffusion.

### 5.3.1 Exciton binding energy

First, we investigate the exciton binding energy by measuring the energy separation between the ground and excited states, which allows to extrapolate the

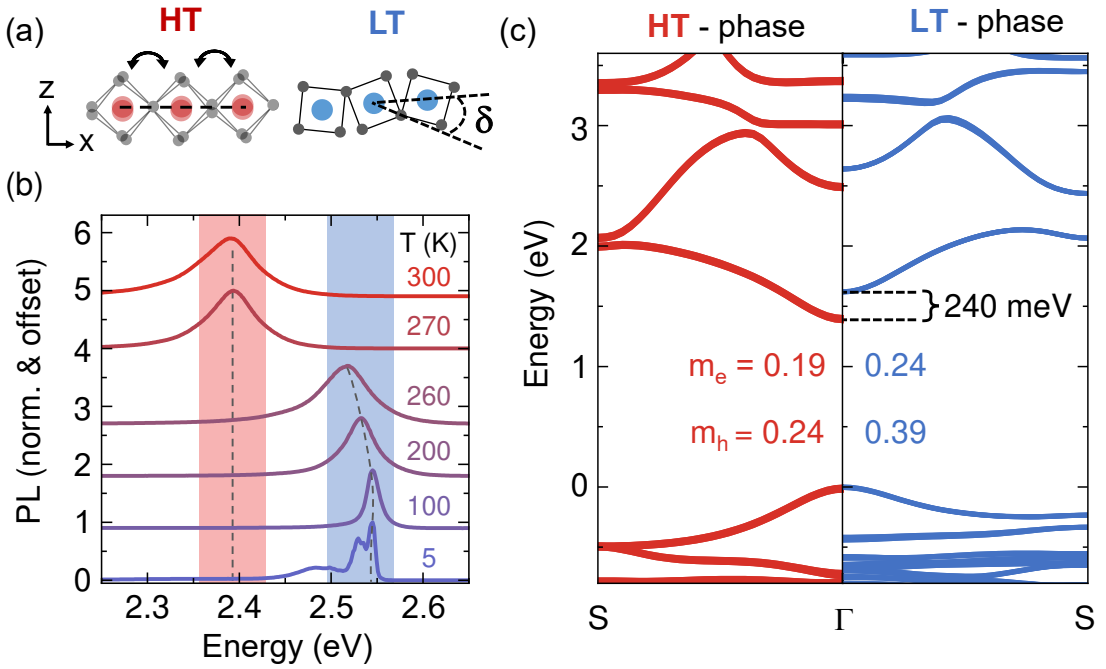


**Figure 5.12: Impact of the phase transition on the optical and electronic properties (a)** The phase transition changes the relative alignment of the in-plane octahedra, which are locked with a high tilt angle $\delta$ below the phase transition, while fluctuations are possible in the high temperature phase. **(b)** Temperature dependent PL emission across the phase transition at 270 K. **(c)** Calculated band structure for the high- (HT) and low- (LT) temperature phase between the Γ and S point. Included are values for the energy shift across the phase transition and the corresponding effective masses extracted at the Γ-point. Calculation performed by Xiangzhou Zhu and David A. Egger, TU München.

binding energy from a certain linear scaling. Here, we make use of two-photon photoluminescence excitation spectroscopy (TPLE), which is sensitive to weak and broadened signals from excited states at elevated temperatures while simultaneously suppressing the ground state contribution due to optical selection rules. Here, we tune the excitation wavelength around half the energy of the expected excited state from 1.24 eV to 1.77 eV. For these below band gap photons, only a two-photon excitation process is possible, which is only allowed for p-type states. After excitation, the p-type excited state can not recombine directly and relaxes to the ground state which is then detected as photoluminescence.

Figure 5.13(a) depicts an exemplary TPLE and the corresponding PL spectrum from an encapsulated BA layer obtained at 5 K. For comparison, the reflectance contrast together with the multi-layer fit of the same sample is shown below. Here, the ground state is the strongest resonance with accompanying features which stem from interference effects. The maximum of the 2-photon absorption then determines the 2p energy with additional contributions of higher p-type states at

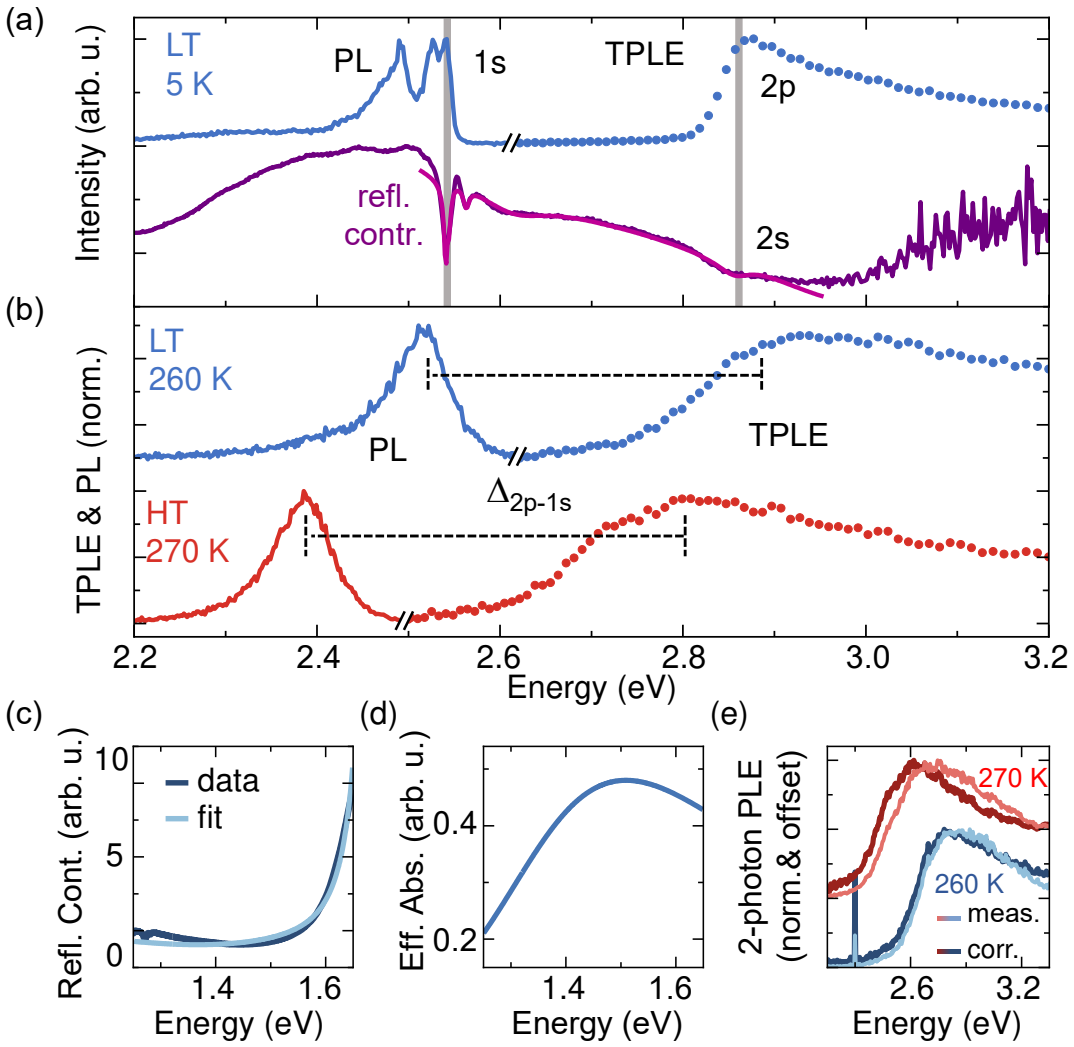


**Figure 5.13: Measurement of the exciton binding energy.** **(a)** Comparison of the two-photon PLE and PL with the reflectance contrast measurement at 5 K. Solid gray lines indicate ground and excited states. **(b)** PL and TPLE spectra obtained for the LT-phase at 260 K in comparison to the HT-phase measured at 270 K. The spectra are corrected for the effective change of absorption as shown in (c)-(e). **(c)** Reflectance contrast spectrum in the spectral range of the fundamental laser energy for the two-photon excitation together with the fit obtained from the transfer-matrix multilayer interference model. **(d)** Simulated absorption of the perovskite layer extracted by adding a small imaginary component to the dielectric function. **(e)** Impact of the correction on the HT and LT phase by comparing the as-measured (lighter color) and the corrected spectra (darker color).

higher energy, in close agreement with the 2s state determined by the reflection contrast. The overall values and the resulting high binding energy match with earlier reports [45, 226, 378, 379].

The resulting TPLE and accompanying PL spectra across the transition are shown in Fig. 5.13(b). First, both spectra are significantly broadened compared

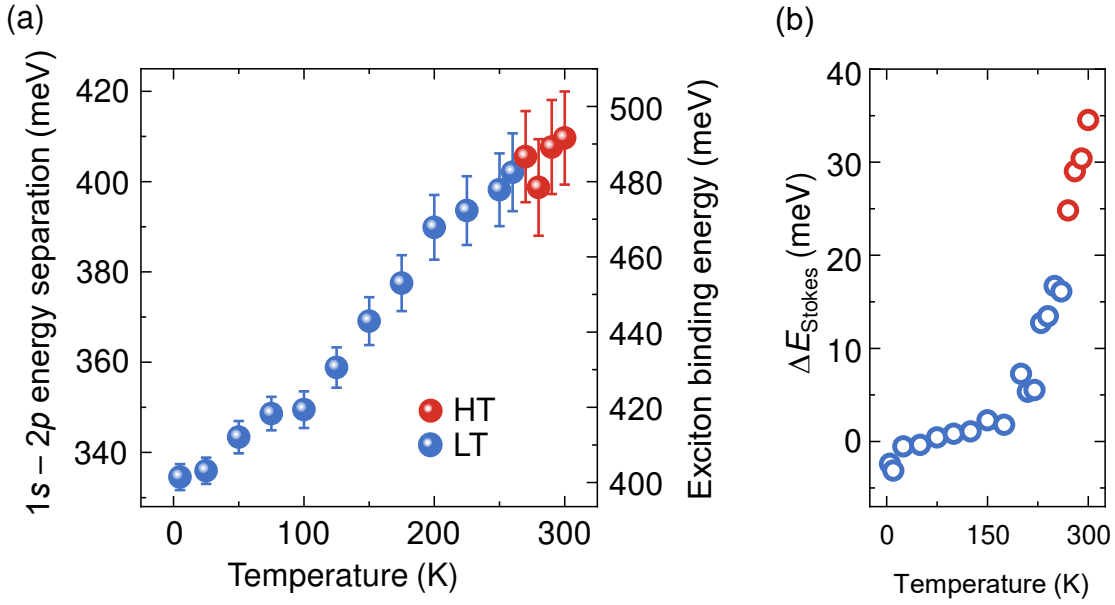


**Figure 5.14: Temperature dependent exciton binding energy. (a)** 2p-1s energy separation (left axis) as function of temperature and phase. In order to exclude any effects arising from a difference in absorption and emission energies, the ground state resonance energy is obtained from the absorption-type reflection contrast. Corresponding binding energies are obtained from $E_B = 1.2\,\Delta_{2p-1s}$ and shown on the right axis. Error bars are estimated from the fit to the TPLE data. **(b)** Temperature dependent Stokes shift, i.e. difference between the absorption and emission energy of a resonance.

to cryogenic temperatures, but do not contain signatures of the respective other phase. Second, both ground and excited state shift to lower energies for the HT phase, as expected from the underlying band structure and PL measurements presented in Fig 5.12(b) and (c). However, the two-photons absorption is also subject to interference effects. In order to account for the impact of the multi-layer structure, we estimate the effective absorption in the spectral range of the fundamental photon energy, as shown in 5.12(c). The resulting effective absorption shown in Fig. 5.12(d) demonstrates the importance of this effect, as the absorption increases by nearly a factor of 2 in the relevant spectral range between 1.3 eV and 1.5 eV. The TPLE data can then be corrected for the change of the absorption due to the spectral shift of the resonance, which can be as high as 50 meV, as depicted in Fig. 5.13.

The temperature dependent values for the 2p-1s separation are summarized in Fig. 5.14(a). The corresponding exciton binding energy can be estimated from the linear scaling between the binding energy of ground and excited states according to $E_B = 1.2\Delta_{2p-1s}$ [379]. In order to exclude any differences arising from the finite

Stokes shift presented in Fig. 5.14(b), the energy of the 1s resonance is determined from the reflection contrast instead of PL. Here, the binding energy of around 0.4 eV at 5 K is in close agreement with reported values [45, 226, 378]. Interestingly, the binding energy continuously increases to nearly 0.5 eV at room temperature. Even more intriguingly, we observe no change at the phase transition. However, from the exciton physics presented in equation 2.1, we would expect the binding energy to linearly follow the sudden decrease of the effective mass from $0.15\,m_0$ in the LT phase to $0.11\,m_0$ in the HT phase. This scaling is expected to be weaker in reality, as the dielectric contrast and modified Coulomb potential in general decrease the dependence of the binding energy with effective mass.

This results suggests that the dependence on the effective mass of the underlying free carrier is much lower than commonly assumed from the prediction of the 2D hydrogen model. Here, different mechanisms can play a role: first, the exciton wave function in reciprocal space could spread beyond the region where the effective mass approximation applies, reducing the effect of the local band curvature. Second, the dependence of the binding energy on the effective mass is reduced by the screening in the modified 2D potential and does not necessarily follow the simple coulombic approximation above. In 3D perovskites, the exciton binding energy shows opposite behavior and *decreases* with increasing temperature, which has been attributed to an increase of the dielectric constant with temperature [79–81, 380]. Similar effects could play a role here and compensate the role of the changing mass, while it is worth noting that the exciton binding energies and radii are substantially different in 2D and 3D perovskites, which changes the degree of such an effect. Additionally, polaronic effects, arising from the strong exciton-phonon coupling, might renormalize or even dominate the effective mass of the exciton. A polaron arises from the interaction between excitons and the lattice, creating a quasi-particle composed of an electron-hole pair and a lattice distortion. Therefore, the mass of the polaron is renormalized by the displaced atoms, but crucially depends on the exciton-phonon coupling. The predicted change in mass should however also be manifested in the diffusion of excitons, which will be investigated in the next section.

### 5.3.2 Exciton diffusion

In addition to the exciton binding energy, the exciton diffusion serves as further process crucially depending on the mass, in this case the translational mass. Therefore, we excite excitons in encapsulated BA layers and directly monitor the exciton diffusion using the streak camera. Again, the resulting image is separated

into time intervals and the emission spot is fitted with a gaussian distribution. Here, the corresponding phase and especially absence of a mixed-phase is verified before each measurement by the characteristic spectral emission.

Figure 5.15(a) shows the time-dependent mean-squared displacement for the high- and low temperature phase, obtained at 270 K and 260 K, respectively. The linear increase highlights the characteristic diffusive propagation, to the related PEA system observed in the previous section. While the spectral position of the emission promptly shifts at the phase transition, the diffusion coefficient, extracted from the slope of the MSD, shows virtually no change. The semi-classical model $D = \frac{k_B T \tau_s}{M}$ not only relies on the total mass, but also the scattering time. The latter is derived from the linewidth, which is shown in Fig. 5.15(b) and also shows nearly no change around the phase transition. The scattering time is therefore assumed to be constant around the phase transition and the change of the total mass from $0.63\,m_0$ for the low temperature to $0.43\,m_0$ for the high temperature phase should dominate the exciton diffusion around the phase transition.

In contrast to the semi-classical expectation, the diffusion coefficient follows the binding energy and stays constant across the phase transition, as also shown in the summary across different measurement series in Fig. 5.15(c). The overall average and data being part of a single measurement series show no difference between the two phases, while the values differ for different samples and positions. The theoretical expectation from the semi-classical model includes the different masses and the similar scattering times and is indicated in Fig. 5.15(c). Despite the scattering of the data, the increase of a factor of 1.5 would be clearly resolvable, but is absent.

Here, similar considerations as for the binding energy can play a role, prominently polaronic effects. Especially for the softer BA compound, local fluctuations and spatially and temporally varying disorder can impact exciton transport, as recently suggested for 3D perovskites [374, 381]. An important point to consider is that the mass is considered as spatially-averaged property, while the exciton diffusion depends on the local physics at its direct position and being subject to different fluctuations. Transport models rely on calculated mass, as exciton masses are hard to directly measure without making many assumptions about the dielectric surrounding and scattering mechanism. While experiments have shown changes of the effective mass across the phase transition, the values in turn could have been renormalized due to the high magnetic fields and modified phonon interaction [114, 376]. Nevertheless, the same model could provide agreement with the

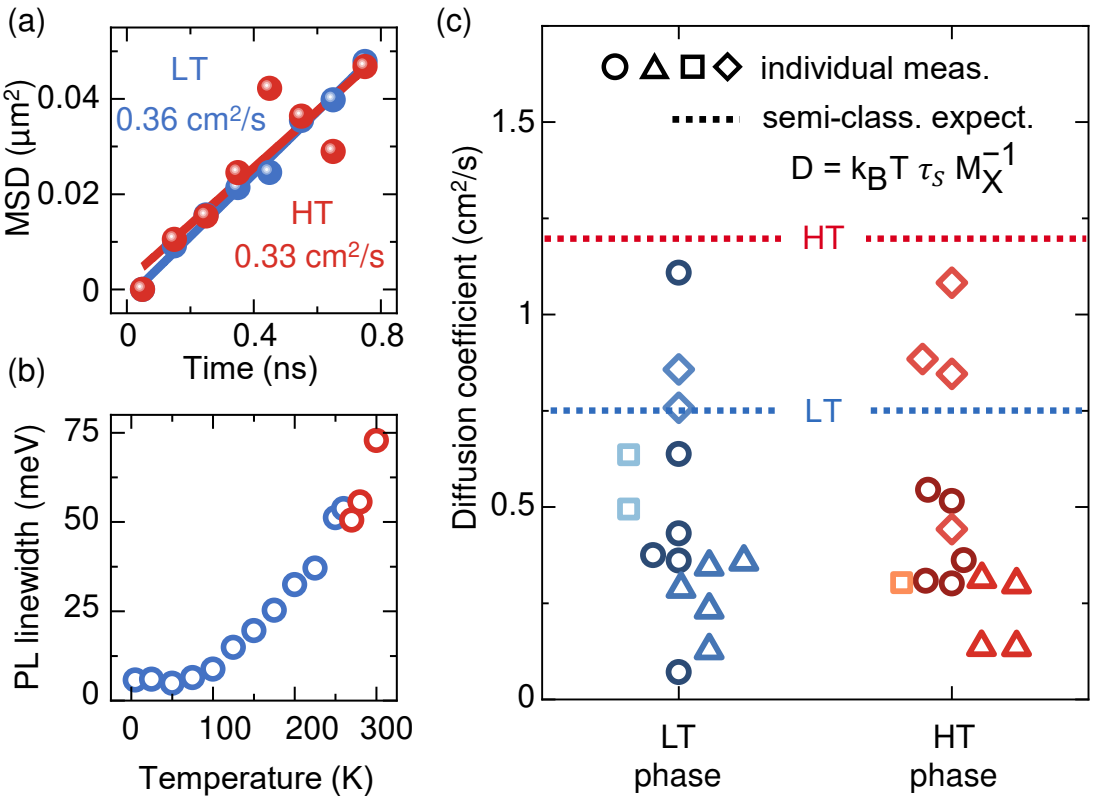


**Figure 5.15: Exciton diffusion for the low- and high temperature phase.** **(a)** Mean-squared-displacement as function of time for the low- and high temperature phase showing the same diffusion coefficient. **(b)** Temperature dependent emission linewidth, with the HT and LT phase indicated by red and blue dots, respectively. **(c)** Histogram summarizing the diffusion values for the two phases across 4 individual measurement series. Before each measurement the phase and homogeneity of the phase are verified from spectrally resolved PL measurements. The temperature range was kept around the phase transition ranging from 260 K to 274 K. Dashed lines indicate the semiclassical expectation for each phase derived from the semi-classical expectation.

temperature-dependent diffusion values for PEA, but fails to resolve the changing mass across the phase transition in BA. Here, the even stronger phonon interaction in BA can further lead to an inapplicability of the semi-classical model and motivate the use of more complex models.

## 5.4 Trion formation in electrically doped layered perovskites

This chapter presents the results on trions in 2D perovskites. Figure 5.16(a) illustrates the approach to electrically inject electron and holes up to densities of $10^{12}\,\mathrm{cm}^{-2}$ into ultra-thin sheets of PEA. Few-layer graphene serves as gate electrode and contact to the PEA flake and allows the bipolar tuning of the charge carrier density by changing the gate voltage $V_g$. An exemplary micrograph of an employed device is depicted in 5.16(b), where the graphene gate and the bottom and top hBN, serving both as environmental protection and gate dielectric, are indicated. The thickness of the perovskite layer is estimated to be only one to a few layers thin, made possible by the direct exfoliation on Si/Si$O_2$ substrates and subsequent pick-up using hBN. Thicker layers, obtained from PDMS exfoliation and stamping, show similar behavior and prove the general applicability of this doping strategy.

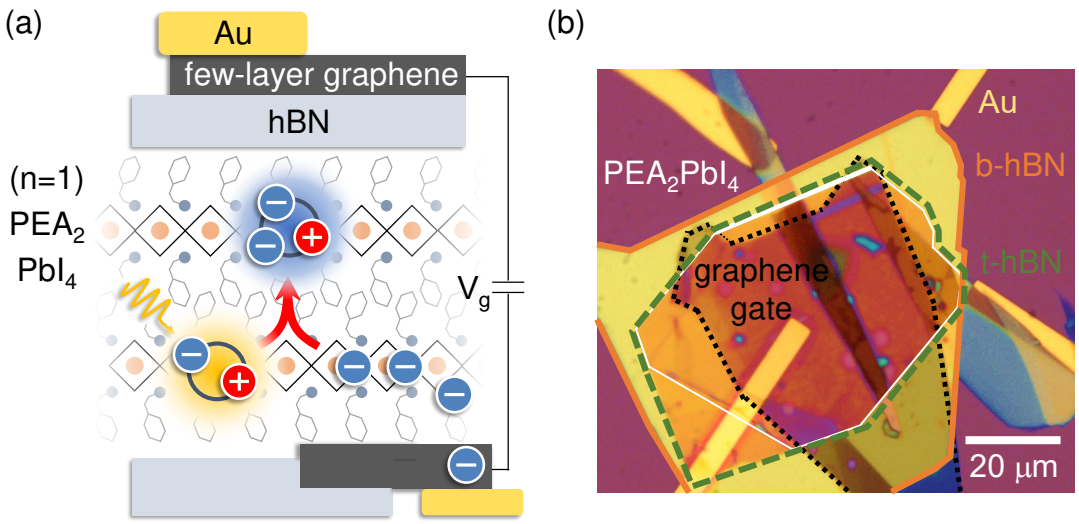


**Figure 5.16: Electrostatical doping of two-dimensional perovskites (a)** Illustration of the doping design using hBN as gate dielectric and few-layer graphene to contact a few nm-thin PEA flake. **(b)** Optical micrograph of an exemplary device fabricated by direct exfoliation, pick-up and subsequent drop-down on few-layer graphene contacted by pre-patterned gold contacts.

Adding free carriers to an excitonic systems leads to the formation of trions, a molecule-like charged state state [382, 383]. The high binding energy in two-dimensional systems such as TMDCs also leads to a high trion binding energy and even the formation of particles with a multitude of carriers involved, such as

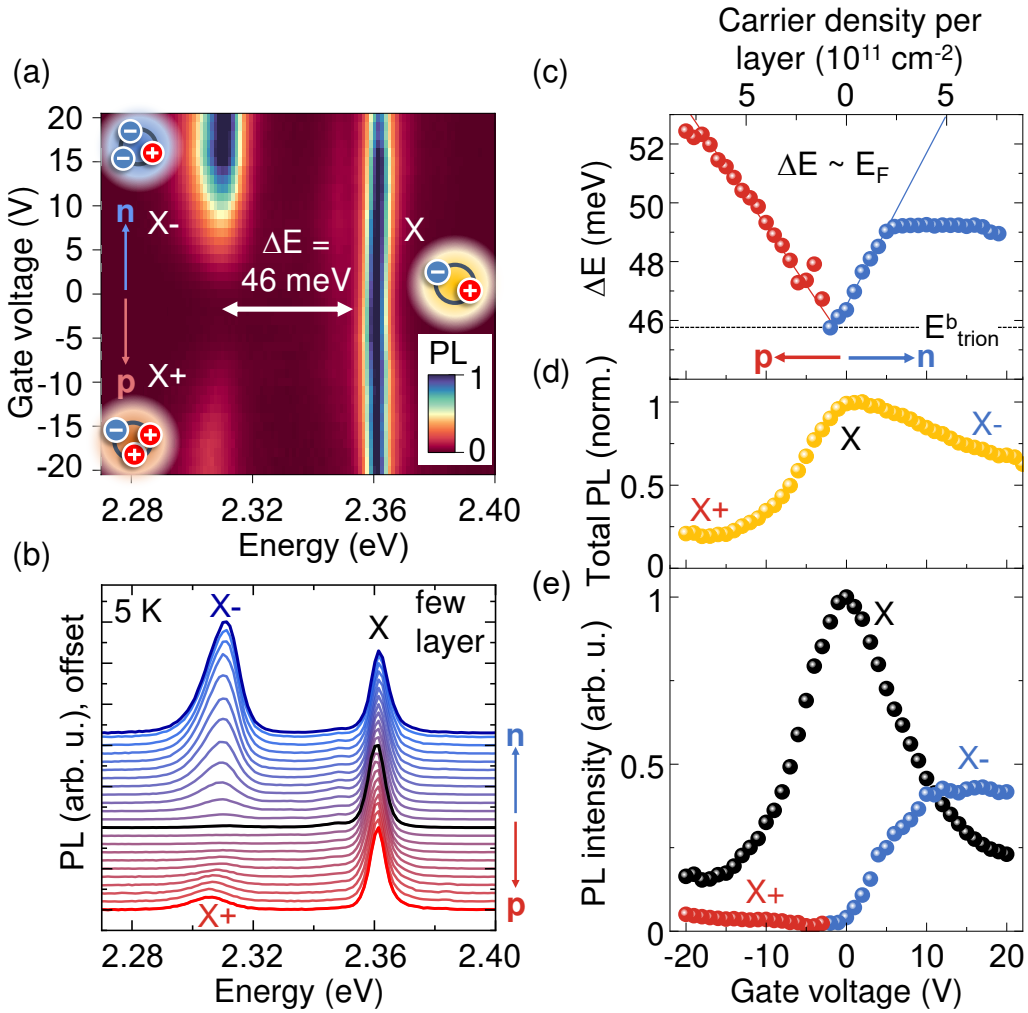


**Figure 5.17: Negatively and positively charged trions in PEA.** **(a)** False-color plot of the gate-voltage dependent PL emission showing emerging positively and negatively charged trions with a binding energy of 46 meV. **(b)** Selected PL spectra normalize to the neutral exciton resonance. **(c)** Energy separation between charged trions and neutral exciton as function of gate voltage (bottom axis) and estimated free carrier density per layer (top axis). The extrapolation to zero density determines the binding energy. **(d)** Spectrally-integrated total PL intensity. **(e)** Relative PL yield for the neutral and charged resonances.

the charged biexciton observed in the $WSe_2$ structure in chapter 4 [279, 286, 287, 293, 294, 384].

Figure 5.17(a) shows the spectrally-resolved PL as function of gate-voltage of a utra-thin sample. Exemplary emission spectra are additionally displayed at selected gate voltages in Fig. 5.17(b). The zero voltage PL is dominated by a single exciton resonance at an energy of 2.36 eV, similar to the samples used to investigate temperature dependent diffusion in section 5.2. Upon increasing the voltage however, an additional resonance appears at lower energies of around

2.31 eV, for both negative and positive voltages. This drastic change of the PL spectrum as function of the applied voltage suggests the formation of positive ($X^+$) and negative ($X^-$) trions. In Fig. 5.17(c) we observe as characteristic feature an increase of the energy separation $\Delta E$ between exciton and trion with increasing gate voltage [286, 385, 386]. The energy separation $\Delta E$ is expected to scale linearly with Fermi-energy of the electrically injected free charge carriers, due to momentum conservation and Pauli blocking as more and more states in the conduction band (for negative trions) are already occupied. The energy separation in the zero density limit then determines the trion binding energy, resulting in values of 46 meV. As comparison, this value is not only higher than the exciton binding energy in most 3D perovskites, but also more than 10 meV higher than typical trion binding energies in TMDCs and an order of magnitude higher than in quantum wells [81, 286, 287, 380, 386] Moreover, from the energy separation $\Delta E$ one can estimate the carrier density via $n_{e,h} = \Delta E \frac{m_{e,h}}{\pi\hbar^2}$ and is shown in the top axis of Fig. 5.17(c)-(e).

Furthermore, the PL intensity, presented in Fig. 5.17(e), is continuously transferred from the exciton to the trion, as with increasing carrier density more and more electrons (or holes) bind to excitons via Coulomb interaction. For the negatively charged trion, the total PL is even moderately conserved. Interestingly, at elevated, positive gate voltages around 10 V, both the energy separation and the PL intensity of the negative trion stay constant. This might be related to experimental issues in further increasing the carrier density beyond a certain point only in one of the layers or additional effects between the layers.

Upon recombination, the remaining carrier can take the momentum of the trion, a process known as the electron recoil effect [386–388]. Figure 5.18(a) illustrates the recombination of a trion, where the trion momentum is transferred to the remaining, free electron. This requires the additional energy $E_{recoil}$, due to the highly different masses of electron and trion, leading to a decrease of the emission energy. In total, this creates a characteristic, low-energy flank depending on the trion distribution. Figure 5.18(b) shows the recoil flank of the negative trion in an exemplary spectrum obtained at 10V.

For a quantitative analysis, the trion line shape is approximated by the convolution of a symmetric Voigt peak function $I_0$ and an exponential function, assuming a thermalized trion distribution:

$$I_{trion} = I_0 * e^{E/\epsilon}\,\Theta(-E), \text{ with } \frac{1}{\epsilon} = \frac{m_e}{m_X}\frac{1}{k_B T} + \frac{1}{E_M} \tag{5.3}$$

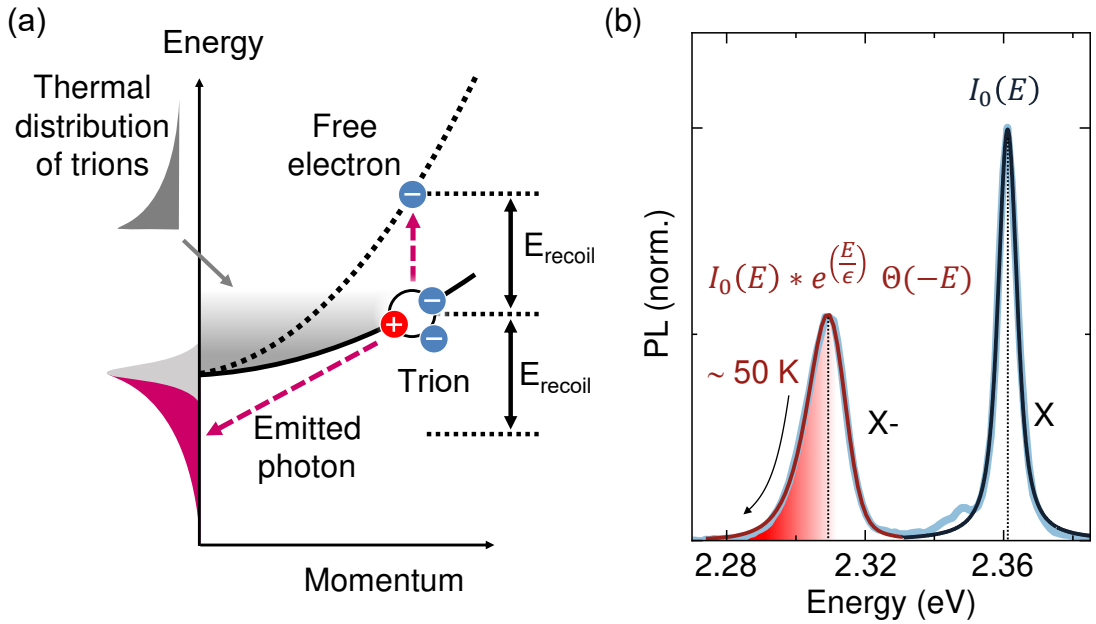


**Figure 5.18: Electron recoil effect (a)** Illustration of the electron recoil effect, where the exciton momentum is transferred to the free electron resulting in additional low energy emission. **(b)** Exemplary PL emission spectra fitted by a symmetric (blue) and asymmetric (red) peak function for the exciton and trion, respectively. The resulting trion temperature of 50 K is indicated. Obtained from 5.17(a) at a gate voltage of 10V.

Here, $E$ is the photon energy relative to the trion resonance and $\Theta$ the Heaviside step function. The energy parameter $\epsilon$ is determined by the temperature dependent trion distribution and the matrix element of the trion, related to the trion binding energy. The mass ratio is directly taken from the calculated values presented in chapter 5.2 and $E_M$ approximated by 10 meV, estimated from the value for $MoSe_2$ of 7 meV. This results in a temperature of 50 K for the trion distribution, which is reasonable in light of the more than 40 meV excess energy between exciton and trion and the possibility of overheated excitons at 5 K. The observation of an asymmetric lineshape with the low-energy flank is a characteristic feature of trions and supports the assignment as trion state. As an interesting side note, the recoil flank is not *a priori* on the low energy side, but depends on the trion to carrier mass ratio. A trion with a negative-mass exciton, for example, could exhibit the recoil flank on the high-energy side [389].

Importantly, during the formation of trions from bright excitons and an additional carrier, some of the oscillator strength of the exciton transfers to the trion. Additional samples with a thickness of more than 10 nm are investigated. Here, we used the PDMS exfoliation to create thicker layers instead of the direct

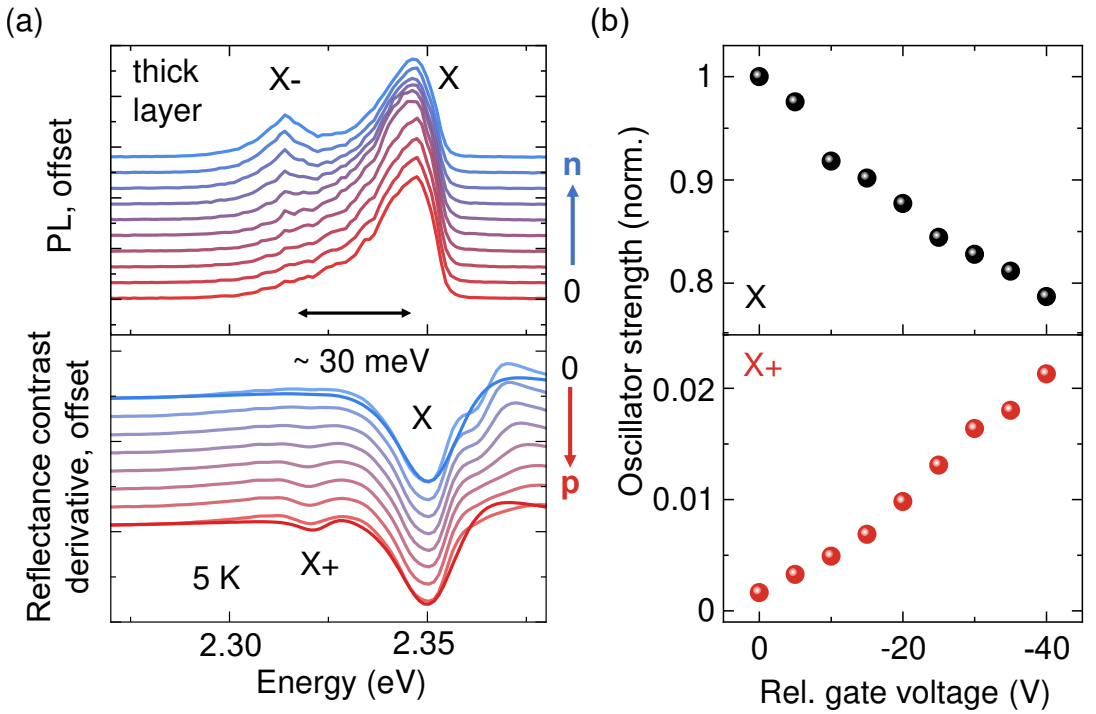


**Figure 5.19: Trion emission and absorption in thicker PEA layers. (a)** Gradual increase of trion emission in PL (top panel) and absorption in reflectance contrast derivative (bottom panel). The trion binding energy renormalizes to lower energies of 30 meV for the thicker layers. **(b)** Oscillator strength of the neutral exciton (top panel) and positively charged trion (bottom panel) normalized to the maximum of the exciton oscillator strength.

exfoliation. First, those thicker layers show similar behavior under electrostatic doping, the emergence of additional low-energy PL resonance, as presented in the top panel of Fig. 5.19(a). A similar feature emerges in the reflectance contrast data at nearly the same energy in the bottom panel of Fig. 5.19(a). This is attributed to the absorption of the trion species, directly separating it from most defect states and dark excitons, which tend to be completely dark or very low in oscillator strength and therefore show no absorption. Quantitatively, the transfer matrix method allows to extract the oscillator strengths of each resonance presented in Fig. 5.19((b), normalized to the maximum of the neutral exciton. Here, the linear increase of the trion oscillator strength with gate voltage and therefore free carrier density, is understood by the trion picture: With increasing charge carriers density, the chance to create a trion by absorption increases. Simultaneously, each absorbed trion is a missing exciton, reducing the oscillator strength of excitons, as observed. In this simple picture the total oscillator strength should be conserved and therefore independent of gate voltage. However, the screening of the additional carriers, Pauli-blocking and effects arising from defects can lead to

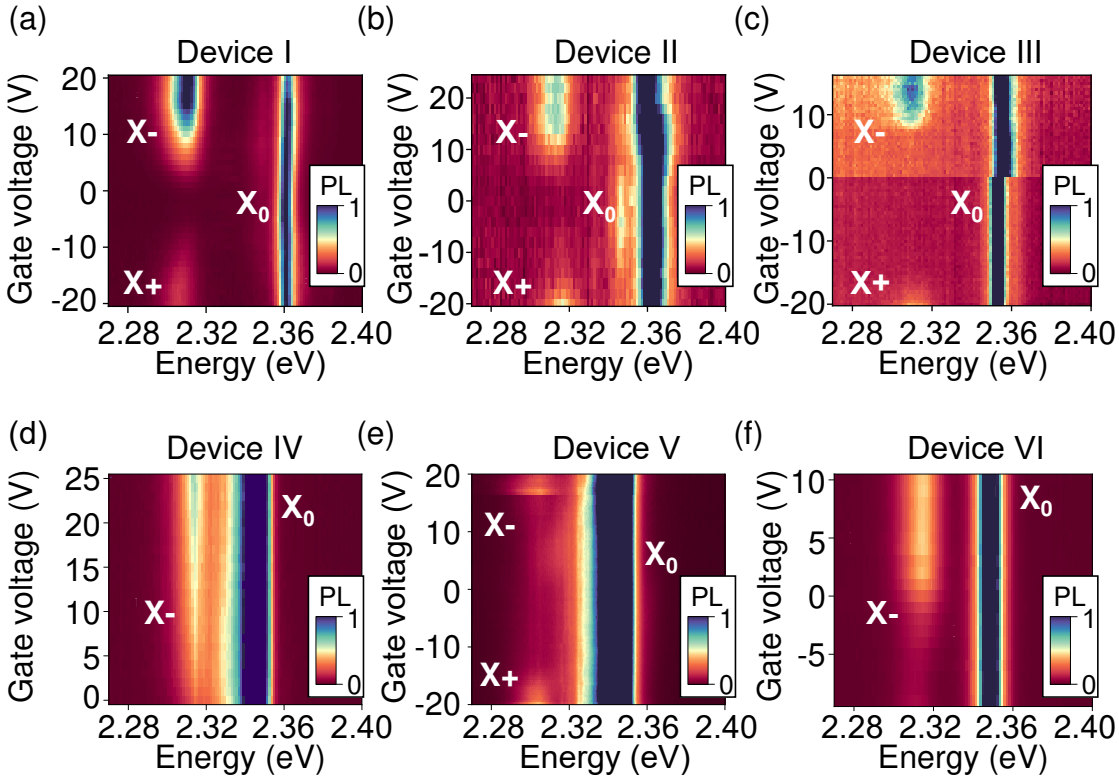


**Figure 5.20: Reproducibility across multiple different devices.** **(a)-(c)** Gate-dependent PL emission for three different ultra-thin devices. Device III two different measurement series for positiv and negative doping are combined. **(d)-(f)** Photoluminescence as function of gate-voltage for thicker devices.

the decrease of the total oscillator strength. These signatures in absorption and the scaling with voltage are a clear evidence for the attribution to trions.

The trion feature is systematically observed in several different devices fabricated in the course of this thesis, as summarized in Fig. 5.20. The top row shows three different devices with ultra-thin layers, while the bottom row shows samples with thicker perovskite layers. This highlights the reproducibility of the employed doping approach to demonstrate trions in 2D perovskites.

The general observations of trions are the same for all perovskite thicknesses, while the trion binding energy is notably reduced to around 30 meV for the thicker samples. This is attributed to a change of the screening, which in turn modifies the Coulomb interaction between carriers. In bulk 2D perovskites, the alternating layers of $PbI_4$ lead to a relatively high, average screening compared with a monolayer encapsulated in hBN with a lower dielectric constant. In order to estimate the impact of the dielectric screening due to different thicknesses, we turn to the exciton binding energy, which should be similarly affected.

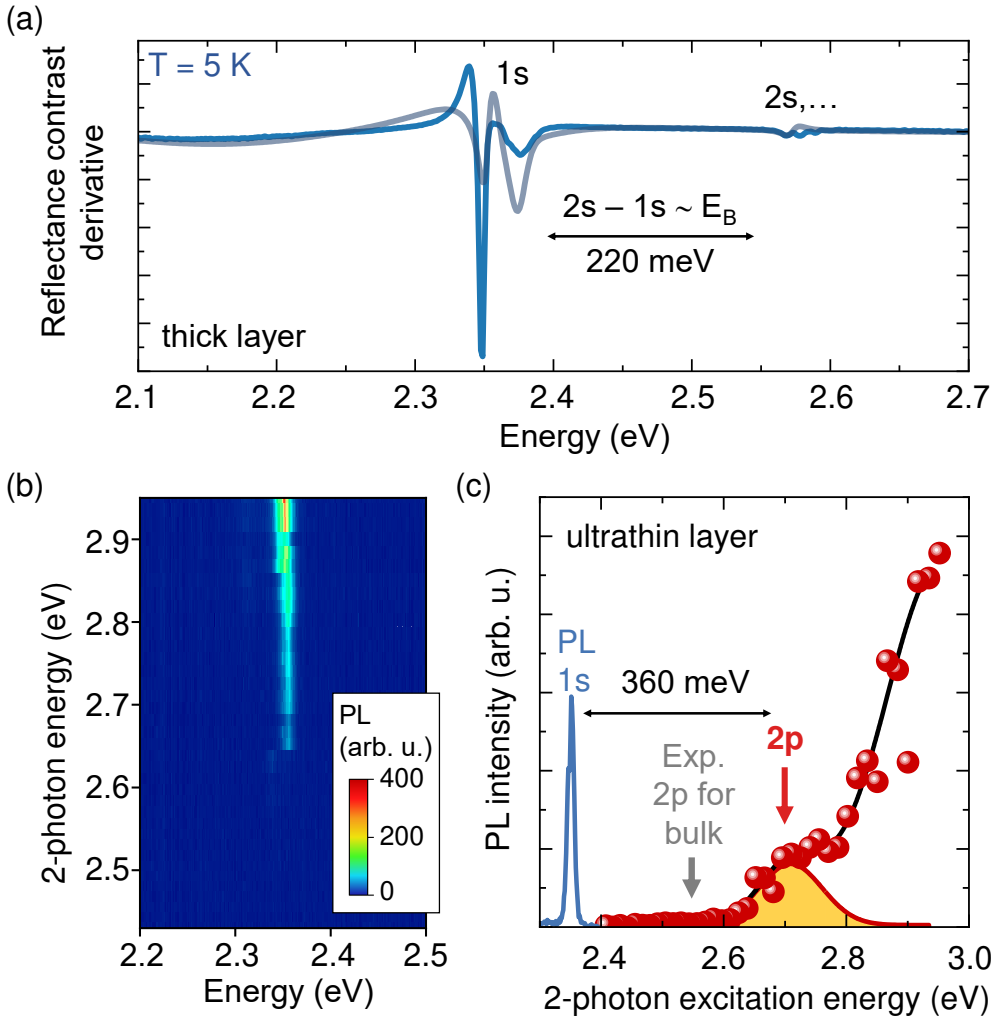


**Figure 5.21: Determination of the exciton binding energy (a)** Reflectance contrast derivative of an encapsulated thicker layer including the ground (1s) and excited states (2s,...). **(b)** Spectrally-resolved PL as function of the two-photon excitation energy of an ultra-thin layer **(c)** Corresponding PL and TPLE spectrum showing the ground state PL and corresponding absorption onset from the 2p-state, fitted by a Gaussian distribution.

The energy separation between ground and excited state serves as probe for the exciton binding energy. For the thicker samples, the reflectance contrast derivative, presented in Fig. 5.21(a) allows to directly extract the energy of the 2s resonance, resulting in a distance of around 220 meV. Consequently, using a linear scaling of $E_B = 1.2\,\Delta_{2s-1s}$, obtained from theory calculations [379], this results in a binding energy of 260 meV, in good agreement with literature [46, 226, 378]. Due to the weak absorption of the ultra-thin layer, we employ TPLE measurements to measure the excited state energy [46]. Figure 5.21(b) shows the spectrally resolved PL emission as function of the two-photon excitation energy. The onset of the two-photon absorption is fitted by a Gaussian distribution and yields an excited-

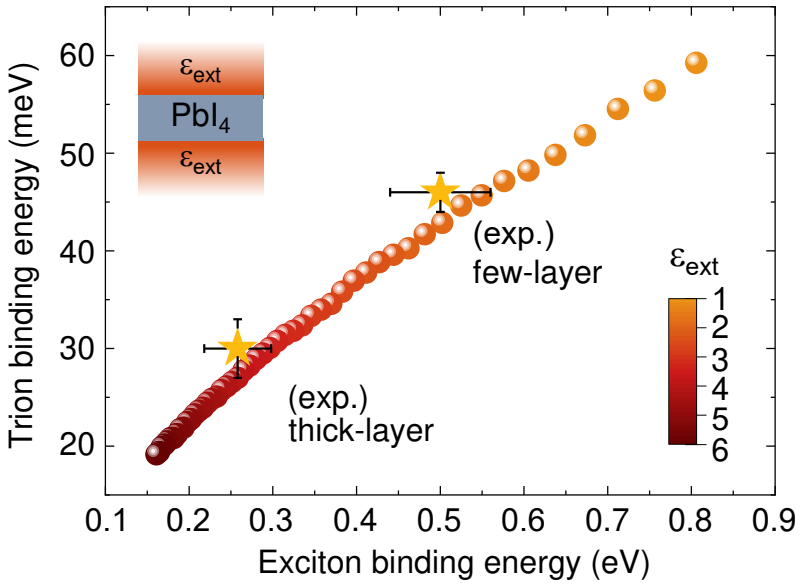


**Figure 5.22: Exciton and trion binding energies** Calculated binding energies of exciton and trion as function of the surrounding effective dielectric constant of a single $PbI_4$ layer, as shown in the inset. The experimentally determined values for the thick and thin layer are included for comparison.

to ground state distance of 360 meV, as presented in Fig. 5.21(c). Notably, the thin sample shows no absorption in the spectral range of the expected 2s/2p resonance for the thick sample. This then results in an significantly higher binding energy of around 430 meV. The values of the exciton binding energy follow the change of the trion binding energy strikingly well.

These values are also directly captured by a change of the dielectric surrounding. Therefore, our colleagues Yeongsu Cho and Timothy C. Berkelbach from the Columbia University New York provided calculations for the exciton and trion binding energies. Here, the energies are calculated by two- and three-body Hamiltonians with interacting charges via the modified Coulomb potential for thin-films, where the dielectric surrounding of a single layer $PbI_4$ is varied. Figure 5.22 presents the determined trion binding energy as function of the exciton binding energies for different dielectric surroundings. The experimentally determined exciton binding energy values are here directly obtained from calculated 2s/2p-1s separations to provide better comparison between the values and to include a small difference between the 2s and 2p energies for different dielectric screenings. Again, the exciton and trion binding energies correlate very well and the changes are directly attributed to a change of the average surrounding dielectric constant.

## 5.5 Mobile charged excitons

Lastly, the question remains whether we observe free trion propagation, and how it compares to neutral exciton diffusion, or if trions are localized. Therefore, the device is negatively doped by a constant gate voltage and excited by the frequency-doubled Ti:Sa laser pulses with a photon energy of 2.82 eV.

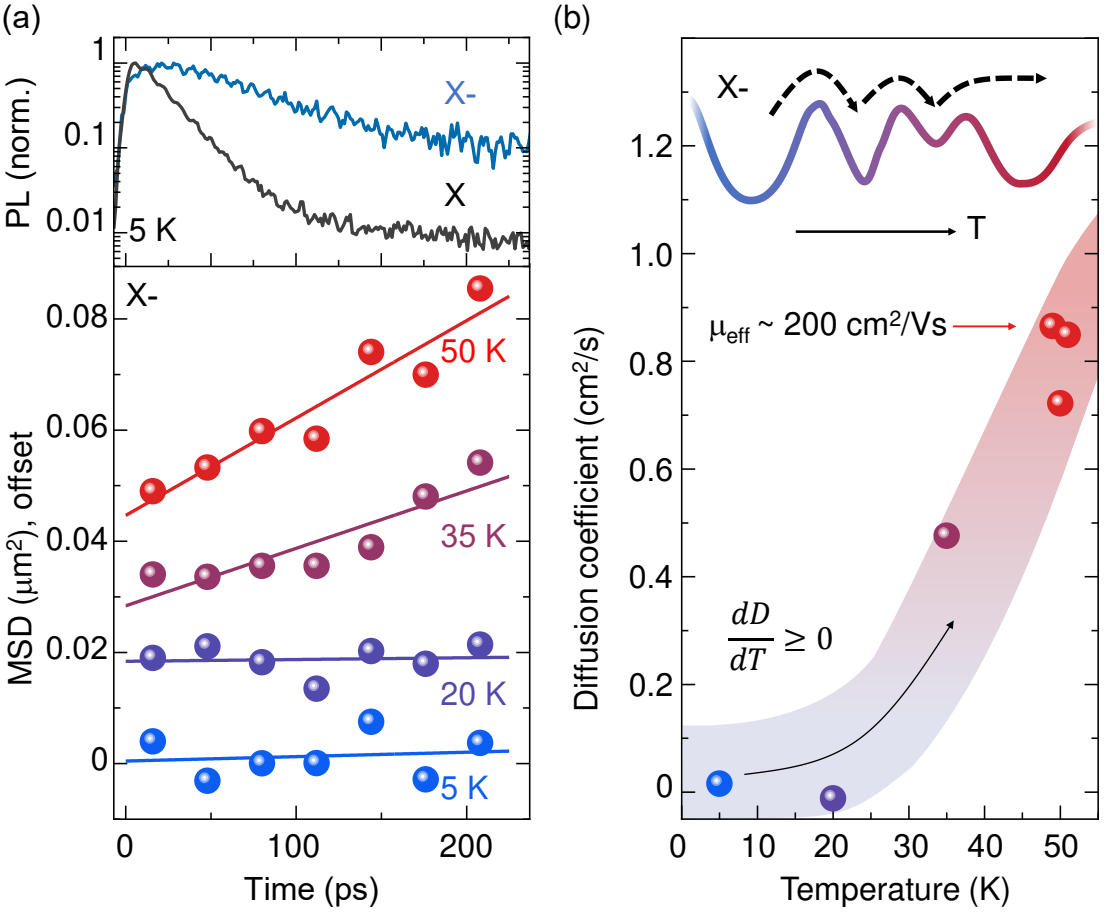


**Figure 5.23: Trion diffusion in two-dimensional perovskites.** **(a)** Time-dependent emission transients of the neutral exciton and charged trion obtained at 5 K. **(b)** Mean-squared displacement of the trion PL as function of time for different temperatures. The emission from the neutral exciton is completely blocked by a spectral filter. For elevated temperatures the MSD increases linearly, evidencing diffusive transport. **(c)** Temperature-dependent diffusion coefficients. Inset illustrates the increasing thermal activation of localized trions. Shaded areas are guides to the eye.

Figure 5.23(a) shows in the top panel the time-dependent PL emission from exciton and trion, where the longer lifetime of the trion is in agreement with similar observations of trions in TMDCs [390, 391]. For time-and spatially resolved PL, a tunable, spectral filter blocks the emission of the neutral exciton, resulting in only the trion PL emission being detected. The spatially resolved emission is

then separated into different time intervalls with 25 ps each. Then, by extracting the broadening over time, the mean-squared displacement, we can determine the diffusion coefficient of trions. The bottom panel of Fig. 5.23(a) displays the MSD of the trion signal for different temperatures. The emission area stays nearly constant for the low temperatures of 5 K, and 20 K, representing a localized distribution. However, upon increasing the temperature, a clear, linear increase is observed for 35 K and 50 K. The diffusion coefficients are quantified from the slope according to $MSD(t) = 2\,D\,t$ and summarized in Fig. 5.23(b). Here we note, that above 50 K the trion resonance is merging with the exciton resonance due to the strong exciton-phonon coupling at elevated temperatures. The overall temperature dependence is very reminiscent of the observations of neutral exciton diffusion in PEA, shown in Fig. 5.8 and indicates therefore thermal activation of localized trions with subsequent free propagation.

The absolute value of around 0.8 $cm^2/s$, corresponding to a mobility of 200 $cm^2/Vs$, is orders of magnitude higher than typical values for hopping transport and organic materials in general [324, 368]. Additionally, the overall smaller diffusivity of trions compared to excitons can be attributed to the higher mass of the trion. Simultaneously, the scattering is increasingly dominated by exciton-carrier scattering, complicating the extraction of separate trion and exciton diffusion coefficients.

In summary, we have introduced a promising doping approach for 2D hybrid materials. This allows to electrically control the optical response via the formation of stable trions with exceptionally high binding energies of 46 meV. For negative doping, the trions even dominate the PL emission without a notable loss of the PL yield. These trions can freely propagate at elevated temperatures and can be used to manipulate the transport due to the additional net charge, for example creating trion currents.

# Chapter 6
# Conclusions and outlook

In the course of this work, the fundamental properties of excitons in two dimensional semiconductors are studied and ways to either control the spatial propagation or modulate the optical response are explored. We investigate two different materials systems, monolayer transition metal dichalcogenides and layered hybrid organic-inorganic perovskites. Both systems are exfoliated using different methods, where the polymer-assisted exfoliation and stamping and the dry-pick are introduced. These techniques have been applied to create high-quality strained $WSe_2$ heterostructures and modified to create gate-tunable layered perovskite devices. Different spectroscopic techniques including transient microscopy and two photon excitation photoluminescence provide access to study spectral and spatial properties of excitons in these systems.

We achieved the spatial confinement of excitons to a quasi-1D channel using a strain potential. Here, the encapsulation in hBN provides unmatched optical quality in the deformed region of a strained monolayer $WSe_2$. This not only allows us to accurately determine the effective strain creating a potential channel of around 10 meV, but also the characteristic impact of strain on the fine structure of excitons in $WSe_2$. The observed change of the bright-dark exciton splitting also provides further evidence for the brightened recombination mechanism of the dark trion state.

The main focus of this study is manipulating the exciton transport. By employing time- and spatially resolved photoluminescence spectroscopy, we directly monitor the guiding of excitons along the strain-induced channel at cryogenic temperatures. The observation of a transport anisotropy of around 90% is quantitatively understood by solving the modified drift-diffusion equation and simulating the exciton transport using experimental parameters. Surprisingly, a similar high exciton diffusion anisotropy is observed at room temperature, despite the relatively low potential depth of 10 meV compared to an average thermal energy of around 25 meV. This is a direct consequence of strain impacting the multi-valley band structure, where the $K\Lambda$ state shifts to higher energies. This drastically reduces the intervalley phonon scattering, which in turn leads to an increase of

the diffusion, as the excitons scatter less frequently. Consequently, in addition to the energetic potential, this creates a high mobility channel in the strained region. Collectively, this leads to the efficient guiding of excitons even at room temperature. The high anisotropy in combination with the observed increased density in the strained region and guiding of excitons towards the center of the channel provides further evidence for funneling [347, 358–360]. Additionally, exciton to trion conversion has been discussed to play a role in strained $MoSe_2$ and $WS_2$ [348, 392]. The future combination of strain in gate-tunable devices could shed more light on the different impact of strain on electrons, holes, excitons and trions.

An interesting pathway for future experiments is 1D regime. In the measured strain-induced channel with a depth of around 10 meV and a width of around 1 µm, the quantum confinement leads to the occupation of around 25 transverse modes. The transition into the true 1D regime, where only one mode is occupied, is expected to occur below 60 nm channel width. Such small channel lengths might be reachable by using either narrow nanowires or etching small ridges into the substrate. Recently, 1D quantum confinement of excitons on a spatial scale of around 10 nm was achieved in $MoSe_2$ by using in-plane electric fields and local doping [393]. This his approach additionally enables the electrical tuning of the potential, whereas the confinement is restricted to excitons and relies on the interaction between excitons and additional charges outside the channel. This could provide a strategy to study exciton transport in the true 1D regime.

Future research could also profit from the scalability of another approach to create a similar confinement, relying on the dielectric sensitivity of both excitonic quasi-particles and the band gap [170, 171, 252, 394]. By patterning the substrate with strongly contrasting dielectric constants, one could generate similar channels in the energetic landscape. Additional tuning can be provided by using a proximate layer of graphene, where the dielectric screening is varied by introducing additional carriers into the graphene [174]. Beside the confining effect of such a channel, one could also increase the spatial scale of the channel to observe the direct guiding of excitons along this potential gradient. This directional exciton transport in TMDCs would then give rise to the valley-hall effect, spatially separating excitons from the $K$ and $-K$ valley [122, 182, 186, 395, 396].

The propagation of interlayer excitons can additionally be controlled via in-plane electric fields, due to their dipole moment. The high binding energy of interlayer excitons allows to build transistors using excitons instead of electrons working at room temperature, based on previous work in quantum wells [133, 134, 177–180]. In summary, characteristic impact of strain on the finestructure, the

tunable control and direct guiding of excitons opens the way for systems using excitons as information carriers and the discovery of intriguing new physics, for example in combination with an underlying moiré pattern.

In the second part of this thesis, we investigate the diffusion of excitons, the impact of a phase-transition and demonstrate stable trions in layered hybrid perovskites. Here, inorganic sheets of $PbI_4$ are sandwiched between organic layers of either PEA ($C_6H_5C_2H_4NH_3$, phenylethlyammonium) or BA ($C_4H_9NH_3$, butylammonium), resembling natural quantum wells. Thin sheets, containing several of these single layers, are exfoliated from single crystals and encapsulated in hBN to provide protection from the environment [397, 398]. First, excitons in these hybrids systems are surprisingly mobile, with a room temperature diffusion constant of around $1\,cm^2/s$ and $0.3\,cm^2/s$ for PEA and BA, respectively. There are no signs of additional, density-dependent effects on the exciton diffusion, due to the low excitation conditions in the experiment supported by reported, low Auger coefficients [235]. The observed efficient diffusion values are orders of magnitude higher than observed for prototypical organic crystals and in good agreement with current literature [231, 235, 368, 370]. The difference between the two materials is attributed to a more rigid lattice for PEA, decreasing the exciton-phonon interaction [231, 370]. This further provides both an opportunity for chemically engineering perovskites to exhibit increased exciton diffusion but also poses an important question on how to understand the exciton transport. The typically applied semi-classical diffusion model can not directly explain the change of diffusion constant, as there is no similar change in the scattering.

The measured temperature dependence of the exciton diffusion reveals two distinct regimes of exciton transport. At elevated temperatures above 50 K, the diffusion coefficient decreases with increasing temperature, a direct evidence for band-like transport. This decrease is well captured by the semi-classical model, using experimental parameters for the scattering time and theoretically calculated exciton masses. In stark contrast, an anomalous diffusion is observed upon further decreasing the temperature, where rapid diffusion is followed by an effective shrinking of the exciton distribution. In the experiment, after the initial quick expansion, a long-lived and immobile exciton distribution remains. However, the diffusion constant obtained at longer times drastically increases with temperature from nearly $0\,cm^2/s$ at 5 K to around $3\,cm^2/s$ at 50 K. This provides clear evidence for localization, in addition to the observed, gradual red-shift of the PL on similar time-scales as the rapid diffusion, obtained from spectrally- and temporally resolved PL. Together, the semi-classical model modified by an additional thermal

activation of localized excitons agrees with the experimental data. Additionally, the impact of impurity scattering has been suggested to explain the non-monotonic temperature dependence [399].

However, the applicability of the semi-classical model needs to be considered, where the investigated excitons are beyond the Mott-Yoffe-Regel criterion nearly at the whole temperature range. Therefore, additional non-classical effects and quantum corrections can play role, as similarly predicted and observed for exciton diffusion in monolayer TMDCs [266, 357, 400]. While the quantitative agreement between the semi-classical model, obtained from calculated electron and hole masses and experimentally determined scattering times, indicates no large renormalization of the mass, further polaronic effects steming from the strong exciton-phonon couple might play a role [109, 116, 375, 381]. Finally, the combination of a fast diffusing and short-lived exciton cloud, attributed to overheated excitons, with a slow, localized distribution allows to explain the observed effective negative diffusion. This two-component model is now also successfully applied to a broad variety of material systems, such as singlet and triplet diffusion in organic crystals or hot excitons and trions in TMDCs, which show similar dynamics as observed for the anomalous diffusion regime [401–403].

The efficient propagation at room temperature is also observed at long spatial scales and further highlights 2D perovskites as promising material for light harvesting [231, 370, 404]. While solar cells consisting of pure 2D perovskite have proven to be stable and efficient [166, 405–407], 2D perovskites have shown to be especially promising in combination with 3D perovskites, exploiting the increased stability of the 2D layer [408–412]. Additionally, hybrid 2D-3D structures can profit from efficient interlayer transport inside the layered perovsktie, as recently shown in PEA [413]. Despite this encouraging progress in solar cell devices, 2D perovskites and hybrid perovskites in general are still surrounded by many open fundamental questions, mostly regarding the soft crystal and corresponding strong exciton-phonon interaction. This includes dynamic disorder of the energetic landscape induced by large atomic motions and the unresolved role of polaronic effects [374, 381, 414–416]. Here, future temperature-dependent studies on exciton transport in different layered perovskites could help to resolve some open questions.

The phase transition in BA offers an interesting scenario to test basic exciton properties and progress in understanding the underlying exciton physics. Here, we observe no change of both exciton binding energy and exciton diffusion coefficient across the phase transition, challenging the current understanding of theoretically predicted and experimentally observed change of the underlying effective mass.

The absence of any change challenges established models and highlights the unconventional behavior of excitons in 2D perovskites. Interestingly, the increase of the binding energy with increasing temperatures exhibits the opposite scaling as observed for 3D perovskite [79–81, 380]. Here, it would be especially interesting to study the exciton binding energy as function of temperature for different inorganic layer thicknesses, e.g. 2D layers which become increasingly 3D. The reduced confinement of thicker inorganic layers reduces the absolute binding energy, which in turn could help to resolve different contributions [226]. A complementary study could contain different organic spacers with strongly different dielectric constants [259], providing more insight into the dielectric properties of 2D perovskites.

The formation of stable trions in layered perovskites has been theoretically predicted, but were missing so far due to issues in introducing doping into perovskites [312]. In the last chapter, we demonstrate the formation of trions by bipolar electrical doping of 2D perovskite. The charged excitons exhibit exceptionally high binding energies of up to 46 meV and even dominate the emission at high n-doping. Additionally, differences in the dielectric screening of ultra-thin layer and thicker layers are experimentally observed by a decreased binding energy of both exciton and trion, supported by theoretical calculations. Especially the observation of the charged features in absorption-type measurements in addition to the asymmetric PL profile, assigned to the electron-recoil effect provide clear evidence for the trion assignment. Trions have been observed at high excitation densities in perovskite nanocrystals [306, 309, 417] and quantum beatings in 3D hybrid perovskites have been assigned to be due to trions. In 2D hybrid perovskites, this is the first observation of trions and the electrically tunable exciton-to-trion conversion.

In general, the mobility of charged excitons is still an open question in many systems, where trions in 2D perovskites are a great opportunity to study the diffusion. Remarkably, the trions show diffusion coefficients up to around $0.8\,\mathrm{cm}^2/\mathrm{s}$ at 50 K, corresponding to mobilities of $200\,\mathrm{cm}^2/\mathrm{Vs}$, while being nearly completely immobile at 5 K. Additionally, the presence of free carriers in a soft crystal opens the way for new interesting many-particle physics. This includes the Fermi-polaron picture, describing trions as the interaction between a Fermi-sea of free carriers and excitons, which could provide further understanding of trions in 2D perovskites [418–420] . Especially the combination of both, an exciton interacting with free carriers and simultaneously with the soft lattice via phonons might allow intriguing new insights. Here, an interesting starting point to study these would be doping- and temperature-dependent transport studies, which might help to differentiate between electron-exciton and exiton-phonon interaction.

The demonstrated gating approach and tunability of the optical response should be transferable to a broad range of different inorganic and organic materials. Here, optimizing the contact material in both more efficient interfaces as well as scalability is crucial to create broadly useable devices, as already proven for organic LEDs [421, 422]. Especially the chemical flexibility providing a broad tunability of the band gap, opens the way for highly efficient blue LEDs. The additional charge of the trion also opens the way for guiding excitonic particles using electric fields [423–429], contributing to the future development of exciton transistors based on 2D perovskites. Altogether, the studied low-dimensional semiconductors hold great promise for exciting new many-particle physics and equal potential for future applications. The investigation of exciton propagation and ways to control it might provide an important puzzle piece to the future of technology and fundamental research.

# Bibliography


[1] J. d. Heinzelin, J. D. Clark, T. White, W. Hart, P. Renne, G. WoldeGabriel, Y. Beyene, and E. Vrba, "Environment and behavior of 2.5-million-year-old bouri hominids", Science **284**, 625–629 (1999) (cit. on p. 1).

[2] S. H. Ambrose, "Paleolithic Technology and Human Evolution", Science **291**, 1748–1753 (2001) (cit. on p. 1).

[3] P. Schmidt and D. H. Avery, "Complex Iron Smelting and Prehistoric Culture in Tanzania", Science **201**, 1085–1089 (1978) (cit. on p. 1).

[4] M. N. Geselowitz, *Technology and Social Change: Ironworking in the Rise of Social Complexity in Iron Age Central Europe* (Springer, Boston, MA, Boston, MA, USA, 1988), pp. 137–154 (cit. on p. 1).

[5] M. Hanagan, "Industrialization and urban society in nineteenth-century france", Journal of urban history **13**, 218–229 (1987) (cit. on p. 1).

[6] E. Hopkins, *Industrialisation and Society* (2000) (cit. on p. 1).

[7] I. M. Ross, "The invention of the transistor", Proceedings of the IEEE **86**, 7–28 (1998) (cit. on p. 1).

[8] M. Riordan and L. Hoddeson, "Crystal fire: the invention, development and impact of the transistor", IEEE Solid-State Circuits Society Newsletter **12**, 24–29 (2007) (cit. on p. 1).

[9] J. Bardeen, "Surface States and Rectification at a Metal Semi-Conductor Contact", Phys. Rev. **71**, 717–727 (1947) (cit. on p. 1).

[10] J. Bardeen and W. H. Brattain, "The Transistor, A Semi-Conductor Triode", Phys. Rev. **74**, 230–231 (1948) (cit. on p. 1).

[11] W. H. Brattain, R. B. Gibney, and B. T. L. Inc, *Three-electrode circuit element utilizing semiconductor materials*, [Online; accessed 2. Nov. 2022], Feb. 1948 (cit. on p. 1).

[12] W. Shockley, "The Theory of p-n Junctions in Semiconductors and p-n Junction Transistors", Bell System Technical Journal **28**, 435–489 (1949) (cit. on p. 1).

[13] W. Shockley, M. Sparks, and G. K. Teal, "$p-n$ Junction Transistors", Phys. Rev. **83**, 151–162 (1951) (cit. on p. 1).

[14]K. Zuse, "Verfahren zur selbsttätigen durchführung von rechnungen mit hilfe von rechenmaschinen", Z23139 IX/42m (11.4. 1936) (1936) (cit. on p. 1).

[15]A. Turing, "On computable numbers, with an application to the n tscheidungsproblem", Proceedings of the London Mathematical Society **42** (1936) (cit. on p. 1).

[16]J. v. Neumann, "First draft of a report on the edvac", Moore School of Electrical Engineering, University of Pennsylvania (1945) (cit. on p. 1).

[17]R. W. Keyes, "Miniaturization of electronics and its limits", IBM J. Res. Dev. **32**, 84–88 (1988) (cit. on p. 1).

[18]R. W. Keyes, "Physical limits of silicon transistors and circuits", Rep. Prog. Phys. **68**, 2701 (2005) (cit. on p. 1).

[19]T. N. Theis and P. M. Solomon, "It's Time to Reinvent the Transistor!", Science **327**, 1600–1601 (2010) (cit. on p. 1).

[20]A. P. Alivisatos, A. L. Harris, N. J. Levinos, M. L. Steigerwald, and L. E. Brus, "Electronic states of semiconductor clusters: Homogeneous and inhomogeneous broadening of the optical spectrum", J. Chem. Phys. **89**, 4001–4011 (1988) (cit. on p. 2).

[21]J. Singh and K. K. Bajaj, "Role of interface roughness and alloy disorder in photoluminescence in quantum-well structures", J. Appl. Phys. **57**, 5433–5437 (1985) (cit. on p. 2).

[22]P. M. Fahey, P. B. Griffin, and J. D. Plummer, "Point defects and dopant diffusion in silicon", Rev. Mod. Phys. **61**, 289–384 (1989) (cit. on p. 2).

[23]I. Akasaki, H. Amano, Y. Koide, K. Hiramatsu, and N. Sawaki, "Effects of ain buffer layer on crystallographic structure and on electrical and optical properties of GaN and Ga1-xAlxN ($0 < x \leqq 0.4$) films grown on sapphire substrate by MOVPE", J. Cryst. Growth **98**, 209–219 (1989) (cit. on p. 2).

[24]S. Nakamura, "The roles of structural imperfections in ingan-based blue light-emitting diodes and laser diodes", Science **281**, 956–961 (1998) (cit. on p. 2).

[25]S. F. Chichibu, A. Uedono, T. Onuma, B. A. Haskell, A. Chakraborty, T. Koyama, P. T. Fini, S. Keller, S. P. DenBaars, J. S. Speck, et al., "Origin of defect-insensitive emission probability in in-containing (al, in, ga) n alloy semiconductors", Nature materials **5**, 810–816 (2006) (cit. on p. 2).

[26]IPCC, *Climate Change 2022: Mitigation of Climate Change. Contribution of Working Group III to the Sixth Assessment Report of the Intergovernmental Panel on Climate Change*, edited by P. Shukla, J. Skea, R. Slade, A. A. Khourdajie, R. van Diemen, D. McCollum, M. Pathak, S. Some, P. Vyas, R. Fradera, M. Belkacemi, A. Hasija, G. Lisboa, S. Luz, and J. Malley (Cambridge University Press, Cambridge, UK and New York, NY, USA, 2022) (cit. on p. 2).

[27]M. A. Green, "Silicon solar cells: evolution, high-efficiency design and efficiency enhancements", Semiconductor science and technology **8**, 1 (1993) (cit. on p. 2).

[28]D. Weber, "CH3NH3PbX3, ein Pb(II)-System mit kubischer Perowskitstruktur / CH3NH3PbX3, a Pb(II)-System with Cubic Perovskite Structure", Zeitschrift fuür Naturforschung B **33**, 1443–1445 (1978) (cit. on pp. 2, 11).

[29]T. Ishihara, J. Takahashi, and T. Goto, "Exciton state in two-dimensional perovskite semiconductor (C10H21NH3)2PbI4", Solid State Commun. **69**, 933–936 (1989) (cit. on pp. 2, 12, 24).

[30]T. Ishihara, J. Takahashi, and T. Goto, "Optical properties due to electronic transitions in two-dimensional semiconductors (CnH2n+1NH3)2PbI4", Phys. Rev. B **42**, 11099–11107 (1990) (cit. on pp. 2, 14).

[31]X. Hong, T. Ishihara, and A. Nurmikko, "Dielectric confinement effect on excitons in PbI4-based layered semiconductors", Phys. Rev. B **45**, 6961–6964 (1992) (cit. on pp. 2, 12).

[32]X. Hong, T. Ishihara, and A. V. Nurmikko, "Photoconductivity and electroluminescence in lead iodide based natural quantum well structures", Solid State Commun. **84**, 657–661 (1992) (cit. on p. 2).

[33]H. Ishihara, K. Watanabe, A. Iwata, K. Yamada, Y. Kinoshita, T. Okuda, V. G. Krishnan, S. Dou, and A. Weiss, "NQR and X-Ray Studies of [N(CH3)4]3M2X9 and (CH3NH3)3M2X9 (M = Sb,Bi; X = Cl,Br)", Z. Naturforsch., A: Phys. Sci. **47**, 65 (1992) (cit. on p. 2).

[34]T. Ishihara, X. Hong, J. Ding, and A. V. Nurmikko, "Dielectric confinement effect for exciton and biexciton states in PbI4-based two-dimensional semiconductor structures", Surface Science **267**, 323–326 (1992) (cit. on p. 2).

[35]M. Hirasawa, T. Ishihara, T. Goto, K. Uchida, and N. Miura, "Magnetoabsorption of the lowest exciton in perovskite-type compound (CH3NH3)PbI3", Phys. B Condens. Matter **201**, 427–430 (1994) (cit. on p. 2).

[36]T. Ishihara, "Optical properties of PbI-based perovskite structures", J. Lumin. **60-61**, 269–274 (1994) (cit. on p. 2).

[37]T. Kataoka, T. Kondo, R. Ito, S. Sasaki, K. Uchida, and N. Miura, "Magneto-Optical Study on the Excitonic Spectrum of (C6H13NH3) 2PbI4", Phys. B **184**, 132 (1993) (cit. on pp. 2–3, 24–25).

[38]T. Kataoka, T. Kondo, R. Ito, S. Sasaki, K. Uchida, and N. Miura, "Magneto-Optical Effects of Excitons in the Layered Perovskite-Type Material (C6H13NH3) 2(CH3NH3) Pb2I7", Phys. B **201**, 423 (1994) (cit. on p. 2).

[39]T. Kondo, S. Iwamoto, S. Hayase, K. Tanaka, J. Ishi, M. Mizuno, K. Ema, and R. Ito, "Resonant Third-Order Optical Nonlinearity in the Layered Perovskite-Type Material (C6H13NH3)2PbI4", Solid State Commun. **105**, 503 (1998) (cit. on p. 2).

[40]T. Kondo, T. Azuma, T. Yuasa, and R. Ito, "Biexciton Lasing in the Layered Perovskite-Type Material (C6H13NH3)2PbI4", Solid State Commun. **105**, 253 (1998) (cit. on p. 2).

[41]Y. Kato, D. Ichii, K. Ohashi, H. Kunugita, K. Ema, K. Tanaka, T. Takahashi, and T. Kondo, "Extremely large binding energy of biexcitons in an organic-inorganic quantum-well material (C4H9NH3)2PbBr4", Solid State Commun. **128**, 15–18 (2003) (cit. on pp. 2, 25).

[42]K. Tanaka, F. Sano, T. Takahashi, T. Kondo, R. Ito, and K. Ema, "Two-dimensional Wannier excitons in a layered-perovskite-type crystal (C6H13NH3)2 PbI4", Solid State Communications **122**, 249–252 (2002) (cit. on pp. 2, 12).

[43]K. Tanaka and T. Kondo, "Bandgap and Exciton Binding Energies in Lead-Iodide-Based Natural Quantum-Well Crystals", Sci. Technol. Adv. Mater. **4**, 599 (2003) (cit. on pp. 2, 24).

[44]K. Tanaka, T. Takahashi, T. Ban, T. Kondo, K. Uchida, and N. Miura, "Comparative Study on the Excitons in Lead-Halide-Based Perovskite-Type Crystals CH3NH3PbBr3 CH3NH3PbI3", Solid State Commun. **127**, 619 (2003) (cit. on p. 2).

[45]K. Tanaka, T. Takahashi, T. Kondo, T. Umebayashi, K. Asai, and K. Ema, "Image charge effect on two-dimensional excitons in an inorganic-organic quantum-well crystal", Phys. Rev. B **71**, 45312 (2005) (cit. on pp. 2, 24, 90, 92).

[46]K. Tanaka, T. Takahashi, T. Kondo, K. Umeda, K. Ema, T. Umebayashi, K. Asai, K. Uchida, and N. Miura, "Electronic and Excitonic Structures of Inorganic-Organic Perovskite-Type Quantum-Well Crystal (C 4 H 9 NH 3 ) 2 PbBr 4", Jpn. J. Appl. Phys. **44**, 5923–5932 (2005) (cit. on pp. 2, 25, 101).

[47] G. C. Papavassiliou, A. P. Patsis, D. J. Lagouvardos, and I. B. Koutselas, "Spectroscopic studies of (C10H21NH3)2PbI4, (CH3NH3) (C10H21 NH3)2 Pb2I7, (CH3 NH3) PbI3, and similar compounds", Synthetic Metals **57**, 3889–3894 (1993) (cit. on p. 2).

[48] G. C. Papavassiliou, I. B. Koutselas, D. J. Lagouvardos, J. Kapoutsis, A. Terzis, and G. J. Papaioannou, "Optical and Related Properties of Some Natural Three and Lower Dimensional Semiconductor Systems", Mol. Cryst. Liq. Cryst. Sci. Technol., Sect. A **253**, 103 (1994) (cit. on pp. 2, 12).

[49] G. C. Papavassiliou, I. B. Koutselas, A. Terzis, and M.-H. Whangbo, "Structural and electronic properties of the natural quantum-well system (C6H5CH2CH2 NH3)2 SnI4", Solid State Communications **91**, 695–698 (1994) (cit. on pp. 2, 12).

[50] G. C. Papavassiliou and I. B. Koutselas, "Structural, Optical and Related Properties of Some Natural Three- and Lower-Dimensional Semiconductor Systems", Synth. Met. **71**, 1713 (1995) (cit. on p. 2).

[51] G. C. Papavassiliou, "Synthetic Three-and Lower-Dimensional Semiconductors Based on Inorganic Units", Mol. Cryst. Liq. Cryst. Sci. Technol. Sect. A. Mol. Cryst. Liq. Cryst. **286**, 231–238 (1996) (cit. on p. 2).

[52] I. B. Koutselas, L. Ducasse, and G. C. Papavassiliou, "Electronic properties of three-and low-dimensional semiconducting materials with Pb halide and Sn halide units", Journal of Physics: Condensed Matter **8**, 1217 (1996) (cit. on p. 2).

[53] G. C. Papavassiliou, G. A. Mousdis, C. P. Raptopoulou, and A. Terzis, "Some New Luminescent Compounds Based on 4-Methylbenzylamine and Lead Halides", Z. Naturforsch., B: J. Chem. Sci. **55**, 536 (2000) (cit. on p. 2).

[54] G. C. Papavassiliou, G. A. Mousdis, I. B. Koutselas, W. J. Blau, P. Lianos, and U. Schubert, *Molecular Materials and Functional Polymers* (2001), p. 113 (cit. on p. 2).

[55] G. C. Papavassiliou, G. A. Mousdis, and I. B. Koutselas, "Excitonic Bands in the Spectra of Some Organic-Inorganic Hybrid Compounds Based on Metal Halide Units", in *Molecular Materials and Functional Polymers* (Springer, Vienna, Wien, Austria, 2001), pp. 113–119 (cit. on p. 2).

[56] D. B. Mitzi, C. A. Feild, W. T. A. Harrison, and A. M. Guloy, "Conducting tin halides with a layered organic-based perovskite structure", Nature **369**, 467–469 (1994) (cit. on pp. 2, 12).

[57]D. B. Mitzi, S. Wang, C. A. Feild, C. A. Chess, and A. M. Guloy, "Conducting Layered Organic-Inorganic Halides Containing -Oriented Perovskite Sheets", Science **267**, 1473 (1995) (cit. on pp. 2, 14).

[58]D. B. Mitzi, "Synthesis, Crystal Structure, and Optical and Thermal Properties of (C 4 H 9 NH 3) 2 MI 4 (M = Ge, Sn, Pb)", Chem. Mater. **8**, 791 (1996) (cit. on p. 2).

[59]D. B. Mitzi, K. Liang, and S. Wang, "Synthesis and Characterization of [NH 2 C(I)NH 2 ] 2 ASnI 5 with A = Iodoformamidinium or Formamidinium: The Chemistry of Cyanamide and Tin(II) Iodide in Concentrated Aqueous Hydriodic Acid Solutions", Inorg. Chem. **37**, 321 (1998) (cit. on p. 2).

[60]D. B. Mitzi, *Synthesis , Structure , and Properties of Organic-Inorganic Perovskites and Related Materials*, 1999 (cit. on pp. 2, 11).

[61]D. Mitzi, "A Layered Solution Crystal Growth Technique and the Crystal Structure of (C6H5C2H4NH3)2PbCl4", J. Solid State Chem. **145**, 694 (1999) (cit. on p. 2).

[62]D. B. Mitzi, K. Chondroudis, and C. R. Kagan, "Design, Structure, and Optical Properties of Organic–Inorganic Perovskites Containing an Oligothiophene Chromophore", Inorg. Chem. **38**, 6246 (1999) (cit. on p. 2).

[63]C. R. Kagan, D. B. Mitzi, and C. D. Dimitrakopoulos, "Organic-inorganic hybrid materials as semiconducting channels in thin-film field-effect transistors", Science **286**, 945–947 (1999) (cit. on p. 2).

[64]K. Chondroudis and D. B. Mitzi, "Electroluminescence from an Organic– Inorganic Perovskite Incorporating a Quaterthiophene Dye within Lead Halide Perovskite Layers", Chem. Mater. **11**, 3028 (1999) (cit. on p. 2).

[65]D. B. Mitzi, "Templating and structural engineering in organic–inorganic perovskites", Journal of the Chemical Society, Dalton Transactions, 1–12 (2001) (cit. on p. 2).

[66]D. B. Mitzi, K. Chondroudis, and C. R. Kagan, "Organic-inorganic electronics", IBM Journal of Research and Development **45**, 29–45 (2001) (cit. on pp. 2, 14).

[67]D. B. Mitzi, C. D. Dimitrakopoulos, and L. L. Kosbar, "Structurally Tailored Organic–Inorganic Perovskites: Optical Properties and Solution-Processed Channel Materials for Thin-Film Transistors", Chem. Mater. **13**, 3728 (2001) (cit. on p. 2).

[68]D. B. Mitzi, D. R. Medeiros, and P. R. L. Malenfant, "Intercalated Organic–Inorganic Perovskites Stabilized by Fluoroaryl–Aryl Interactions", Inorg. Chem. **41**, 2134 (2002) (cit. on p. 2).

[69]Z. Xu, D. B. Mitzi, C. D. Dimitrakopoulos, and K. R. Maxcy, "Semiconducting Perovskites (2-XC 6 H 4 C 2 H 4 NH 3) 2 SnI 4 (X = F, Cl, Br): Steric Interaction between the Organic and Inorganic Layers", Inorg. Chem. **42**, 2031 (2003) (cit. on p. 2).

[70]Z. Xu and D. B. Mitzi, "$CH_3(CH_2)_11$ NH3 $SnI_3$: A Hybrid Semiconductor with $MoO_3$ type Tin(II) Iodide Layers", Inorganic Chemistry **42**, PMID: 14552605, 6589–6591 (2003) (cit. on pp. 2, 14).

[71]A. Kojima, K. Teshima, Y. Shirai, and T. Miyasaka, "Organometal halide perovskites as visible-light sensitizers for photovoltaic cells", Journal of the American Chemical Society **131**, 6050–6051 (2009) (cit. on pp. 2, 11).

[72]H. J. Snaith, "Perovskites: The Emergence of a New Era for Low-Cost, High-Efficiency Solar Cells", J. Phys. Chem. Lett. **4**, 3623–3630 (2013) (cit. on p. 2).

[73]N.-G. Park, "Organometal Perovskite Light Absorbers Toward a 20% Efficiency Low-Cost Solid-State Mesoscopic Solar Cell", J. Phys. Chem. Lett. **4**, 2423–2429 (2013) (cit. on p. 2).

[74]H. J. Snaith, "Present status and future prospects of perovskite photovoltaics", Nature materials **17**, 372–376 (2018) (cit. on pp. 2, 11).

[75]*National Renewable Energy Laboratory Best Research-Cell Efficiency Chart*, https://www.nrel.gov/pv/cell-efficiency.html, Online; accessed 2. Nov. 2022, Nov. 2022 (cit. on p. 2).

[76]E. Menéndez-Proupin, P. Palacios, P. Wahnón, and J. C. Conesa, "Self-Consistent Relativistic Band Structure of the CH3NH3PbI3 Perovskite", Phys. Rev. B: Condens. Matter Mater. Phys. **90**, 45207 (2014) (cit. on p. 2).

[77]J. Even, L. Pedesseau, and C. Katan, "Analysis of Multivalley and Multibandgap Absorption and Enhancement of Free Carriers Related to Exciton Screening in Hybrid Perovskites", J. Phys. Chem. C **118**, 11566 (2014) (cit. on p. 2).

[78]V. D'Innocenzo, G. Grancini, M. J. P. Alcocer, A. R. S. Kandada, S. D. Stranks, M. M. Lee, G. Lanzani, H. J. Snaith, and A. Petrozza, "Excitons versus free charges in organo-lead tri-halide perovskites", Nat. Commun. **5**, 1–6 (2014) (cit. on p. 2).

[79]Y. Yamada, T. Nakamura, M. Endo, A. Wakamiya, and Y. Kanemitsu, "Photoelectronic Responses in Solution-Processed Perovskite $CH_3NH_3PbI_3$ Solar Cells Studied by Photoluminescence and Photoabsorption Spectroscopy", IEEE J. Photovoltaics **5**, 401–405 (2014) (cit. on pp. 2, 92, 109).

[80]Q. Lin, A. Armin, R. C. R. Nagiri, P. L. Burn, and P. Meredith, "Electro-optics of perovskite solar cells", Nat. Photonics **9**, 106–112 (2015) (cit. on pp. 2, 92, 109).

[81]A. Miyata, A. Mitioglu, P. Plochocka, O. Portugall, J. T.-W. Wang, S. D. Stranks, H. J. Snaith, and R. J. Nicholas, "Direct Measurement of the Exciton Binding Energy and Effective Masses for Charge Carriers in Organic–Inorganic Tri-Halide Perovskites", Nat. Phys. **11**, 582 (2015) (cit. on pp. 2, 92, 97, 109).

[82]J. Berry, T. Buonassisi, D. A. Egger, G. Hodes, L. Kronik, Y.-L. Loo, I. Lubomirsky, S. R. Marder, Y. Mastai, J. S. Miller, D. B. Mitzi, Y. Paz, A. M. Rappe, I. Riess, B. Rybtchinski, O. Stafsudd, V. Stevanovic, M. F. Toney, D. Zitoun, A. Kahn, D. Ginley, and D. Cahen, "Hybrid Organic–Inorganic Perovskites (HOIPs): Opportunities and Challenges", Adv. Mater. **27**, 5102–5112 (2015) (cit. on p. 2).

[83]T. M. Brenner, D. A. Egger, L. Kronik, G. Hodes, and D. Cahen, "Hybrid organic—inorganic perovskites: low-cost semiconductors with intriguing charge-transport properties", Nat. Rev. Mater. **1**, 1–16 (2016) (cit. on pp. 2, 11).

[84]Y. Yang, D. P. Ostrowski, R. M. France, K. Zhu, J. van de Lagemaat, J. M. Luther, and M. C. Beard, "Observation of a hot-phonon bottleneck in lead-iodide perovskites", Nat. Photonics **10**, 53–59 (2016) (cit. on p. 2).

[85]A. D. Wright, C. Verdi, R. L. Milot, G. E. Eperon, M. A. Pérez-Osorio, H. J. Snaith, F. Giustino, M. B. Johnston, and L. M. Herz, "Electron-phonon coupling in hybrid lead halide perovskites", Nat. Commun. **7**, 11755 (2016) (cit. on p. 2).

[86]K. Miyata, T. L. Atallah, and X.-Y. Zhu, "Lead halide perovskites: Crystal-liquid duality, phonon glass electron crystals, and large polaron formation", Sci. Adv. **3**, 10.1126/sciadv.1701469 (2017) (cit. on pp. 2, 28).

[87]L. M. Herz, "How Lattice Dynamics Moderate the Electronic Properties of Metal-Halide Perovskites", J. Phys. Chem. Lett. **9**, 6853–6863 (2018) (cit. on pp. 2, 15).

[88]D. A. Egger, A. Bera, D. Cahen, G. Hodes, T. Kirchartz, L. Kronik, R. Lovrincic, A. M. Rappe, D. R. Reichman, and O. Yaffe, "What Remains Unexplained about the Properties of Halide Perovskites?", **30**, 1800691 (2018) (cit. on pp. 2–3, 15, 77).

[89]Y. Guo, O. Yaffe, T. D. Hull, J. S. Owen, D. R. Reichman, and L. E. Brus, "Dynamic emission Stokes shift and liquid-like dielectric solvation of band edge carriers in lead-halide perovskites", Nature Communications **10**, 1175 (2019) (cit. on p. 2).

[90]J. M. Ball and A. Petrozza, "Defects in perovskite-halides and their effects in solar cells", Nat. Energy **1**, 1–13 (2016) (cit. on p. 2).

[91]D. J. Keeble, J. Wiktor, S. K. Pathak, L. J. Phillips, M. Dickmann, K. Durose, H. J. Snaith, and W. Egger, "Identification of lead vacancy defects in lead halide perovskites", Nat. Commun. **12**, 1–7 (2021) (cit. on p. 2).

[92]M. Pratheek, T. Abhinav, S. Bhattacharya, G. K. Chandra, and P. Predeep, "Recent progress on defect passivation in perovskites for solar cell application", Mater. Sci. Energy Technol. **4**, 282–289 (2021) (cit. on p. 2).

[93]N. Ahn, K. Kwak, M. S. Jang, H. Yoon, B. Y. Lee, J.-K. Lee, P. V. Pikhitsa, J. Byun, and M. Choi, "Trapped charge-driven degradation of perovskite solar cells", Nat. Commun. **7**, 1–9 (2016) (cit. on p. 2).

[94]C. Boyd, R. Cheacharoen, T. Leijtens, and M. D. McGehee, "Understanding Degradation Mechanisms and Improving Stability of Perovskite Photovoltaics", Chem. Rev. **119**, 3418–3451 (2019) (cit. on p. 2).

[95]R. Wang, M. Mujahid, Y. Duan, Z.-K. Wang, J. Xue, and Y. Yang, "A Review of Perovskites Solar Cell Stability", Adv. Funct. Mater. **29**, 1808843 (2019) (cit. on p. 2).

[96]L. Lanzetta, N. Aristidou, and S. A. Haque, "Stability of Lead and Tin Halide Perovskites: The Link between Defects and Degradation", J. Phys. Chem. Lett. **11**, 574–585 (2020) (cit. on p. 2).

[97]J. Wei, Q. Wang, J. Huo, F. Gao, Z. Gan, Q. Zhao, and H. Li, "Mechanisms and Suppression of Photoinduced Degradation in Perovskite Solar Cells", Adv. Energy Mater. **11**, 2002326 (2021) (cit. on p. 2).

[98]A. Fick, "Ueber Diffusion", Ann. Phys. **170**, 59–86 (1855) (cit. on pp. 3, 26).

[99]A. Einstein, "Zur Elektrodynamik bewegter Körper", Ann. Phys. **322**, 891–921 (1905) (cit. on pp. 3, 27).

[100]T. Fließbach, *Statistische Physik* (Springer, Berlin, Germany, 2018) (cit. on pp. 3, 26).

[101]S. M. Menke, W. A. Luhman, and R. J. Holmes, "Tailored exciton diffusion in organic photovoltaic cells for enhanced power conversion efficiency", Nat. Mater. **12**, 152–157 (2013) (cit. on p. 3).

[102] S. D. Stranks, G. E. Eperon, G. Grancini, C. Menelaou, M. J. P. Alcocer, T. Leijtens, L. M. Herz, A. Petrozza, and H. J. Snaith, "Electron-Hole Diffusion Lengths Exceeding 1 Micrometer in an Organometal Trihalide Perovskite Absorber", Science **342**, 341–344 (2013) (cit. on p. 3).

[103] S. M. Menke and R. J. Holmes, "Exciton diffusion in organic photovoltaic cells", Energy Environ. Sci. **7**, 499–512 (2014) (cit. on p. 3).

[104] E. Elahi, G. Dastgeer, A. S. Siddiqui, S. A. Patil, M. W. Iqbal, and P. R. Sharma, "A review on two-dimensional (2D) perovskite material-based solar cells to enhance the power conversion efficiency", Dalton Trans. **51**, 797–816 (2022) (cit. on p. 3).

[105] J. Even, L. Pedesseau, J.-M. Jancu, and C. Katan, "Importance of Spin–Orbit Coupling in Hybrid Organic/Inorganic Perovskites for Photovoltaic Applications", J. Phys. Chem. Lett. **4**, 2999 (2013) (cit. on p. 3).

[106] J. Even, L. Pedesseau, J.-M. Jancu, and C. Katan, "DFT and k · p Modelling of the Phase Transitions of Lead and Tin Halide Perovskites for Photovoltaic Cells", Phys. Status Solidi RRL **8**, 31 (2014) (cit. on p. 3).

[107] J. Even, L. Pedesseau, and C. Katan, "Analysis of Multivalley and Multibandgap Absorption and Enhancement of Free Carriers Related to Exciton Screening in Hybrid Perovskites", J. Phys. Chem. C **118**, 11566–11572 (2014) (cit. on p. 3).

[108] J. Even, L. Pedesseau, C. Katan, M. Kepenekian, J.-S. Lauret, D. Sapori, and E. Deleporte, "Solid-State Physics Perspective on Hybrid Perovskite Semiconductors", J. Phys. Chem. C **119**, 10161 (2015) (cit. on pp. 3, 14).

[109] K. Gauthron, J.-S. Lauret, L. Doyennette, G. Lanty, A. Al Choueiry, S. J. Zhang, A. Brehier, L. Largeau, O. Mauguin, and J. Bloch, "Optical Spectroscopy of Two-Dimensional Layered (C6H5C2H4-NH3)2-PbI4 Perovskite", Opt. Express **18**, 5912 (2010) (cit. on pp. 3, 25, 84, 108).

[110] D. B. Straus, S. Hurtado Parra, N. Iotov, J. Gebhardt, A. M. Rappe, J. E. Subotnik, J. M. Kikkawa, and C. R. Kagan, "Direct Observation of Electron-Phonon Coupling and Slow Vibrational Relaxation in Organic-Inorganic Hybrid Perovskites", J. Am. Chem. Soc. **138**, 13798–13801 (2016) (cit. on pp. 3, 14, 20, 25, 82).

[111] S. Neutzner, F. Thouin, D. Cortecchia, A. Petrozza, C. Silva, and A. R. Srimath Kandada, "Exciton-polaron spectral structures in two-dimensional hybrid lead-halide perovskites", Phys. Rev. Mater. **2**, 064605 (2018) (cit. on pp. 3, 25).

[112]F. Thouin, D. A. Valverde-Chávez, C. Quarti, D. Cortecchia, I. Bargigia, D. Beljonne, A. Petrozza, C. Silva, and A. R. Srimath Kandada, "Phonon coherences reveal the polaronic character of excitons in two-dimensional lead halide perovskites", Nat. Mater. **18**, 349–356 (2019) (cit. on pp. 3, 25).

[113]F. Thouin, D. Cortecchia, A. Petrozza, A. R. Srimath Kandada, and C. Silva, "Enhanced screening and spectral diversity in many-body elastic scattering of excitons in two-dimensional hybrid metal-halide perovskites", Phys. Rev. Res. **1**, 032032 (2019) (cit. on pp. 3, 25).

[114]M. Baranowski, S. J. Zelewski, M. Kepenekian, B. Traoré, J. M. Urban, A. Surrente, K. Galkowski, D. K. Maude, A. Kuc, E. P. Booker, R. Kudrawiec, S. D. Stranks, and P. Plochocka, "Phase-Transition-Induced Carrier Mass Enhancement in 2D Ruddlesden-Popper Perovskites", ACS Energy Lett. **4**, 2386–2392 (2019) (cit. on pp. 3, 13, 15, 25, 88, 93).

[115]C. Mauck, A. France-Lanord, A. C. Hernandez Oendra, N. S. Dahod, J. C. Grossman, and W. A. Tisdale, "Inorganic Cage Motion Dominates Excited-State Dynamics in 2D-Layered Perovskites (CxH2x+1NH3)2PbI4 (x = 4–9)", J. Phys. Chem. C **123**, 27904–27916 (2019) (cit. on pp. 3, 25, 84).

[116]A. R. Srimath Kandada and C. Silva, "Exciton Polarons in Two-Dimensional Hybrid Metal-Halide Perovskites", J. Phys. Chem. Lett. **11**, 3173–3184 (2020) (cit. on pp. 3, 25, 87, 108).

[117]D. B. Straus, S. Hurtado Parra, N. Iotov, Q. Zhao, M. R. Gau, P. J. Carroll, J. M. Kikkawa, and C. R. Kagan, "Tailoring Hot Exciton Dynamics in 2D Hybrid Perovskites through Cation Modification", ACS Nano **14**, 3621–3629 (2020) (cit. on pp. 3, 25).

[118]X. Chen, H. Lu, Z. Li, Y. Zhai, P. F. Ndione, J. J. Berry, K. Zhu, Y. Yang, and M. C. Beard, "Impact of Layer Thickness on the Charge Carrier and Spin Coherence Lifetime in Two-Dimensional Layered Perovskite Single Crystals", ACS Energy Lett. **3**, 2273–2279 (2018) (cit. on p. 3).

[119]H. Tsai, W. Nie, J.-C. Blancon, C. C. Stoumpos, C. M. M. Soe, J. Yoo, J. Crochet, S. Tretiak, J. Even, A. Sadhanala, G. Azzellino, R. Brenes, P. M. Ajayan, V. Bulović, S. D. Stranks, R. H. Friend, M. G. Kanatzidis, and A. D. Mohite, "Stable Light-Emitting Diodes Using Phase-Pure Ruddlesden-Popper Layered Perovskites", Adv. Mater. **30**, 1704217 (2018) (cit. on p. 3).

[120]Y. Liu, J. Cui, K. Du, H. Tian, Z. He, Q. Zhou, Z. Yang, Y. Deng, D. Chen, X. Zuo, Y. Ren, L. Wang, H. Zhu, B. Zhao, D. Di, J. Wang, R. H. Friend, and Y. Jin, "Efficient blue light-emitting diodes based on quantum-confined bromide perovskite nanostructures", Nat. Photonics **13**, 760–764 (2019) (cit. on p. 3).

[121]L. Gyongyosi and S. Imre, "A survey on quantum computing technology", Computer Science Review **31**, 51–71 (2019) (cit. on p. 3).

[122]H.-L. Huang, D. Wu, D. Fan, and X. Zhu, "Superconducting quantum computing: a review", Science China Information Sciences **63**, 1–32 (2020) (cit. on pp. 3, 106).

[123]N. P. de Leon, K. M. Itoh, D. Kim, K. K. Mehta, T. E. Northup, H. Paik, B. Palmer, N. Samarth, S. Sangtawesin, and D. Steuerman, "Materials challenges and opportunities for quantum computing hardware", Science **372**, eabb2823 (2021) (cit. on p. 3).

[124]I. Žutić, J. Fabian, and S. Das Sarma, "Spintronics: Fundamentals and applications", Rev. Mod. Phys. **76**, 323–410 (2004) (cit. on p. 3).

[125]D. D. Awschalom and M. E. Flatté, "Challenges for semiconductor spintronics", Nat. Phys. **3**, 153–159 (2007) (cit. on p. 3).

[126]F. Pulizzi, "Spintronics", Nat. Mater. **11**, 367 (2012) (cit. on p. 3).

[127]I. A. Walmsley, "Quantum optics: science and technology in a new light", Science **348**, 525–530 (2015) (cit. on p. 3).

[128]A. Maser, B. Gmeiner, T. Utikal, S. Götzinger, and V. Sandoghdar, "Few-photon coherent nonlinear optics with a single molecule", Nat. Photonics **10**, 450–453 (2016) (cit. on p. 3).

[129]Z. Ying, C. Feng, Z. Zhao, S. Dhar, H. Dalir, J. Gu, Y. Cheng, R. Soref, D. Z. Pan, and R. T. Chen, "Electronic-photonic arithmetic logic unit for high-speed computing", Nat. Commun. **11**, 1–9 (2020) (cit. on p. 3).

[130]A. V. Zasedatelev, A. V. Baranikov, D. Sannikov, D. Urbonas, F. Scafirimuto, V. Y. Shishkov, E. S. Andrianov, Y. E. Lozovik, U. Scherf, T. Stöferle, R. F. Mahrt, and P. G. Lagoudakis, "Single-photon nonlinearity at room temperature", Nature **597**, 493–497 (2021) (cit. on p. 3).

[131]G. P. Agrawal, "Nonlinear fiber optics: its history and recent progress", JOSA B **28**, A1–A10 (2011) (cit. on p. 3).

[132]G. P. Agrawal, "Optical communication: its history and recent progress", Optics in our time, 177–199 (2016) (cit. on p. 3).

[133]A. A. High, E. E. Novitskaya, L. V. Butov, M. Hanson, and A. C. Gossard, "Control of Exciton Fluxes in an Excitonic Integrated Circuit", Science **321**, 229–231 (2008) (cit. on pp. 3, 106).

[134]Y. Y. Kuznetsova, M. Remeika, A. A. High, A. T. Hammack, L. V. Butov, M. Hanson, and A. C. Gossard, "All-optical excitonic transistor", Opt. Lett. **35**, 1587–1589 (2010) (cit. on pp. 3, 106).

[135]Novoselov K.S. Geim A.K. Morozov S.V. Jiang D Zhang Y Dubonos S.V. Grigorieva I.V. Firsov A.A, "Electric Field Effect in Atomically Thin Carbon Films", Science **306**, 666–669 (2004) (cit. on pp. 3, 8).

[136]K. S. Novoselov, D. Jiang, F. Schedin, T. J. Booth, V. V. Khotkevich, S. V. Morozov, and A. K. Geim, "Two-dimensional atomic crystals.", Proc. Natl. Acad. Sci. USA **102**, 10451–10453 (2005) (cit. on pp. 3, 8).

[137]K. S. Novoselov, A. K. Geim, S. V. Morozov, D. Jiang, M. I. Katsnelson, I. V. Grigorieva, S. V. Dubonos, and A. A. Firsov, "Two-dimensional gas of massless Dirac fermions in graphene", Nature **438**, 197–200 (2005) (cit. on p. 3).

[138]A. K. Geim and I. V. Grigorieva, "Van der Waals heterostructures", Nature **499**, 419–425 (2013) (cit. on p. 4).

[139]Y. Liu, N. O. Weiss, X. Duan, H.-C. Cheng, Y. Huang, and X. Duan, "Van der Waals heterostructures and devices", Nat. Rev. Mater. **1**, 1–17 (2016) (cit. on p. 4).

[140]R. Frisenda, Y. Niu, P. Gant, M. Muñoz, and A. Castellanos-Gomez, "Naturally occurring van der Waals materials", npj 2D Mater. Appl. **4**, 1–13 (2020) (cit. on p. 4).

[141]L. Wang, I. Meric, P. Y. Huang, Q. Gao, Y. Gao, H. Tran, T. Taniguchi, K. Watanabe, L. M. Campos, D. a. Muller, J. Guo, P. Kim, J. Hone, K. L. Shepard, and C. R. Dean, "One-dimensional electrical contact to a two-dimensional material.", Science **342**, 614–617 (2013) (cit. on pp. 4, 39).

[142]A. Castellanos-Gomez, L. Vicarelli, E. Prada, J. O. Island, K. L. Narasimha-Acharya, S. I. Blanter, D. J. Groenendijk, M. Buscema, G. a. Steele, J. V. Alvarez, H. W. Zandbergen, J. J. Palacios, and H. S. J. van der Zant, "Isolation and characterization of few-layer black phosphorus", 2D Mater. **1**, 25001 (2014) (cit. on p. 4).

[143]D. G. Purdie, N. M. Pugno, T. Taniguchi, K. Watanabe, A. C. Ferrari, and A. Lombardo, "Cleaning interfaces in layered materials heterostructures", Nat. Commun. **9**, 1–12 (2018) (cit. on pp. 4, 39, 46).

[144]Q. Zhao, T. Wang, Y. K. Ryu, R. Frisenda, and A. Castellanos-Gomez, "An inexpensive system for the deterministic transfer of 2D materials", J. Phys.: Mater. **3**, 016001 (2020) (cit. on p. 4).

[145]K. Tran, G. Moody, F. Wu, X. Lu, J. Choi, K. Kim, A. Rai, D. A. Sanchez, J. Quan, A. Singh, J. Embley, A. Zepeda, M. Campbell, T. Autry, T. Taniguchi, K. Watanabe, N. Lu, S. K. Banerjee, K. L. Silverman, S. Kim, E. Tutuc, L. Yang, A. H. MacDonald, and X. Li, "Evidence for moiré excitons in van der Waals heterostructures", Nature **567**, 71–75 (2019) (cit. on p. 4).

[146]S. Carr, S. Fang, and E. Kaxiras, "Electronic-structure methods for twisted moiré layers", Nat. Rev. Mater. **5**, 748–763 (2020) (cit. on p. 4).

[147]H. Baek, M. Brotons-Gisbert, Z. X. Koong, A. Campbell, M. Rambach, K. Watanabe, T. Taniguchi, and B. D. Gerardot, "Highly energy-tunable quantum light from moiré-trapped excitons", Sci. Adv. **6**, eaba8526 (2020) (cit. on p. 4).

[148]L. J. McGilly, A. Kerelsky, N. R. Finney, K. Shapovalov, E.-M. Shih, A. Ghiotto, Y. Zeng, S. L. Moore, W. Wu, Y. Bai, K. Watanabe, T. Taniguchi, M. Stengel, L. Zhou, J. Hone, X. Zhu, D. N. Basov, C. Dean, C. E. Dreyer, and A. N. Pasupathy, "Visualization of moiré superlattices", Nat. Nanotechnol. **15**, 580–584 (2020) (cit. on p. 4).

[149]E. Y. Andrei, D. K. Efetov, P. Jarillo-Herrero, A. H. MacDonald, K. F. Mak, T. Senthil, E. Tutuc, A. Yazdani, and A. F. Young, "The marvels of moiré materials", Nat. Rev. Mater. **6**, 201–206 (2021) (cit. on p. 4).

[150]C. N. Lau, M. W. Bockrath, K. F. Mak, and F. Zhang, "Reproducibility in the fabrication and physics of moiré materials", Nature **602**, 41–50 (2022) (cit. on p. 4).

[151]K. F. Mak and J. Shan, "Semiconductor moiré materials", Nat. Nanotechnol. **17**, 686–695 (2022) (cit. on p. 4).

[152]E. C. Regan, "Mott and generalized wigner crystal states in wse2/ws2 moiré superlattices", Nature **579**, 10.1038/s41586-020-2092-4 (2020) (cit. on p. 4).

[153]T. Smoleński, P. E. Dolgirev, C. Kuhlenkamp, A. Popert, Y. Shimazaki, P. Back, X. Lu, M. Kroner, K. Watanabe, T. Taniguchi, I. Esterlis, E. Demler, and A. Imamoğlu, "Signatures of Wigner crystal of electrons in a monolayer semiconductor", Nature **595**, 53–57 (2021) (cit. on p. 4).

[154]S. Miao, T. Wang, X. Huang, D. Chen, Z. Lian, C. Wang, M. Blei, T. Taniguchi, K. Watanabe, S. Tongay, Z. Wang, D. Xiao, Y.-T. Cui, and S.-F. Shi, "Strong interaction between interlayer excitons and correlated electrons in WSe2/WS2 moiré superlattice", Nat. Commun. **12**, 1–6 (2021) (cit. on p. 4).

[155]H. Li, S. Li, E. C. Regan, D. Wang, W. Zhao, S. Kahn, K. Yumigeta, M. Blei, T. Taniguchi, K. Watanabe, S. Tongay, A. Zettl, M. F. Crommie, and F. Wang, "Imaging two-dimensional generalized Wigner crystals", Nature **597**, 650–654 (2021) (cit. on pp. 4, 14).

[156]F. Wu, T. Lovorn, E. Tutuc, and A. H. MacDonald, "Hubbard model physics in transition metal dichalcogenide moiré bands", Phys. Rev. Lett. **121**, 10.1103/PhysRevLett.121.026402 (2018) (cit. on p. 4).

[157]L. Wang, "Correlated electronic phases in twisted bilayer transition metal dichalcogenides", Nat. Mater. **19**, 10.1038/s41563-020-0708-6 (2020) (cit. on p. 4).

[158]Y. Xu, "Correlated insulating states at fractional fillings of moiré superlattices", Nature **587**, 10.1038/s41586-020-2868-6 (2020) (cit. on pp. 4, 19).

[159]L. Balents, C. R. Dean, D. K. Efetov, and A. F. Young, "Superconductivity and strong correlations in moiré flat bands", Nat. Phys. **16**, 10.1038/s41567-020-0906-9 (2020) (cit. on p. 4).

[160]Y. Zhang, N. F. Q. Yuan, and L. Fu, "Moiré quantum chemistry: charge transfer in transition metal dichalcogenide superlattices", Phys. Rev. B **102**, 10.1103/PhysRevB.102.201115 (2020) (cit. on p. 4).

[161]H. Pan, F. Wu, and S. Sarma, "Quantum phase diagram of a moiré-hubbard model", Phys. Rev. B **102**, 10.1103/PhysRevB.102.201104 (2020) (cit. on p. 4).

[162]N. Morales-Durán, P. Potasz, and A. H. MacDonald, "Metal-insulator transition in transition metal dichalcogenide heterobilayer moiré superlattices", Phys. Rev. B **103**, 10.1103/PhysRevB.103.L241110 (2021) (cit. on p. 4).

[163]Y. Tang, "Simulation of hubbard model physics in wse2/ws2 moiré superlattices", Nature **579**, 10.1038/s41586-020-2085-3 (2020) (cit. on p. 4).

[164]C. Jin, "Stripe phases in wse2/ws2 moiré superlattices", Nat. Mater. **20**, 10.1038/s41563-021-00959-8 (2021) (cit. on p. 4).

[165]H. Pan and S. Sarma, "Interaction-driven filling-induced metal-insulator transition in 2d moiré lattices", Phys. Rev. Lett. **127**, 10.1103/PhysRevLett.127.096802 (2021) (cit. on p. 4).

[166]X. Huang, "Correlated insulating states at fractional fillings of the ws2/wse2 moiré lattice", Nat. Phys. **17**, 10.1038/s41567-021-01171-w (2021) (cit. on pp. 4, 108).

[167]A. Wietek, R. Rossi, F. Šimkovic, M. Klett, P. Hansmann, M. Ferrero, E. M. Stoudenmire, T. Schäfer, and A. Georges, "Mott Insulating States with Competing Orders in the Triangular Lattice Hubbard Model", Phys. Rev. X **11**, 041013 (2021) (cit. on p. 4).

[168]Y. Lin, X. Ling, L. Yu, S. Huang, A. L. Hsu, Y.-H. Lee, J. Kong, M. S. Dresselhaus, and T. Palacios, "Dielectric screening of excitons and trions in single-layer mos2", Nano letters **14**, 5569–5576 (2014) (cit. on p. 4).

[169]I. Kylänpää and H.-P. Komsa, "Binding energies of exciton complexes in transition metal dichalcogenide monolayers and effect of dielectric environment", Physical Review B **92**, 205418 (2015) (cit. on p. 4).

[170]M. Rösner, C. Steinke, M. Lorke, C. Gies, F. Jahnke, and T. O. Wehling, "Two-Dimensional Heterojunctions from Nonlocal Manipulations of the Interactions", Nano Letters **16**, 2322–2327 (2016) (cit. on pp. 4, 19, 106).

[171]A. Raja, A. Chaves, J. Yu, G. Arefe, H. M. Hill, A. F. Rigosi, T. C. Berkelbach, P. Nagler, C. Schüller, T. Korn, et al., "Coulomb engineering of the bandgap and excitons in two-dimensional materials", Nature communications **8**, 1–7 (2017) (cit. on pp. 4, 16, 19, 60, 106).

[172]K. T. Winther and K. S. Thygesen, "Band structure engineering in van der Waals heterostructures via dielectric screening: the G$\Delta$W method", 2D Materials **4**, 25059 (2017) (cit. on pp. 4, 16, 19, 60).

[173]A. Raja, L. Waldecker, J. Zipfel, Y. Cho, S. Brem, J. D. Ziegler, M. Kulig, T. Taniguchi, K. Watanabe, E. Malic, T. F. Heinz, T. C. Berkelbach, and A. Chernikov, "Dielectric disorder in two-dimensional materials", Nature Nanotechnology **14**, 832–837 (2019) (cit. on pp. 4, 16, 19, 39, 60).

[174]A. C. Riis-Jensen, J. Lu, and K. S. Thygesen, "Electrically controlled dielectric band gap engineering in a two-dimensional semiconductor", Phys. Rev. B **101**, 121110 (2020) (cit. on pp. 4, 19, 106).

[175]A. Popert, Y. Shimazaki, M. Kroner, K. Watanabe, T. Taniguchi, A. Imamoğlu, and T. Smoleński, "Optical sensing of fractional quantum Hall effect in graphene", arXiv, 10.48550/arXiv.2111.12887 (2021) (cit. on pp. 4, 19).

[176]Y. Xu, K. Kang, K. Watanabe, T. Taniguchi, K. F. Mak, and J. Shan, "A tunable bilayer Hubbard model in twisted WSe2", Nat. Nanotechnol. **17**, 934–939 (2022) (cit. on p. 4).

[177]D. Unuchek, A. Ciarrocchi, A. Avsar, K. Watanabe, T. Taniguchi, and A. Kis, "Room-temperature electrical control of exciton flux in a van der waals heterostructure", Nature **560**, 340–344 (2018) (cit. on pp. 4, 106).

[178]D. Unuchek, A. Ciarrocchi, A. Avsar, Z. Sun, K. Watanabe, T. Taniguchi, and A. Kis, "Valley-polarized exciton currents in a van der Waals heterostructure", Nat. Nanotechnol. **14**, 1104–1109 (2019) (cit. on pp. 4, 106).

[179]A. Ciarrocchi, F. Tagarelli, A. Avsar, and A. Kis, "Excitonic devices with van der Waals heterostructures: valleytronics meets twistronics", Nat. Rev. Mater. **7**, 449–464 (2022) (cit. on pp. 4, 106).

[180]D. N. Shanks, F. Mahdikhanysarvejahany, T. G. Stanfill, M. R. Koehler, D. G. Mandrus, T. Taniguchi, K. Watanabe, B. J. LeRoy, and J. R. Schaibley, "Interlayer Exciton Diode and Transistor", Nano Lett. **22**, 6599–6605 (2022) (cit. on pp. 4, 106).

[181]S.-i. Kuga, S. Murakami, and N. Nagaosa, "Spin Hall effect of excitons", Phys. Rev. B **78**, 205201 (2008) (cit. on p. 4).

[182]Y.-M. Li, J. Li, L.-K. Shi, D. Zhang, W. Yang, and K. Chang, "Light-Induced Exciton Spin Hall Effect in van der Waals Heterostructures", Phys. Rev. Lett. **115**, 166804 (2015) (cit. on pp. 4, 106).

[183]T. Yu and M. W. Wu, "Valley depolarization dynamics and valley Hall effect of excitons in monolayer and bilayer $MoS_2$", Phys. Rev. B **93**, 045414 (2016) (cit. on p. 4).

[184]M. Onga, Y. Zhang, T. Ideue, and Y. Iwasa, "Exciton Hall effect in monolayer MoS2", Nat. Mater. **16**, 1193–1197 (2017) (cit. on p. 4).

[185]Z. Huang, Y. Liu, K. Dini, Q. Tan, Z. Liu, H. Fang, J. Liu, T. Liew, and W. Gao, "Robust Room Temperature Valley Hall Effect of Interlayer Excitons", Nano Lett. **20**, 1345–1351 (2020) (cit. on p. 4).

[186]N. Lundt, Ł. Dusanowski, E. Sedov, P. Stepanov, M. M. Glazov, S. Klembt, M. Klaas, J. Beierlein, Y. Qin, S. Tongay, M. Richard, A. V. Kavokin, S. Höfling, and C. Schneider, "Optical valley Hall effect for highly valley-coherent exciton-polaritons in an atomically thin semiconductor", Nat. Nanotechnol. **14**, 770–775 (2019) (cit. on pp. 4, 106).

[187]B. L. Evans and P. A. Young, "Exciton spectra in thin crystals: the diamagnetic effect", **91**, 10.1088/0370-1328/91/2/327 (1967) (cit. on p. 7).

[188]J. A. Wilson and A. D. Yoffe, "The transition metal dichalcogenides discussion and interpretation of the observed optical, electrical and structural properties", Advances in Physics **18**, 193–335 (1969) (cit. on pp. 7–9).

[189]R. G. Dickinson and L. Pauling, "THE CRYSTAL STRUCTURE OF MOLYBDENITE", Journal of the American Chemical Society **45**, 1466–1471 (1923) (cit. on p. 7).

[190]G.-b. Liu, D. Xiao, Y. Yao, X. Xu, and W. Yao, "Electronic structures and theoretical modelling of two-dimensional group-VIB transition metal dichalcogenides", Chem. Soc. Rev. **44**, 2643–2663 (2015) (cit. on p. 8).

[191]G. Eda, T. Fujita, H. Yamaguchi, D. Voiry, M. Chen, and M. Chhowalla, "Coherent Atomic and Electronic Heterostructures of Single-Layer MoS2", ACS Nano **6**, 7311–7317 (2012) (cit. on p. 8).

[192]W. Yao, D. Xiao, and Q. Niu, "Valley-dependent optoelectronics from inversion symmetry breaking", Physical Review B **77**, 10.1103/physrevb.77.235406 (2008) (cit. on pp. 8, 10).

[193]R. Suzuki, M. Sakano, Y. J. Zhang, R. Akashi, D. Morikawa, A. Harasawa, K. Yaji, K. Kuroda, K. Miyamoto, T. Okuda, K. Ishizaka, R. Arita, and Y. Iwasa, "Valley-dependent spin polarization in bulk MoS2 with broken inversion symmetry", Nature Nanotechnology **9**, 611–617 (2014) (cit. on p. 8).

[194]L. F. Mattheiss, "Energy Bands for 2H-$NbSe_2$ and 2H-$MoS_2$", Phys. Rev. Lett. **30**, 784–787 (1973) (cit. on p. 9).

[195]L. F. Mattheiss, "Band Structures of Transition-Metal-Dichalcogenide Layer Compounds", Phys. Rev. B **8**, 3719–3740 (1973) (cit. on p. 9).

[196]M. Liu, M. B. Johnston, and H. J. Snaith, "Efficient planar heterojunction perovskite solar cells by vapour deposition", Nature, 10.1038/nature12509 (2013) (cit. on p. 9).

[197]R. A. Bromley, R. B. Murray, and A. D. Yoffe, "The band structures of some transition metal dichalcogenides. III. Group VIA: trigonal prism materials", Journal of Physics C: Solid State Physics **5**, 759–778 (1972) (cit. on p. 9).

[198]R. F. Frindt, "The optical properties of single crystals of WSe2 and MoTe2", Journal of Physics and Chemistry of Solids **24**, 1107–1108 (1963) (cit. on p. 9).

[199]K. F. Mak, C. Lee, J. Hone, J. Shan, and T. F. Heinz, "Atomically thin $MoS_2$: A new direct-gap semiconductor", Phys. Rev. Lett. **105**, 136805 (2010) (cit. on p. 9).

[200]A. Splendiani, L. Sun, Y. Zhang, T. Li, J. Kim, C.-Y. Chim, G. Galli, and F. Wang, "No Title", Nano Letters **10**, 1271–1275 (2010) (cit. on pp. 9–10).

[201]A. Kuc, N. Zibouche, and T. Heine, "Influence of quantum confinement on the electronic structure of the transition metal sulfide $TS_2$", Phys. Rev. B **83**, 245213 (2011) (cit. on p. 9).

[202]W. S. Yun, S. W. Han, S. C. Hong, I. G. Kim, and J. D. Lee, "Thickness and strain effects on electronic structures of transition metal dichalcogenides: 2H-$MX_2$ semiconductors (M = Mo, W; X = S, Se, Te)", Phys. Rev. B **85**, 33305 (2012) (cit. on p. 9).

[203]W. Zhao, Z. Ghorannevis, L. Chu, M. Toh, C. Kloc, P.-H. Tan, and G. Eda, "Evolution of electronic structure in atomically thin sheets of $WS_2$ and $WSe_2$.", ACS Nano **7**, 791–797 (2013) (cit. on p. 9).

[204]Z. Y. Zhu, Y. C. Cheng, and U. Schwingenschlögl, "Giant spin-orbit-induced spin splitting in two-dimensional transition-metal dichalcogenide semiconductors", Phys. Rev. B **84**, 153402 (2011) (cit. on pp. 9–10).

[205]A. Kormányos, G. Burkard, M. Gmitra, J. Fabian, V. Zólyomi, N. D. Drummond, and V. Falko, "K· p theory for two-dimensional transition metal dichalcogenide semiconductors", 2D Materials **2**, 22001 (2015) (cit. on pp. 9–10, 76).

[206]D. Xiao, G.-B. Liu, W. Feng, X. Xu, and W. Yao, "Coupled spin and valley physics in monolayers of MoS 2 and other group-VI dichalcogenides", **108**, 196802 (2012) (cit. on p. 10).

[207]A. Kormányos, V. Zólyomi, N. D. Drummond, and G. Burkard, "Spin-Orbit Coupling, Quantum Dots, and Qubits in Monolayer Transition Metal Dichalcogenides", Phys. Rev. X **4**, 11034 (2014) (cit. on p. 10).

[208]H. Wang, C. Zhang, and F. Rana, "Ultrafast Dynamics of Defect-Assisted Electron-Hole Recombination in Monolayer MoS 2", Nano Lett. **15**, 339–345 (2015) (cit. on p. 10).

[209]A. Arora, M. Koperski, K. Nogajewski, J. Marcus, C. Faugeras, and M. Potemski, "Excitonic resonances in thin films of WSe <sub>2</sub> : from monolayer to bulk material", Nanoscale **7**, 10421–10429 (2015) (cit. on p. 10).

[210]F. Withers, O. Del Pozo-Zamudio, S. Schwarz, S. Dufferwiel, P. M. Walker, T. Godde, A. P. Rooney, A. Gholinia, C. R. Woods, P. Blake, S. J. Haigh, K. Watanabe, T. Taniguchi, I. L. Aleiner, A. K. Geim, V. I. Fal'ko, A. I. Tartakovskii, and K. S. Novoselov, "WSe2 Light-Emitting Tunneling Transistors with Enhanced Brightness at Room Temperature", Nano Letters **15**, 8223–8228 (2015) (cit. on p. 10).

[211]T. Cao, G. Wang, W. Han, H. Ye, C. Zhu, J. Shi, Q. Niu, P. Tan, E. Wang, B. Liu, and J. Feng, "Valley-selective circular dichroism of monolayer molybdenum disulphide", Nature Communications **3**, 887 (2012) (cit. on p. 10).

[212]K. F. Mak, K. He, J. Shan, and T. F. Heinz, "Control of valley polarization in monolayer MoS 2 by optical helicity", Nature Nanotechnology **7**, 494 (2012) (cit. on p. 10).

[213]M. D. Graef and M. E. McHenry, *Structure of Materials: An Introduction to Crystallography, Diffraction, and Symmetry*, 2nd (Cambridge Univ. Press, 2012) (cit. on p. 11).

[214]J. Hwang, R. R. Rao, L. Giordano, Y. Katayama, Y. Yu, and Y. Shao-Horn, "Perovskites in catalysis and electrocatalysis", Science **358**, 751–756 (2017) (cit. on p. 11).

[215]F. Brivio, J. M. Frost, J. M. Skelton, A. J. Jackson, O. J. Weber, M. T. Weller, A. R. Gonñi, A. M. A. Leguy, P. R. F. Barnes, and A. Walsh, "Lattice dynamics and vibrational spectra of the orthorhombic, tetragonal, and cubic phases of methylammonium lead iodide", Phys. Rev. B **92**, 144308 (2015) (cit. on p. 11).

[216]J. Yin, P. Maity, L. Xu, A. M. El-Zohry, H. Li, O. M. Bakr, J.-L. Breédas, and O. F. Mohammed, "Layer-Dependent Rashba Band Splitting in 2D Hybrid Perovskites", Chem. Mater. **30**, 8538–8545 (2018) (cit. on p. 11).

[217]R. Lin, J. Xu, M. Wei, Y. Wang, Z. Qin, Z. Liu, J. Wu, K. Xiao, B. Chen, S. M. Park, G. Chen, H. R. Atapattu, K. R. Graham, J. Xu, J. Zhu, L. Li, C. Zhang, E. H. Sargent, and H. Tan, "All-perovskite tandem solar cells with improved grain surface passivation", Nature **603**, 73–78 (2022) (cit. on p. 11).

[218]W. Nie, H. Tsai, R. Asadpour, J.-C. Blancon, A. J. Neukirch, G. Gupta, J. J. Crochet, M. Chhowalla, S. Tretiak, M. A. Alam, H.-L. Wang, and A. D. Mohite, "High-efficiency solution-processed perovskite solar cells with millimeter-scale grains", Science **347**, 522–525 (2015) (cit. on p. 11).

[219]E. Jokar, C.-H. Chien, C.-M. Tsai, A. Fathi, and E. W.-G. Diau, "Robust Tin-Based Perovskite Solar Cells with Hybrid Organic Cations to Attain Efficiency Approaching 10%", Advanced Materials **31**, 1804835 (2019) (cit. on p. 12).

[220]R. Wang, M. Mujahid, Y. Duan, Z.-K. Wang, J. Xue, and Y. Yang, "A Review of Perovskites Solar Cell Stability", Advanced Functional Materials **29**, 1808843 (2019) (cit. on p. 12).

[221]V. M. Goldschmidt, "Crystal structure and chemical constitution", Trans. Faraday Soc. **25**, 253–283 (1929) (cit. on p. 12).

[222]G. Kieslich, S. Sun, and A. K. Cheetham, "An extended Tolerance Factor approach for organic–inorganic perovskites", Chem. Sci. **6**, 3430–3433 (2015) (cit. on p. 12).

[223]C. Katan, N. Mercier, and J. Even, "Quantum and Dielectric Confinement Effects in Lower-Dimensional Hybrid Perovskite Semiconductors", Chemical Reviews **119**, 3140–3192 (2019) (cit. on p. 12).

[224]M. P. Hautzinger, J. Dai, Y. Ji, Y. Fu, J. Chen, I. A. Guzei, J. C. Wright, Y. Li, and S. Jin, "Two-Dimensional Lead Halide Perovskites Templated by a Conjugated Asymmetric Diammonium", Inorg. Chem. **56**, 14991 (2017) (cit. on p. 12).

[225]L. Mao, W. Ke, L. Pedesseau, Y. Wu, C. Katan, J. Even, M. R. Wasielewski, C. C. Stoumpos, and M. G. Kanatzidis, "Hybrid Dion–Jacobson 2D Lead Iodide Perovskites", J. Am. Chem. Soc. **140**, 3775 (2018) (cit. on p. 12).

[226]J.-C. Blancon, A. V. Stier, H. Tsai, W. Nie, C. C. Stoumpos, B. Traore, L. Pedesseau, M. Kepenekian, F. Katsutani, G. T. Noe, J. Kono, S. Tretiak, S. A. Crooker, C. Katan, M. G. Kanatzidis, J. J. Crochet, J. Even, and A. D. Mohite, "Scaling law for excitons in 2D perovskite quantum wells", Nature Communications **9**, 2254 (2018) (cit. on pp. 13–14, 18, 24, 90, 92, 101, 109).

[227]D. G. Billing and A. Lemmerer, "Synthesis, characterization and phase transitions in the inorganic-organic layered perovskite-type hybrids [(CnH2n+1 NH3) 2PbI4], n = 4, 5 and 6", Acta Crystallogr., Sect. B: Struct. Sci. **63**, 5 (2007) (cit. on pp. 13–15, 88).

[228]J. Gebhardt, Y. Kim, and A. M. Rappe, "Influence of the Dimensionality and Organic Cation on Crystal and Electronic Structure of Organometallic Halide Perovskites", J. Phys. Chem. C **121**, 6569–6574 (2017) (cit. on p. 14).

[229]B. Traore, L. Pedesseau, L. Assam, X. Che, J.-C. Blancon, H. Tsai, W. Nie, C. C. Stoumpos, M. G. Kanatzidis, S. Tretiak, A. D. Mohite, J. Even, M. Kepenekian, and C. Katan, "Composite Nature of Layered Hybrid Perovskites: Assessment on Quantum and Dielectric Confinements and Band Alignment", ACS Nano **12**, 3321–3332 (2018) (cit. on pp. 14–15, 88).

[230]D. G. Billing and A. Lemmerer, "Synthesis, characterization and phase transitions of the inorganicorganic layered perovskite-type hybrids [(CnH2n1 NH3)2 PbI4] (n = 12, 14, 16 and 18)", New Journal of Chemistry **32**, 1736 (2008) (cit. on p. 14).

[231]X. Xiao, M. Wu, Z. Ni, S. Xu, S. Chen, J. Hu, P. N. Rudd, W. You, and J. Huang, "Ultrafast Exciton Transport with a Long Diffusion Length in Layered Perovskites with Organic Cation Functionalization", Adv. Mater. **32**, 2004080 (2020) (cit. on pp. 14, 77, 80, 107–108).

[232]C. C. Stoumpos, D. H. Cao, D. J. Clark, J. Young, J. M. Rondinelli, J. I. Jang, J. T. Hupp, and M. G. Kanatzidis, "Ruddlesden-Popper Hybrid Lead Iodide Perovskite 2D Homologous Semiconductors", Chem. Mater. **28**, 2852–2867 (2016) (cit. on p. 14).

[233]H. Tsai, W. Nie, J.-C. Blancon, C. C. Stoumpos, R. Asadpour, B. Harutyunyan, A. J. Neukirch, R. Verduzco, J. J. Crochet, S. Tretiak, L. Pedesseau, J. Even, M. A. Alam, G. Gupta, J. Lou, P. M. Ajayan, M. J. Bedzyk, M. G. Kanatzidis, and A. D. Mohite, "High-efficiency two-dimensional Ruddlesden-Popper perovskite solar cells", Nature **536**, 312–316 (2016) (cit. on p. 14).

[234]J.-C. Blancon, H. Tsai, W. Nie, C. C. Stoumpos, L. Pedesseau, C. Katan, M. Kepenekian, C. M. M. Soe, K. Appavoo, M. Y. Sfeir, S. Tretiak, P. M. Ajayan, M. G. Kanatzidis, J. Even, J. J. Crochet, and A. D. Mohite, "Extremely efficient internal exciton dissociation through edge states in layered 2D perovskites", Science **355**, 1288–1292 (2017) (cit. on p. 14).

[235]S. Deng, E. Shi, L. Yuan, L. Jin, L. Dou, and L. Huang, "Long-range exciton transport and slow annihilation in two-dimensional hybrid perovskites", Nature Communications **11**, 664 (2020) (cit. on pp. 14, 78, 80, 107).

[236]J. Even, L. Pedesseau, M.-A. Dupertuis, J.-M. Jancu, and C. Katan, "Electronic model for self-assembled hybrid organic/perovskite semiconductors: Reverse band edge electronic states ordering and spin-orbit coupling", Physical Review B **86**, 10.1103/physrevb.86.205301 (2012) (cit. on p. 14).

[237]Y. Rakita, S. R. Cohen, N. K. Kedem, G. Hodes, and D. Cahen, "Mechanical properties of APbX3 (A = Cs or CH3NH3; X = I or Br) perovskite single crystals", MRS Communications **5**, 623–629 (2015) (cit. on p. 14).

[238]T. Baikie, N. S. Barrow, Y. Fang, P. J. Keenan, P. R. Slater, R. O. Piltz, M. Gutmann, S. G. Mhaisalkar, and T. J. White, "A combined single crystal neutron/X-ray diffraction and solid-state nuclear magnetic resonance study of

the hybrid perovskites CH 3 NH 3 PbX 3 (X = I, Br and Cl)", J. Mater. Chem. A **3**, 9298–9307 (2015) (cit. on p. 14).

[239] S. Sun, Y. Fang, G. Kieslich, T. J. White, and A. K. Cheetham, "Mechanical properties of organic–inorganic halide perovskites, CH 3 NH 3 PbX 3 (X = I, Br and Cl), by nanoindentation", J. Mater. Chem. A **3**, 18450–18455 (2015) (cit. on p. 14).

[240] A. Létoublon, S. Paofai, B. Rufflé, P. Bourges, B. Hehlen, T. Michel, C. Ecolivet, O. Durand, S. Cordier, C. Katan, and J. Even, "Elastic Constants, Optical Phonons, and Molecular Relaxations in the High Temperature Plastic Phase of the CH3NH3PbBr3 Hybrid Perovskite", The Journal of Physical Chemistry Letters **7**, 3776–3784 (2016) (cit. on p. 14).

[241] A. N. Beecher, O. E. Semonin, J. M. Skelton, J. M. Frost, M. W. Terban, H. Zhai, A. Alatas, J. S. Owen, A. Walsh, and S. J. L. Billinge, "Direct Observation of Dynamic Symmetry Breaking above Room Temperature in Methylammonium Lead Iodide Perovskite", ACS Energy Lett. **1**, 880–887 (2016) (cit. on p. 15).

[242] O. Yaffe, Y. Guo, L. Z. Tan, D. A. Egger, T. Hull, C. C. Stoumpos, F. Zheng, T. F. Heinz, L. Kronik, M. G. Kanatzidis, J. S. Owen, A. M. Rappe, M. A. Pimenta, and L. E. Brus, "Local Polar Fluctuations in Lead Halide Perovskite Crystals", Physical Review Letters **118**, 10.1103/physrevlett.118.136001 (2017) (cit. on p. 15).

[243] H. Haug, *Quantum Theory Of The Optical And Electronic Properties Of Semiconductors (5Th Edition)* (Wspc, 2009) (cit. on p. 16).

[244] C. Klingshirn, *Semiconductor Optics*, 3rd (Springer, Berlin Heidelberg New York, 2007) (cit. on pp. 16–17, 20, 50).

[245] R. Gross and A. Marx, *Festkörperphysik* (Oldenbourg Wissenschaftsverlag, Aug. 2014) (cit. on pp. 16–17).

[246] A. Chernikov, T. C. Berkelbach, H. M. Hill, A. Rigosi, Y. Li, O. B. Aslan, D. R. Reichman, M. S. Hybertsen, and T. F. Heinz, "Exciton binding energy and nonhydrogenic Rydberg series in monolayer WS2", Physical review letters **113**, 76802 (2014) (cit. on pp. 16, 18–19).

[247] M. M. Ugeda, A. J. Bradley, S.-F. Shi, H. Felipe, Y. Zhang, D. Y. Qiu, W. Ruan, S.-K. Mo, Z. Hussain, Z.-X. Shen, et al., "Giant bandgap renormalization and excitonic effects in a monolayer transition metal dichalcogenide semiconductor", Nature materials **13** (2014) (cit. on p. 16).

[248] G. H. Wannier, "The structure of electronic excitation levels in insulating crystals", Physical Review **52**, 191 (1937) (cit. on p. 16).

[249] S. Dong, M. Puppin, T. Pincelli, S. Beaulieu, D. Christiansen, H. Hübener, C. W. Nicholson, R. P. Xian, M. Dendzik, Y. Deng, Y. W. Windsor, M. Selig, E. Malic, A. Rubio, A. Knorr, M. Wolf, L. Rettig, and R. Ernstorfer, "Direct measurement of key exciton properties: energy, dynamics, and spatial distribution of the wave function", Natural Sciences **1**, e10010 (2021) (cit. on pp. 17–18).

[250] G. Wang, A. Chernikov, M. M. Glazov, T. F. Heinz, X. Marie, T. Amand, and B. Urbaszek, "Colloquium : Excitons in atomically thin transition metal dichalcogenides", Reviews of Modern Physics **90**, 21001 (2018) (cit. on pp. 17, 21).

[251] M. K. L. Man, J. Madéo, C. Sahoo, K. Xie, M. Campbell, V. Pareek, A. Karmakar, E. L. Wong, A. Al-Mahboob, N. S. Chan, D. R. Bacon, X. Zhu, M. M. M. Abdelrasoul, X. Li, T. F. Heinz, F. H. da Jornada, T. Cao, and K. M. Dani, "Experimental measurement of the intrinsic excitonic wave function", Science Advances **7**, eabg0192 (2021) (cit. on p. 18).

[252] A. V. Stier, N. P. Wilson, G. Clark, X. Xu, and S. A. Crooker, "Probing the influence of dielectric environment on excitons in monolayer $WSe_2$: insight from high magnetic fields", Nano Letters **16**, 7054–7060 (2016) (cit. on pp. 18, 106).

[253] A. V. Stier, N. P. Wilson, K. A. Velizhanin, J. Kono, X. Xu, and S. A. Crooker, "Magnetooptics of Exciton Rydberg States in a Monolayer Semiconductor", Physical Review Letters **120**, 57405 (2018) (cit. on pp. 18–19, 59).

[254] A. Chernikov, O. Yaffe, B. Kumar, Y. Zhong, C. Nuckolls, and T. F. Heinz, "Spectroscopic Study of Anisotropic Excitons in Single Crystal Hexacene", J. Phys. Chem. Lett. **5**, 3632–3635 (2014) (cit. on p. 18).

[255] K. He, N. Kumar, L. Zhao, Z. Wang, K. F. Mak, H. Zhao, and J. Shan, "Tightly bound excitons in monolayer $WSe_2$", Phys. Rev. Lett. **113**, 26803 (2014) (cit. on p. 19).

[256] Y. Cho and T. C. Berkelbach, "Environmentally sensitive theory of electronic and optical transitions in atomically thin semiconductors", Physical Review B **97**, 41409 (2018) (cit. on p. 19).

[257] T. C. Berkelbach and D. R. Reichman, "Optical and Excitonic Properties of Atomically Thin Transition-Metal Dichalcogenides", Annu. Rev. Condens. Matter Phys. **9**, 379–396 (2018) (cit. on p. 19).

[258] M. Florian, M. Hartmann, A. Steinhoff, J. Klein, A. W. Holleitner, J. J. Finley, T. O. Wehling, M. Kaniber, and C. Gies, "The Dielectric Impact of Layer Distances on Exciton and Trion Binding Energies in van der Waals Heterostructures", Nano Lett. **18**, 2725–2732 (2018) (cit. on p. 19).

[259] B. Cheng, T.-Y. Li, P. Maity, P.-C. Wei, D. Nordlund, K.-T. Ho, D.-H. Lien, C.-H. Lin, R.-Z. Liang, X. Miao, I. A. Ajia, J. Yin, D. Sokaras, A. Javey, I. S. Roqan, O. F. Mohammed, and J.-H. He, "Extremely reduced dielectric confinement in two-dimensional hybrid perovskites with large polar organics", Commun. Phys. **1**, 1–8 (2018) (cit. on pp. 19, 109).

[260] Y. Chen, Y. Sun, J. Peng, J. Tang, K. Zheng, and Z. Liang, "2d ruddlesden–popper perovskites for optoelectronics", Advanced Materials **30**, 1703487 (2018) (cit. on p. 19).

[261] C. R. Dean, A. F. Young, I. Meric, C. Lee, L. Wang, S. Sorgenfrei, K. Watanabe, T. Taniguchi, P. Kim, K. L. Shepard, and J. Hone, "Boron nitride substrates for high-quality graphene electronics", Nature Nanotechnology **5**, 722–726 (2010) (cit. on p. 19).

[262] M. K. L. Man, S. Deckoff-Jones, A. Winchester, G. Shi, G. Gupta, A. D. Mohite, S. Kar, E. Kioupakis, S. Talapatra, and K. M. Dani, "Protecting the properties of monolayer MoS2 on silicon based substrates with an atomically thin buffer", Scientific Reports **6**, 10.1038/srep20890 (2016) (cit. on p. 19).

[263] F. Cadiz, E. Courtade, C. Robert, G. Wang, Y. Shen, H. Cai, T. Taniguchi, K. Watanabe, H. Carrere, D. Lagarde, M. Manca, T. Amand, P. Renucci, S. Tongay, X. Marie, and B. Urbaszek, "Excitonic Linewidth Approaching the Homogeneous Limit in MoS2-Based van der Waals Heterostructures", Phys. Rev. X **7**, 21026 (2017) (cit. on p. 19).

[264] S. Brem, J. Zipfel, M. Selig, A. Raja, L. Waldecker, J. D. Ziegler, T. Taniguchi, K. Watanabe, A. Chernikov, and E. Malic, "Intrinsic lifetime of higher excitonic states in tungsten diselenide monolayers", Nanoscale **11**, 12381–12387 (2019) (cit. on p. 20).

[265] M. M. Glazov, "Phonon wind and drag of excitons in monolayer semiconductors", Physical Review B **100**, 45426 (2019) (cit. on p. 21).

[266] M. M. Glazov, "Quantum Interference Effect on Exciton Transport in Monolayer Semiconductors", Phys. Rev. Lett. **124**, 166802 (2020) (cit. on pp. 21, 85, 108).

[267] G. Moody, J. Schaibley, and X. Xu, "Exciton dynamics in monolayer transition metal dichalcogenides", J. Opt. Soc. Am. B **33**, C39 (2016) (cit. on p. 21).

[268] G.-B. Liu, W.-Y. Shan, Y. Yao, W. Yao, and D. Xiao, "Three-band tight-binding model for monolayers of group-VIB transition metal dichalcogenides", Physical Review B **88**, 85433 (2013) (cit. on p. 21).

[269] M. M. Glazov, T. Amand, X. Marie, D. Lagarde, L. Bouet, and B. Urbaszek, "Exciton fine structure and spin decoherence in monolayers of transition metal dichalcogenides", Physical Review B **89**, 201302 (2014) (cit. on p. 21).

[270] T. C. Berkelbach, M. S. Hybertsen, and D. R. Reichman, "Bright and dark singlet excitons via linear and two-photon spectroscopy in monolayer transition-metal dichalcogenides", Physical Review B **92**, 85413 (2015) (cit. on p. 21).

[271] E. Malic, M. Selig, M. Feierabend, S. Brem, D. Christiansen, F. Wendler, A. Knorr, and G. Berghäuser, "Dark excitons in transition metal dichalcogenides", Physical Review Materials **2**, 10.1103/physrevmaterials.2.014002 (2018) (cit. on pp. 21, 23).

[272] G. Berghäuser, P. Steinleitner, P. Merkl, R. Huber, A. Knorr, and E. Malic, "Mapping of the dark exciton landscape in transition metal dichalcogenides", Physical Review B **98**, 10.1103/physrevb.98.020301 (2018) (cit. on p. 21).

[273] X.-X. Zhang, T. Cao, Z. Lu, Y.-C. Lin, F. Zhang, Y. Wang, Z. Li, J. C. Hone, J. A. Robinson, D. Smirnov, S. G. Louie, and T. F. Heinz, "Magnetic brightening and control of dark excitons in monolayer WSe2", Nature Nanotechnology **12**, 883–888 (2017) (cit. on p. 22).

[274] J. P. Echeverry, B. Urbaszek, T. Amand, X. Marie, and I. C. Gerber, "Splitting between bright and dark excitons in transition metal dichalcogenide monolayers", Physical Review B **93**, 10.1103/physrevb.93.121107 (2016) (cit. on p. 22).

[275] G. Wang, C. Robert, M. Glazov, F. Cadiz, E. Courtade, T. Amand, D. Lagarde, T. Taniguchi, K. Watanabe, B. Urbaszek, and X. Marie, "In-Plane Propagation of Light in Transition Metal Dichalcogenide Monolayers: Optical Selection Rules", Physical Review Letters, 1–7 (2017) (cit. on p. 22).

[276] Z. Li, T. Wang, C. Jin, Z. Lu, Z. Lian, Y. Meng, M. Blei, S. Gao, T. Taniguchi, K. Watanabe, T. Ren, S. Tongay, L. Yang, D. Smirnov, T. Cao, and S.-F. Shi, "Emerging photoluminescence from the dark-exciton phonon replica in monolayer WSe2", Nature Communications **10**, 2469 (2019) (cit. on p. 22).

[277] E. Liu, J. van Baren, C.-T. Liang, T. Taniguchi, K. Watanabe, N. M. Gabor, Y.-C. Chang, and C. H. Lui, "Multipath Optical Recombination of Intervalley Dark Excitons and Trions in Monolayer $WSe_2$", Phys. Rev. Lett. **124**, 196802 (2020) (cit. on p. 22).

[278] M. He, P. Rivera, D. Van Tuan, N. P. Wilson, M. Yang, T. Taniguchi, K. Watanabe, J. Yan, D. G. Mandrus, H. Yu, et al., "Valley phonons and exciton complexes in a monolayer semiconductor", Nature communications **11**, 1–7 (2020) (cit. on pp. 22, 62).

[279] M. Yang, L. Ren, C. Robert, D. Van Tuan, L. Lombez, B. Urbaszek, X. Marie, and H. Dery, "Relaxation and darkening of excitonic complexes in electrostatically doped monolayer $WSe_2$: Roles of exciton-electron and trion-electron interactions", Phys. Rev. B **105**, 85302 (2022) (cit. on pp. 22, 24, 62, 96).

[280] T. Deilmann and K. S. Thygesen, "Finite-momentum exciton landscape in mono-and bilayer transition metal dichalcogenides", 2D Materials **6**, 35003 (2019) (cit. on p. 23).

[281] R. Rosati, K. Wagner, S. Brem, R. Perea-Causin, E. Wietek, J. Zipfel, J. D. Ziegler, M. Selig, T. Taniguchi, K. Watanabe, A. Knorr, A. Chernikov, and E. Malic, "Temporal Evolution of Low-Temperature Phonon Sidebands in Transition Metal Dichalcogenides", ACS Photonics **7**, 2756–2764 (2020) (cit. on pp. 23, 72).

[282] G. Plechinger, P. Nagler, J. Kraus, N. Paradiso, C. Strunk, C. Schüller, and T. Korn, "Identification of excitons, trions and biexcitons in single-layer WS2", physica status solidi (RRL) - Rapid Research Letters **9**, 457–461 (2015) (cit. on p. 23).

[283] Z. Ye, L. Waldecker, E. Y. Ma, D. Rhodes, A. Antony, B. Kim, X.-X. Zhang, M. Deng, Y. Jiang, Z. Lu, D. Smirnov, K. Watanabe, T. Taniguchi, J. Hone, and T. F. Heinz, "Efficient generation of neutral and charged biexcitons in encapsulated WSe2 monolayers", Nature Communications **9**, 3718 (2018) (cit. on p. 23).

[284] P. Nagler, M. V. Ballottin, A. A. Mitioglu, M. V. Durnev, T. Taniguchi, K. Watanabe, A. Chernikov, C. Schüller, M. M. Glazov, P. C. Christianen, and T. Korn, "Zeeman Splitting and Inverted Polarization of Biexciton Emission in Monolayer WS2", Physical Review Letters **121**, 10.1103/physrevlett.121.057402 (2018) (cit. on p. 23).

[285] A. Steinhoff, M. Florian, A. Singh, K. Tran, M. Kolarczik, S. Helmrich, A. W. Achtstein, U. Woggon, N. Owschimikow, F. Jahnke, and X. Li, "Biexciton fine structure in monolayer transition metal dichalcogenides", Nature Physics **14**, 1199–1204 (2018) (cit. on p. 23).

[286] K. F. Mak, K. He, C. Lee, G. H. Lee, J. Hone, T. F. Heinz, and J. Shan, "Tightly bound trions in monolayer MoS2", Nature Materials **12**, 207–211 (2013) (cit. on pp. 23, 96–97).

[287] J. S. Ross, S. Wu, H. Yu, N. J. Ghimire, A. M. Jones, G. Aivazian, J. Yan, D. G. Mandrus, D. Xiao, W. Yao, and X. Xu, "Electrical control of neutral and charged excitons in a monolayer semiconductor", Nature Communications **4**, 1474 (2013) (cit. on pp. 23, 96–97).

[288] G. Plechinger, P. Nagler, A. Arora, R. Schmidt, A. Chernikov, A. G. del Águila, P. C. M. Christianen, R. Bratschitsch, C. Schüller, and T. Korn, "Trion fine structure and coupled spinvalley dynamics in monolayer tungsten disulfide", Nature Communications **7**, 12715 (2016) (cit. on p. 23).

[289] E. Courtade, M. Semina, M. Manca, M. M. Glazov, C. Robert, F. Cadiz, G. Wang, T. Taniguchi, K. Watanabe, M. Pierre, W. Escoffier, E. L. Ivchenko, P. Renucci, X. Marie, T. Amand, and B. Urbaszek, "Charged excitons in monolayer WSe2: Experiment and theory", Physical Review B **96**, 85302 (2017) (cit. on p. 23).

[290] J. Zipfel, K. Wagner, J. D. Ziegler, T. Taniguchi, K. Watanabe, M. A. Semina, and A. Chernikov, "Light–matter coupling and non-equilibrium dynamics of exchange-split trions in monolayer WS2", J. Chem. Phys. **153**, 034706 (2020) (cit. on p. 24).

[291] M. Danovich, V. Zólyomi, and V. I. Fal'ko, "Dark trions and biexcitons in WS2 and WSe2 made bright by e-e scattering", Scientific Reports **7**, 10.1038/srep45998 (2017) (cit. on p. 24).

[292] E. Liu, J. van Baren, Z. Lu, M. M. Altaiary, T. Taniguchi, K. Watanabe, D. Smirnov, and C. H. Lui, "Gate Tunable Dark Trions in Monolayer WSe2", Physical Review Letters **123**, 10.1103/physrevlett.123.027401 (2019) (cit. on pp. 24, 62).

[293] M. Barbone, A. R.-P. Montblanch, D. M. Kara, C. Palacios-Berraquero, A. R. Cadore, D. D. Fazio, B. Pingault, E. Mostaani, H. Li, B. Chen, K. Watanabe, T. Taniguchi, S. Tongay, G. Wang, A. C. Ferrari, and M. Atatüre, "Charge-tuneable biexciton complexes in monolayer WSe2", Nature Communications **9**, 3721 (2018) (cit. on pp. 24, 96).

[294] D. Van Tuan, S.-F. Shi, X. Xu, S. A. Crooker, and H. Dery, "Six-Body and Eight-Body Exciton States in Monolayer $WSe_2$", Phys. Rev. Lett. **129**, 076801 (2022) (cit. on pp. 24, 96).

[295]K. Ema, K. Umeda, M. Toda, C. Yajima, Y. Arai, H. Kunugita, D. Wolverson, and J. Davies, "Huge exchange energy and fine structure of excitons in an organic-inorganic quantum well material", Phys. Rev. B **73**, 241310 (2006) (cit. on p. 24).

[296]J. Even, "Pedestrian Guide to Symmetry Properties of the Reference Cubic Structure of 3D All-Inorganic and Hybrid Perovskites", J. Phys. Chem. Lett. **6**, 2238 (2015) (cit. on p. 24).

[297]R. Ben Aich, S. Ben Radhia, K. Boujdaria, M. Chamarro, and C. Testelin, "Multiband k·p Model for Tetragonal Crystals: Application to Hybrid Halide Perovskite Nanocrystals", J. Phys. Chem. Lett. **11**, 808–817 (2020) (cit. on p. 24).

[298]H.-H. Fang, J. Yang, S. Adjokatse, E. Tekelenburg, M. E. Kamminga, H. Duim, J. Ye, G. R. Blake, J. Even, and M. A. Loi, "Band-Edge Exciton Fine Structure and Exciton Recombination Dynamics in Single Crystals of Layered Hybrid Perovskites", Adv. Funct. Mater. **30**, 1907979 (2020) (cit. on pp. 24, 86).

[299]M. Dyksik, H. Duim, D. K. Maude, M. Baranowski, M. A. Loi, and P. Plochocka, "Brightening of dark excitons in 2D perovskites", Sci. Adv. **7**, eabk0904 (2021) (cit. on pp. 24–25, 86).

[300]H. Fu, L.-W. Wang, and A. Zunger, "Excitonic exchange splitting in bulk semiconductors", Phys. Rev. B **59**, 5568–5574 (1999) (cit. on p. 24).

[301]P. Tamarat, M. I. Bodnarchuk, J.-B. Trebbia, R. Erni, M. V. Kovalenko, J. Even, and B. Lounis, "The ground exciton state of formamidinium lead bromide perovskite nanocrystals is a singlet dark state", Nat. Mater. **18**, 717–724 (2019) (cit. on pp. 24, 86).

[302]T. T. H. Do, A. Granados del Águila, D. Zhang, J. Xing, S. Liu, M. A. Prosnikov, W. Gao, K. Chang, P. C. M. Christianen, and Q. Xiong, "Bright Exciton Fine-Structure in Two-Dimensional Lead Halide Perovskites", Nano Lett. **20**, 5141–5148 (2020) (cit. on p. 25).

[303]K. Posmyk, N. Zawadzka, M. Dyksik, A. Surrente, D. K. Maude, T. Kazimierczuk, A. Babiński, M. R. Molas, W. Paritmongkol, M. Mączka, W. A. Tisdale, P. Płochocka, and M. Baranowski, "Quantification of Exciton Fine Structure Splitting in a Two-Dimensional Perovskite Compound", J. Phys. Chem. Lett. **13**, 4463–4469 (2022) (cit. on p. 25).

[304]R. Canet-Albiach, M. Krečmarová, J. B. Bailach, A. F. Gualdrón-Reyes, J. Rodríguez-Romero, S. Gorji, H. Pashaei-Adl, I. Mora-Seró, J. P. Martínez Pastor, J. F. Sánchez-Royo, and G. Muñoz-Matutano, "Revealing Giant Exciton Fine-Structure Splitting in Two-Dimensional Perovskites Using van der Waals Passivation", Nano Lett. **22**, 7621–7627 (2022) (cit. on p. 25).

[305]F. Thouin, S. Neutzner, D. Cortecchia, V. A. Dragomir, C. Soci, T. Salim, Y. M. Lam, R. Leonelli, A. Petrozza, A. R. S. Kandada, and C. Silva, "Stable biexcitons in two-dimensional metal-halide perovskites with strong dynamic lattice disorder", Phys. Rev. Mater. **2**, 34001 (2018) (cit. on p. 25).

[306]N. S. Makarov, S. Guo, O. Isaienko, W. Liu, I. Robel, and V. I. Klimov, "Spectral and Dynamical Properties of Single Excitons, Biexcitons, and Trions in Cesium–Lead-Halide Perovskite Quantum Dots", Nano Lett. **16**, 2349–2362 (2016) (cit. on pp. 25, 109).

[307]B. Li, H. Huang, G. Zhang, C. Yang, W. Guo, R. Chen, C. Qin, Y. Gao, V. P. Biju, A. L. Rogach, L. Xiao, and S. Jia, "Excitons and Biexciton Dynamics in Single CsPbBr3 Perovskite Quantum Dots", J. Phys. Chem. Lett. **9**, 6934–6940 (2018) (cit. on p. 25).

[308]N. Yarita, T. Aharen, H. Tahara, M. Saruyama, T. Kawawaki, R. Sato, T. Teranishi, and Y. Kanemitsu, "Observation of positive and negative trions in organic-inorganic hybrid perovskite nanocrystals", Physical Review Materials **2**, 116003 (2018) (cit. on p. 25).

[309]S. Nakahara, H. Tahara, G. Yumoto, T. Kawawaki, M. Saruyama, R. Sato, T. Teranishi, and Y. Kanemitsu, "Suppression of Trion Formation in CsPbBr3 Perovskite Nanocrystals by Postsynthetic Surface Modification", J. Phys. Chem. C **122**, 22188–22193 (2018) (cit. on pp. 25, 109).

[310]Y. Kanemitsu, "Trion dynamics in lead halide perovskite nanocrystals", J. Chem. Phys. **151**, 170902 (2019) (cit. on p. 25).

[311]U. N. Huynh, Y. Liu, A. Chanana, D. R. Khanal, P. C. Sercel, J. Huang, and Z. V. Vardeny, "Transient quantum beatings of trions in hybrid organic triiodine perovskite single crystal", Nat. Commun. **13**, 1–11 (2022) (cit. on p. 25).

[312]J. Euvrard, Y. Yan, and D. B. Mitzi, "Electrical doping in halide perovskites", Nat. Rev. Mater. **6**, 531–549 (2021) (cit. on pp. 25, 109).

[313]C. Huang, S. Wu, A. M. Sanchez, J. J. P. Peters, R. Beanland, J. S. Ross, P. Rivera, W. Yao, D. H. Cobden, and X. Xu, "Lateral heterojunctions within monolayer MoSe2-WSe2 semiconductors", Nat. Mater. **13**, 1096–1101 (2014) (cit. on p. 26).

[314]N. Kumar, Q. Cui, F. Ceballos, D. He, Y. Wang, and H. Zhao, "No Title", Nanoscale **6**, 4915–4919 (2014) (cit. on p. 26).

[315]S. Mouri, Y. Miyauchi, M. Toh, W. Zhao, G. Eda, and K. Matsuda, "Nonlinear photoluminescence in atomically thin layeredWSe2arising from diffusion-assisted exciton-exciton annihilation", Physical Review B **90**, 10.1103/physrevb.90.155449 (2014) (cit. on p. 26).

[316]M. Kulig, J. Zipfel, P. Nagler, S. Blanter, C. Schüller, T. Korn, N. Paradiso, M. M. Glazov, and A. Chernikov, "Exciton Diffusion and Halo Effects in Monolayer Semiconductors", Phys. Rev. Lett. **120**, 207401 (2018) (cit. on pp. 26, 77–78).

[317]R. S. Knox and C. E. Swenberg, "Direct Radiative Exciton-Exciton Annihilation", J. Chem. Phys. **44**, 2577–2580 (1966) (cit. on p. 26).

[318]N. S. Ginsberg and W. A. Tisdale, "Spatially Resolved Exciton and Charge Transport in Emerging Semiconductors", Annual Review of Physical Chemistry **71**, 1–30 (2020) (cit. on pp. 27–28, 53).

[319]M. von Smoluchowski, "Zur kinetischen Theorie der Brownschen Molekularbewegung und der Suspensionen", Ann. Phys. **326**, 756–780 (1906) (cit. on p. 27).

[320]P. Drude, "Zur Elektronentheorie der Metalle", Ann. Phys. **306**, 566–613 (1900) (cit. on pp. 27–28).

[321]J. Erland, B. S. Razbirin, K.-H. Pantke, V. G. Lyssenko, and J. M. Hvam, "Exciton diffusion in CdSe", Phys. Rev. B **47**, 3582–3587 (1993) (cit. on p. 28).

[322]L. M. Smith, D. R. Wake, J. P. Wolfe, D. Levi, M. V. Klein, J. Klem, T. Henderson, and H. Morkoç, "Picosecond imaging of photoexcited carriers in quantum wells: Anomalous lateral confinement at high densities", Physical Review B **38**, 5788–5791 (1988) (cit. on p. 28).

[323]H. Zhu, K. Miyata, Y. Fu, J. Wang, P. P. Joshi, D. Niesner, K. W. Williams, S. Jin, and X.-Y. Zhu, "Screening in crystalline liquids protects energetic carriers in hybrid perovskites", Science **353**, 1409–1413 (2016) (cit. on p. 28).

[324]O. V. Mikhnenko, P. W. M. Blom, and T.-Q. Nguyen, "Exciton diffusion in organic semiconductors", Energy Environ. Sci. **8**, 1867–1888 (2015) (cit. on pp. 28, 104).

[325]P. W. Anderson, "Absence of Diffusion in Certain Random Lattices", Phys. Rev. **109**, 1492–1505 (1958) (cit. on p. 28).

[326]D. Emin, *Polarons* (Cambridge University Press, Cambridge, England, UK, Nov. 2012) (cit. on p. 28).

[327]C. Katan, A. D. Mohite, and J. Even, "Entropy in Halide Perovskites", Nat. Mater. **17**, 377 (2018) (cit. on p. 28).

[328]S. Baranovski and O. Rubel, *Discription of charge transport in disorderd semiconductors* (John Wileys and Sons Ltd., 2006), pp. 49–93 (cit. on pp. 28–29).

[329]T. Förster, "Zwischenmolekulare energiewanderung und fluoreszenz", Annalen der Physik **437**, 55–75 (1948) (cit. on p. 28).

[330]D. L. Dexter, "A theory of sensitized luminescence in solids", The Journal of Chemical Physics **21**, 836–850 (1953) (cit. on p. 28).

[331]B. Kim, Y. Luo, D. Rhodes, Y. Bai, J. Wang, S. Liu, A. Jordan, B. Huang, Z. Li, T. Taniguchi, K. Watanabe, J. Owen, S. Strauf, K. Barmak, X. Zhu, and J. Hone, "Free Trions with Near-Unity Quantum Yield in Monolayer MoSe2", ACS Nano **16**, 140–147 (2022) (cit. on p. 33).

[332]A. Castellanos-Gomez, M. Buscema, R. Molenaar, V. Singh, L. Janssen, H. S. J. der Zant, and G. A. Steele, "Deterministic transfer of two-dimensional materials by all-dry viscoelastic stamping", 2D Materials **1**, 11002 (2014) (cit. on p. 35).

[333]A. S. Mayorov, R. V. Gorbachev, S. V. Morozov, L. Britnell, R. Jalil, L. A. Ponomarenko, P. Blake, K. S. Novoselov, K. Watanabe, T. Taniguchi, and A. K. Geim, "Micrometer-Scale Ballistic Transport in Encapsulated Graphene at Room Temperature", Nano Lett. **11**, 2396–2399 (2011) (cit. on p. 38).

[334]S. J. Haigh, A. Gholinia, R. Jalil, S. Romani, L. Britnell, D. C. Elias, K. S. Novoselov, L. A. Ponomarenko, A. K. Geim, and R. Gorbachev, "Cross-sectional imaging of individual layers and buried interfaces of graphene-based heterostructures and superlattices", Nature Materials **11**, 764–767 (2012) (cit. on p. 38).

[335]A. V. Kretinin, Y. Cao, J. S. Tu, G. L. Yu, R. Jalil, K. S. Novoselov, S. J. Haigh, A. Gholinia, A. Mishchenko, M. Lozada, T. Georgiou, C. R. Woods, F. Withers, P. Blake, G. Eda, A. Wirsig, C. Hucho, K. Watanabe, T. Taniguchi, A. K. Geim, and R. V. Gorbachev, "Electronic Properties of Graphene Encapsulated with Different Two-Dimensional Atomic Crystals", Nano Lett. **14**, 3270–3276 (2014) (cit. on p. 38).

[336]E. Khestanova, F. Guinea, L. Fumagalli, A. K. Geim, and I. V. Grigorieva, "Universal shape and pressure inside bubbles appearing in van der Waals heterostructures", Nat. Commun. **7**, 1–10 (2016) (cit. on p. 38).

[337]S. Puebla, H. Li, H. Zhang, and A. Castellanos-Gomez, "Apparent Colors of 2D Materials", Adv. Photonics Res. **3**, 2100221 (2022) (cit. on p. 40).

[338] A. Weston, Y. Zou, V. Enaldiev, A. Summerfield, N. Clark, V. Zólyomi, A. Graham, C. Yelgel, S. Magorrian, M. Zhou, J. Zultak, D. Hopkinson, A. Barinov, T. H. Bointon, A. Kretinin, N. R. Wilson, P. H. Beton, V. I. Fal'ko, S. J. Haigh, and R. Gorbachev, "Atomic reconstruction in twisted bilayers of transition metal dichalcogenides", Nat. Nanotechnol. **15**, 592–597 (2020) (cit. on p. 46).

[339] S. J. Byrnes, "Multilayer optical calculations", arXiv preprint arXiv:1603.02720 (2016) (cit. on p. 50).

[340] J. Zipfel, "Excitons in monolayer semiconductors in complex environments and under external fields", PhD thesis (University of Regensburg, June 2020) (cit. on p. 50).

[341] F. Dirnberger, J. D. Ziegler, P. E. F. Junior, R. Bushati, T. Taniguchi, K. Watanabe, J. Fabian, D. Bougeard, A. Chernikov, and V. M. Menon, "Quasi-1D exciton channels in strain-engineered 2D materials", Sci. Adv. **7**, eabj3066 (2021) (cit. on p. 56).

[342] S. Bertolazzi, J. Brivio, and A. Kis, "Stretching and Breaking of Ultrathin MoS2", ACS Nano **5**, 9703–9709 (2011) (cit. on p. 56).

[343] A. Castellanos-Gomez, R. Roldán, E. Cappelluti, M. Buscema, F. Guinea, H. S. J. van der Zant, and G. a. Steele, "Local strain engineering in atomically thin MoS2.", Nano Lett. **13**, 5361–5366 (2013) (cit. on pp. 56–57, 61).

[344] C. Lee, X. Wei, J. W. Kysar, and J. Hone, "Measurement of the elastic properties and intrinsic strength of monolayer graphene", Science **321**, 385–388 (2008) (cit. on p. 56).

[345] R. C. Cooper, C. Lee, C. A. Marianetti, X. Wei, J. Hone, and J. W. Kysar, "Nonlinear elastic behavior of two-dimensional molybdenum disulfide", Phys. Rev. B **87**, 035423 (2013) (cit. on p. 56).

[346] K. Zollner, P. E. Faria Junior, and J. Fabian, "Strain-tunable orbital, spin-orbit, and optical properties of monolayer transition-metal dichalcogenides", Physical Review B **100**, 195126 (2019) (cit. on pp. 56–57, 61).

[347] H. Moon, G. Grosso, C. Chakraborty, C. Peng, T. Taniguchi, K. Watanabe, and D. Englund, "Dynamic Exciton Funneling by Local Strain Control in a Monolayer Semiconductor", Nano Lett. **20**, 6791–6797 (2020) (cit. on pp. 56, 65, 106).

[348] M. G. Harats, J. N. Kirchhof, M. Qiao, K. Greben, and K. I. Bolotin, "Dynamics and efficient conversion of excitons to trions in non-uniformly strained monolayer ws 2", Nature Photonics **14**, 324–329 (2020) (cit. on pp. 56, 106).

[349] M. R. Rosenberger, H.-J. Chuang, M. Phillips, V. P. Oleshko, K. M. McCreary, S. V. Sivaram, C. S. Hellberg, and B. T. Jonker, "Twist Angle-Dependent Atomic Reconstruction and Moiré Patterns in Transition Metal Dichalcogenide Heterostructures", ACS Nano **14**, 4550–4558 (2020) (cit. on p. 57).

[350] J. Holler, S. Meier, M. Kempf, P. Nagler, K. Watanabe, T. Taniguchi, T. Korn, and C. Schüller, "Low-frequency Raman scattering in WSe 2 - MoSe 2 heterobilayers: Evidence for atomic reconstruction", Appl. Phys. Lett. **117**, 013104 (2020) (cit. on p. 57).

[351] I. Niehues, R. Schmidt, M. Drüppel, P. Marauhn, D. Christiansen, M. Selig, G. Berghäuser, D. Wigger, R. Schneider, L. Braasch, R. Koch, A. Castellanos-Gomez, T. Kuhn, A. Knorr, E. Malic, M. Rohlfing, S. Michaelis de Vasconcellos, and R. Bratschitsch, "Strain control of exciton–phonon coupling in atomically thin semiconductors", Nano letters **18**, 1751–1757 (2018) (cit. on pp. 57, 70).

[352] O. B. Aslan, M. Deng, and T. F. Heinz, "Strain tuning of excitons in monolayer WSe 2", Phys. Rev. B **98**, 115308 (2018) (cit. on pp. 57, 70).

[353] F. Carrascoso, H. Li, R. Frisenda, and A. Castellanos-Gomez, "Strain engineering in single-, bi-and tri-layer mos2, mose2, ws2 and wse2", Nano Research **14**, 1698–1703 (2021) (cit. on p. 57).

[354] M. Feierabend, Z. Khatibi, G. Berghäuser, and E. Malic, "Dark exciton based strain sensing in tungsten-based transition metal dichalcogenides", Physical Review B **99**, 195454 (2019) (cit. on p. 61).

[355] M. W. Iqbal, K. Shahzad, R. Akbar, and G. Hussain, "A review on Raman finger prints of doping and strain effect in TMDCs", Microelectron. Eng. **219**, 111152 (2020) (cit. on p. 61).

[356] J.-S. Tu, S. Borghardt, D. Grützmacher, and B. E. Kardynał, "Experimental observation of a negative grey trion in an electron-rich WSe2 monolayer", J. Phys.: Condens. Matter **31**, 415701 (2019) (cit. on p. 62).

[357] K. Wagner, J. Zipfel, R. Rosati, E. Wietek, J. D. Ziegler, S. Brem, R. Perea-Causin, T. Taniguchi, K. Watanabe, M. M. Glazov, E. Malic, and A. Chernikov, "Nonclassical Exciton Diffusion in Monolayer WSe2", Phys. Rev. Lett. **127**, 76801 (2021) (cit. on pp. 64, 85, 108).

[358] A. Tyurnina, D. A. Bandurin, E. Khestanova, V. G. Kravets, M. Koperski, F. Guinea, A. N. Grigorenko, A. K. Geim, and I. V. Grigorieva, "Strained Bubbles in van der Waals Heterostructures as Local Emitters of Photoluminescence with Adjustable Wavelength", ACS Photonics **6**, 516–524 (2019) (cit. on pp. 65, 106).

[359] R. Rosati, S. Brem, R. Perea-Causin, R. Schmidt, I. Niehues, S. Michaelis de Vasconcellos, R. Bratschitsch, and E. Malic, "Strain-dependent exciton diffusion in transition metal dichalcogenides", 2D Mater. **8**, 15030 (2021) (cit. on pp. 65, 70, 106).

[360] R. Rosati, R. Schmidt, S. Brem, R. Perea-Causin, I. Niehues, J. Kern, J. A. Preuß, R. Schneider, S. Michaelis de Vasconcellos, R. Bratschitsch, and E. Malic, "Dark exciton anti-funneling in atomically thin semiconductors", Nat. Commun. **12**, 1–7 (2021) (cit. on pp. 65, 106).

[361] J. Zipfel, M. Kulig, R. Perea-Causin, S. Brem, J. D. Ziegler, R. Rosati, T. Taniguchi, K. Watanabe, M. M. Glazov, E. Malic, and A. Chernikov, "Exciton diffusion in monolayer semiconductors with suppressed disorder", Phys. Rev. B **101**, 115430 (2020) (cit. on pp. 69, 77).

[362] Z. Khatibi, M. Feierabend, M. Selig, S. Brem, C. Linderälv, P. Erhart, and E. Malic, "Impact of strain on the excitonic linewidth in transition metal dichalcogenides", 2D Materials **6**, 015015 (2018) (cit. on p. 70).

[363] R. Yang, R. Li, Y. Cao, Y. Wei, Y. Miao, W. L. Tan, X. Jiao, H. Chen, L. Zhang, Q. Chen, H. Zhang, W. Zou, Y. Wang, M. Yang, C. Yi, N. Wang, F. Gao, C. R. McNeill, T. Qin, J. Wang, and W. Huang, "Oriented Quasi-2D Perovskites for High Performance Optoelectronic Devices", Adv. Mater. **30**, 1804771 (2018) (cit. on p. 73).

[364] C. Ortiz-Cervantes, P. Carmona-Monroy, and D. Solis-Ibarra, "Two-Dimensional Halide Perovskites in Solar Cells: 2D or not 2D?", ChemSusChem **12**, 1560–1575 (2019) (cit. on p. 73).

[365] J. D. Ziegler, J. Zipfel, B. Meisinger, M. Menahem, X. Zhu, T. Taniguchi, K. Watanabe, O. Yaffe, D. A. Egger, and A. Chernikov, "Fast and Anomalous Exciton Diffusion in Two-Dimensional Hybrid Perovskites", Nano Lett. **20**, 6674–6681 (2020) (cit. on p. 74).

[366] J. D. Ziegler, K.-Q. Lin, B. Meisinger, X. Zhu, M. Kober-Czerny, P. K. Nayak, C. Vona, T. Taniguchi, K. Watanabe, C. Draxl, H. J. Snaith, J. M. Lupton, D. A. Egger, and A. Chernikov, "Excitons at the Phase Transition of 2D Hybrid Perovskites", ACS Photonics **2022**, 10.1021/acsphotonics.2c01035 (2022) (cit. on pp. 74, 80).

[367] G. M. Akselrod, P. B. Deotare, N. J. Thompson, J. Lee, W. A. Tisdale, M. A. Baldo, V. M. Menon, and V. Bulović, "Visualization of exciton transport in ordered and disordered molecular solids", Nat. Commun. **5**, 3646 (2014) (cit. on p. 77).

[368] M. Delor, H. L. Weaver, Q. Yu, and N. S. Ginsberg, "Imaging material functionality through three-dimensional nanoscale tracking of energy flow", Nat. Mater. **19**, 56–62 (2020) (cit. on pp. 77, 104, 107).

[369] N. Kumar, Q. Cui, F. Ceballos, D. He, Y. Wang, and H. Zhao, "Exciton-exciton annihilation in $MoSe_2$ monolayers", Phys. Rev. B **89**, 125427 (2014) (cit. on p. 77).

[370] M. Seitz, A. J. Magdaleno, N. Alcázar-Cano, M. Meléndez, T. J. Lubbers, S. W. Walraven, S. Pakdel, E. Prada, R. Delgado-Buscalioni, and F. Prins, "Exciton diffusion in two-dimensional metal-halide perovskites", Nat. Commun. **11**, 2035 (2020) (cit. on pp. 77, 80, 107–108).

[371] J. T. Warren, K. E. O'Hara, and J. P. Wolfe, "Two-body decay of thermalized excitons in CuO2", Phys. Rev. B **61**, 8215–8223 (2000) (cit. on p. 78).

[372] Z. Gan, X. Wen, C. Zhou, W. Chen, F. Zheng, S. Yang, J. A. Davis, P. C. Tapping, T. W. Kee, H. Zhang, and B. Jia, "Transient Energy Reservoir in 2D Perovskites", Adv. Opt. Mater. **7**, 1900971 (2019) (cit. on p. 86).

[373] G. Folpini, D. Cortecchia, A. Petrozza, and A. R. Srimath Kandada, "The role of a dark exciton reservoir in the luminescence efficiency of two-dimensional tin iodide perovskites", J. Mater. Chem. C **8**, 10889–10896 (2020) (cit. on p. 86).

[374] M. Mayers, L. Z. Tan, D. A. Egger, A. M. Rappe, and D. R. Reichman, "How Lattice and Charge Fluctuations Control Carrier Dynamics in Halide Perovskites", Nano Lett. **18**, 8041–8046 (2018) (cit. on pp. 87, 93, 108).

[375] Z. Guo, X. Wu, T. Zhu, X. Zhu, and L. Huang, "Electron-Phonon Scattering in Atomically Thin 2D Perovskites", ACS Nano **10**, 9992–9998 (2016) (cit. on pp. 87, 108).

[376] M. Dyksik, H. Duim, X. Zhu, Z. Yang, M. Gen, Y. Kohama, S. Adjokatse, D. K. Maude, M. A. Loi, D. A. Egger, M. Baranowski, and P. Plochocka, "Broad Tunability of Carrier Effective Masses in Two-Dimensional Halide Perovskites", ACS Energy Lett. **5**, 3609–3616 (2020) (cit. on pp. 88, 93).

[377] M. Menahem, Z. Dai, S. Aharon, R. Sharma, M. Asher, Y. Diskin-Posner, R. Korobko, A. M. Rappe, and O. Yaffe, "Strongly Anharmonic Octahedral Tilting in Two-Dimensional Hybrid Halide Perovskites", ACS Nano **15**, 10153–10162 (2021) (cit. on p. 88).

[378] O. Yaffe, A. Chernikov, Z. M. Norman, Y. Zhong, A. Velauthapillai, A. van der Zande, J. S. Owen, and T. F. Heinz, "Excitons in ultrathin organic-inorganic perovskite crystals", Physical Review B **92**, 45414 (2015) (cit. on pp. 90, 92, 101).

[379] Y. Cho and T. C. Berkelbach, "Optical Properties of Layered Hybrid Organic-Inorganic Halide Perovskites: A Tight-Binding GW-BSE Study", J. Phys. Chem. Lett. **10**, 6189–6196 (2019) (cit. on pp. 90–91, 101).

[380] J. Even, L. Pedesseau, and C. Katan, "Understanding Quantum Confinement of Charge Carriers in Layered 2D Hybrid Perovskites", ChemPhysChem **15**, 3733–3741 (2014) (cit. on pp. 92, 97, 109).

[381] M. J. Schilcher, P. J. Robinson, D. J. Abramovitch, L. Z. Tan, A. M. Rappe, D. R. Reichman, and D. A. Egger, "The Significance of Polarons and Dynamic Disorder in Halide Perovskites", ACS Energy Lett. **6**, 2162–2173 (2021) (cit. on pp. 93, 108).

[382] K. Kheng, R. Cox, M. d'Aubigné, F. Bassani, K. Saminadayar, and S. Tatarenko, "Observation of negatively charged excitons X- in semiconductor quantum wells", Phys. Rev. Lett. **71**, 1752–1755 (1993) (cit. on p. 95).

[383] G. Astakhov, D. Yakovlev, V. Kochereshko, W. Ossau, J. Nürnberger, W. Faschinger, and G. Landwehr, "Charged excitons in ZnSe-based quantum wells", Phys. Rev. B **60**, R8485–R8488 (1999) (cit. on p. 95).

[384] T. C. Berkelbach, M. S. Hybertsen, and D. R. Reichman, "Theory of neutral and charged excitons in monolayer transition metal dichalcogenides", Physical Review B **88**, 45318 (2013) (cit. on p. 96).

[385] V. Huard, R. T. Cox, K. Saminadayar, A. Arnoult, and S. Tatarenko, "Bound States in Optical Absorption of Semiconductor Quantum Wells Containing a Two-Dimensional Electron Gas", Phys. Rev. Lett. **84**, 187–190 (2000) (cit. on p. 97).

[386] A. Esser, R. Zimmermann, and E. Runge, "Theory of Trion Spectra in Semiconductor Nanostructures", Phys. status solidi **227**, 317–330 (2001) (cit. on p. 97).

[387] A. Esser, E. Runge, R. Zimmermann, and W. Langbein, "Trions in GaAs Quantum Wells: Photoluminescence Lineshape Analysis", Phys. Stat. Sol. **178**, 489 (2000) (cit. on p. 97).

[388] J. Zipfel, K. Wagner, M. A. Semina, J. D. Ziegler, T. Taniguchi, K. Watanabe, M. M. Glazov, and A. Chernikov, "Electron recoil effect in electrically tunable $MoSe_2$ monolayers", Phys. Rev. B **105**, 75311 (2022) (cit. on p. 97).

[389] K.-Q. Lin, C. S. Ong, S. Bange, P. E. Faria Junior, B. Peng, J. D. Ziegler, J. Zipfel, C. Bäuml, N. Paradiso, K. Watanabe, T. Taniguchi, C. Strunk, B. Monserrat, J. Fabian, A. Chernikov, D. Y. Qiu, S. G. Louie, and J. M. Lupton, "Narrow-band high-lying excitons with negative-mass electrons in monolayer WSe2", Nat. Commun. **12**, 1–8 (2021) (cit. on p. 98).

[390] H. H. Fang, B. Han, C. Robert, M. A. Semina, D. Lagarde, E. Courtade, T. Taniguchi, K. Watanabe, T. Amand, B. Urbaszek, M. M. Glazov, and X. Marie, "Control of the Exciton Radiative Lifetime in van der Waals Heterostructures", Phys. Rev. Lett. **123**, 67401 (2019) (cit. on p. 103).

[391] C. Robert, R. Picard, D. Lagarde, G. Wang, J. P. Echeverry, F. Cadiz, P. Renucci, A. Högele, T. Amand, X. Marie, I. C. Gerber, and B. Urbaszek, "Excitonic properties of semiconducting monolayer and bilayer MoTe2", Phys. Rev. B **94**, 155425 (2016) (cit. on p. 103).

[392] H. Lee, Y. Koo, J. Choi, S. Kumar, H.-T. Lee, G. Ji, S. H. Choi, M. Kang, K. K. Kim, H.-R. Park, H. Choo, and K.-D. Park, "Drift-dominant exciton funneling and trion conversion in 2D semiconductors on the nanogap", Sci. Adv. **8**, eabm5236 (2022) (cit. on p. 106).

[393] D. Thureja, A. Imamoglu, T. Smoleński, I. Amelio, A. Popert, T. Chervy, X. Lu, S. Liu, K. Barmak, K. Watanabe, T. Taniguchi, D. J. Norris, M. Kroner, and P. A. Murthy, "Electrically tunable quantum confinement of neutral excitons", Nature **606**, 298–304 (2022) (cit. on p. 106).

[394] L. Waldecker, A. Raja, M. Rösner, C. Steinke, A. Bostwick, R. J. Koch, C. Jozwiak, T. Taniguchi, K. Watanabe, E. Rotenberg, T. O. Wehling, and T. F. Heinz, "Rigid Band Shifts in Two-Dimensional Semiconductors through External Dielectric Screening", Phys. Rev. Lett. **123**, 206403 (2019) (cit. on p. 106).

[395] T. Yu and M. W. Wu, "Valley depolarization dynamics and valley Hall effect of excitons in monolayer and bilayer $MoS_2$", Phys. Rev. B **93**, 045414 (2016) (cit. on p. 106).

[396] M. M. Glazov and L. E. Golub, "Skew Scattering and Side Jump Drive Exciton Valley Hall Effect in Two-Dimensional Crystals", Phys. Rev. Lett. **125**, 157403 (2020) (cit. on p. 106).

[397] J. Holler, L. Bauriedl, T. Korn, A. Seitz, F. Özyigit, M. Eichinger, C. Schüller, K. Watanabe, T. Taniguchi, C. Strunk, and N. Paradiso, "Air tightness of hBN encapsulation and its impact on Raman spectroscopy of van der Waals materials", 2D Materials **7**, 15012 (2019) (cit. on p. 107).

[398] M. Seitz, P. Gant, A. Castellanos-Gomez, and F. Prins, "Long-Term Stabilization of Two-Dimensional Perovskites by Encapsulation with Hexagonal Boron Nitride", Nanomaterials **9**, 1120 (2019) (cit. on p. 107).

[399] Z.-G. Yu, "Omnidirectional exciton diffusion in quasi-2D hybrid organic– inorganic perovskites", J. Chem. Phys. **156**, 124706 (2022) (cit. on p. 108).

[400] M. M. Glazov, Z. A. Iakovlev, and S. Refaely-Abramson, "Phonon-induced exciton weak localization in two-dimensional semiconductors", arXiv, 10.48550/arXiv.2208.08501 (2022) (cit. on p. 108).

[401] A. M. Berghuis, T. V. Raziman, A. Halpin, S. Wang, A. G. Curto, and J. G. Rivas, "Effective Negative Diffusion of Singlet Excitons in Organic Semiconductors", J. Phys. Chem. Lett. **12**, 1360–1366 (2021) (cit. on p. 108).

[402] Q. Liu, K. Wei, Y. Tang, Z. Xu, X. Cheng, and T. Jiang, "Visualizing Hot-Carrier Expansion and Cascaded Transport in WS2 by Ultrafast Transient Absorption Microscopy", Adv. Sci. **9**, 2105746 (2022) (cit. on p. 108).

[403] D. Beret, L. Ren, C. Robert, L. Foussat, P. Renucci, D. Lagarde, A. Balocchi, T. Amand, B. Urbaszek, K. Watanabe, T. Taniguchi, X. Marie, and L. Lombez, "Non-linear diffusion of negatively charged excitons in WSe2 monolayer", arXiv, 10.48550/arXiv.2208.00734 (2022) (cit. on p. 108).

[404] M. Kober-Czerny, S. G. Motti, P. Holzhey, B. Wenger, J. Lim, L. M. Herz, and H. J. Snaith, "Excellent Long-Range Charge-Carrier Mobility in 2D Perovskites", Adv. Funct. Mater. **32**, 2203064 (2022) (cit. on p. 108).

[405] I. C. Smith, E. T. Hoke, D. Solis-Ibarra, M. D. McGehee, and H. I. Karunadasa, "A Layered Hybrid Perovskite Solar-Cell Absorber with Enhanced Moisture Stability", Angew. Chem. Int. Ed. **53**, 11232–11235 (2014) (cit. on p. 108).

[406] H. Lai, D. Lu, Z. Xu, N. Zheng, Z. Xie, and Y. Liu, "Organic-Salt-Assisted Crystal Growth and Orientation of Quasi-2D Ruddlesden–Popper Perovskites for Solar Cells with Efficiency over 19%", Adv. Mater. **32**, 2001470 (2020) (cit. on p. 108).

[407] Y. Zhang and N.-G. Park, "Quasi-Two-Dimensional Perovskite Solar Cells with Efficiency Exceeding 22%", ACS Energy Lett. **7**, 757–765 (2022) (cit. on p. 108).

[408] A. A. Sutanto, P. Caprioglio, N. Drigo, Y. J. Hofstetter, I. Garcia-Benito, V. I. E. Queloz, D. Neher, M. K. Nazeeruddin, M. Stolterfoht, Y. Vaynzof, and G. Grancini, "2D/3D perovskite engineering eliminates interfacial recombination losses in hybrid perovskite solar cells", Chem **7**, 1903–1916 (2021) (cit. on p. 108).

[409] X. Li, J. M. Hoffman, and M. G. Kanatzidis, "The 2d halide perovskite rulebook: how the spacer influences everything from the structure to optoelectronic device efficiency", Chemical Reviews **121**, PMID: 33476131, 2230–2291 (2021) (cit. on p. 108).

[410] G. Wu, R. Liang, M. Ge, G. Sun, Y. Zhang, and G. Xing, "Surface Passivation Using 2D Perovskites toward Efficient and Stable Perovskite Solar Cells", Adv. Mater. **34**, 2105635 (2022) (cit. on p. 108).

[411] S. Sidhik, Y. Wang, M. De Siena, R. Asadpour, A. J. Torma, T. Terlier, K. Ho, W. Li, A. B. Puthirath, X. Shuai, A. Agrawal, B. Traore, M. Jones, R. Giridharagopal, P. M. Ajayan, J. Strzalka, D. S. Ginger, C. Katan, M. A. Alam, J. Even, M. G. Kanatzidis, and A. D. Mohite, "Deterministic fabrication of 3D/2D perovskite bilayer stacks for durable and efficient solar cells", Science **377**, 1425–1430 (2022) (cit. on p. 108).

[412] M. A. Mahmud, T. Duong, J. Peng, Y. Wu, H. Shen, D. Walter, H. T. Nguyen, N. Mozaffari, G. D. Tabi, K. R. Catchpole, K. J. Weber, and T. P. White, "Origin of Efficiency and Stability Enhancement in High-Performing Mixed Dimensional 2D-3D Perovskite Solar Cells: A Review", Adv. Funct. Mater. **32**, 2009164 (2022) (cit. on p. 108).

[413] A. J. Magdaleno, M. Seitz, M. Frising, A. Herranz de la Cruz, A. I. Fernandez-Dominguez, and F. Prins, "Efficient interlayer exciton transport in two- dimensional metal-halide perovskites", Mater. Horiz. **8**, 639–644 (2021) (cit. on p. 108).

[414] C. Gehrmann and D. A. Egger, "Dynamic shortening of disorder potentials in anharmonic halide perovskites", Nat. Commun. **10**, 1–9 (2019) (cit. on p. 108).

[415] A. Lacroix, G. T. de Laissardière, P. Quémerais, J.-P. Julien, and D. Mayou, "Modeling of Electronic Mobilities in Halide Perovskites: Adiabatic Quantum Localization Scenario", Phys. Rev. Lett. **124**, 196601 (2020) (cit. on p. 108).

[416]C. Gehrmann, S. Caicedo-Dávila, X. Zhu, and D. A. Egger, "Transversal Halide Motion Intensifies Band-To-Band Transitions in Halide Perovskites", Adv. Sci. **9**, 2200706 (2022) (cit. on p. 108).

[417]G. Rainò, G. Nedelcu, L. Protesescu, M. I. Bodnarchuk, M. V. Kovalenko, R. F. Mahrt, and T. Stöferle, "Single Cesium Lead Halide Perovskite Nanocrystals at Low Temperature: Fast Single-Photon Emission, Reduced Blinking, and Exciton Fine Structure", ACS Nano **10**, 2485 (2016) (cit. on p. 109).

[418]A. V. Koudinov, C. Kehl, A. V. Rodina, J. Geurts, D. Wolverson, and G. Karczewski, "Suris Tetrons: Possible Spectroscopic Evidence for Four-Particle Optical Excitations of a Two-Dimensional Electron Gas", Phys. Rev. Lett. **112**, 147402 (2014) (cit. on p. 109).

[419]M. Sidler, P. Back, O. Cotlet, A. Srivastava, T. Fink, M. Kroner, E. Demler, and A. Imamoglu, "Fermi polaron-polaritons in charge-tunable atomically thin semiconductors", Nature Physics **13**, 255–261 (2016) (cit. on p. 109).

[420]D. K. Efimkin and A. H. MacDonald, "Many-body theory of trion absorption features in two-dimensional semiconductors", Phys. Rev. B **95**, 35417 (2017) (cit. on p. 109).

[421]K. Walzer, B. Maennig, M. Pfeiffer, and K. Leo∗, "Highly Efficient Organic Devices Based on Electrically Doped Transport Layers", Chem. Rev. **2007**, , 4 (2007) (cit. on p. 110).

[422]B. Lüssem, M. Riede, and K. Leo, "Doping of organic semiconductors", Phys. Status Solidi A **210**, 9–43 (2012) (cit. on p. 110).

[423]D. Sanvitto, F. Pulizzi, A. J. Shields, P. C. M. Christianen, S. N. Holmes, M. Y. Simmons, D. A. Ritchie, J. C. Maan, and M. Pepper, "Observation of Charge Transport by Negatively Charged Excitons", Science **294**, 837–839 (2001) (cit. on p. 110).

[424]F. Pulizzi, D. Sanvitto, P. C. M. Christianen, A. J. Shields, S. N. Holmes, M. Y. Simmons, D. A. Ritchie, M. Pepper, and J. C. Maan, "Optical imaging of trion diffusion and drift in GaAs quantum wells", Phys. Rev. B **68**, 205304 (2003) (cit. on p. 110).

[425]F. Takano, T. Tokizaki, H. Akinaga, S. Kuroda, and K. Takita, "Real-time observation of charged exciton drift in modulation-doped (Cd,Mn)Te quantum well", Phys. Rev. B **71**, 125326 (2005) (cit. on p. 110).

[426]T. Kato and T. Kaneko, "Transport Dynamics of Neutral Excitons and Trions in Monolayer WS 2", ACS Nano **10**, 9687–9694 (2016) (cit. on p. 110).

[427]T. Chervy, P. Knüppel, H. Abbaspour, M. Lupatini, S. Fält, W. Wegscheider, M. Kroner, and A. xn–Imamolu-hmc, "Accelerating Polaritons with External Electric and Magnetic Fields", Phys. Rev. X **10**, 011040 (2020) (cit. on p. 110).

[428]P. Soubelet, J. Klein, J. Wierzbowski, R. Silvioli, F. Sigger, A. V. Stier, K. Gallo, and J. J. Finley, "Charged Exciton Kinetics in Monolayer MoSe2 near Ferroelectric Domain Walls in Periodically Poled LiNbO3", Nano Lett. **21**, 959–966 (2021) (cit. on p. 110).

[429]G. Cheng, B. Li, Z. Jin, M. Zhang, and J. Wang, "Observation of Diffusion and Drift of the Negative Trions in Monolayer WS2", Nano Lett. **21**, 6314–6320 (2021) (cit. on p. 110).

# List of Publications

1. K.Q. Lin, **J.D. Ziegler**, M.A. Semina, J.V. Mamedov, K. Watanabe, T. Taniguchi, S. Bange, A. Chernikov, M.M. Glazov and J.M. Lupton. *High-lying valley-polarized trions in 2D semiconductors*, Nat Commun., 13, 6980 (2022)
2. **J.D. Ziegler**, K-Q. Lin, B. Meisinger, X. Zhu, M. Kober-Czerny, P.K. Nayak, C. Vona, T. Taniguchi, K. Watanabe, C. Draxl, H.J. Snaith, J.M. Lupton, D.A. Egger and A. Chernikov. *Robust excitons across the phase transition of two-dimensional hybrid perovskites*, ACS Photonics, 9, 11, 3609 –3616 (2022)
3. M. M. Glazov, F. Dirnberger, V.M. Menon, T. Taniguchi, K. Watanabe, D. Bougeard, **J. D. Ziegler** and A. Chernikov. *Exciton fine structure splitting and linearly polarized emission in strained transition-metal dichalcogenide monolayers*, Phys. Rev. B., 105, 075311 (2022)
4. J. Zipfel, K. Wagner, M.A. Semina, **J. D. Ziegler**, T. Taniguchi, K. Watanabe, M. M. Glazov and A. Chernikov. *Electron recoil effect in electrically tunable MoSe2 monolayers*, Phys. Rev. B., 105, 075311 (2022)
5. M. Karpinska, J. Jasinski, R. Kempt, **J.D. Ziegler**, H. Sansom, T. Taniguchi, K. Watanabe, H. J. Snaith, A. Surrente, M. Dyksik, D.K. Maude, L. Klopotowksi, A. Chernikov, A. Kuc, M. Baranowski and P. Plochocka. *Interlayer excitons in MoSe2/2D perovskite hybrid heterostructures – the interplay between charge and energy transfer*, Nanoscale, 14, 8085-8095 (2022)
6. D. Erkenstein, S. Brem, K. Wagner, R. Gillen, R. Perea-Causín, **J.D. Ziegler**, T. Taniguchi, K. Watanabe, A. Knorr, E. Malic and A. Chernikov. *Dark exciton-exciton annihilation in monolayer WSe2*, Phys. Rev. B., 104, L241406 (2021)
7. V. Funk. K. Wagner, E. Wietek, **J. D. Ziegler**, J. Förste, J. Lindlau, M. Förg, K. Watanabe, T. Taniguchi, A. Chernikov and A. Högele. *Spectral asymmetry of phonon sideband luminescence in monolayer and bilayer WSe2*, Phys. Rev. Research, 3, L042019 (2021)

8. F. Dirnberger*, **J.D. Ziegler***, P.E. Faria Junior, R. Bushati, T. Taniguchi, K. Watanabe, J. Fabian, A. Chernikov, and V.M. Menon. *Quasi-1D Exciton channels in strain-engineered 2D materials*, Science Advances, 7, 44 (2021)
*both authors contributed equally to the work

9. K-Q Lin, C.S. Ong, S. Bange, P.E. Faria Junior, B. Peng, **J. D. Ziegler**, J. Zipfel, C. Bäuml, N. Paradiso, K. Watanabe, T. Taniguchi, C. Strunk, B. Monserrat, J. Fabian, A. Chernikov, D.Y. Qiu, S.G. Louie, J.M. Lupton. *Narrow-band high-lying excitons with negative-mass electrons in monolayer WSe2*, Nature Commun 12, 5500 (2021)

10. K. Wagner, J. Zipfel, R. Rosati, E. Wietek, **J. D. Ziegler**, S. Brem, R. Perea-Causín, T. Taniguchi, K. Watanabe, M. M. Glazov, E. Malic and A. Chernikov. *Nonclassical Exciton Diffusion in Monolayer WSe2*, Phys. Rev. Lett., 127, 076801 (2021)

11. R. Rosati, K. Wagner, S. Brem, R. Perea-Causín, **J.D. Ziegler**, J. Zipfel, T. Taniguchi, K. Watanabe, E. Malic and A. Chernikov. *Non-equilibrium diffusion of dark excitons in atomically thin semiconductors*, Nanoscale, 13, 19966-19972 (2021)

12. K. Wagner, E. Wietek, **J. D. Ziegler**, M. Semina, T. Taniguchi, K. Watanabe, J. Zipfel, M. M. Glazov and A. Chernikov. *Autoionization and dressing of excited excitons by free carriers in monolayer WSe2*, Phys. Rev. Lett., 125, 267401 (2020)

13. R. Rosati, K. Wagner, S. Brem, R. Perea-Causín, E. Wietek, J. Zipfel, **J.D. Ziegler**, M. Selig, T. Taniguchi, K. Watanabe, A. Knorr, E. Malic and A. Chernikov. *Temporal evolution of low-temperature phonon sidebands in transition metal dichalcogenides*, ACS Photonics 2020, 7, 10, 2756–2764 (2020)

14. **J.D. Ziegler**, J. Zipfel, B. Meisinger, M. Menahem, X. Zhu, T. Taniguchi, K. Watanabe, O. Yaffe, D. A. Egger and A. Chernikov. *Fast and Anomalous Exciton Diffusion in Two-Dimensional Hybrid Perovskites*, Nano Lett., 20, 9, 6674–6681 (2020)

15. J. Zipfel, K. Wagner, **J. D. Ziegler**, T. Taniguchi, K. Watanabe, M. A. Semina and A. Chernikov. *Light-matter coupling and non-equilibrium dynamics of exchange-split trions in monolayer WS2*, Journal of Chem. Phys., 153, 034706 (2020)

16. J. Zipfel, M. Kulig, R. Perea-Causín, S. Brem, **J. D. Ziegler**, R. Rosati, T. Taniguchi, K. Watanabe, M.M. Glazov, E. Malic and A. Chernikov. E*xciton*

*diffusion in monolayer semiconductors with suppressed disorder*, Phys. Rev. B., 101, 115430 (2020)

17. R. Perea-Causin, S. Brem, R. Rosati, R. Jago, M. Kulig, **J. D. Ziegler**, J. Zipfel, A. Chernikov and E. Malic. *Exciton propagation and halo formation in two-dimensional materials*, Nano Lett., 19, 7317-7323 (2019)
18. A. Raja, L. Waldecker, J. Zipfel, Y. Cho, S. Brem, **J. D. Ziegler**, M. Kulig, T. Taniguchi, K. Watanabe, E. Malic, T. F. Heinz, T. C. Berkelbach and A. Chernikov. *Dielectric disorder in two-dimensional materials*, Nature Nano., 14, 832-837 (2019)
19. R. Perea-Causn, S. Brem, R. Rosati, R. Jago, M. Kulig, **J. D. Ziegler**, J. Zipfel, A. Chernikov and E. Malic. *Exciton propagation and halo formation in two-dimensional materials*, Nano Lett., 19, 7317-7323 (2019)
20. S. Brem, J. Zipfel, M. Selig, A. Raja, L. Waldecker, **J. D. Ziegler**, T. Taniguchi, K. Watanabe, A. Chernikov and E. Malic, *Intrinsic lifetime of higher excitonic states in tungsten diselenide monolayers*, Nanoscale, 11, 12381-12387 (2019)

**In revision**:

21. **J.D. Ziegler**, Y. Cho, S. Terres, M. Menahem, T. Taniguchi, K. Watanabe, O. Yaffe, T.C. Berkelbach and A. Chernikov. *Electrically tunable hybrid heterostructures based on ultrathin 2D perovskites*
22. K.Q. Lin, P.E. Faria Junior, **J.D. Ziegler**, F. Hofmann, K. Watanabe, T. Taniguchi, A. Chernikov, J. Fabian, S. Bange and J.M. Lupton. *UV-emissive interlayer excitons and trions from bilayer WSe2*
23. K. Wagner, Z. Iakovlev, **J. D. Ziegler**, M. Cuccu, T. Taniguchi, K. Watanabe, M. M. Glazov and A. Chernikov. *Diffusion of excitons immersed in a two-dimensional Fermi sea of free charges*
24. S. Dong, S. Beaulieu, M. Selig, P. Rosenzweig, D. Christiansen, T. Pincelli, M. Dendzik, **J. D. Ziegler**, J. Maklar, R. P. Xian, A. Neef, A. Mohammed, A. Schulz, M. Stadler, M. Jetter, P. Michler, T. Taniguchi, K. Watanabe, H. Takagi, U. Starke, A. Chernikov, Martin Wolf, H. Nakamura, A. Knorr, L. Rettig and R. Ernstorfer. *Observation of ultrafast interfacial Meitner-Auger energy transfer in a van der Waals heterostructure*, arXiv:2108.06803 (2021)

# Acknowledgements

First of all, I want to thank Prof. David A. Egger, who agreed to be the second examiner of this work as well as Prof. Dominique Bougeard and Prof. Vladimir Braun who volunteered as additional examiners.

All the results from the different projects would not have been possible without the fruitful collaborations, sample and knowlegde exchange and helpful discussions with our colleagues. Entries are in no particular order.

1. *Department of Physics, University of Regensburg, Germany*
   Christian Schüller
   Dominique Bougeard
   Imke Gronwald
   Viola Zeller
   John M. Lupton
   Kaiqiang Lin
   Jaroslav Fabian
   Paulo E. Faria Junior

2. *Technical University Munich, Germany*
   David A. Egger
   Zhangzhou Zhu

3. *Department of Physics, City College of New York, USA*
   Vinod M. Menon
   Florian G. Dirnberger

4. *Department of Chemistry, Columbia University, New York, USA*
   Timothy C. Berkelbach
   Yeongsu Cho

5. *Ioffe Institute, Saint Petersburg, Russian Federation*
   Mikhail M. Glazov

Marina Semina

6. *Laboratoire National des Champs Magnetiques Intenses, Grenoble and Toulouse, France and Department of Experimental Physics, Faculty of Fundamental Problems of Technology, Wroclaw University of Science and Technology, Poland*
   Paulina Plochocka
   Jakub Jasinski
   Miriam Karpińska

7. *Department of Materials and Interfaces, Weizmann Institute of Science, Rehovot, Israel*
   Omer Yaffe
   Matan Menahem
8. *Fachbereich Physik, Philipps-Universität, Marburg, Germany and Department of Physics, Chalmers University of Technology, Gothenburg, Sweden*
   Ermin Malic
   Raül Perea-Causin
   Daniel Erkenstein
   Samuel Brem
   Roberto Rosati

9. *National Institute for Materials Science, Ibaraki, Japan*
   Takashi Taniguchi
   Kenji Watanabe

# Words of gratitude

At last, follow particularly important pages, as I am especially grateful to those people who made the last three years possible and even more important, fun.
There are a few people I want to thank in particular:
First and foremost my advisor, *Alexey Chernikov*, who not only advise, but also mentor and help beyond scientific questions. I really do thank you for all of those things I could learn from you and the trust you put in me the past three years. I really enjoyed working with you, as you always trusted my scientific understanding and took my arguments seriously. I hope that we may continue working together in the same joyful and pleasant way.
*Koloman Wagner*, my colleague and partner in crime from the very beginning when we started our master thesis. From the start of our PhD projects we already were the perfect fit, helping each other whenever we can and you were always there for me when I needed you, even for a bloody lift to the doctor. Unfortunately, we could not enjoy much conference time, but even more I enjoyed our nearly weekly coffee meetings during the writing of the thesis. We shared a dubious flat in Dresden for 2 weeks, which was just as funny as sleeping on Marzias floor with you and your company made the trips to Dresden much less tiring. During the many talks in the last few years you changed my view on arts and even uncovered my poorly educated art mind. Thanks for being my colleague and friend, it could not have been funnier and better.
*Florian Dirnberger* for being an amazing lab partner and turning into a real friend! Your enthusiasm for science and enjoyment of life is literally contagious, regardless whether we actually discuss about the shape of our strain potential, baking bread or cheese making. Naturally, I enjoyed the times outside the lab even more, in particular competing in squash or finishing the partner-boulder together! Lastly, many thanks for joining me in Boston and hosting me in New York and for showing me around Manhattan (and for showing me *the* Manhattan), a trip I will never forget.
*Jonas Zipfel* for being amazing supervisor and colleague. Thank you for showing me everything you know and lending me some of your scientific self-esteem. Lab and office time was always easy going with you, and even more I enjoyed the conference trips around the world from St. Petersburg to Hawaii. Here, our common

ground on enjoying good food culminated in eating Poke bowl twice a day and even more when you were hosting me for a week in Berkeley, where without any hesitation you welcomed me to your group and home!
*Kai-Qiang Lin*, for trusting my exfoliation skills and being a close colleague from the beginning. Working with you was a charm and thanks for helping me in many projects. I really enjoyed our afternoon walks with icecream or coffee, but even more the dinner where you showed me authentic chinese cuisine and even showed me how to cook them!
*Edith Wietek*, Special thanks for letting me crash on your couch and then even having the coffee ready jsut for me in the morning!
*Sophia Terres*, my fellow perovskite comrade, many thanks for helping me from the start in the projects! Without hesitation you always supported me, even for the dirty work of sorting through the exfoliation trash and introduced me to k-pop and korean food. With your chemical skills and quick learning the perovskites are in the best hands!
*Marzia Cuccu*, despite not really knowing us for long and just after moving in, you gave Koloman and me shelter for the first few weeks in dresden, many thanks for that! Already before moving to Dresden, I really enjoyed learning from your italian cooking skills.
*Marius Markl*, thanks for being a great master student and despite having to deal with a stressed supervisor always happy, motivated and up for a coffee.
Furthermore, I thank everyone who supported me during the last three years and made the projects work. Special thanks to the Helium guys for really always providing freshly drawn liquid helium, despite Koloman and me ordering at short notice. Sebastian Bange, many thanks for always dropping everything and solving my Labview issues and problems with the cryostat and especially your joy and motivation for solving problems. I also want to thank Imke Gronwald for your help in the chemistry lab and Martin Furthmaier, Sebastian Krug, and Fritz Wünsch for always having time for us when we had a problem. Also the mechanical workshop and especially the electronic workshop and Dieter Riedl, who quickly had the perfect idea in mind providing important upgrades for our setup.

Lastly, the most important people, first my girlfriend *Helena* for always being there for me, helping me deal with irrational referee reports, your endless support when I destroyed a sample and giving me new motivation. Special thanks for proof reading this thesis, it improved a lot. *Andi*, for helping in hard times in science and private life, always up for a coffee, beer or sushi. Many thanks for keeping me mentally sane and physically fit during all this time by hard competitions

from frisbee over squash to spikeball. *Benni*, for the welcoming distractions with Negronis and showing me one of the best music bands in the world.

I would also like to thank*my parents and grandparents*, my brother *Patrick* and all my friends for relentlessly asking when I will finally be finished. Nonetheless, they were always supportive, took at lot of time to give advice where they could and always provide a welcoming distraction from work. All in all, thank you all for contributing that the time just flew by the last few years.

Thanks to all of you!
**von ganzem Herz, Danke!**